Jordan Journal of Mechanical and Industrial Engineering (JJMIE)

JJMIE is a high-quality scientific journal devoted to fields of Mechanical and Industrial Engineering. It is published by the Hashemite University in corporation with the Jordanian Scientific Research Support Fund.

SUBMISSION ADDRESS:

Prof. **Mousa S. Mohsen**, Editor-in-Chief
Jordan Journal of Mechanical & Industrial Engineering,
Hashemite University, PO Box 330127, Zarqa, 13133 , Jordan
E-mail: jjmie@hu.edu.jo

Hashemite Kingdom of Jordan

Hashemite University

Jordan Journal of Mechanical and Industrial Engineering

JJMIE

An International Peer-Reviewed Scientific Journal

Special issue devoted for selected papers presented at the Seventh Jordanian International Mechanical Engineering Conference (JIMEC'7), September 27 - 29, 2010, Amman, Jordan.

http://jjmie.hu.edu.jo/

ISSN 1995-6665

Jordan Journal of Mechanical and Industrial Engineering (JJMIE)

JJMIE is a high-quality scientific journal devoted to fields of Mechanical and Industrial Engineering. It is published by the Hashemite University in corporation with the Jordanian Scientific Research Support Fund.

Introduction: The Editorial Board is very committed to build the Journal as one of the leading international journals in mechanical and industrial engineering sciences in the next few years. With the support of the Ministry of Higher Education and Scientific Research and Jordanian Universities, it is expected that a heavy resource to be channeled into the Journal to establish its international reputation. The Journal's reputation will be enhanced from arrangements with several organizers of international conferences in publishing selected best papers of the conference proceedings.

Aims and Scope: Jordan Journal of Mechanical and Industrial Engineering (JJMIE) is a refereed international journal to be of interest and use to all those concerned with research in various fields of, or closely related to, mechanical and industrial engineering disciplines. Jordan Journal of Mechanical and Industrial Engineering aims to provide a highly readable and valuable addition to the literature which will serve as an indispensable reference tool for years to come. The coverage of the journal includes all new theoretical and experimental findings in the fields of mechanical and industrial engineering or any closely related fields. The journal also encourages the submission of critical review articles covering advances in recent research of such fields as well as technical notes.

Guide for Authors

Manuscript Submission

High-quality submissions to this new journal are welcome now and manuscripts may be either submitted online or mail.

Online: For online submission upload one copy of the full paper including graphics and all figures at the online submission site, accessed via E-mail: jjmie@hu.edu.jo. The manuscript must be written in MS Word Format. All correspondence, including notification of the Editor's decision and requests for revision, takes place by e-mail and via the Author's homepage, removing the need for a hard-copy paper trail.

By Mail: Manuscripts (1 original and 3 copies) accompanied by a covering letter may be sent to the Editor-in-Chief. However, a copy of the original manuscript, including original figures, and the electronic files should be sent to the Editor-in-Chief. Authors should also submit electronic files on disk (one disk for text material and a separate disk for graphics), retaining a backup copy for reference and safety.

Note that contributions may be either submitted online or sent by mail. Please do NOT submit via both routes. This will cause confusion and may lead to delay in article publication. Online submission is preferred.

Submission address and contact:

Prof. **Mousa S. Mohsen**, Editor-in-Chief
Jordan Journal of Mechanical & Industrial Engineering,
Hashemite University,
PO Box 330127, Zarqa, 13133 , Jordan
E-mail: jjmie@hu.edu.jo

Types of contributions: Original research papers

Corresponding author: Clearly indicate who is responsible for correspondence at all stages of refereeing and publication, including post-publication. Ensure that telephone and fax numbers (with country and area code) are provided in addition to the e-mail address and the complete postal address. Full postal addresses must be given for all co-authors.

Original material: Submission of an article implies that the work described has not been published previously (except in the form of an abstract or as part of a published lecture or academic thesis), that it is not under consideration for publication elsewhere, that its publication is approved by all authors and that, if accepted, it will not be published elsewhere in the same form, in English or in any other language, without the written consent of the Publisher. Authors found to be deliberately contravening the submission guidelines on originality and exclusivity shall not be considered for future publication in this journal.

Supplying Final Accepted Text on Disk: If online submission is not possible: Once the paper has been accepted by the editor, an electronic version of the text should be submitted together with the final hardcopy of the manuscript. The electronic version must match the hardcopy exactly. We accept MS Word format only. Always keep a backup copy of the electronic file for reference and safety. Label the disk with your name. Electronic files can be stored on CD.

Notification: Authors will be notified of the acceptance of their paper by the editor. The Publisher will also send a notification of receipt of the paper in production.

Copyright: All authors must sign the Transfer of Copyright agreement before the article can be published. This transfer agreement enables Jordan Journal of Mechanical and Industrial Engineering to protect the copyrighted material for the authors, but does not relinquish the authors' proprietary rights. The copyright transfer covers the exclusive rights to reproduce and distribute the article, including reprints, photographic reproductions, microfilm or any other reproductions of similar nature and translations.

PDF Proofs: One set of page proofs in PDF format will be sent by e-mail to the corresponding author, to be checked for typesetting/editing. The corrections should be returned within 48 hours. No changes in, or additions to, the accepted (and subsequently edited) manuscript will be allowed at this stage. Proofreading is solely the author's responsibility. Any queries should be answered in full. Please correct factual errors only, or errors introduced by typesetting. Please note that once your paper has been proofed we publish the identical paper online as in print.

Author Benefits

Page charge: Publication in this journal is free of charge.

Free off-prints: Three journal issues of which the article appears in along with twenty-five off-prints will be supplied free of charge to the corresponding author. Corresponding authors will be given the choice to buy extra off-prints before printing of the article.

Manuscript Preparation:

General: Editors reserve the right to adjust style to certain standards of uniformity. Original manuscripts are discarded after publication unless the Publisher is asked to return original material after use. If online submission is not possible, an electronic copy of the manuscript on disk should accompany the final accepted hardcopy version. Please use MS Word for the text of your manuscript.

Structure: Follow this order when typing manuscripts: Title, Authors, Affiliations, Abstract, Keywords, Introduction, Main text, Conclusions, Acknowledgements, Appendix, References, Figure Captions, Figures and then Tables. For submission in hardcopy, do not import figures into the text - see Illustrations. For online submission, please supply figures imported into the text AND also separately as original graphics files. Collate acknowledgements in a separate section at the end of the article and do not include them on the title page, as a footnote to the title or otherwise.

Text Layout: Use double spacing and wide (3 cm) margins. Ensure that each new paragraph is clearly indicated. Present tables and figure legends on separate pages at the end of the manuscript. If possible, consult a recent issue of the journal to become familiar with layout and conventions. All footnotes (except for table and corresponding author footnotes) should be identified with superscript Arabic numbers. To conserve space, authors are requested to mark the less important parts of the paper (such as records of experimental results) for printing in smaller type. For long papers (more that 4000 words) sections which could be deleted without destroying either the sense or the continuity of the paper should be indicated as a guide for the editor. Nomenclature should conform to that most frequently used in the scientific field concerned. Number all pages consecutively; use 12 or 10 pt font size and standard fonts. If submitting in hardcopy, print the entire manuscript on one side of the paper only.

Corresponding author: Clearly indicate who is responsible for correspondence at all stages of refereeing and publication, including post-publication. The corresponding author should be identified with an asterisk and footnote. Ensure that telephone and fax numbers (with country and area code) are provided in addition to the e-mail address and the complete postal address. Full postal addresses must be given for all co-authors. Please consult a recent journal paper for style if possible.

Abstract: A self-contained abstract outlining in a single paragraph the aims, scope and conclusions of the paper must be supplied.

Keywords: Immediately after the abstract, provide a maximum of six keywords (avoid, for example, 'and', 'of'). Be sparing with abbreviations: only abbreviations firmly established in the field may be eligible.

Symbols: All Greek letters and unusual symbols should be identified by name in the margin, the first time they are used.

Units: Follow internationally accepted rules and conventions: use the international system of units (SI). If other quantities are mentioned, give their equivalent in SI.

Maths: Number consecutively any equations that have to be displayed separately from the text (if referred to explicitly in the text).

References: All publications cited in the text should be presented in a list of references following the text of the manuscript.

Text: Indicate references by number(s) in square brackets in line with the text. The actual authors can be referred to, but the reference number(s) must always be given.

List: Number the references (numbers in square brackets) in the list in the order in which they appear in the text.

Examples:

Reference to a journal publication:

[1] M.S. Mohsen, B.A. Akash, "Evaluation of domestic solar water heating system in Jordan using analytic hierarchy process". Energy Conversion & Management, Vol. 38, No. 9, 1997, 1815-1822.

Reference to a book:

[2] Strunk Jr W, White EB. The elements of style. 3rd ed. New York: Macmillan; 1979.

Reference to a conference proceeding:

[3] B. Akash, S. Odeh, S. Nijmeh, "Modeling of solar-assisted double-tube evaporator heat pump system under local climate conditions". 5th Jordanian International Mechanical Engineering Conference, Amman, Jordan, 2004.

Reference to a chapter in an edited book:

[4] Mettam GR, Adams LB. How to prepare an electronic version of your article. In: Jones BS, Smith RZ, editors. Introduction to the electronic age, New York: E-Publishing Inc; 1999, p. 281-304

Free Online Color: If, together with your accepted article, you submit usable color and black/white figures then the journal will ensure that these figures will appear in color on the journal website electronic version.

Tables: Tables should be numbered consecutively and given suitable captions and each table should begin on a new page. No vertical rules should be used. Tables should not unnecessarily duplicate results presented elsewhere in the manuscript (for example, in graphs). Footnotes to tables should be typed below the table and should be referred to by superscript lowercase letters.

JJMIE

Volume 5 , Number 1, February 2011
ISSN 1995-6665

Jordan Journal of Mechanical and Industrial Engineering

Editorial Preface

This special issue of Jordan Journal of Mechanical and Industrial Engineering (JJMIE) contains selected papers contributed to the Seventh Jordanian International Mechanical Engineering Conference (JIMEC'7) held in September 27–29, 2010 in Amman , Jordan; the Conference was organized by Jordan Engineers Association (JEA). This conference was an attempt to address issues in research and developments in the various fields of mechanical engineering. JIMEC'7 was a fruitful scientific gathering that provided an international forum for engineers and researchers. It covered important issues in mechanical engineering such as new and renewable energies, industrial engineering, thermal engineering, applied mechanics, mechatronics, and modeling and simulation.

I take this opportunity to thank all of those who have contributed to the issue, and also those scientists who, often on short notice, were kind enough to provide informed and valuable opinions on the submitted manuscripts. All the articles in this issue were thoroughly refereed, and I particularly thank the unnamed referees for their careful and timely job. Finally I would like to thank Prof. Mohammad Dado and Prof. Omar Badran, the guest editors of this special issue for their efforts and editorial help.

Prof. Mousa S. Mohsen

Editor-in-Chief

Hashemite University

Zarqa, February 2011

JJMIE

Volume 5, Number 1, Febreuary 2011
ISSN 1995-6665

Jordan Journal of Mechanical and Industrial Engineering www.jjmie.hu.edu.jo

JJMIE

Volume 5, Number 1, February 2011
ISSN 1995-6665
Pages 1 - 8

Jordan Journal of Mechanical and Industrial Engineering

Modeling and Optimization for Disassembly Planning

Ahmed Azab, Aiman Ziout, and Waguih ElMaraghy

Intelligent Manufacturing Systems (IMS) Centre, University of Windsor, Canada

Abstract

For the past two decades, increased efforts by both governments and the general public have been enforced through stricter legislations and more awareness to make manufacturing more environmentally conscious. Product refurbishing and component re-use are being applied on a wider scale worldwide. Disassembly, hence, has attracted more attention both in academia and the industry. Concepts and methods for disassembly planning should be further developed to support this new manufacturing environment. A semi-generative macro disassembly process planning approach based on the Traveling Salesperson formulation has been developed and is reported in this paper. Precedence graphs, which depict the precedence relationships between disassembly operations, are being utilized. The problem of generating optimal macro-level process plans is combinatorial in nature and proven NP-hard. Hence, a random-based hill-climbing heuristic based on Simulated Annealing is tailored for this problem. Finally, a realistic case study is presented to illustrate the working of the proposed methodology. The presented method produced good quality suboptimal solutions and is proven efficient in terms of computation time as demonstrated by the obtained results.

Keywords: Disassembly, Process Planning, Mathematical Programming, Non-traditional Optimization

1. Introduction

Short technology lifecycle and ever-changing customer needs shorten product life cycle [1]. This contributes to the increasing rate of products disposal at their end of life; these products are dumped to the environment causing different impacts [2]. Many governments respond to the environmental problems caused by the industry by introducing and forcing new environmental legislations, which regulate waste management and recycling of products at its end-of life. Industries have to adapt with these new environmental regulations, which force the manufacturers to be held responsible of their products throughout the phases of its life cycle, including end-of-life phases. Product life cycle engineering (LCE) incorporates sustainability issues in product design at its early development stages [3]. LCE aims at optimizing the entire product life cycle including end-of-life phase through reusing, remanufacturing, or recycling retired products [1]. To facilitate these options product disassembly is needed at product end-of life.

Product disassembly is needed not only for end-of-life purposes, but also for product service and maintenance during product useful life. Because of this, product disassembly has been receiving more attention by both the industry and academia [4]. Product disassembly can be defined as a systematic method for separating a product into its constituent parts, components, subassemblies or other grouping [5]. Disassembly process has two main issues. First, is to determine to which level disassembly should be done. Disassembly level is usually based on the optimal economical and environmental benefits of product disassembly. For this paper, complete disassembly of the products is carried out; i.e., non-selective. Second is determining the optimal sequence of disassembly processes. Optimal sequence of the disassembly processes is the scope of this paper. Automated and hybrid disassembly systems lack the ability to handle the variations in the incoming flow of collected product. Hence, for the considered products range (household devices) where many variants exist for every model, manual assembly was advised. A case study of a coffee maker will be used to demonstrate the validity and effectiveness of the methodology.

2. Conceptual model

Disassembly sequence planning is critical in minimizing resources invested and maximizing the level of automation of the disassembly process and the quality of parts recovered [6]. Generally, an assembly that consists of many components can be decomposed via a multitude of sequences [7]. Although, the disassembly sequence planning literature has benefited from assembly sequence planning, there are several characteristic differences between the two processes. In other words, disassembly in most cases is not the reverse of assembly and hence, this invalidates the direct use of plans generated for assembly for the use of disassembly and vice versa [6]. For a more detailed account of the main differences between the two process, see [7].

Assembly plans are ordered sequences of operations that transform one configuration of parts into another. The amount and type of detail to be included in process planning is a critical design issue [8]; the more detail is included the more difficult the planning problem could be. Hence, it was suggested that planning be divided into two consecutive phases [9]: macro planning concerned with high-level decisions such as identification of the planning tasks and their sequencing, followed by a more thorough micro planning, which would take into account the finer details of a disassembly plan such as setup (fixtures), tooling, end-effectors, trajectory planning, collision avoidance and generation of executable robot program files in case of robotic/flexible automated assembly- and the like.

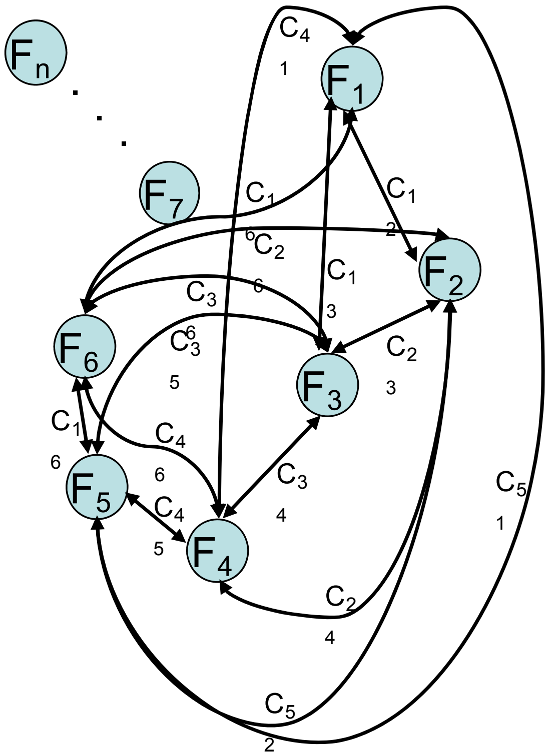

Figure 1. Problem is modeled as TSP problem, where n features $\{F_1, F_2, \ldots, F_n\}$ are to be sequenced

The problem of macro-level disassembly planning is proven to be of combinatorial nature. For systematic algorithmic, graph theoretic and mathematical methods of the problem at hand, see [10-13]. It is important to note that few attempts have been made in the literature to classify the different graphical representations and data structures used to model precedence relationships and sequences; for an example of these works, see [14]. In this paper, an implicit form of representations have been used, which is the precedence graph (figure 4).

According to [15], the sum of operation times in disassembly depends on tool change times because the pure operation time does not depend on its immediate preceding operations; hence, the non-dependent sequence disassembly time. Therefore, in the limit the optimum is the point where the changeover time is minimum. The problem of ordering n disassembly operations is formulated in this work as a Travelling Salesperson Problem (TSP), where each disassembly task is modelled as a city that has to be visited once and only once by a salesperson (see figure 1). The main constraint is precedence relations between disassembly operations. Sequence independent operation times are assumed. Authors in [16] classified quantitatively a disassembly task according to task difficulty and performance. Their five categories included accessibility, positioning, force, base time and one last special category named *"special"* that covers circumstances not considered in their standard task model. In the proposed time objective function of the TSP model, it is required to find the optimal tour that would minimize the total distance travelled by the salesperson such that the optimal solution obtained contains no sub-tours. In this case, the total travel to be minimized is that of the disassembly tool such that all the tasks would be performed with a minimum total transient time between each two consecutive tasks. The time objective function, as mentioned earlier, is composed mainly of three different components: part orientation changes, tool changes, and tool traverse. Tool traverse in this case is quite indicative of accessibility. Rectilinear distances were taken. Currently, it is being investigated how to develop a CAD macro to measure the exact distances between successive features and avoid collision in the to-be-generated tool path. Setup change (part orientation) cost has been taken of the highest cost. A ration of 3:1 was used between the part orientation and the tool changeover cost components. As for the tool traverse, a speed of 0.1 unit distance/unit time was applied for the case study.

3. Solution method

In disassembly planning, the objective is to sequence a global set of operations of a given product, subject to a number of precedence constraints. This problem has already been proven to be NP-hard. Hence, a new search heuristic based on Simulated Annealing (SA) has been developed. SA is a hill-climbing search method suitable for solving combinatorial problems as well as continuous problems with multi-modal objective functions [17]. A search heuristic based on SA is tailored towards the problem at hand.

The proposed algorithm is detailed in figure 2; it is comprised of two nested loops, an outer loop where the annealing temperature (t) decreases and an inner one, which iterates a number of loops that decrease with t. In the inner loop new moves to neighboring solutions are accepted if they are of better quality to allow for hill climbing; lower quality solutions are also accepted with an exponential probability distribution. An algorithm is developed to validate the generated relaxed sequences against the precedence constraints and, then as needed, repair them if no valid feasible solutions are generated after a certain number of moves. The reason behind this validation process is that the solution space before the application of the constraints is factorial in size; it is also believed that the size of this part of the solution space is exponential in nature, which renders the search infeasible after applying the constraints. Therefore, it would be inefficient to wait until a feasible solution is generated randomly since the probability of its generation was shown to be poorly low. Also a Genetic Algorithms mutation operator is applied at the end of each outer loop to increase the chances of exploring more parts of the feasible solution space. The best solution found is always stored and updated. Generation of the objective function cost matrices for the different configurations of a given part was automated using an algorithm that exploited the symmetry property of the objective function matrices.

4. Case study

The product chosen is a household device. Mr. Coffee® is a popular brand of coffee makers. Figure 3 shows the coffee machine disassembled and in an exploded view. Part count for this example is 25 (see Table 1). The basic idea for the operation of the coffee maker is the use of electrical heating element (coil) which is assembled together with metal tube. The theory of operation of this device is as follows: the cold water contained in the water reservoir pass through the metal tube, the water reaches boiling due to the heat coming from the heating element; this forces the boiling water to climb up the metal tube to the top and then dripping through the grains inside the filter.

The purpose of the disassembly of the coffee maker could be either for part reuse or material recycling. In either case disassembly is required to obtain the parts for reuse or separating incompatible material. Since electrical wire cannot be used again because of safety reasons, hence, destructive disassembly for theses component is a valid option. All disassembly operations have been carried out manual. Complete disassembly was required (not selective). Non destructive disassembly was performed, except for the electrical wires and connectors as explained before. Setups used and preferred product orientations were selected based on the ergonomics and accessibility. No power tools were used. See figure 4 for the precedence diagram

Except for the electrical wires and connectors as explained before. Setup the screw driver's head used for each is different. Operation 18a is the scenario followed solving this case study. For table 2, tool 1 was no tool (i.e., by hand); tool 2 is screw driver (cross headed); tool 3 is screw driver (star headed); tool 4 is pliers and finally tool 5 is a wire cutter. For product orientation, *"V"* indicates a vertical product s used and preferred product orientations were selected based on the ergonomics and accessibility. No power tools were used. See figure 4 for the precedence diagram.

Disassembly operations with their respective required tooling, part orientations/setups and coordinates are given in Table 3 (see Appendix). It is worth noting that operations 18a and 18b are the same operation except that the screw driver's head used for each is different. Operation 18a is the scenario followed solving this case study. For table 2, tool 1 was no tool (i.e., by hand); tool 2 is screw driver (cross headed); tool 3 is screw driver (star headed); tool 4 is pliers and finally tool 5 is a wire cutter. For product orientation, *"V"* indicates a vertical orientation whereas *"H"* indicates a horizontal one. Note, when a disassembly operation involves the disassembly of more than one part, the farthest part is considered for the location info. That is to be more conservative. For the origin, see figure 3.

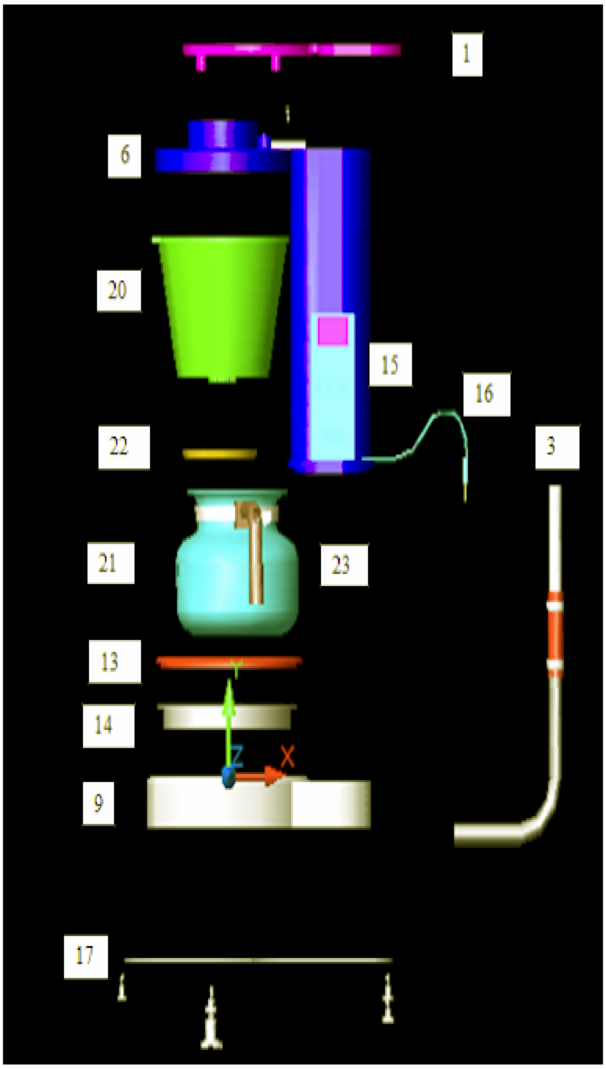

Figure 3. Exploded View of Coffee Maker

Ten SA runs were performed for the disassembly of the coffee maker. The near optimal operation sequences are given in Table 2. The mean and standard deviation of the objective function values are 8.8 and 1.95 time units respectively.

For this case study, it can be concluded from the small difference in magnitude (2.96 time units) between the best objective function values obtained and the averages, as well as the small values of the standard deviation that the results obtained were consistent. In many cases, more than

One solution is obtained with close value of the objective function. The search algorithm parameters were tested to arrive at the best working ranges. Figure 5 is exemplary; it demonstrates the output and convergence for one of the runs.

© 2011 Jordan Journal of Mechanical and Industrial Engineering. All rights reserved – Volume 5, Number 1 (ISSN 1995-6665)

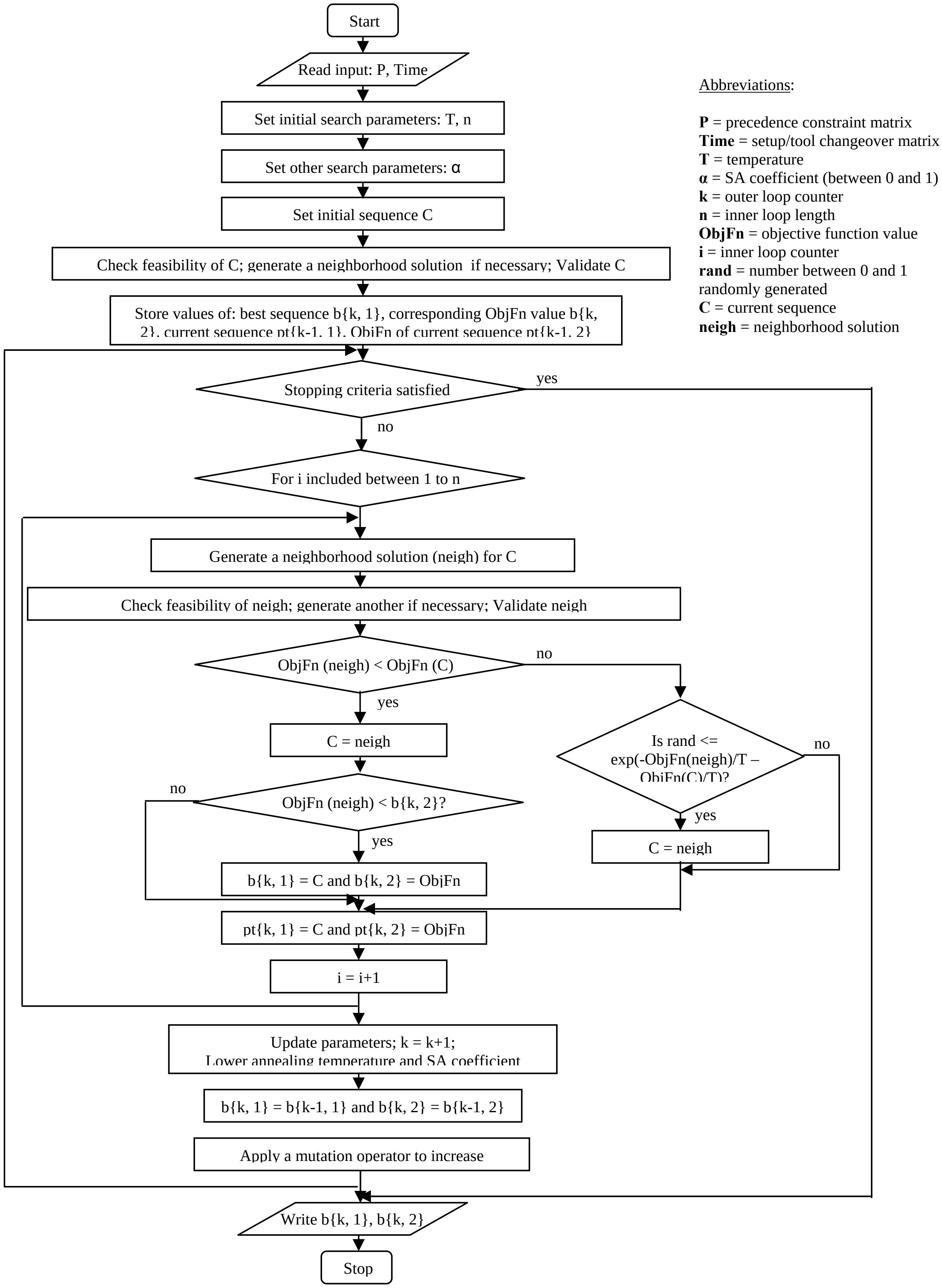

Figure 2. Flow chart of the developed Simulated Annealing algorithm

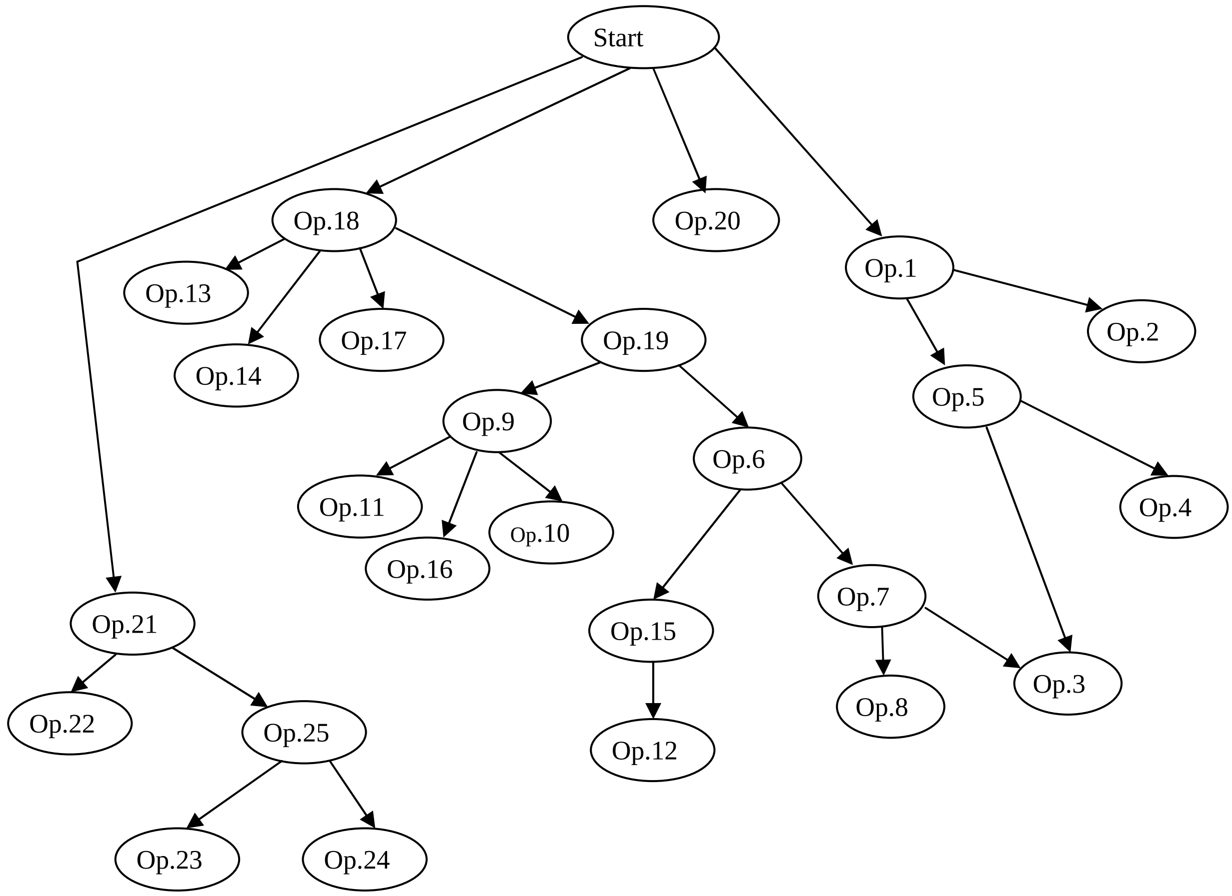

Figure 4. The precedence diagram

Table 1. Bill of Materials for the Coffee Maker

#	Part Name	Quantity	#	Part Name	Quantity
01	Top cover's screws	1	16	Electrical cord	1
02	Top cover	3	17	Bottom cover	1
03	Hot water pipe	1	18	Bottom cover's screws	6
04	Small metal plate	1	19	Water reservoir's screws	3
05	Metal plate's screws	2	20	Coffee filter case	1
06	Water reservoir	1	21	Pot	1
07	Clips	4	22	Pot's lid	1
08	Connection hoses	4	23	Pot's handle	1
09	Base	1	24	Pot's ring	1
10	Electrical wires	2	25	Handle's screw	1
11	Electrical connector	2			
12	Thermo switch	1			
13	Heating plate	1			
14	Support ring	1			
15	Control unit	1			

Table 2. Planning runs results for the coffee maker case study

#	Plan Sequences	Objective Function Value (Time Units)
1st Run	21 1 18 5 19 4 9 6 25 16 7 3 20 24 17 8 23 14 15 10 2 13 22 12 11	10.76
2nd Run	21 18 1 19 9 5 25 16 10 6 23 11 7 8 4 22 3 15 12 2 24 17 14 20 13	5.96
3rd Run	20 18 19 9 10 6 16 7 1 5 4 21 17 15 12 8 11 25 24 23 14 3 22 2 13	7.44
4th Run	19 9 6 1 18 16 5 21 14 7 10 2 4 15 13 22 12 25 24 20 8 3 23 17 11	10.38
5th Run	**20 18 1 5 19 6 2 21 14 9 25 24 23 15 17 7 3 13 22 8 12 11 10 16 4**	**5.84**
6th Run	19 1 21 20 6 25 5 18 9 2 17 14 22 13 10 11 23 15 4 24 16 7 8 12 3	10.00
7th Run‡	1 5 18 21 19 6 9 7 25 14 24 23 3 13 22 2 4 15 17 20 11 16 10 12 8	11.68
8th Run	18 21 19 1 20 9 25 6 7 5 17 14 2 24 23 13 3 22 16 15 11 8 12 10 4	9.44
9th Run	18 1 21 19 9 25 5 24 6 23 7 8 3 17 4 14 15 22 11 10 16 13 2 20 12	7.22
10th Run	18 1 21 5 19 9 6 7 25 16 3 20 24 8 23 17 10 2 4 14 22 13 15 11 12	9.42
	Mean	8.8
	Standard Deviation	1.95

‡ *Solution in bold face is the best one obtained.*

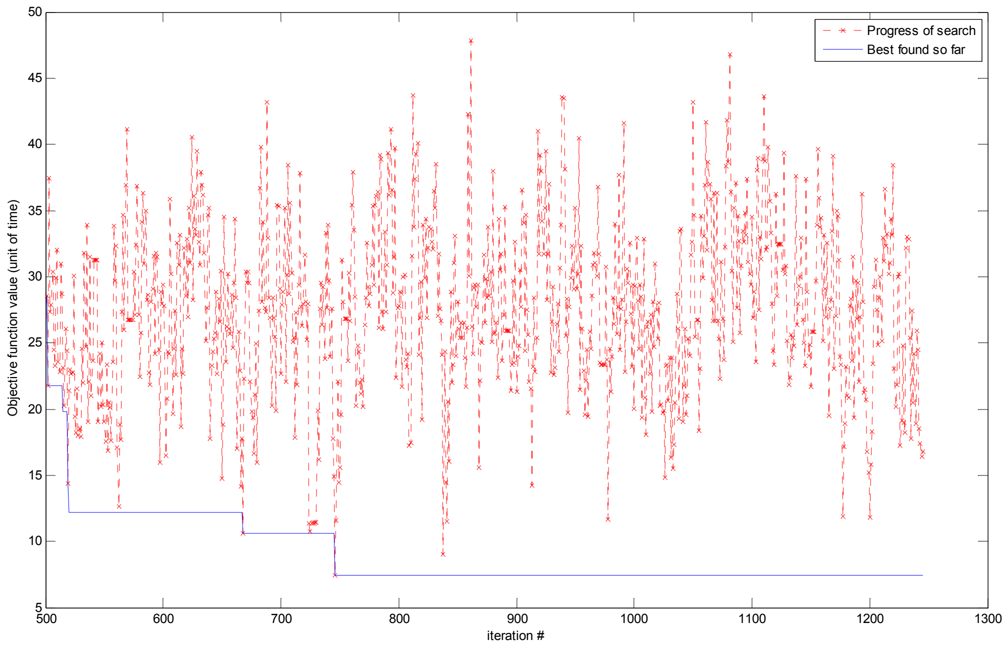

Figure 5 Conversion curve for one of the 10 SA runs performed

5. Concluding remarks

A practical semi-generative macro-level planning approach suitable for disassembly has been developed. The macro-level disassembly process plan is formulated as a sequence of operations corresponding to a set of features in the part. The interactions between the product's different disassembly operations are modeled using Operations Precedence Graphs. A random-based heuristic is developed to obtain optimal or near-optimal solutions for the proposed TSP model. A validation scheme is developed and used to maintain the specified precedence relationships.

For the developed objective function of the TSP model, three cost components have been proposed: time required to change disassembly orientation, tool changeover time and tool traverse time. The last component (tool traverse) here is a measure of accessibility of the part to be disassembled. The proposed method is applied to a household device. Ten macro-level disassembly process plans are generated. Although this re-planning is normally done off-line, the developed heuristic has the advantage of being fast (few seconds on average per run on a 1.4GHz Dual Core with 3 GB RAM and 3 MB L2 cache memory); hence, multiple runs are possible to arrive at alternate solutions efficiently. Moreover, converting the code deployed on MATLAB™ (an interpreter) into an executable could further reduce the algorithm execution time. For future work, a hybrid heuristic with Genetic Algorithms may be developed to transform the point search into a population search, and hence more than one sub-optimal solution could be obtained from a single run.

References

[1] Ishii, K., "Life Cycle Engineering Design." Journal of mechanical design, Vol. 117, 1995, 42-47.

[2] Chen, K. Z., "Development of Integrated Design for Disassembly and Recycling in Concurrent Engineering" Journal of Integrated Manufacturing Systems, Vol. 12, No. 1, 2001, 67-79.

[3] Hauschild, M., J. Jeswiet, et al., "From Life Cycle Assessment to Sustainable Production: Status and Perspectives." CIRP annals, Vol. 54, No. 2, 2005, 535-555.

[4] Gungor, A. and S. M. Gupta, "Issues in environmentally conscious manufacturing and product recovery" Computers and industrial engineering , Vol. 33, No. 2, 1999, 329-332.

[5] Gupta, S. M. and K. N. Taleb, "Scheduling disassembly." International Journal of Production Research, Vol. 32, No. 8, 1994, 1857-1866.

[6] Gungor, A. and S. M. Gupta, "Disassembly sequence plan generation using a branch-and-bound algorithm." International Journal of Production Research, Vol. 39, 2001, 481-509

[7] Lambert, A. J. D., "Disassembly sequencing: a survey." International Journal of Production Research, Vol. 41, No. 16, 2003, 3721-3759.

[8] Wolter, J. D., On the Automatic Generation of Assembly Plans. Computer-Aided Mechanical Assembly Planning. L. S. Homem de Mello and S. Lee, Kluwer Academic Publishers, 1991.

[9] ElMaraghy, H. A., "Evolution and future perspecives of CAPP." CIRP Annals, Vol. 42, No. 2, 1993, 739-751

[10] de Fazio, T. L. and D. E. Whitney, "Simplified generation of all mechanical assembly sequences." IEEE Journal of Robotics and Automation, Vol. 3, No. 6, 1987, 640-658.

[11] Whitney, D. E., Mechanical Assemblies: Their Design, Manufacture, and Role in Product Development, Oxford University Press, 2004.

[12] Mello, L. S. H. d. and A. C. Sanderson, "Representations of mechanical assembly sequences." IEEE Transactions on Robotics and Automation, Vol. 7, No. 2, 1991, 211-227.

[13] Henrioud, J.-M. and A. Bourjault, LEGA: A Computer Aided Generator of Assembly Plans. Computer-Aided Mechanical Assembly Planning. L. S. Homem de Mello and S. Lee, Kluwer Academic Publishers, 1991.

[14] Delchambre, A. , A pragmatic approach to computer-aided assembly planning, Cincinnati, OH, USA, IEEE Comput. Soc. Press, 1990.

[15] Kang, J. G., D. H. Lee, "Parallel disassembly sequencing with sequence-dependent operation times." CIRP Annals - Manufacturing Technology, Vol. 50, 2001, 343-346.

[16] Kroll, E. and T. A. Hanft, "Quantitative Evaluation of Product Disassembly for Recycling." Research in Engineering Design, Vol. 10, 1998, 1-14.

[17] Vidal, R., Applied simulated annealing, Springer-Verlag, 1993.

Appendix

Table 3. Disassembly operations data for Coffee Maker

operation I.D. #	Operation Description	Disassembly time (s)	Setup (Product orientation)	Tool used	Location (x,y,z)
1	Unscrew top cover's screws	9	V	2	4,35,4
2	Removing top cover	6	V	1	5,35,5
3	Removing hot water pipe	5	V	1	3,30,2
4	Removing Small metal plate	3	V	1	-5,32,5
5	Unscrewing Metal plate's screws	9	V	2	-5,32,4
6	Releasing Water reservoir	6	H	1	5,30,5
7	unclamping Clips	4	H	4	3,22,2
8	Pulling Connection hoses	2	H	4	3,24,2
9	Releasing Base	5	H	1	5,0,5
10	Disconnect Electrical wires	9	H	5	3,-2,3
11	Disconnect Electrical connector	8	H	4	3,-2,3
12	Removing Thermo switch	6	H	1	4,17,3
13	Removing Heating plate	7	V	1	5,2,5
14	Removing Support ring	2	V	1	5,1,5
15	Releasing Control unit	5	V	1	4,16,3
16	Disconnecting Electrical cord	5	H	5	5,4,2
17	Removing Bottom cover	6	V	1	5,-3,5
18[a]	Unscrewing Bottom cover's screws	3	V	3	4,-3,4
18[b]	Unscrewing Bottom cover's screws	16	V	2	0,-3,0
19	Unscrewing Water reservoir's screws	13	V	2	4,6,2
20	Releasing Coffee filter case	6	V	1	0,27,5
21	Releasing Pot	2	V	1	0,22,5
22	Removing Pot's lid	2	V	1	0,23,5
23	Removing Pot's handle	4	H	1	0,20,5
24	Removing Pot's ring	12	V	1	0,20,3
25	Unscrewing Handle's screw	11	H	2	0,20,4

JJMIE

Volume 5 , Number 1, February.2011
ISSN 1995-6665
Pages 9 - 16

Jordan Journal of Mechanical and Industrial Engineering

Jig Design, Assembly Line Design and Work Station Design and their Effect to Productivity

Adi Saptari, Wong Soon Lai, Mohd. Rizal Salleh

Faculty of Manufacturing Engineering
Universiti Teknikal Malaysia Melaka, Hang Tuah Jaya, Ayer Keroh, 76100 Melaka, Malaysia

Abstract

This report discussed the effect of workstation design, assembly design, jig design and working posture on the assembly of plugs. Two different designs of jig (vertical and rectangular) and two sets of assembly line design (one and two operators) and two set of workstations design (sitting and standing) were studied to observe their effects to productivity. Design of Experiments 2^3 with two levels of each factor is used to conduct an experiment for obtaining the most productive jig and assembly line design. Two groups of workers were employed to assemble the plug in 8 different ways. Number of replication is 32 for each setting and total of electric plugs produced by each group is 256 units. The results shows that jig design have the most significant effect to the assembly time. Furthermore, the other factors: assembly design and workstation design are also show significant factors to assembly time. However, interaction combinations of two or three factors were not significant to assembly time. The most productive assembly line design which achieved the lowest assembly time is the combination of one operator, with rectangular jig and work station design sitting. Meanwhile the working posture of workstation design that provides the lowest RULA score was sitting position, it provided score 2 which is safe.

Keywords: Jig design, design of assembly, workstation design, productivity, working posture.

1. Introduction

An assembly line is designed by determining the sequences of operations to manufacture of components as well as the final product. Each movement of material is made as simple and short as possible, with no cross flow or backtracking. All operations performed along the line are balanced. Design of assembly line plays the important role in manufacturing which will directly influence its productivity.

Previous researchers [13], [19-20] explained assembly line is a widely used in production systems. The main objective of assembly lines designers is to increase the efficiency of the line by maximizing the ratio between throughput and costs. Chow [5] stated that “A simple process design criterion is to balance the assembly line so that each operation takes approximately the same amount of time. A balanced line often means better resource utilization and consequently lower production cost.”

Jig is a special tool used for locating and firmly holding work piece in the proper position during the manufacturing or assembly operation. It also guides the tool or work piece during the operation. Jig is designed to increase the productivity of operation assisting worker to do job easier, faster and more comfortable.

Meanwhile, applying principles of ergonomics in the job environments such as improving working posture and workstation design as part of ergonomics efforts on enhance productivity and safe working condition have been extensively discussed by many authors [7] [8] [2] [22]. The studies discussed ergonomics intervention may improve productivity, quality, operators’ working condition, occupational health and safety (OHS), and even cost effectiveness. The areas of working environment studied include workplace layouts, working tables and chairs of appropriate height, fixing hand-tools, better lighting and job rotation and also working postures. This research studied several parameters afore mentioned: i.e. design of workstation, design of assembly process, design of jig, their effects to productivity in the assembly line of plugs. Other variables such as equipment and skill of worker which may contribute to productivity are assumed kept constant. The hypothesis to be tested that either one or more of the parameters or combinations of parameters contribute to better production performance in this case assembly time or cycle time.

Two designs of jig were introduced, one has rectangular shape and the other has line or vertical shape or vertical orientation. Two design of assembly were tested one with single operator and the other with two operators. Design of workstation was created by applying common industrial practices in assembly line i.e. standing or sitting position. For working poster assessment, RULA (Rapid Upper Limb Assessment) analysis was conducted to examine different workstation designs effect to safe working postures.

2. Methods

2.1 Product Design

For the purpose of this experiment an electric product was chosen as a case. This product was selected since it widely used in the household, it was not a complex in design and components. The design of product is shown in Figure 1. This electric product is a plug product number BS 1363, it has 8 components. These are: base cover, neutral pin, earth pin, live pin, fuse holder, fuse, top cover and one screw. The dimension of the product is shown as Figure 1. Plug can assume as rectangular block (dimension 51mm X 49 mm X 21 mm) with 3 pin (earth, neutral and live terminal pin). The central point of live and neutral pin is located 22 mm below the central point of earth pin. The distance between central point of live and neutral pin is also 22 mm. Accuracy of position and dimension of the plug's pin are important when design the jig, this is to let plug able to locate and secure through the jig.

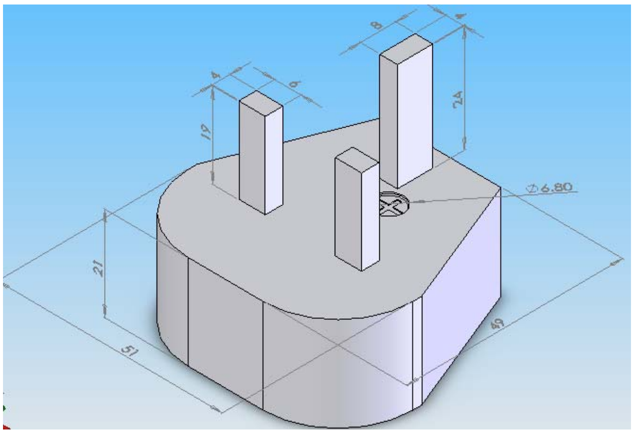

Figure 1 Plug design and dimensions

2.2 Design of Jig

The purpose of jig on this research is holding the plug's earth pin with cover in the proper position, other components locate and secure into the jig when the assembly process.

Two jigs were designed and produced by researchers, these designs were based on industry practice. The two were differentiated based on its orientation. The first one has orientation vertical shape in one line; the other has rectangular shape (see Figure 2). The size of the jig, the vertical one has 275 mm x 80 mm; the rectangular one has 136 mm x 145 mm. Both Jigs can accommodate 4 plugs at one time.

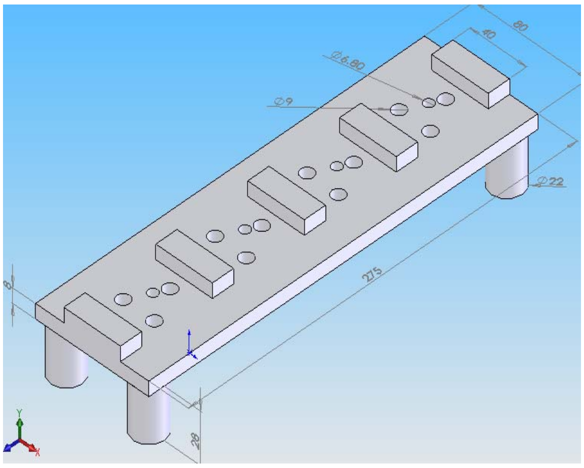

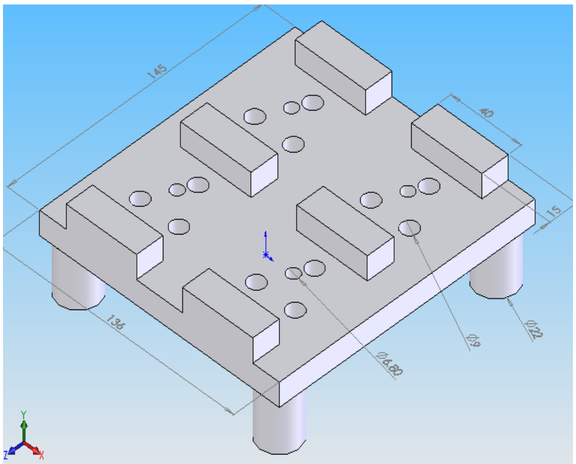

Figure 2 Two jig designs, a vertical shape and a rectangular shape

2.3 Design of Assembly line

Two designs of assembly line were created these were based on manufacturing practices one with single operator and the other with two operators. The process of designing assembly as follow: at the first stage was to recognize components and the second stage was to comprehend assembly processes of product which is BS1363. Once it has done, the assembly processes sequence were determined. These sequences as follow: put plug's base cover on the jig, insert the child components (neutral pin, earth pin, live pin, fuse holder and fuse) into the base cover. Then, assembly the top and base cover together by screw. For screwing process, the jig is flipped and tightens with the screw driver powered by air pressure. The sequence planning for the assembly process of electric plug is presented in the precedence graph below:

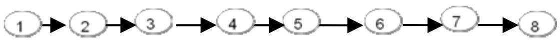

1 – Place base cover on jig	5 – Insert fuse holder
2 – Insert earth pin	6 – Insert fuse
3 – Insert neutral pin	7 – Put top cover
4 – Insert live pin	8 – Screwing process

Figure 3: Precedence graph of plug assembly

Table 1is shown the result of each assembly task based on the precedence graph constructed in Figure 3. To obtain the balance of time for two operators, the assembly tasks assigned for each operator should be equal for eliminating the waiting time of another operator.

Table 1: Average time of each plug assembly task for line balancing

Task No.	Assembly Task	Average time per plug (sec)	Cumulative Assembly Time
1	Place base cover on jig	0.83	0.83
2	Insert earth pin	2.52	3.35
3	Insert neutral pin	1.94	5.29
4	Insert live pin	2.46	7.75
5	Insert fuse holder	1.91	9.66
6	Insert fuse	2.30	11.96
7	Put top cover	2.02	13.98
8	Screwing process	5.02	19.00

According to the table above, the total time for assemble one electrical plug is 19.00s. The single operator did all the tasks from the beginning to the end of assembly processes. For design of two operators, in order to obtain a good line balancing for 2 operators, the total assembly time must divide equally into two, which is 9.5 sec. Hence, the most nearly cumulative assembly on Table 1 is on task 5 which is 9.66 sec. This means that the first operator will stop at the end of task 5 which is insert fuse holder. The second operator will start from task 6, insert fuse to final assembly. Assuming that there were work in process, therefore, the second operator did not required waiting for the first operator and could start the experiment at the same time.

2.4 Design of Workstation

Workstation design of an assembly line may contribute to performance of workers when he or she performed his/her job on position either standing or sitting. Grandjean [11] has made exploration on work surface height for different kinds of jobs. He proposed precision work for men should be set at 100-110 cm, light work around 90-95 cm and heavier work around 75-90 cm. Since the assembly of plugs is considered as a light work, the workstation design for assembly was set at the height 91 cm for either standing or sitting position.

2.4.1 Standing Position

Figure 4 shows isometric, and front side views, while performing the task with an operator and in standing position. The table height is fixed to 91 cm.

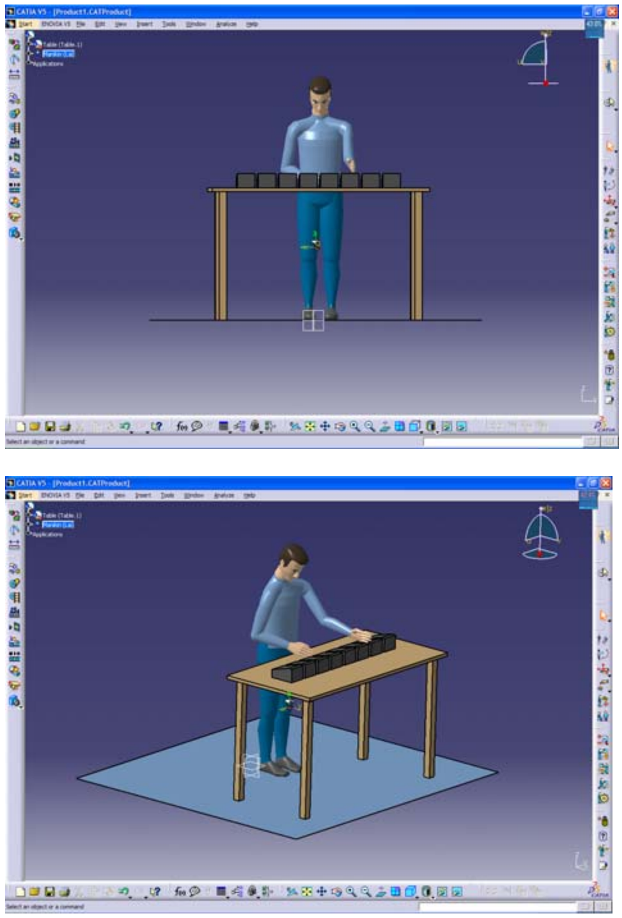

Figure 4: Standing position, isometric view and front view

2.4.2 Sitting Position

Figure 5 illustrates isometric and front side views of a subject performing the task with an operator in sitting position. The table height is fixed to 91 cm.

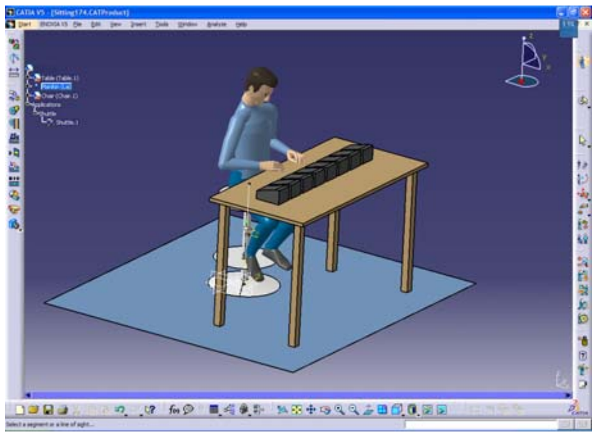

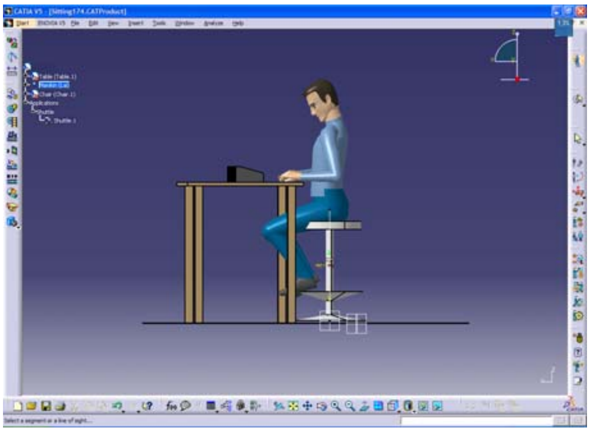

Figure 5: Sitting position, isometric view and side view

2.5 Design of Experiment

The design of experiment took three factors and two levels (2^3), the factors were jig design, assembly design and workstation design. The first factor, jig design, it has two different designs. The second factor, assembly design, it has two levels, one single operator and two operators. The third factor, workstation design, with two levels the first setting was sitting the second setting standing. Based on this design eight (8) different ways of assembling line were formed. Table 2 shows the design of experiment for assembly line.

Table 2: Summary of Design experiment

	One Operator		Two Operators	
Position	Vertical jig	Rectan-gular jig	Vertical jig	Rectan gular jig
Standing	X1	X2	X5	X7
Sitting	X3	X4	X6	X8

2.6 Experimental Procedure

Two groups of worker participate in this experiment. Each group has two subgroups, one with single operator and the other with two operators. These two groups will be compared and test whether their performance were the same, and whether the results of experiment were consistent.

Each group performed 8 different sets of assembly process according to the full factorial design. Thirty two repetitions for each different set of assembly were done. Each set was selected randomly, once it was selected, 32 plugs were produced. Hence, total of electric plug required to assemble for each group are 256 electric plugs.

Measurement of performance for this experiment was the assembly time required to finish one product. Before recording the assembly time, the performance of each group was tested to ensure their work has reached a consistent performance. The assembly time or cycle time was recorded by using stop watch. This assembly time became the dependent variable, while different factors were set as independent variables.

2.7 Subjects

The subjects participated in this experiment were young workers age in average 24 years old, all were male subjects. Their height is on range of 170 – 180 cm. They have experiences and involved in industrial works for less than a year. Training to assembly this product was given prior to the experiment. This was necessary to ensure that learning time has reached. Their time was recorded to ensure the consistent performance of their jobs.

3. RESULT & DISCUSSION

3.1 Group's Performance

The First test is to verify whether two groups of workers have different quality of work or performance. This is necessary to make sure the inferences made from the results may work for both groups. Hence, the F test and t-test were used to examine whether two groups showed different performance. The F test were used to verify whether the group has significant different in variance. Based on the F test result, these two groups then were tested for t-test: paired two samples for means.

Table 3: t-test: paired two sample means between two groups

	Group 1	**Group 2**
Mean	19.564	19.739
Variance	1.397	1.027
Observations	256	256
Pearson Correlation	0.255	
Hypothesized Mean Difference	0.000	
Df	255	
t Stat	**-2.080**	
P(T<=t) one-tail	0.019	
t Critical one-tail	**1.651**	
P(T<=t) two-tail	0.039	
t Critical two-tail	**1.969**	

According to t-test performed on Table 3, t Stat (2.080) is greater than t Critical one-tail (1.651) or t Critical two-tail (1.969). This result recommends reject the hypothesis that the two groups have the same means. It is shown that the assembly time for two groups is significantly different. Hence, the performance of each group has significantly different whereby the group 1 (19.564 sec) performed more productive than group 2 (19.739 sec). However, group 2 was more consistent in assembly time than group 1 because the variance of data for group 1 (1.397 sec) is greater than group 2 (1.027 sec).

Further investigation is to observe whether there is a significant different among the setting of experiments in each group of workers, Analysis of Variance (ANOVA) for single factor for group 1 and group 2 were used. The F Test for both groups suggest that there exist a significant different among the setting of the experiments, meaning jig design (jig's orientation), assembly design (different number of operators), and work station design (working position) are contribute to significant different to the response time (assembly time). Table 4 and 5 shows the ANOVA analysis for single factor of group 1 and 2.

Table 4 ANOVA for Single Factor for Group 1

Groups	Count	Sum	Average	Variance	
X1	32	638.84	19.96	0.69	
X2	32	615.08	19.22	0.40	
X3	32	598.64	18.71	0.75	
X4	32	587.44	18.36	0.62	
X5	32	670.8	20.96	1.09	
X6	32	651.48	20.36	0.75	
X7	32	632	19.75	0.77	
X8	32	614.16	19.19	1.04	
ANOVA					
Source of Variation	SS	df	MS	**F**	P-value
Between Groups	167.25	7	23.893	**31.346**	6.08 E-31
Within Groups	189.03	248	0.762		
Total	356.28	255			

Table 5 ANOVA for Single Factor for Group 2

Groups	Count	Sum	Average	Variance	
Y1	32	642.84	20.09	0.51	
Y2	32	626.64	19.58	0.46	
Y3	32	616.84	19.28	0.38	
Y4	32	603.68	18.87	0.68	
Y5	32	666	20.81	1.24	
Y6	32	646.76	20.21	0.90	
Y7	32	630.68	19.71	0.55	
Y8	32	619.8	19.37	0.99	
ANOVA					
Source of Variation	SS	df	MS	**F**	P-value
Between Groups	84.42	7	12.061	**16.853**	3.64 E-18
Within Groups	177.47	248	0.716		
Total	261.90	255			

Figure 6 shows mean statistics of different setting workstation design for group 1 (X). First assessment of the results shows that design of jig either vertical or rectangular provides the most significant different to assembly time by assuming other factors such as number of operator and workstation design are in the same set. This is shown column X1 and X3 for one operator the average assembly time 19.96 sec, for vertical jig and 18.71 sec for rectangular jig. While with two (2) operators (column X5 and X7) provide 20.96 sec and 19.75 sec. The second greater significant different to assembly time is the number of operator either 1 or 2 operators with assuming other factors such as jig's orientation (jig design) and workstation design are in the same set. This shown by column X1 and X5 with vertical jig and standing position provides average assembly time 19.96 sec for one operator and 20.96 sec for 2 operators, while with sitting position (X2 and X6) provides 19.22 sec and 20.36 sec. Lastly, the result shows that workstation's design either standing or sitting provides the smallest significant different to assembly time by assuming other factors such as number of operators and jig design are in the same set. This shown by column X1 and X2 with an operator and vertical orientation of jig provides average assembly time 19.96 sec for standing position and 19.22 sec for sitting position, while with 2 operators (X5 and X6) provides 20.96 sec and 20.36 sec.

For group 2 (Y), the results is similar with group 1 which The orientation of jig provides the most significant different to assembly time, follows with the number of operator and the working position.

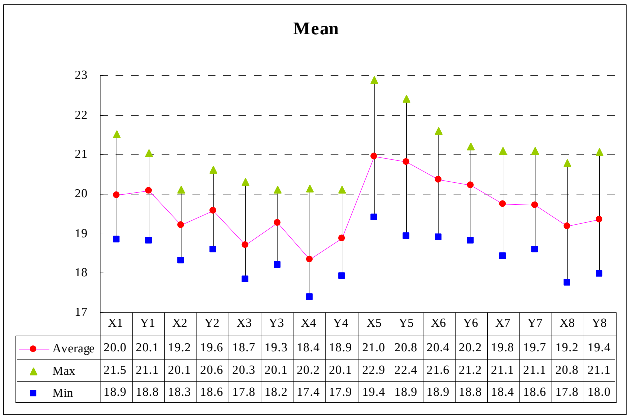

Figure 6: Mean for two groups with different set of factors

3.2 Analysis of Variance

Further analysis of variance, Table 6 illustrates the result ANOVA for each factor: Jig design, assembly design (number of operators) and workstation design, and its interaction of two ways and three ways to the response i.e. assembly time. The significant factors are determined by using the p-value (P) in the Factorial fit table. Using level of significant at 0.05, the main effects for number of operator, orientation of jig and design of workstation are statistically significant where their p-values are less than 0.05. Among the main effects, the most significant factor is the orientation of jig where its effect value is the greatest value, 1.1247. However none of combination factors are significant.

Table 6: Factorial fit for: assembly time versus number of operator, orientation of jig and design of workstation

Estimated Effects and Coefficients for Assembly Time (coded units)					
Term	Effect	Coef	SE Coef	T	P
Constant		19.5642	0.05457	358.54	0.000
Number of Operator	1.0034	0.5017	0.05457	9.19	**0.000**
Orientation of Jig	**-1.1247**	-0.5623	0.05457	-10.31	**0.000**
Design of Workstation	-0.5634	-0.2817	0.05457	-5.16	**0.000**
Number of Operator * Orientation of Jig	-0.0647	-0.0323	0.05457	-0.59	0.554
Number of Operator * Design of Workstation	-0.0172	-0.0086	0.05457	-0.16	0.875
Orientation of Jig * Design of Workstation	0.1097	0.0548	0.05457	1.01	0.316
Number of Operator * Orientation of Jig * Design of Workstation	-0.0866	-0.0433	0.05457	-0.79	0.428

For further confirmation of results of Table 6, the normal probability plot of the standardized effects were evaluated to observe which factors influence the response i.e. assembly time. As shown in Figure 7 significant factors are identified by a square such as number of operator, orientation of jig and design of workstation. Moreover, Figure 8 shows the main effects plot, it shows that assembly time is:

(a) Increase from single operator assembly process to two operators.

(b) Decrease from using the vertical jig to rectangular jig for jig's orientation.

(c) Decrease from standing position to sitting position for workstation's design.

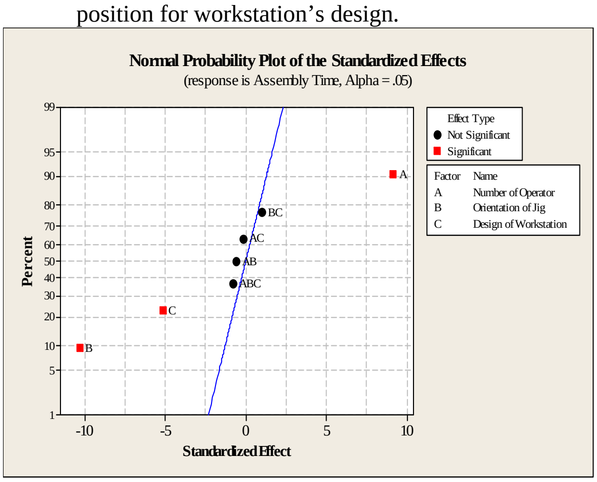

Figure 7: Normal probability of the standardized effects

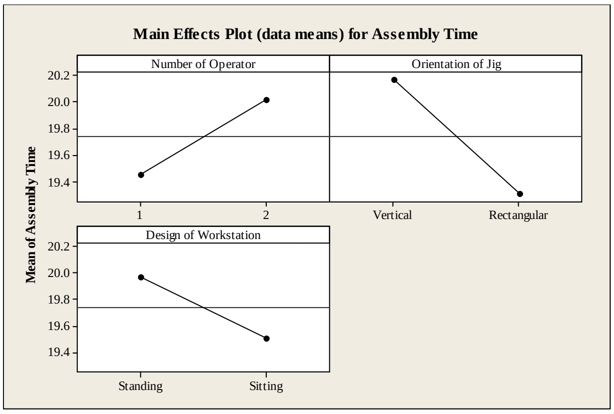

Figure 8: Main Effect plot for assembly time

Further investigation is on which setting of combination factors contribute to the lowest assembly time. Figure 9 Box plot of assembly time shows that the lowest Mean average assembly time is achieved at the assembly line design of 1 operator, rectangular orientation of jig and with the sitting working posture, the assembly time is 18.3575 sec. This combination also contributes the lowest assembly time which is 17.38 sec and the lowest upper bound is 20.15 sec.

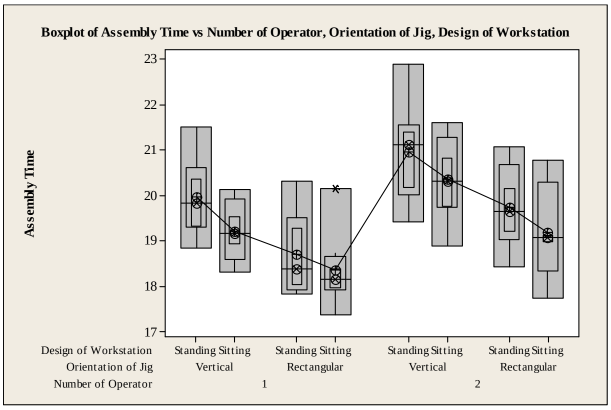

Figure 9: Box plot of assembly time

3.3 Working Posture Analysis

In a workstation, an operator may perform a task in various working posture. Working posture may expose to the hazards. Improper workstation design will expose to occupational hazards associated with awkward working posture. Therefore, an attention on working posture has priority to ensure it is safe to operators. There are various tools that have been introduced to analyze working posture; one of the common tools is RULA (Rapid Upper Limb Assessment) analysis.

For RULA analysis, this project assessed only a single operator from group 1 and group 2 with sitting and standing working posture. The factor of jig's orientation (rectangular or vertical) is assumed not significant affecting the results because jig is located at the normal working area which is 25cm from operator. RULA analysis is conducted by using CATIA software as shown in Figure 10. All dimensions required are according to the actual dimension such as anthropometry of operator, 91cm height of table, 25cm work area and others to ensure the accuracy of results.

Figure 10 illustrates one of RULA analyses of an operator group 1 with standing position. As depicted in the figures, the column at the right hand side of dialogue box, it states the posture score of every part of the body. At the left hand side, the dialogue box recorded condition of posture (static, intermittent, and repeated); repeat frequency of the posture (< 4 times/minute or > 4 times/minute); condition of arm (supported, across body midline, and balance) amount of load handled by the subject; and the RULA Score.

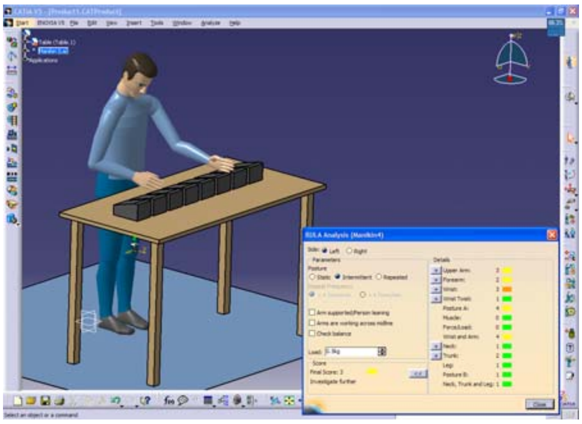

Figure 10: RULA analysis of an operator from group 1 with standing position

The results show the posture scores for every part of the body are in a range from 1 to 4. Orientation of forearm, muscles, neck, trunk and legs are considered safe, as the posture score 1 or 2. As illustrated in Figure 10, the score of wrist posture is 3 when the operator flexed his wrist at 15° while performing task in standing position. Hence, further attention and investigation should be carried-out because the final score reaches 3.

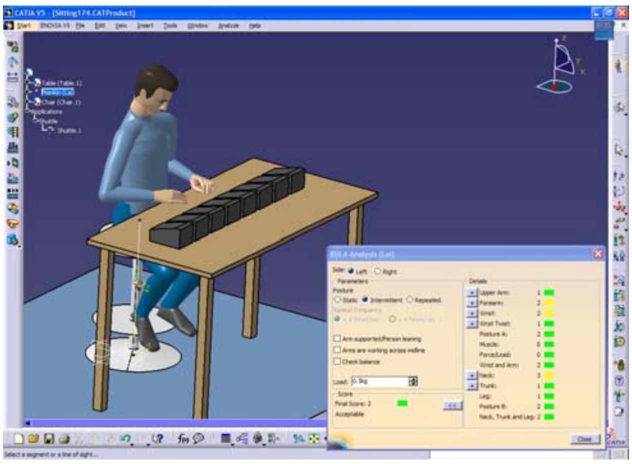

Figure 11: RULA analysis of an operator of group 2 with sitting position

Figure 11 illustrates one of the example RULA analyses of an operator from group 2 with sitting position. From the presented results, the posture scores for every part of the body are in a range from 1 to 3. Orientation of upper arm, forearm, wrist, muscles, neck, trunk and legs are considered safe, as the score 1 or 2. As illustrated in Figure 11, the final score reaches 2 which mean that the sitting working posture is acceptable and safe on this assembly line.

Table 7: Summary of RULA analysis

Position	**Group**	**RULA Score**	**Result**	**Indication**
Standing	1	4	Working posture needs further investigation	Wrist is flexed at 15°
	2	3	Working posture needs further investigation	Wrist is flexed at 10°
Sitting	1	2	Working posture is acceptable	
	2	2	Working posture is acceptable	

Table 7 is shown that the summary of the result obtained from the RULA analysis. Based on the table, the sitting working posture is safer than the standing working posture with the table height of 91cm. Hence, the sitting position not only contributes the lowest assembly time but also provides the safe working posture for operators.

4 . Conclusions and Recommendations

The following findings are concluded:

(a) There is a significant different in the performance of two groups of workers. Group1 is performed more productive than group 2; however, group 2 is performed more consistent than group 1.

(b) For the both groups, among the single factors: Jig Design (Jig's orientation), Design of assembly (number of operators), and Workstation design (standing and sitting) have significant contribution to assembly time with significance level 0.05. The most significant factors that contribute to assembly time were: jig design (vertical or rectangular). The second most significant factor is the number of operators (1 or 2) and the smallest significant factor is the workstation design (standing or sitting).

(c) For combination of two or three factors, the results show that no evidence to claims there is significant contribution to the assembly time.

(d) The assembly time increase from single operator assembly process to two operators assembly process; Decrease from using the vertical jig to rectangular jig for jig's orientation; Decrease from standing position to sitting position for workstation's design.

(e) Among the setting of assembly line design, the most productive assembly line design is the combination of 1 operator, with jig design rectangular orientation and working posture is sitting. This set of assembly provides average

18.3575 second per product, with the lowest reached 17.38 second.

(f) The sitting position working posture, is the most safe workstation design for this assembly line.

There are some areas that can recommend for the further study, among others are:

(a) The design of jig such as the shape, material used, number of quantity in a jig may further be investigated.

(b) Human variability such as gender, age, occupational, race and others which might contribute significant effect to the assembly line.

References

[1] Antony, J., “Improving the Manufacturing Process Quality Using Design of Experiments: A Case Study.” *International Journal of Operations & Production Management*. Vol. 21, No.5/6, 2001, 812-822.

[2] Barker, T.B., “Quality by Experimental Design.” 3rd Edition. Chapman & Hall, Boca Raton, 2005.

[3] Baudin, M., “Lean Assembly: the Nuts and Bolts of Making Assembly Operations Flow.” Productivity Press, New York, 2002.

[4] Box, G.E.P. and N.R. Draper, “Empirical Model-Building and Response Surfaces.” John Wiley & Sons, New York, 1987.

[5] Chow, W.-M., “Assembly Line Design: Methodology and Applications.” Marcel Dekker, New York, 1990.

[6] Choobineh, A., Mostafa Hosseini, Mohammad Lahmi, Reza Khani Jazani and Houshang, “Musculoskeletal problems in Iranian hand-woven carpet industry: Guidelines for workstation design”. Applied Ergonomics, Vol. 38, No. 5, 2007, 617-624.

[7] Dellman, N.J. and Jan, D., ”Sewing machine operation: workstation adjustment, working posture and worker perceptions. International Journal of Industrial Ergonomics, Vol. 30, No. 6, 2002, 341-353.

[8] Dellman, N.J. ,”Pres Operation: Workstation adjustment, working posture, and workers’ perceptions”, Occupational ergonomics Vol.3, 2003, 153-164.

[9] Goh, T.N., “Operating Frameworks for Statistical Quality Engineering.” *International Journal of Quality and Reliability Management*. Vol. 17, No.2, 2000, 180-188.

[10] Gursel, A.S., “Designing Parallel Assembly Lines.” *Computers & Industrial Engineering*. Vol. 35, 1988, 467-470.

[11] Hinkelmann, K., and O. Kempthorne, “Design and Analysis of Experiments. Volume I: Introduction to Experimental Design.” John Wiley & Sons, New York, 1994.

[12] Ismail, N. et al., “Improving Productivity and Efficiency of a Vehicle Seat Assembly Line in Manufacturing Company.” *Student Conference on Research and Development Proceedings*, 2002, 94-97.

[13] Khan, A. and Andrew, J.D., “A Knowledge Based Design Methodology for Manufacturing Assembly Lines.” *Computers & Industrial Engineering*. Vol. 41, 2002, 441-467.

[14] Montgomery, D.C., “Design and Analysis of Experiments.” 6th Edition. John Wiley & Sons, New York, 2005.

[15] P.H.P Yeow, and Rabindra Nath Sen,” Quality, productivity, occupational Health and safety and cost effectiveness of ergonomic improvements in the test workstation of an electronic factory”, International Journal of Industrial Ergonomics, Vol 32, No. 3, 2003, 147-163.

[16] Pierre, D.L. et. al., “A New Philosophy for the Design of a Product and its Assembly Line.” *International Symposium on Assembly and Task Planning*, 1999, 381-386.

[17] Qian, H.W, “List Representation of Assembly Sequences.” *IEEE International Conference on Industrial Technology*, 1996, 315-319.

[18] Rekiek, B., “Designing Mixed Product Assembly Lines.” *IEEE Transactions on Robotic and Automation*. Vol.26, No.3, 2000, 268-280.

[19] Rekiek, B., “State of Art of Optimization Methods for Assembly Line Design.” *Annual Review in Control*. Vol. 26, 2002, 163-174.

[20] Resnick, M.L. and A.Zanotti, “Using Ergonomics to target productivity improvements”, Computers & Industrial Engineering, Vol. 33 No.1/2, 1997, 185-188.

[21] Saptari, “A Plug Assembly Line: An Assessment of Workstation Design and Working Posture, *Journal of Biomechanics*, Vol.40, *Supplement 2, 2007, Page S15*.

[22] Zhu, X.W., “Sequence Planning to Minimize Complexity in Mixed Model Assembly Lines.” *International Symposium on Assembly and Manufacturing*, 2007, 251-258.

JJMIE

Volume 5 , Number 1, February 2011
ISSN 1995-6665
Pages 17 - 22

Jordan Journal of Mechanical and Industrial Engineering

The Effect of Tool Fixturing Quality on the Design of Condition Monitoring Systems for Detecting Tool Conditions

Jabbar Abbas, Amin Al-Habaibeh*, Daizhong Su

Advanced Design and Manufacturing Engineering Centre ADMEC,

School of Architecture, Design and the Built Environment,

Nottingham Trent University, Nottingham, UK.

Abstract

Condition monitoring systems of machining processes are essential technology for improving productivity and automation. Tool wear monitoring of cutting tools is one of the important applications in this area. In this paper, the effect of collet fixturing quality on the design of condition monitoring systems to detect tool wear is discussed. The paper investigates the difference in the system's behaviour and the changes in the condition monitoring system when the cutting tool is not rigidly fastened to the collet. A group of sensors, namely acoustic emission, force, strain, vibration and sound, are used to design the condition monitoring system. Automated Sensor and Signal Processing Selection (ASPS) approach[1] is implemented to address the effect of the tool holding device (collet) on the monitoring system and the most sensitive sensors and signal processing method to detect tool wear. The results prove that the change in the fixturing quality could have significant effect on the design of the condition monitoring system and the behaviour of the system.

Keywords: : Collet, Condition Monitoring, Milling, Machining Operation, Signal Processing, Sensor Fusion, Tool Wear.

1. Introduction

Fixtures are essential devices in production systems as they are required in most of the automated manufacturing, inspection, and assembly operations. Fixtures locate precisely a work piece or a cutting tool in a given orientation and position to allow the machining or measuring process to be accurately performed. There are many standard work holding devices such as jaw chucks, machine holder, drill chucks, collets, which are commonly used in workshops for general applications such as machining and measuring [1]. Collets have proven to be as useful on today's CNC equipment, with state-of-the-art control systems, as they were on the early engine lathes and multi-spindle automatic machines from the 1920s [2]. Surprisingly, after more than 90 years of successful applications, there is still no better workholding element for the new high-tech, high speed spindles than the workholding collet [3]. Collet remains a proven solution for most metal –working applications, and 90% of manufacturing processes use collet chucks while the other 10% use hydraulic chucks [4].

For any manufacturer, accuracy of machined components is one of the most critical aspects. Faults in machining can be defined as any deviation in the position of the cutting edge from the theoretically required value to produce a workpiece of a specified tolerance [5-6].

*Corresponding author. Amin.Al-Habaibeh@ntu.ac.uk

In end milling, there are four major sources of faults which are geometric and kinematics' errors, temperature induced errors, fixturing errors and cutting forces errors. The correct installation of the tool in the collet is important to prevent unnecessary strain on the collet and to ensure a proper fit. Engineers should use a collet designed to fit the tool shank diameter and the tool's flute should not extend into the collet; doing so can score the inside of the surface, as well as force debris into the collet, putting the entire assembly off-balance and potentially damaging the spindle. These errors will affect the stability of machining operation [7]. Consequently, the cutting tool and the collet which holds it are a major source of error, in addition to tool deflection, tool wear, vibration and burr formation [8].

Although advances in fixture design have greatly improved fixture accuracy and repeatability, fixture faults (or errors) are still a major cause of quality variation. Where most of the literature on fixture analysis has emphasised the positions of fixture elements on the workpiece rather than the contact condition between the mating surfaces. In addition, significant research has been conducted in the area of machine fault detection/diagnosis, but relatively little has been done on fixture fault detection and monitoring [9]. The effect of fixturing systems on the design of condition monitoring systems is an area which is not significantly covered in literature.

Studies performed in industry have shown that the main causes of downtime are end of tool life (wear) and tool breakage and they account for 40 to 45% of downtime in milling, turning and drilling operations [10]. Hence Condition monitoring is normally used as a strategy to detect or prevent such faults using Tool Condition Monitoring (TCM)) [11]. Manufacturers who used TCM systems have documented savings of 3 to 5% of manufacturing costs [12]. A condition monitoring system consists of sensors, signal processing stages, and decision making systems to interpret the sensory information and to decide on the essential corrective action. The success of any TCM system is dependent on two factors, the quality of the data acquired by the sensors and the diagnosis algorithm used to analyse the sensory information and determine tool state [13].

The effect of fixturing type on machining signals has been investigated by [14]. The results showed that the fixturing type could have some influence on the captured machining sensory signals.

This paper investigates the effect of collet fixturing quality on the design of condition monitoring system. The hypothesis is that the collet fixturing quality will change the dynamics of the system introducing different variables and parameters which makes the design of tool condition monitoring a complex task.

2. Tool Fixturing Systems

Conventional split-steel collets provide maximum gripping efficiency only at actual bored or nominal capacity. They loose parallelism when chucking bars due to the size over or under this capacity. This significantly reduces gripping strength and accuracy. Rubber collets are used in some cases to avoid the problem of contact and the flexibility of rubber can provide the freedom of the steel slot to create full contact with shaft or tool as shown in Figure 1.

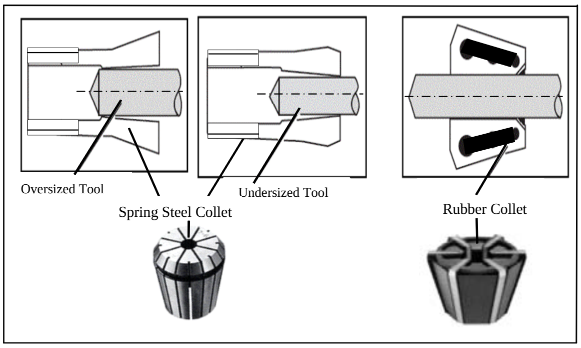

Figure 1. The difference between Rubber collet with other types in gripping parts.

The first author [15] has investigated the area of collet design in previous research work and it has been found that the nature of contact between mating surfaces could be categorised into three groups, namely full, partial and point contact as shown in Figure 2. The objective is to reach to the full contact by increasing the applied load without exceeding the yield stress for the work piece or tool to avoid plastic deformation. In this research, a novel approach of using rubber sleeve on the cutting tool is used to emulate loose and flexible contact between the mating surfaces.

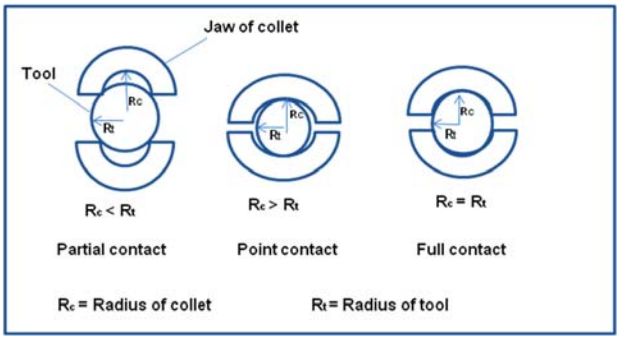

Figure 2. Types of contact between the collet and tool surfaces.

As seen from previous discussion, there is limited work in the effect of collet type on the design of condition monitoring systems. Also, there is limited literature on the relationship between collet type, material and other design parameters on the quality of the machining process and efficiency of the clamping system.

The proposed clamping system of using rubber sleeve is presented in Figure 3. A rubber sleeve will be used between the spring steel collet and the tool to emulate loose collet, and the effect of this on the design of the condition monitoring system will be investigated.

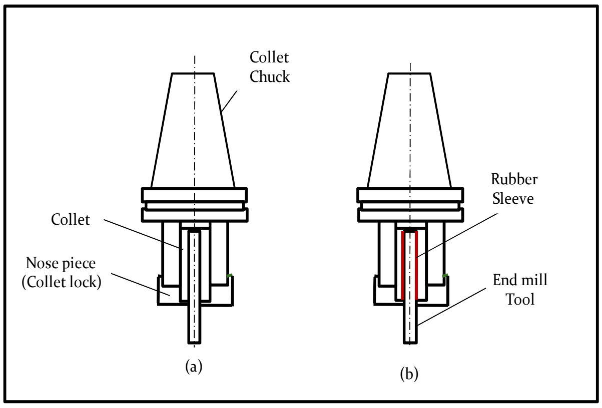

Figure 3. A schematic diagram of a normal tool fixturing system (a) and the one with introduced rubber sleeve (b).

3. Experimental Setup

As illustrated in Figure 4, the experimental work of the condition monitoring system of this study is performed on a milling CNC machine type (DENFORD). Several sensory signals are used in this study including cutting forces (Fx, Fy and Fz), strain, accelerometer (vibration), Acoustic Emission sensor (AE), and microphone for measuring sound. The force signals are monitored using 3-component Dynamometer (Kistler 9257A) and the work piece is fixed on the dynamometer. The dynamic and quasistatic force signals are monitored using a strain sensor (Kistler 9232A). Both the force dynamometer and the strain sensor are connected to a 4-channel charge amplifier (Kistler 5070A). The AE sensor (Kistler 8152b111) is attached to the workpiece to monitor AE signals transmitted during machining and connected to AE coupler (Kistler 5125B). The accelerometer (B&K4366) is mounted on the moveable table of machine and connected to charge amplifier (Kistler 5001). Sound signals are collected using a microphone (type –EM400) placed in the direct vicinity of the workpiece. All the wires and cables of the sensors are connected to a National instrument connection box (SCB-100). The signals are monitored using data acquisition card NI PCI-6071E from National Instrument using special data acquisition software written using the National Instrument CVI programming package. The experimental work is performed on milling machine using Aluminium workpiece. The milling process is carried out at the conditions as shown in the Table 1.

Table 1. The machining parameters of the milling process.

Machining condition	specifications
Feed rate	250 mm/min
Depth of cut	0.22 mm
Coolant type	No coolant (Dry)
Spindle speed	2490 RPM
Diameter of tool	3mm
Material of tool	Solid Carbide (End mill Solid Carbide)
Type of tool	End mill Tool(4 Flutes, Uncoated)

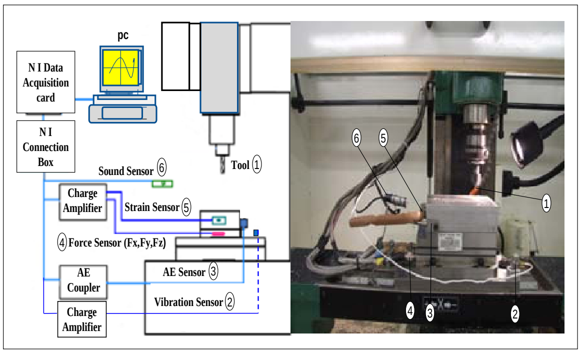

Figure 4. Schematic diagram of experimental setup for the monitoring system on milling machine.

4. Experimental Results and Discussion

The shank of the tool is covered by a rubber sleeve to emulate a fixturing system with low rigidity. The tests start with a fresh tool and finished with completely worn tool as shown in Figure 5. Figure 6 presents the data from both tools, normal and with the rubber sleeve. The raw signals for the tools are collected from the sensors to monitor 43 machining runs/samples for each type of tools as illustrated in Figures 6 and 7. Because milling process has complex machining signals, it has been found difficult to predict the most sensitive signals and signal processing methods to tool wear directly from raw data. Therefore, signal processing and analysis is needed to extract the important information from the signals (i.e. Sensory Characteristic Features (SCFs)).

Figure 5. The two states of the milling tool (fresh and worn tool).

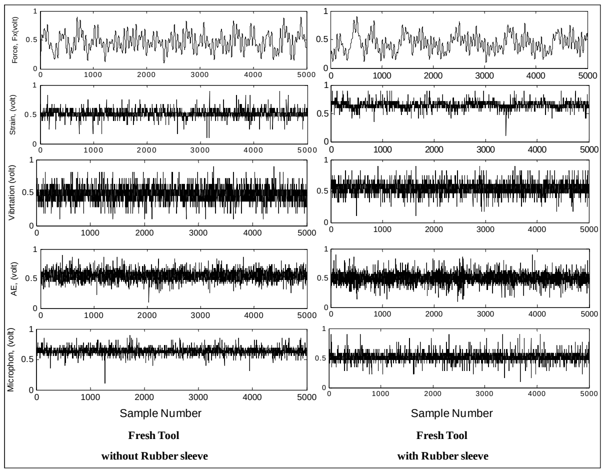

Figure 6. Example of the raw signals of the machining process for both conditions (fresh tool).

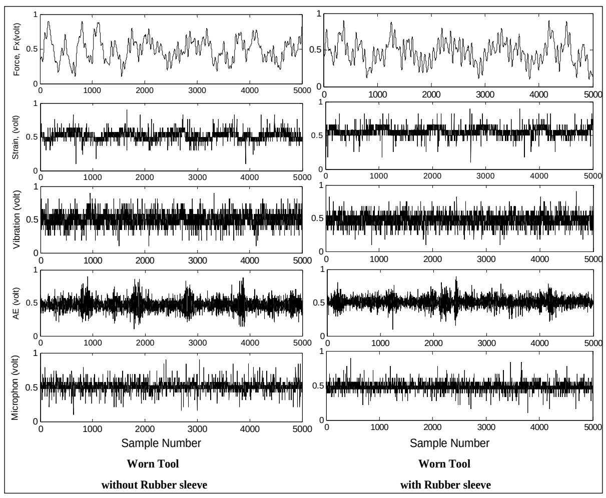

Figure 7. Example of the raw signals of the machining process for both conditions (worn tool).

The raw signals are processed using several time domain signal processing methods to extract the Sensory

Characteristic Features (SCFs). The signal processing methods used are maximum (max), minimum (min) ,standard deviations (*std*), the average (μ), the range, the skew, kurtosis value (*K*) and power. The 8 signal processing methods are used to process the 8 sensory signals to construct an Association Matrix ASM of (8 × 8) which allows the investigation of 64 sensory characteristic features (SCFs) for the design of the monitoring system. The SCFs are arranged according to their sensitivities to tool wear based on the absolute slope of the linear regression method as shown in Figure 8. Figure 8 presents examples of high, medium and low-sensitivity SCFs to tool wear.

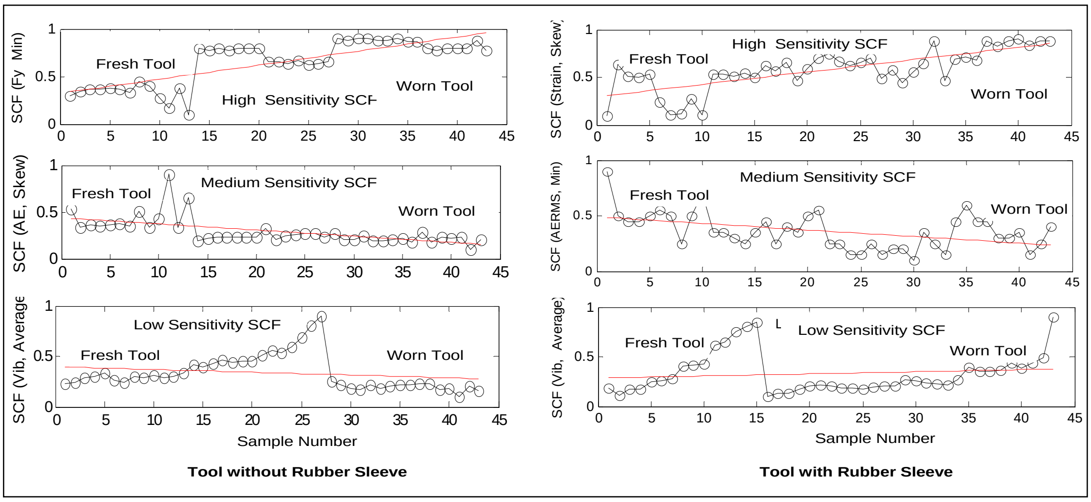

Figure 8. .Example of low, medium and high sensitivity SCF for the tool's wear.

The SCFs are visually inspected and it has been found that SCFs with high absolute slope show higher sensitivity to the fault. Table 2 presents the highest sensitive SCFs as detected by the ASPS approach. Notice that Table 2 and Figure 8 prove that the change in the characteristic of the fixturing system has caused change in the most sensitive sensors and signal processing systems that can be used to detect tool wear. For example, with normal fixturing system, force signals are found to be the most sensitive to detect tool wear. However, with the rubber sleeve system, strain and sound signals are found to be the most sensitive signals to detect tool wear.

Table 2. The most sensitive SCFs detected by the ASPA approach.

Tool without Rubber sleeve			**Tool with Rubber sleeve**		
Sensor	**Signal Processing Method**	**Sensitivity**	**Sensor**	**Signal Processing Method**	**Sensitivity**
Fy	Min	0.7015	Strain	Skew	0.6401
Fy	Average	0.6509	Microphone	Power	0.6182
Fx	Average	0.6377	Microphone	Std	0.6051
Fy	Range	0.6107	Strain	Std	0.5838
Fy	Std	0.5281	Vibration	Kurtosis	0.5583
Fz	kurtosis	0.4902	Microphone	Kurtosis	0.5422
Fy	Max	0.4507	Fy	Average	0.5061
Fz	Range	0.4505	Fy	Min	0.5000
AERMS	Max	0.4472	Microphone	Range	0.4967
AERMS	Std	0.4228	Fy	Max	0.4889

5. Conclusion

Recently, more attention has been directed towards improving sensor fusion techniques to detect or predict faults in manufacturing processes. This paper has investigated the effect of collet fixturing quality on the design of condition monitoring systems to detect tool wear. The paper has investigated the difference in the system's behaviour and the changes in the condition monitoring system when the cutting tool is not rigidly fastened to the collet which is emulated using a rubber sleeve. A group of sensors, namely acoustic emission, force, strain, vibration, force, strain, vibration and sound, have been utilised to design the condition monitoring system.

Automated sensor and signal Sensor and Signal Processing Selection (ASPS) approach [16] has been implemented to address the effect of the tool holding device (collet) on the monitoring system and the most sensitive sensors and signal processing method to detect tool wear. The results indicate that the change in the fixturing quality has caused variation in the dynamics of the system and demonstrated significant effect on most sensitive sensors and signal processing methods for the detection of tool wear. Therefore, this paper has proved that minor changes in the setup of the machining operation could have significant influence on the condition monitoring system.

References

[1] Robert b.Ruce, Thompson P. C. Krishnamachary, Annual StudentLight,fixture Design Compwetion 2007,july 4th,2008.online. www.i-m-a-d-e.org/robert-bruce-thompson-annual-student-light-fixture-design-competition.

[2] McIlwraith A H, Collets and friction", Measurement Science and Technology, Vol. 16, 2005, 1442–1448, Online. www.iop.org/EJ/article/0957 0233/16/7/006/mst5_7_006.pdf [Accessed on 9/9/2009].

[3] Daniel P. Soroka, Work holding Collets and Factors That Affect Grip Force, Article from: Production Machining, Harding Workholding Division Posted on: 8/24/2004, [Online]. www.productionmachining.com › Articles [Accessed on 18/8/2009].

[4] Destefani Jim, Holding the precision line, Sme.org/manufacturing engineering, 57.5/2002[Online]. www.tmsmith.com/Holding_the_Precision_Line.pdf*[Accessed on 10/9/2009]*.

[5] Ramesh R., Mannan M. A. And Poo A. N, Error compensation in machine tools — a review: Part I: geometric, cutting-force induced and fixture-dependent errors", International Journal of Machine Tools and Manufacture, Vol. 40, No. 9, 2000, 1235-1256.

[6] Govender Evandarin, An intelligent deflection prediction system for machining of flexible components, PhD thesis, Nottingham University, UK,2001..

[7] CNC Router Technology - Technical Section Catalog - spindlesOnline]. www.technocnc.co.uk/cncpages/HTML/Tech_Section_7.html[Accessedon 26/8/2009.

[8] Uriarte L., Herrero A., Zatarain M., Santiso G., Lopéz de Lacalle L.N., Lamikiz A., Albizuri J., Error budget and stiffness chain assessment in a micromilling machine equipped with tools less than 0.3 mm in diameter", Precision Engineering, Vol. 31, No. 1, 2007, 1-12.

[9] Yeh J.H. and Liou F.W**,** Clamping Fault Detection in a Fixturing System'', Journal of Manufacturing Processes", Vol. 2, No. 3, 2000, 194-202.

[10] Rakowski Leo, Monitoring Improves Machine up Time and Shop Efficiency, Article from**:** Production Machining, Postedon:9/1/2003,[Online]. www.productionmachining.com › Articles [Accessed on 28/8/2009].

[11] Brophy B., Kelly K. and Byrne G**.,** AI-based condition monitoring of the drilling process'', Journal of Materials Processing Technology, Vol. 124, No. 3, 2002, 305-310.

[12] Montronix, Inc., Process Monitoring to Improve Machine Tool Performance", Research and data for Status Report 95-02-0020 were collected during July 2003.

www.Statusreports.atp.nist.gov/reports/95-02-0020PDF[accessed on 17/9/2009].

[13] Al-Habaibeh A. , Zorriassatine F. and Gindy N., Comprehensive experimental evaluation of a systematic approach for cost effective and rapid design of condition monitoring systems using Taguchi's method , Journal of Materials Processing Technology, Vol. 124, No. 3, 2002, 372-383.

[14] Al-Habaibeh A, Gindy N and Parkin R M , Experimental design and investigation of a pin-type reconfigurable clamping system for manufacturing aerospace components**"**, Proceedings of the Institution of Mechanical Engineers, Part B: Journal of Engineering Manufacture, Vol. 217, No. 12, 2003, 1771-1777.

[15] Abbas Jabbar K., Design and Performance Evaluation of Mechanically Guided Fixture for gripping Cylindrical Parts using Computer modelling, MSc thesis, University of Technology, Baghdad, Iraq, 2001.

[16] Al-Habaibeh A., Al-Azmi, N. Radwan and Yang Song, The Application of Force and Acoustic Emission Sensors for Detecting Tool Damage in Turning Processes Key Engineering Materials, Vols. 419-420, pp 381-384.

JJMIE

Volume 5 , Number 1, February 2011
ISSN 1995-6665
Pages 23 - 28

Jordan Journal of Mechanical and Industrial Engineering

Static and Dynamic Analysis of Hydrodynamic Four-lobe Journal Bearing with Couple Stress Lubricants

Boualem Chetti*

Institute of sciences and Technology, Center University of Khemis Miliana, Ain Defla, Algeria

Abstract

In this work, the static and dynamic performance characteristics of four-lobe bearing operating with couple stress lubricant are presented. The modified Reynolds equation has been solved using the finite difference method. The effects of the couple stress parameter on the key performance of a four-lobe journal bearing such as; the load carrying capacity, the friction force, side leakage, the stiffness and damping, the critical mass and whirl ratio are determined. The computed results show that the presence of couple stresses improves the performance characteristics of a four-lobe bearing compared to that lubricated with Newtonian fluids.

Keywords: Four-lobe bearings, stability analysis, couple-stress fluids.

1. Introduction

The problem of instability is often faced by hydrodynamic bearings operating at high speeds. The non-circular bearings are known to have better stiffness and stability characteristics. The earliest work directed towards establishing the study of the steady state performance characteristics of non-circular bearings was carried out by Pinkus [1, 2]. The stability criterion for a multi-lobe bearing was developed by Lund et al. [3] based on linearization of the Reynolds equation by small perturbation theory. Allaire, Li and Choy [4] carried out an analysis of the transient response of four multi-lobe journal bearings (elliptical, three-lobe, offset and four-lobe) subject to unbalance both below and above the linearised stability thresholds for the bearing. Pressures were measured at various locations in the four-lobe bearing by Flack et al.[5]. A pair of preloaded four-lobe bearing with flexible rotor and determined the unbalance response and instability threshold was tested experimentally by Leader et al. [6]. Static and dynamic characteristics of 6 types of multi-lobe journal bearings in turbulent flow regime have been studied by Abdul-Wahed et al. [7]. Ma and Taylor [8] presented a theoretical evaluation of five commonly used types of bearings through a comparison of their steady state performance characteristics. The results show that in general the performance of the noncircular bearing is inferior to that of the circular bearing. The new type of bearing, namely, four-lobe pressure-dam bearing was studied by Mehta et a. [9].

Many practical lubrication applications may be found where the Newtonian fluid constitutive approximation is not a satisfactory engineering approach to lubrication problems. The theory of Stokes [10] is the simplest generalization of the classical theory of fluids which allows for polar effects such as the presence of a non-symmetric stress tensor and couple stresses. The couple stress may appear to a noticeable extent in the flow of liquids containing additives or in a lubricant containing long-chain molecules.

The performance characteristics of hydrodynamic journal bearings using lubricants with couple stress have been studied by many researchers [11, 12]. Mokhiamer et al. [13] investigated the effects of the couple stress parameter on the static characteristics of finite journal bearings with flexible bearing linear material. Elsharkawy et al.[14] presented an inverse solution for a finite journal bearing lubricated by a couple stress fluid. A numerical study of the performance of a dynamically loaded journal bearing lubricated with couple stress fluids was given by Wang et al.[15]. Guha [16] presented the effects of couple stress fluids on the dynamic characteristics of finite journal bearings. Recently, Crosby et al.[17] studied the static and dynamic characteristics of two-lobe journal bearing lubricated with couple stress fluids.

In this paper, the four-lobe journal bearing lubricated with Newtonian and couple stress fluid have been analyzed. The effects of the couple stress on the static and dynamic characteristics have been studied in terms of the load carrying capacity, the friction force, side leakage, the stiffness and damping, the critical mass and whirl ratio.

*Corresponding author. b.chetti@gmail.com

2. Theoretical Analysis

2.1. Governing Equations

According to Stokes micro-continuum theory, a couple stress fluid is characterized by two constants μ and η whereas only one constant μ appears for a Newtonian fluid. This new material constant η responsible for the couple stress property could be determined by some experiments as discussed by Stokes [10]. With the dimension of $l = (\eta/\mu)^{1/2}$ being length, it could be considered as the characteristics length of various additives blended in Newtonian lubricant. The influence of couple stress on the system is dominated by this couple stress parameter. The modified Reynolds equation for the couple- stress fluids [17] in the non-dimensional form is given by:

$$\frac{\partial}{\partial\theta}\left(\frac{\bar{G}\left(\bar{h},\bar{l}\right)}{12}\frac{\partial\bar{P}}{\partial\theta}\right)+\left(\frac{R}{L}\right)^{2}\left\{\frac{\partial}{\partial\bar{z}}\left(\frac{\bar{G}\left(\bar{h},\bar{l}\right)}{12}\frac{\partial\bar{P}}{\partial\bar{z}}\right)\right\}=\frac{1}{2}\frac{\partial\bar{h}}{\partial\theta}+\frac{\partial\bar{h}}{\partial t} \qquad (1)$$

where

$$\theta=\frac{x}{R},\ \bar{z}=\frac{z}{L},\ \varepsilon=\frac{e}{c},\ \bar{P}=\frac{P(c/R)^{2}}{\mu\omega},\ \bar{l}=\frac{l}{c}$$

and

$$\bar{G}(\bar{h},\bar{l})=\bar{h}^{3}-12\bar{l}^{-2}\bar{h}+24\bar{l}^{-3}\tanh\left(\frac{\bar{h}}{2\bar{l}}\right) \qquad (2)$$

2.2 Bearing Configuration

The configuration of the four-lobe bearing is shown in Fig.1. The non-dimensional fluid film thickness for each lobe is given by Mehta [9]:

$$\bar{h}_i=1+\bar{\varepsilon}_i\cos(\theta-\phi_i) \quad i = 1, 2, 3,4 \qquad (3)$$

where $\bar{h}=\frac{h}{c}$, $\bar{\varepsilon}=\varepsilon(1-\delta)$

The eccentricity ratios of each lobe for the bearing are given by Mehta [9].

$$\begin{aligned}
\varepsilon_1^2&=\varepsilon^2+\delta^2-2\varepsilon\delta\cos\left(\frac{\pi}{4}-\phi\right)\\
\varepsilon_2^2&=\varepsilon^2+\delta^2-2\varepsilon\delta\sin\left(\frac{\pi}{4}-\phi\right)\\
\varepsilon_3^2&=\varepsilon^2+\delta^2-2\varepsilon\delta\sin\left(\frac{\pi}{4}+\phi\right)\\
\varepsilon_4^2&=\varepsilon^2+\delta^2-2\varepsilon\delta\cos\left(\frac{\pi}{4}+\phi\right)
\end{aligned} \qquad (4)$$

and the attitude angles of each lobe for the bearing are given by:

$$\begin{aligned}
\phi_1&=\frac{5\pi}{4}+\sin^{-1}\left[\frac{\varepsilon}{\varepsilon_1}\sin\left(\frac{\pi}{4}-\phi\right)\right]\\
\phi_2&=2\pi-\sin^{-1}\left[\frac{\varepsilon}{\varepsilon_2}\cos\left(\frac{\pi}{4}+\phi\right)\right]\\
\phi_3&=\frac{\pi}{4}-\sin^{-1}\left[\frac{\varepsilon}{\varepsilon_3}\cos\left(\frac{\pi}{4}+\phi\right)\right]\\
\phi_4&=\frac{3\pi}{4}-\sin^{-1}\left[\frac{\varepsilon}{\varepsilon_4}\sin\left(\frac{\pi}{4}+\phi\right)\right]
\end{aligned} \qquad (5)$$

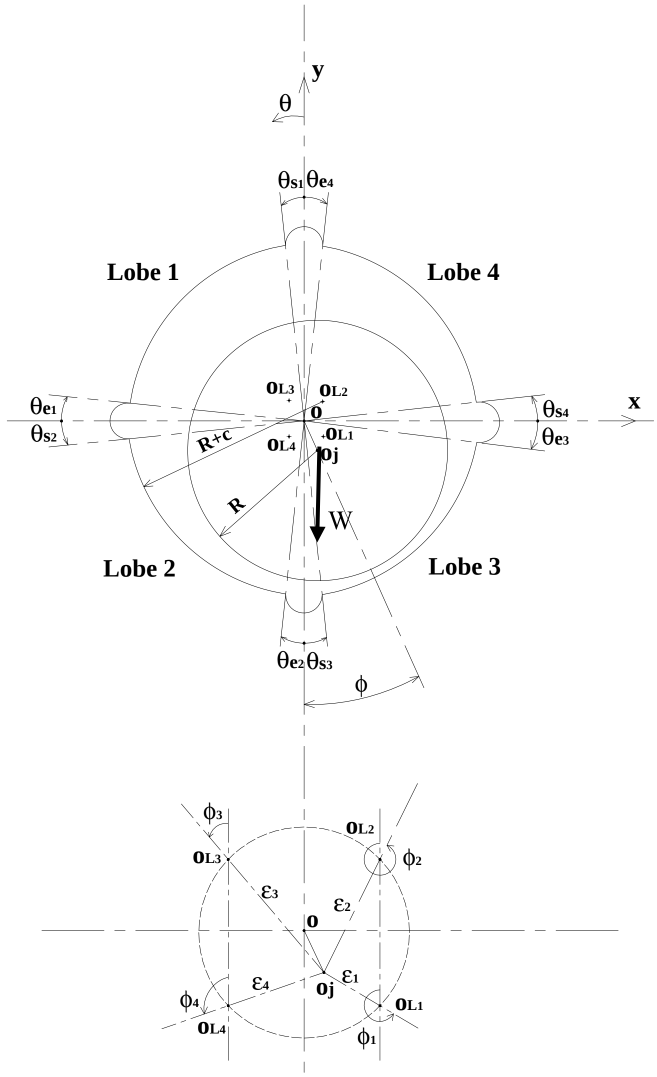

Figure 1. Bearing Geometry

2.3. Boundary Conditions

$$\bar{P}=0 \quad \text{at } \bar{z}=0 \text{ and } \bar{z}=1 \qquad (6a)$$

$\bar{P}=0$ at $\theta=\theta_{s1}$, $\theta=\theta_{s2}$ $\theta=\theta_{s3}$ and

$$\theta = \theta_{s4} \tag{6b}$$

$\frac{\partial \bar{P}}{\partial \theta} = 0$ at $\theta = \theta_{t1}$, $\theta = \theta_{t2}$, $\theta = \theta_{t3}$ and

$$\theta = \theta_{t4} \tag{6c}$$

$\bar{P} = 0$ for $\theta_{e1} \geq \theta \geq \theta_{t1}$, $\theta_{e2} \geq \theta \geq \theta_{t2}$,

$$\theta_{e3} \geq \theta \geq \theta_{t3} \text{ and } \theta_{e4} \geq \theta \geq \theta_{t4} \tag{6d}$$

Equations (6c) and (6d) are the Swift-Stieber boundary conditions at the trailing edges.

2.4. Static Characteristics

Equation (1) with boundary conditions were solved using iterative finite difference methods in which the value of any pressure is given by

$$A_0 \bar{P}_{i,j} + A_1 \bar{P}_{i+1,j} + A_2 \bar{P}_{i-1,j} + A_3 \bar{P}_{i,j+1} + A_4 \bar{P}_{i,j-1} = B_{i,j} \tag{7}$$

The bearing's static characteristics are obtained by solving the modified Reynolds equation (1) for static loading ($\frac{\partial h}{\partial t} = 0$). Thus, the pressure distribution, load components, and friction force could be obtained. The friction factor is

$$C_f = \frac{\int_0^{2\pi} \int_0^1 \left(\frac{1}{\bar{h}} + \frac{\bar{h}}{2} \frac{\partial \bar{P}}{\partial \theta} \right) d\theta \, d\bar{z}}{W} \tag{8}$$

The side leakage flow is:

$$\bar{Q}_s = \int_0^{2\pi} \frac{\partial \bar{P}}{\partial \bar{z}} \Big|_{\bar{z}=0} \left[\bar{h}^{-3} - 12\bar{l}^{-2} \bar{h} + 24\bar{l}^{-3} \tanh\left(\frac{\bar{h}}{2\bar{l}} \right) \right] d\theta \tag{9}$$

2.5. Dynamic characteristics

The fluid film stiffness and damping coefficients are respectively given by

$$\begin{pmatrix} K_{xx} & K_{xy} \\ K_{yx} & K_{yy} \end{pmatrix} = -\begin{Bmatrix} \partial / \partial x \\ \partial / \partial y \end{Bmatrix} \begin{bmatrix} W_x & W_y \end{bmatrix} \tag{10}$$

$$\begin{pmatrix} C_{xx} & C_{xy} \\ C_{yx} & C_{yy} \end{pmatrix} = -\begin{Bmatrix} \partial / \partial \dot{x} \\ \partial / \partial \dot{y} \end{Bmatrix} \begin{bmatrix} W_x & W_y \end{bmatrix} \tag{11}$$

by giving small values for $\dot{x}$ and $\dot{y}$ around the equilibrium position, the partial derivatives of $\dot{x}$ and $\dot{y}$ can be calculated.

2.6. Stability Analysis

The linearized equations of the disturbed motion of the journal centre are [7]:

$$\begin{aligned} M\ddot{x} + K_{xx} x + C_{xx} \dot{x} + K_{xy} y + C_{xy} \dot{y} = 0 \\ M\ddot{x} + K_{yx} x + C_{yx} \dot{x} + K_{yy} y + C_{yy} \dot{y} = 0 \end{aligned} \tag{12}$$

Equations (12) are used to study the stability of the bearing system. Harmonic solution of the type:

$$x = x e^{\lambda t}, \quad y = y e^{\lambda t} \tag{13}$$

will be assumed [7] where $\lambda = \eta + i\nu$ is a complex frequency. The sign of the real part η allows the system stability to be defined. If ($\eta < 0$) the system is stable and vice versa. On the threshold of stability $\eta = 0$, x and y are pure harmonic motions with a frequency $\lambda = i\nu$. Thus equations (12) can be written as:

$$\begin{bmatrix} K_{xx} - M\nu^2 + i\nu C_{xx} & K_{xy} + i\nu C_{xy} \\ K_{yx} + i\nu C_{yx} & K_{yy} - M\nu^2 + i\nu C_{yy} \end{bmatrix} \begin{bmatrix} x \\ y \end{bmatrix} = 0 \tag{14}$$

For a nontrivial solution the determinant must vanish and equating the real and imaginary parts to zero gives:

$$\bar{M}\gamma^2 = \frac{\bar{C}_{xx} \bar{K}_{yy} + \bar{C}_{yy} \bar{K}_{xx} - \bar{C}_{xy} \bar{K}_{yx} - \bar{C}_{yx} \bar{K}_{xy}}{\bar{C}_{xx} + \bar{C}_{yy}} \tag{15}$$

$$\gamma^2 = \frac{\left(\bar{K}_{xx} - \bar{M}\gamma^2 \right)\left(\bar{K}_{yy} - \bar{M}\gamma^2 \right) - \bar{K}_{yx} \bar{K}_{xy}}{\bar{C}_{xx} \bar{C}_{yy} - \bar{C}_{xy} \bar{C}_{yx}} \tag{16}$$

where

$\bar{C}_{ij} = C_{ij} \frac{c\omega}{W}$, $\bar{K}_{ij} = K_{ij} \frac{c}{W}$, $\bar{M} = \frac{Mc\omega^2}{W}$, $\gamma = \frac{\nu}{\omega}$

From equations (15) and (16), the critical mass and the whirl ratio γ are calculated. $\bar{M}_c$ is the critical mass parameter above which the bearing is unstable.

3.Results and Discussion

The results are obtained for this bearing with journal radius to bearing length $R/L = 1$, and couple stress parameter $\bar{l}$ ranging from 0.0, 0.2 and 0.4 ($\bar{l} = 0$ is the Newtonian lubricant case). The ellipticity ratio used in this study is 0.5.

The pressure distribution for the four-lobe bearing lubricated with Newtonian fluid is compared with the results obtained in [9] and the comparison is good.

Figure 2. depicts the pressure distribution along the circumferential at bearing mid-plane for various values of a couple stress fluid parameters. It can be seen that the pressure increases with the increase of the couple stress fluid parameter.

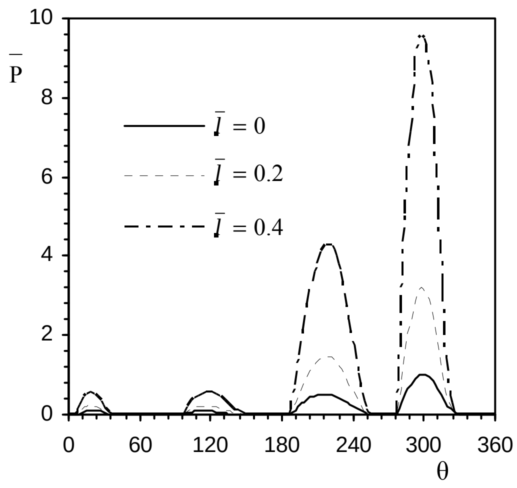

Figure 2. Pressure distribution for various values of couple stress parameter

As results of the increasing of the pressure, the load carrying capacity increases with the increase of the couple stress parameter and this can be shown in figure.3.

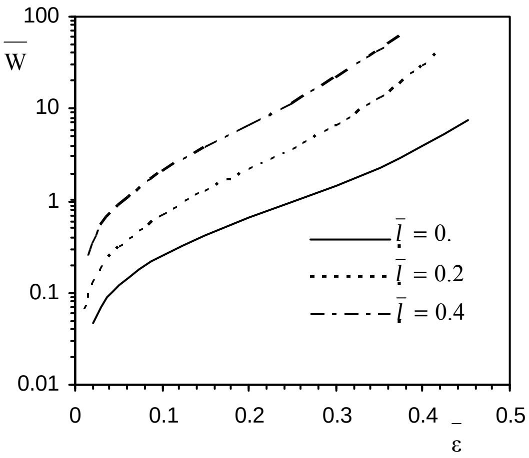

Figure 3. $\bar{W}$ versus $\bar{\varepsilon}$ for different values of $\bar{l}$

Figure 4 shows the friction coefficient versus with the eccentricity ratio for various values of the couple stress parameter. The friction coefficient deceases with increasing the couple stress parameter and its effect is more pronounced at high values of eccentricity ratio.

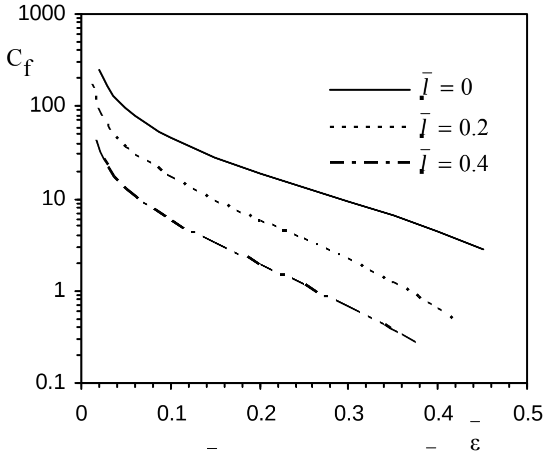

Figure 4. C_f versus $\bar{\varepsilon}$ for different values of $\bar{l}$

Figure 5 gives the variation of the dimensionless side leakage with the eccentricity ratio for different values of the couple stress parameter. The figure indicates that the effect of the couple stress parameter is not significant on the side leakage.

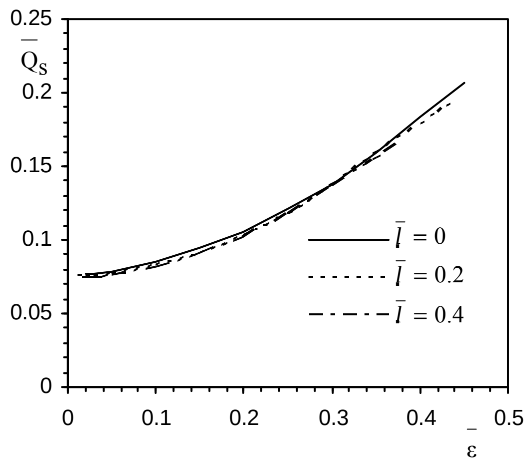

Figure 5. $\bar{Q}_S$ versus $\bar{\varepsilon}$ for different values of $\bar{l}$

Figure 6 shows the stability chart for various values of couple stress parameter. The lower and upper sides of each curve correspond to stable and unstable regions respectively. It can be seen that the stable regions for the bearings lubricated with a couple stress fluid are higher than for those lubricated with a Newtonian fluid. By increasing the couple stress parameter $\bar{l}$ the stable region increases for full range of eccentricity ratios. At high values of the eccentricity ratio the effect of the couple stress parameter $\bar{l}$ is more pronounced.

In Figure 7, the effect of couple stress parameter on the whirl ratio is shown. It is observed that the whirl ratio decreases with the increasing of the couple stress parameter and its effect is very important at higher values of eccentricity ratio.

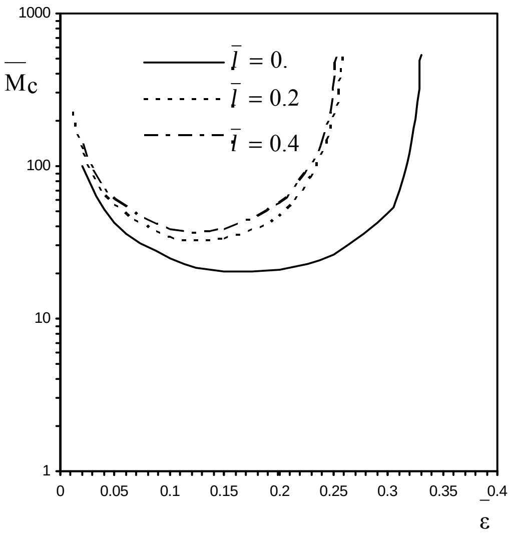

Figure 6. $\overline{M}_c$ versus $\bar{\varepsilon}$ for different values of $\bar{l}$

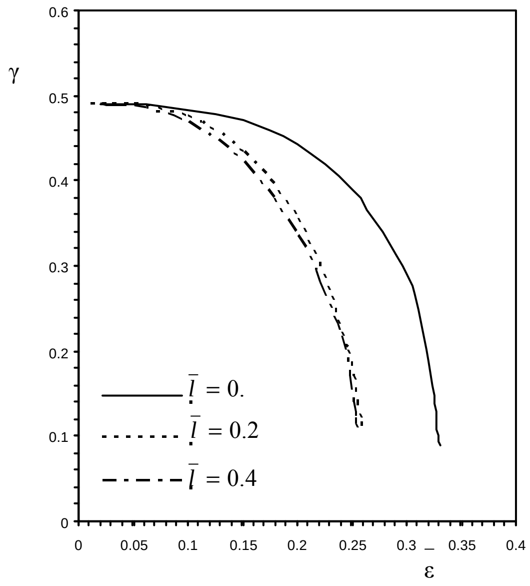

Figure 7. γ versus $\bar{\varepsilon}$ for different values of $\bar{l}$

4. Conclusions

According to the results evaluated, conclusions can be drawn as follows:

1) The effects of the couple tress parameter provide an increase in the pressure and the load carrying capacity.
2) The friction coefficient decreases with an increase of the couple stress parameter.
3) The effect of the couple stress on the side leakage is not remarkable.
4) The four-lobe journal bearing lubricated with couple stress fluid is more stable than that lubricated with Newtonian fluids.
5) The whirl ratio decreases with increasing of the couple stress parameter thus indicating more stable performance.

Nomenclature

c	major clearance
c_m	minor clearance
$\overline{C}_{ij}$	dimensionless damping coefficients
e	eccentricity
e_p	$c - c_m$, ellipticity
h	oil film thickness
$\overline{K}_{ij}$	dimensionless stiffness coefficients
L	bearing length
l	couple-stress parameter
$\bar{l}$	dimensionless couple- stress para- meter
M	mass of journal
P	pressure
R	journal radius
W'	bearing load
W	$W'(c/R)^2/\mu_i RL$, non-dimensional bearing load
x, y, z	circumferential, radial and axial co-ordinates respectively
δ	e_p/c , ellipticity ratio
ε	*e/c*, eccentricity ratio based on major clearance
$\bar{\varepsilon}$	e/c_m, eccentricity ratio based on minor clearance
θ	angular coordinate
$\theta_{e1}, \theta_{e2}, \theta_{e3}, \theta_{e4}$	angular coordinates at the end of bearing pads
$\theta_{s1}, \theta_{s2}, \theta_{s3}, \theta_{s4}$	angular coordinates at the start of bearing pads
$\theta_{t1}, \theta_{t2}, \theta_{t3}, \theta_{t4}$	angular coordinates at the trailing edges
μ	lubricant Viscosity
ν	whirl frequency
γ	whirl ratio
ϕ	attitude angle
ω	angular velocity of the journal

References

[1] O. Pinkus, Analysis of elliptical bearings, ASME Trans., Journal of basic Engineering, Vol. 78, 1956, 965-973.

[2] O.Pinkus , Analysis and characteristics of the thee-lobe bearing , ASME Trans. Journal of Basic Engineering , 1959, 49-55.

[3] J.W.Lund and K.K.Thomson , A Calculation Method and Data for the Dynamic Coefficients of Oil-Lubricated Journal Bearing , Topics in Fluid Bearing and Rotor Bearing System Design and Optimist the ASME Design Eng-Conf, 1978, 1-29.

[4] P. E. Allaire, D. F. Li and K. C. Choy, Transient unbalance response of four multilobe journal bearings, ASME Trans., Journal of Lubrication Technology, Vol. 102, 1980, 300-307.

[5] R. D. Flack, M. E. Leader and P. E. Allaire, An experimental and theoretical investigation of pressures in four lobe bearings, wear, Vol. 61, 1980, 233-242.

[6] M. E. Leader, R. D. Flack and D. W. Lewis, An experimental determination of the instability of a flexible rotor in four-lobe bearings, Wear, Vol. 58, 1980, 35-47.

[7] N. Abdul-Wahed, D. Nicolas and M. T. Pascal, Stability and Unbalance Response of Large Turbine Bearings, J. Lubric. Technol. ASME.Trans, Vol. 104, 1982, 66-75.

[8] M. T. Ma and C. M. Taylor, A comparative thermal analysis of the static performance of different fixed profile bore plain bearings, J. Proc. Instn. Mech. Engrs., Vol. 213, 1999, 13-30.

[9] N. P. Mehta, S. S. Ratten and G. Bhushan, Static and dynamic characteristics of four-lobe pressure-dam bearings, J. Tribology Letters, Vol. 15, 2003, 415-420.

[10] V. K. Stokes, Couple stress in fluids, Phys.Fluids, Vol. 9, 1966, 1709.

[11] P. Sinha , C. Singh and K. R. Prasad, Couple stresses in journal bearing lubricants and the effects of cavitations, Wear, Vol. 67, 1981, 15-24.

[12] J. Lin, Effects of Couple Stresses on the Lubrication of Finite Journal Bearings, Wear, Vol. 206, 1997, 171-178.

[13] U. M. Mokhiamer, W. A. Crosby and H. A.El-Gamal , A Study of a Journal Bearing Lubricated by Fluids with Couple Stress Considering the Elasticity of The Liner , Wear, Vol. 224, 1999,194-201.

[14] A. Elshakawy and L. H. Guedouar, An Inverse Solution for Finite Bearings Lubricated with Couple Stress Fluids, J. Tribology Int. Vol. 34, 2001,107-118.

[15] X. Wang, K. Zhu and S. Wen, On the Performance of Dynamically Loaded Journal Bearings Lubricated with Couple Stress Fluids, J. Tribology Int. Vol. 35, 2002,185-191.

[16] S. K. Guha, A Theoretical Analysis of Dynamic Characteristics of Finite Hydrodynamic Journal Bearings Lubricated with Coupled Stress Fluids, J. Pro. Instn. Mech. Engrs. Vol. 218 part j, 2004, 125-133.

[17] W. A. Crosby and B. Chetti, The static and Dynamic Characteristics of Two-lobe Journal Bearing Lubricated with Couple Stress Fluid , Tribology Trans. Vol. 52, 2009,262-268.

JJMIE

Volume5 , Number1, February.2011
ISSN 1995-6665
Pages 29- 32

Jordan Journal of Mechanical and Industrial Engineering

Thermal Analysis of Discrete Water supply in Domestic Hot Water Storage Tank

N. Beithou[a]*, M. Abu Hilal[b], I. Abu-Alshaikh[a]

[a] *Department of Mechanical and Industrial Engineering, Applied Science University, ,Amman, Jordan.*
[b] *Department of Mechanical Engineering, An-Najah National University, Nablus, Palestine.*

Abstract

Energy and water are very important commodities to human life. The world is suffering from a critical shortage in water and energy; the researchers must work hard to find sources of potable water and renewable energy. Energy and water saving techniques have a great importance especially in this transmission period. In this paper analyses were done for discrete water supply in hot water storage tanks, aiming to reduce energy and water losses. The analyses were based on an experimental study for the temperature distribution in the hot water storage tank for different flow rates and off periods, 3, 6, and 9 L/min, and 5, 10, and 15 minutes were considered for flow rates and off periods respectively. It has been found that increasing the hot water consumption rate reduces the total delivered hot water to the consumer. The analyses indicated increase in the usable hot water for small and medium off periods. This increase results in water and energy saving for the consumer.

Keywords: Discrete water supply, domestic storage tank, hot water management, Energy Saving, Usable energy.

1. Introduction

As overall the world is suffering from a critical shortage in water and energy resources. The water and energy costs have reached new levels and are expected to continue to rise. The ramifications of this large increase in water and energy costs, will pose serious challenges to the economies of most developing nations, and this may results in an undesired serious conflicts between nations. It's the role of researchers to minimize the energy and water consumption and seek new resources. In the way to minimize heat losses and reduce hot water consumption, different researchers over the past years investigated hot water systems, use patterns, and consumption loads [1,3,5,6,8]. S.A. Ahmed et al.[2], in their study to understand the reasons of wasting water by contamination, examined different methods of collection and storage, and found that mostly safe water is contaminated during storage periods. Other researches studied insulation to reduce heat losses in the Hot Water Storage Tank (HWST) [4,9], special heat exchangers were considered by Industrial Technology to recover the energy wasted during usage, on the same direction the role of women and modern water supply systems were discussed in [7].
N. Beithou in 2006[10], analyzed the mixing nature of the cold and hot water inside the storage tank, he observed that high turbulent mixing occurs especially at high flow rates which resulted in a lower amount of the available hot water for customs use. The supply features of cold water and methods to minimize turbulences in the HWST were discussed in [11], approximately 17% saving in usable hot water was achieved by using a round curved cover on the bottom supply line.

Conservation of resources can be defined as more efficient use of these resources. In this study the thermal analyses of the discrete water usage from a HWST were investigated. 3, 6, and 9 lpm, and 5, 10, and 15 minutes were considered for flow rates and off periods respectively. The analyses were dependent on the temperature distributions all over the HWST and the amount of usable hot water out of the HWST.

*Corresponding author: nabil@asu.edu.jo

2. Experimental Test Rig

In order to investigate and analyze the nature of hot water temperature variations within the HWST, data on the variation of the hot water temperatures should be collected under the different variable conditions. To achieve these data, an experimental rig has been constructed as shown in Figure 1. This rig consists of hot water reservoir, cold water reservoir, water pump, flow meter, hot water storage tank, and Data Acquisition System (DAS) (Lab-View software). The DAS automatically collect the temperatures from the storage tank at different times and positions then stores them in a separate excel file.

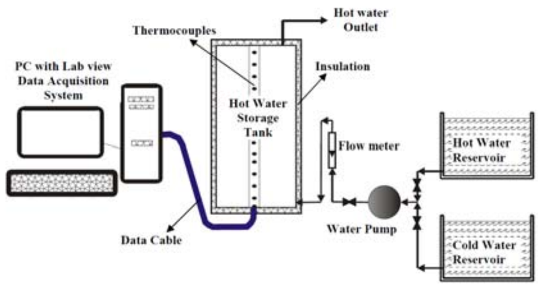

Figure 1. Schematic Diagram for the Experimental Rig.

The dimensions and the important parameters of the HWST are listed in Table 1. This tank has a total capacity of 108 liters and is provided with 15 thermocouples mounted at the middle of the HWST to record the temperatures throughout the tank. Different supply flow rates and off use periods were considered to understand the effect of discrete water supply on the usable hot water inside the HWST.

Table 1. Dimensions and data for the hot water storage tank experiments

Hot Water Storage Tank	
Height	***0.78 m***
Internal diameter	***0.42 m***
Number of thermocouples	***15***
Distance between thermocouples	***0.05 m***
Insulation thickness	***0.04 m***
Tank total capacity	***0.108 m^3***
Flow rate range	***3-9 lpm***
Waiting Periods	***5, 10, 15 min***
Time step used	***5 seconds***
Piping Diameter	***0.5 in***

2.1 Experimental Procedure

In the experiments performed, hot water is filled into the HWST from the hot water reservoir, circulated until having a uniform temperature of 62 °C inside the tank; then the cold water is pumped from the cold water reservoir at a specific flow rate into the HWST through the supply line, different flow rates were investigated with different off use periods, the temperature-changes resulting from the mixing process are then recorded for analyses purposes.

3. Experiments Performed

In this study, experiments were performed for different flow rates (3, 6, and 9 L/min) and for different off use periods (5, 10, and 15 min) simulating the domestic hot water consumption.

3.1 Continuous versus discrete flow

A single case was considered to compare the contineuous and discrete flow rates. Figure 2 shows the temperature distributions of the 15 thermocouples inside the HWST for 3.5 liters per second for the case of continuous flow [11].

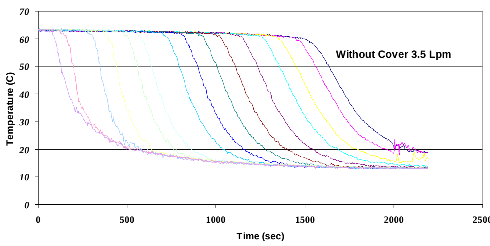

Figure 2. Temperature distributions of the 15 thermocouples versus time. [Side supply without cover, flow rate = 3.5 L/min].

The figure shows smooth temperature distributions as the flow rate is relatively small. This can be compared to the case of discrete supply shown in figure 3. for flow rate 3 L/min with 10 minutes waiting period. The heat transfer between the layers is clear especially at the beginning of the water supply where the temperature differences are large, as the time passes heat transfer between layers is reduced as the temperatures differences comes to be closer. This heat transfer affect the total amount of usable hot water user can achieve.

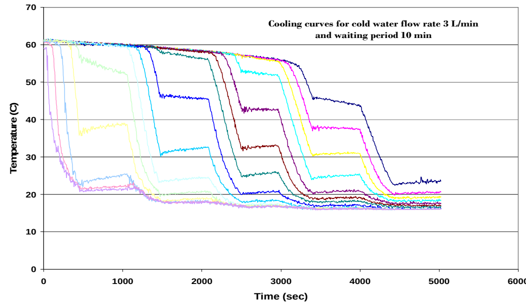

Figure 3. Temperature distributions of the 15 thermocouples versus time.[3 L/min, with 10 minutes waiting period].

3.2. Flow rate variation

Increasing the flow rate in the continuous supply feature reduces the amount of usable hot water [10]. In this study different flow rates were considered as well to analyze the effect of flow rate on the total usable energy from the HWST. For a moderate waiting period of 10 minutes Figure 3. shows the temperature distributions inside the HWST for 3 L/min. and Figure 4. shows the temperature distributions inside the HWST at 6 L/min.

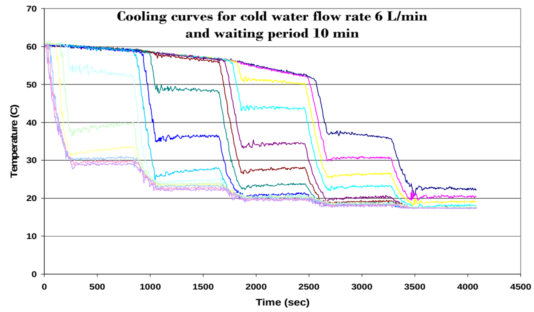

Figure 4. Temperature distributions of the 15 thermocouples versus time.[6 L/min, with 10 minutes waiting period].

The variation in temperature distributions shows longer periods of heat transfer at the lower flow rates but between close temperature differences. Figure 5. shows the effect of flow rate variation on the total usable energy for waiting periods 10 minutes. It is clear that increasing the flow rate reduces the amount of usable hot water delivered to the consumer.

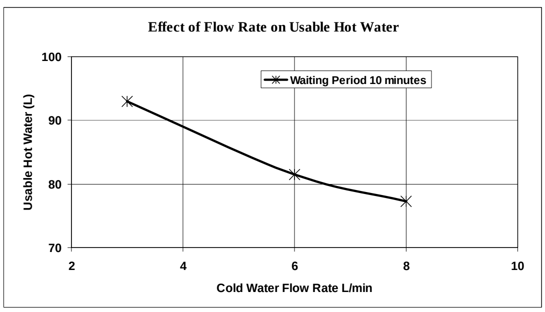

Figure 5. The variation of usable hot water delivered versus flow rate.

3.3. Discrete Use Effect

To understand the effect of off use periods on the total usable energy received from the HWST, different waiting periods starting from 5 to 15 minutes were considered.

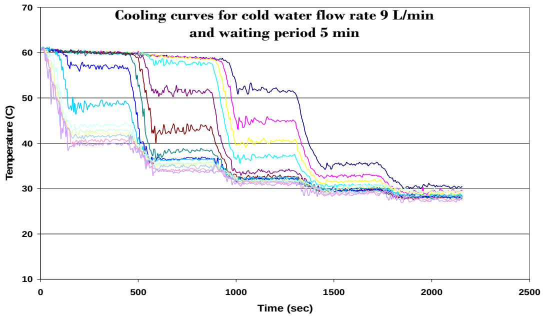

Figure 6. Temperature distributions of the 15 thermocouples versus time.[9 L/min, with 5 minutes waiting period].

Figure 6. shows the temperature distribution for a flow rate of 9 L/min, and 5 minutes off use period. The fluctuation in the figure is due to high flow rate used. The heat transfer occurs between closer temperatures. The effect of the off use periods on the usable hot water is shown in figure 7.

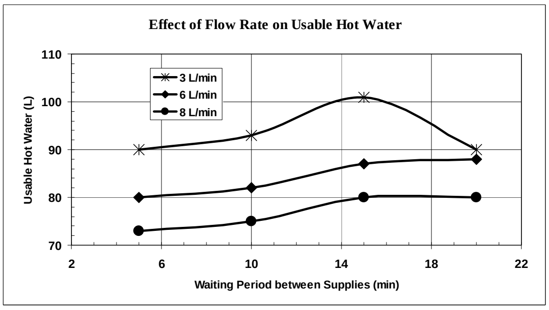

Figure 7. Total Usable Hot water Versus Waiting Periods.

Figure 7. indicates an increase in the usable hot water for small and medium off use periods because heat transfer between the hot and cold water layers. This increase results in water and energy saving for the consumer. The curves in figure 7. state that for each flow rate there is an optimum off period which produce a maximum usable hot water. The amount of usable hot water is decreased after while for the different flow rates as expected.

This optimum off use periods is valuable to save water and energy, and can be integrated with the solar radiation in solar heating systems in winter and summer to determine the new optimum off use periods for the different locations and times in the world. Such information can be very helpful for consumers for maximizing the usable hot water in the HWST.

4. Conclusions

To help saving water and energy resources in the world an experimental study of the usable water in the domestic hot water storage tank for the case of discrete water supply was performed. Different experiments with different flow rates and different off use periods have been done. The temperature distributions for the different cases were analyzed. It has been found that for discrete flow, increasing the flow rates decreases the amount of usable hot water exactly as been found for continuous flow cases in the previous studies. The distinguished result of this study was the increase in the usable hot water achieved at small and medium off use periods. Also the optimum off use periods for different flow rates after which the usable hot water is decrease as expected.

It is recommended to integrate the results of this study with the solar radiations absorbed by the solar heating hot water tanks, this integration will result in determining the optimum or permissible off use periods in summer or winter seasons at different latitudes and solar time.

5. References

[1] K.T. Papakostas, N.E. Papageorgiou, B.A. Sotiropoulos," Residential Hot Water Use Patterns in Greece", Solar Energy; Vol. 54, Vol. 6, 1995, 369-374.

[2] S. Ahmed, B. Hoque, A. Mahmud,' Water management practices in rural and urban homes: a case study from Bangladesh on ingestion of polluted water', Public Health, Vol. 112, 1998, 317-321.

[3] Wiehagen J., Sikora J.L.," Performance Comparison of Residential Hot Water Systems" NAHB Research Center, Upper Marlboro, Maryland, NREL/2003.

[4] Barta L., "Energy Conservation of Domestic Hot Water Distribution Systems", 27th International Symposium CIB W62 Water Supply and Drainage for Buildings, September 17-20, 2001, Portoroz, Slovenia.

[5] Takata H., Murakawa S., Nishina D., and Koshikawa Y., "An Analysis on the Load of Hot Water Consumption in the Apartment Houses", 27th International Symposium CIB W62 Water Supply and Drainage for Buildings, September 17-20, 2001, Portoroz, Slovenia.

[6] Merrigan, T," Residential Conservation Demonstration Program: Domestic Hot Water", Florida Solar Energy Center, Cape Canaveral (USA), Technical Report, 2001 May 13.

[7] N. Singh, P. Bhattacharya, G. Jacks, J. Gustafsson,' Women and Modern Domestic Water Supply Systems: Need for a Holistic Perspective', Water Resources Management, Vol. 18, 2004, 237–248.

[8] I. Sezai, L. B. Y. Aldabbagh, U. Atikol, H. Hacisevki "Performance Improvement by using Dual Heaters in a Storage-type Domestic Electrical Water-Heater", Applied Energy, Vol. 81, 2005, 291-305.

[9] N. Altuntop, Z. Kilik, V. Ozceyhan, O. Kincay,' Effect of water inlet velocity on thermal stratification in a mantled hot water storage tank', Int. J. Energy Res., Vol. 30, 2006, 63–176

[10] N. Beithou," Heat Transfer Aspects in Bottom Flow Mixing of Cold Water and Hot Water in Domestic Hot Water Storage Tank", Journal of Mechanical Engineering, Vol. 57, No. 1 , 2006, 34-44.

[11] N. Beithou, M. Abu Hilal," Hot Water Management of DHW Storage Tank: Supply Features", accepted for publication in JJMIE.

JJMIE

Volume 5, Number 1, February 2011
ISSN 1995-6665
Pages 33 - 38

Jordan Journal of Mechanical and Industrial Engineering

Synthesis of Hard Coatings and Nano Modification with Ion Implantation

Branko Skoric*, Damir Kakas, and Aleksandar Miletic

Department of Production Engineering, University of Novi Sad, Serbia,

Abstract

In this paper, we present the results of a study of TiN films which are deposited by a Physical Vapor Deposition and Ion Beam Assisted Deposition. In the present investigation the subsequent ion implantation was provided with N^{2+} ions. The ion implantation was applied to enhance the mechanical properties of surface. The film deposition process exerts a number of effects such as crystallographic orientation, morphology, topography, densification of the films. The evolution of the microstructure from porous and columnar grains to denser packed grains is accompanied by changes in mechanical and physical properties. A variety of analytic techniques were used for characterization, such as scratch test, calo test, SEM, AFM, XRD and EDAX. The experimental results indicated that the mechanical hardness is elevated by penetration of nitrogen, whereas the Young's modulus is significantly elevated.

Keywords: Solar cells, Hard coatings, Ion implantation, Synthesis, Microstructure, Nanohardness .

1. Introduction

The film deposition process exerts a number of effects such as crystallographic orientation, morphology, topography, densification of the films. The optimization procedure for coated parts could be more effective, knowing more about the fundamental physical and mechanical properties of a coating. In this research are present the results of a study of the relationship between the process, composition, microstructure and nanohardness of duplex TiN coatings and modified with ion implantation.

A duplex surface treatment involves the sequential application of two surface technologies to produce a surface composition with combined properties [1]. A typical duplex process involves plasma nitriding and the coating treatment of materials. In the paper are presented characteristics of hard coatings deposited by PVD (physical vapor deposition) and IBAD (ion beam assisted deposition). The duplex coating method can improve further of the tribological properties and load-bearing capacity of materials beyond metals. The synthesis of the TiN film by IBAD has been performed by irradiation of Ar ions. The evolution of the microstructure from porous and columnar grains to dense packed grains is accompanied by changes in mechanical and physical properties. Subsequent ion implantation was provided with N^{5+} ions. Ion implantation has the capabilities of producing new compositions and structures unattainable by conventional means. Implantation may result in changes in the surface properties of a material, including hardness, wear, coefficient of friction and other properties.

Thin hard coatings deposited by physical vapor deposition (PVD), e.g. titanium nitride (TiN) are frequently used to improve tribological performance in many engineering applications [2]. In many cases single coating cannot solve the wear problems [3]. The combination of nitriding and hard coating allows the production of duplex coatings, which are distinguished by a high resistance against complex loads, since the advantages of both individual processes are combined here. The film deposition process exerts a number of effects such as crystallographic orientation, morphology, topography, densification of the films. The optimization procedure for coated parts could be more effective, knowing more about the fundamental physical and mechanical properties of a coating, their interdependence and their influence on the wear behavior. The effects on the structure as well as mechanical and tribological properties of the films were investigated in detail in the present research.

The results were correlated with properties determined from mechanical and tribological characterization. Therefore, by properly selecting the processing parameters, well-adherent TiN films with low friction coefficient, low wear rate and high hardness can be obtained on engineering steel substrates, and show a potential for tribological applications.

Conventional TiN and correspondingly alloyed systems show high hardness and good adhesion strength. However,

*Corresponding author. skoricb@uns.ac.rs

these coatings have poor cracking resistance especially in high speed machining. The duplex surface treatment was used to enhance adhesion strength and hardness of hard coatings.

This paper describes the successful use of the nanoindentation technique for determination of hardness and elastic modulus. The depth of nanopenetration provides an indirect measure of the area of contact at full load and thus hardness is obtained by dividing the maximum applied load with the contact area. Micro hardness testing, Vickers micro hardness, is dependent on visual resolution of the residual indent for accurate measurement. The diagonal of the indent, which is the key for hardness determination, is sometimes very hard to resolve if the load is low enough to avoid cracking and again this would be much more difficult if cracking occurs at high load within the indent site.

In the nanoindentation technique, hardness and Young's modulus can be determined by the Oliver and Pharr method [4].In nanoindentation, the Young's Modulus, E, can be obtained from:

$$\frac{1}{E_r} = \frac{1-\nu^2}{E} + \frac{1-\nu_i^2}{E_i} \quad \ldots\ldots\ldots\ldots\ldots\ldots\ldots\ldots..(1)$$

Where v_i=Poisson ratio of the diamond indenter (0.07) and Ei=Young's modulus of the diamond indenter.

On the other hand, in the Vickers micro hardness tester, the hardness can be calculated by measuring the residual indent area with the help of an optical microscope and the value is fully dependent on the visual resolution of the indentation

Therefore, in recent years, a number of measurements have been made in which nanoindentation and AFM have been combined.

2. Experimental

The substrate material used was high speed steel type S 6-5-2. Prior to deposition the substrate was mechanically polished to a surface roughness of 0.12 μm (R_a). The specimens were first austenized, quenched and than tempered to the final hardness of 850 HV. In order to produce good adhesion of the coating, the substrates were plasma nitrided at low pressure (1×10^{-3} Pa), prior to deposition of the coating. The PVD treatment was performed in a Balzers Sputron installation with rotating specimen. The gas flow into the deposition chamber was controlled by mass flow meters and the partial pressures of argon and nitrogen were measured. The deposition parameters were as follows: Base pressure in the chamber was 1×10^{-5} mbar, bias voltage U_b=1 kV, discharge current I_d=50 mA, substrate temperature T_s=200 °C, target to substrate distance d_s–t=120 mm. The partial pressure of Ar during deposition was $P_{Ar}=(3.1–6.6)\times10^{-6}$ mbar and partial pressure of N_2 was $P_{N2}=6.0\times10^{-6}–1.1\times10^{-5}$ mbar. Deposition rate a_D=0.1 nm/s. Prior to entering the deposition chamber the substrates were cleaned.

The other samples were produced with IBAD technology in DANFYSIK chamber. The IBAD system consists of an e-beam evaporation source for evaporating Ti metal and 5-cm-diameter Kaufman ion source for providing argon ion beam. Base pressure in the IBAD chamber was 1×10^{-6} mbar. The partial pressure of Ar during deposition was $(3.1–6.6) \times 10^{-6}$ mbar and partial pressure of N_2 was $6.0 \times 10^{-6}–1.1 \times 10^{-5}$ mbar. The ion energy (E_{Ar}=1.5–2 keV), ion beam incident angle (15°), target to substrate distance d_s–t=360 mm, and substrate temperature T_s=200 °C, were chosen as the processing variables. Deposition rate a_D=0.05–0.25 nm/s. Quartz crystal monitor was used to gauge the approximate thickness of the film. Additional analyze the thickness of coatings, the ball crater method (calo-test), allows prompt and sufficiently precise results to be obtained. After deposition, the samples were irradiated with 22 keV N^{2+} ions at room temperature (RT). N^{2+} ions were supplied by an electron cyclotron resonance (ECR) ion source. The implanted fluences were in the range from 0.6×10^{17} to 1×10^{17} ions/cm^2

A pure titanium intermediate layer with a thickness of about 50nm has been deposited first for all the coatings to enhance the interfacial adhesion to the substrates. After deposition, the samples were irradiated with 120 keV, N^{5+} ions at room temperature (RT). The Ion Source is a multiply charged heavy ion injector, based on the electron cyclotron resonance effect (ECR). The implanted fluencies were in the range from 0.6×10^{17} to 1×10^{17} ions/cm^2.

The mechanical properties on coated samples were characterized using a Nanohardness Tester (NHT) developed by CSM Instruments, Switzerland. Nanoindentation testing was carried out with applied loads in the range of 10 to 20 mN. The nanohardness tester was calibrated by using fused silica samples for a range of operating conditions. A Berkovich diamond indenter was used for all the measurements. The tip radius of the indenter was approximately 50 nm and the displacement resolution of the machine was 0.03 nm. The data was processed using proprietary software to produce load–displacement curves and the mechanical properties were calculated using the Oliver and Pharr method. At least ten measurements were made at each load on the coated sample. Measurement of hardness was also carried out using a conventional Vickers microhardness tester.

The Nano-Hardness tester uses an already established method where a Berkovich indenter tip with a known geometry is driven into a specific site of the material to be tested, by applying an increasing normal load. For each loading/unloading cycle, the applied load value is plotted with respect to the corresponding position of the indenter. The resulting load/displacement curves provide data specific to the mechanical nature of the material under examination. Established models are used to calculate quantitative hardness and modulus values for such data. The NHT is especially suited to load and penetration depth measurements at nanometer length scales. The maximum indentation depth for measuring H and E was fixed at one tenth of the coating thickness.

The analysis of the indents was performed by Atomic Force Microscope (AFM). Acoustic Emission (AE) is an important tool for the detection and characterization of failures in the framework of non-destructive testing. The analyzed AE signal was obtained by a scratching test designed for adherence evaluation. Scratch tests were performed under controlled conditions with a device that consisted of a loaded probe with a diamond indenter moving linearly along the sample with a constant speed and continuously increasing force. The steadily increasing contact load causes tensile stress behind the indenter tip and compressive stress ahead of the cutting tip. Detection of elastic waves generated as a result of the formation and propagation of microcracks. The AE sensor is insensitive to mechanical vibration frequencies of the instrument. This enables the force fluctuations along the scratch length to be followed, and the friction coefficient to be measured. The scratch tester equipment with an acoustic sensor (CSM-REVETEST) was used.

X-ray diffraction studies were undertaken in an attempt to determine the phases present, and perhaps an estimate of grain size from line broadening. The determination of phases was realized by X-ray diffraction using PHILIPS APD 1700 X-ray diffractometer. The X-ray sources were from CuKα with wavelength of 15.443 nm (40 kV, 40 mA) at speed 0.9°/min. The surface roughness was measured using stylus type (Talysurf Taylor Hobson) instruments. The most popular experimental XRD approach to the evaluation of residual stresses in polycrystalline materials is the $\sin^2\psi$ method. For each selected (hkl) crystallographic direction, diffraction data are collected at different ψ tilting angles. The method requires a θ-2θ scan for every ψ angle around the selected diffraction peak and, in order to emphasize the peak shifts, it is important to work at the highest possible 2θ angle.

3. Results

The nitrogen to metal ratio, EDX, table 1, is stoichiometries for IBAD technology and something smaller from PVD. For sample with additional ion implantation, value is significantly different, smaller.

It is possibly diffused from the layer of TiN to the interface. The TiN coatings only show a golden surface and after ion implantation the color is dark golden

Table 1. Atomic ratio N/Ti in coating

	Coating	Ratio N/Ti (atomic)
1	IBAD	1.00
2	PVD	0.98
3	PVD/III	0.89

.

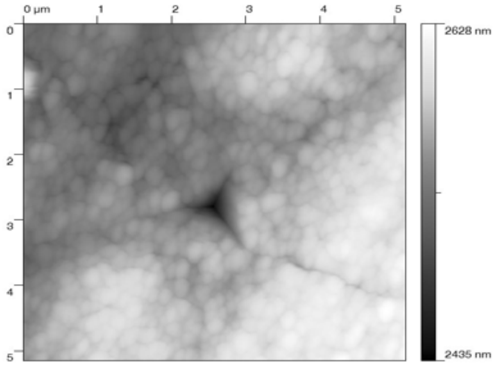

1a)

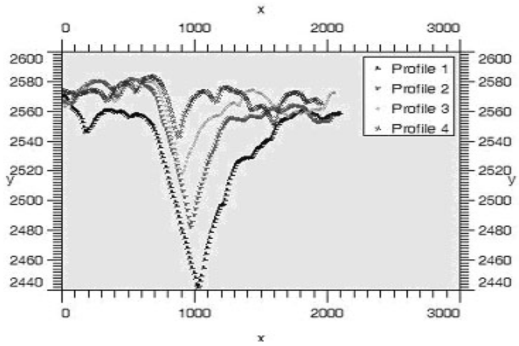

1b)

Figure 1a. AFM image of a nanoindentation 1b. *Cross-section of the indentation*

All the results of nanohardness are obtained with the Oliver & Pharr method and using a supposed sample Poisson's ratio of 0.3 for modulus calculation.

The analysis of the indents was performed by Atomic Force Microscope (Figure 1a).It can be seen, from cross section of an indent during indentation, that the indents are regularly shaped with the slightly concave edges tipically seen where is significant degree of elastic recovery.(Figure 1b).

The nanohardness values and microhardness are shown in table 2. For each measurement, the penetration (Pd), the residual penetration (Rd), the acoustic emission (AE) and the frictional force are recorded versus the normal load. The breakdown of the coatings was determined both by AE signal analysis and optical and scanning electron microscopy.

Table 2. Surface microhardness ($HV_{0.03}$) and nanohardness (load-10mN).

Unit	pn/IBAD	PVD	pn/PVD/II	Fused Silica
Vickers	2007	3028	3927	943
GPa	21.6	32.6	42.6	10,1

AE permits an earlier detection, because the shear stress is a maximum at certain depth beneath the surface, where a subsurface crack starts. Critical loads are presents in Table 3.

Table 3. Critical load for different type of coating.

	pn/TiN(IBAD)	pn/TiN(PVD)
Lc1	-	23
Lc2	100	54
Lc3	138	108

The critical load Lc1 corresponds to the load inducing the first crack on the coating. No cracks were observed on sample 1.The critical load Lc2 corresponds to the load inducing the partial delamination of the coating. The critical load Lc3 corresponds to the load inducing the full delamination of the coating. AE permits an earlier detection, because the shear stress is a maximum at certain depth beneath the surface, where a subsurface crack starts (PVD), figure 2.

It was found that the plasma-nitriding process enhanced the coating to substrates adhesion. In some places of hard coatings cohesive failure of the coating and the delamination of the coating was observed (Fig. 3).

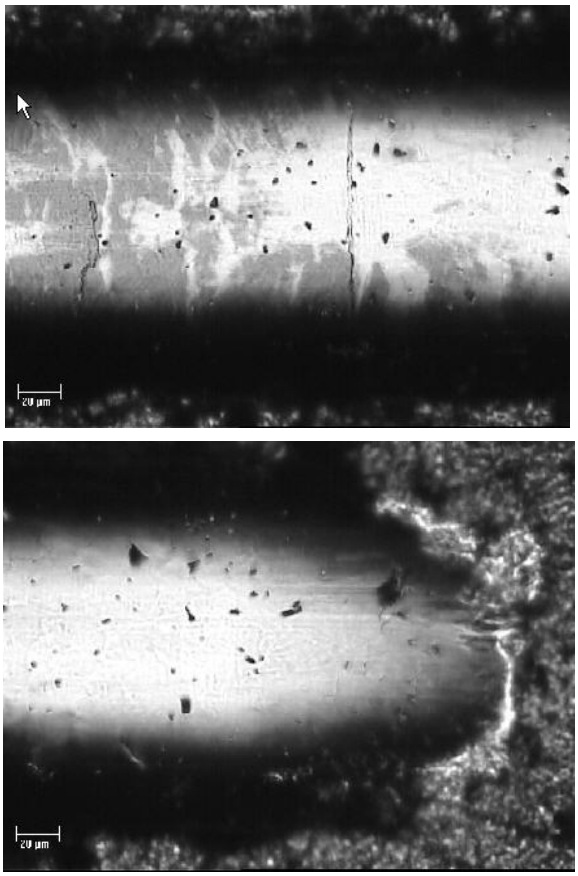

Figure 2. Partial delamination of coating

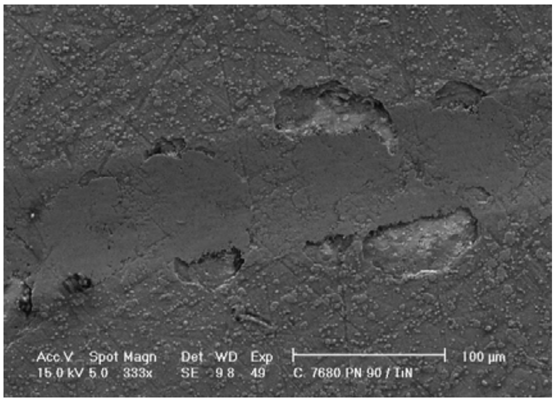

Figure 3. SEM morphology of scratch test: pn/TiN(PVD).

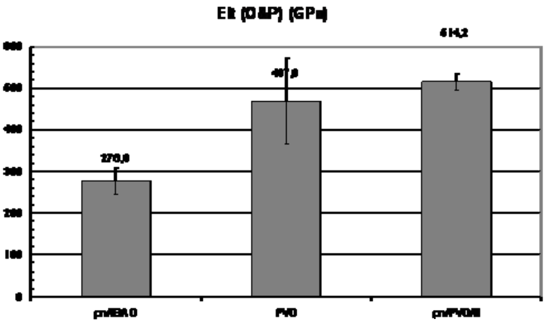

Figure 4. Young's elastic module.

The nanoindentation elastic modulus was calculated using the Oliver–Pharr data analysis procedure. The individual values of E are the different for all measurements, figure 4. The errors related to the measurements and estimations were different and for duplex coating with ion implantation is less than 4%. Good agreement could be achieved between the E_c values and nanohardness.

The tribological behaviour of the coatings was studied also by means of pin-on-ring contact configuration in dry sliding conditions, described elsewhere [5]. The friction coefficient of sample with duplex coating with additional ion implantation, is presented in Fig. 5

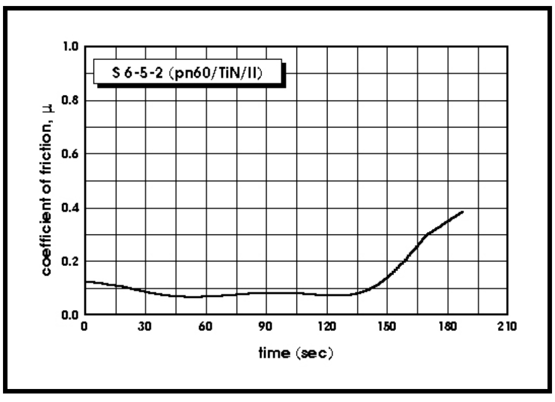

.

Figure 5 . Friction Coefficient of pn/TiN/II

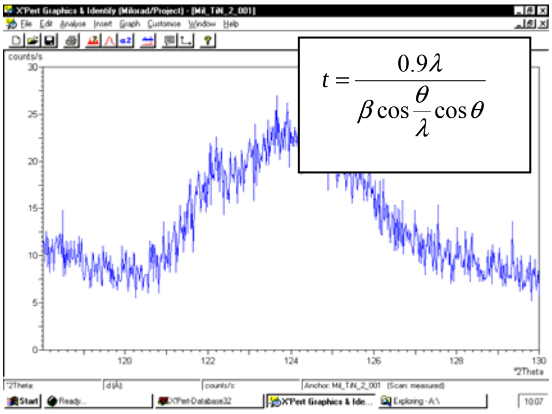

Figure 6. XRD diffraction peak of TiN(422).

The width of column is derived from the width of the diffraction peaks (Figure 6), (λ=0.154nm, θ=62.5^{o} and β=0.056rad), and it is 70 nm.

The stress determination follows the conventional $\sin^2\psi$ method. Stress determination was performed using a PHILIPS XPert diffractometer. The (422) diffraction peak was recorded in a 2θ interval between 118^{o} and 130^{o}, with tilting angle: ψ_o^1=0°, ψ_o^2=18.75°, ψ_o^3=27.03°, ψ_o^4=33.83°, ψ_o^5=40°. A typical result for compact film, with residual stresses σ = -4.28Gpa, has TiN(PVD).

4. Discussion

A hardness increase is observed for implanted samples. This can be attributed to iron nitride formation in the near surface regions. The standard deviation of the results is relatively important due to the surface roughness of the samples. Because the thickness of the TiN coatings presented here is sufficiently large, which for all coatings is about 2900 nm (TiN-PVD), the hardness measurements will not be affected by the substrate, as in three times thinner (900 nm TiN-IBAD).

The individual values of E are the different for all measurements. The errors related to the measurements and estimations were differnt and for duplex coating with ion implantation is less than 4%. Good agreement could be achieved between the E_c values and nanohardness.

The wear resistance of the TiN coating was obviously improved by the presence of a nitride interlayer. Such an improvements is probably due to the adequate bonding between the nitrided layer and substrate. Energy depressive analyze with X-ray (EDAX), of the transfer layer showed that the transfer layer consists of small amount of counter material (adhesive wear), Fig.7.

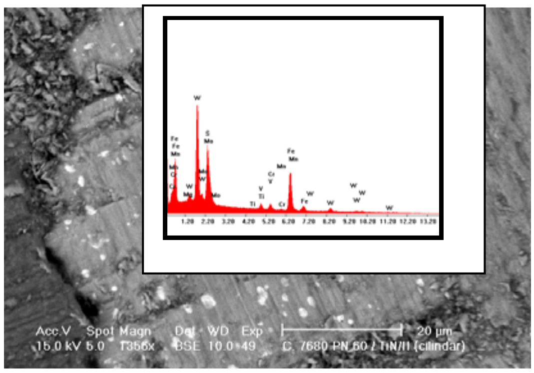

Figure 7. SEM micrograph of wear track (BSE), with wear debris and EDAX image of wear debris.

It is generally expected that an increase in hardness results in an increase in wear resistance.

The topography of TiN coatings was investigated SEM (Figure 8).

The PVD coating process did not significantly change roughness. For the practical applications of IBAD coatings, it is important to know that the roughness of the surface decreased slightly after deposition (from Ra=0.19 µm to Ra=0.12 µm).

The curves of friction coefficient are clearly reproducible and distinctively show a lower rise in friction coefficient for the composite (pn/TiN) coated specimens and much more for sample with additional ion implantation (under 0.1). It is generally expected that an increase in hardness results in an increase in wear resistance.

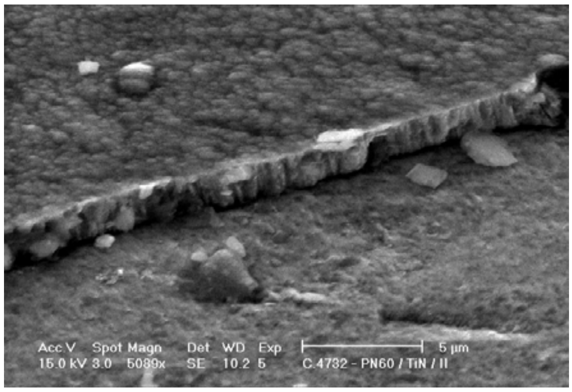

Figure 8. Surface morphologies of pn/TiN(PVD)/II.

The formation of TiN by IBAD has its origin in a kinetically controlled growth. The nitrogen atoms occupy the octahedric sites in varying number according to the energy that these atoms possess to cross the potential barriers created by the surrounding titanium anions. The ion bombardment is believed to enhance the mobility of the atoms on the sample surface. XRD analysis revealed the presence of only one phase, δ-TiN, and there is no evidence for other phases, such as Ti_2N, could be found. The ε-Ti_2N does not lead to an improvement in the tribological behavior.

The coating morphology was evaluated using the well-known structure zone model of Thornton. All observed morphologies, figure 8, are believed to be from region of zone I (PVD) and from the border of region zone T (IBAD). It has been suggested [**Combadiere,1996]**. That the transition from open porous coatings with low microhardness and rough surface, often in tensile stress to dense coatings films with greater microhardness, smooth surface occurs at a well defined critical energy delivered to the growing film.

5. Conclusions

It was concluded that the formation of a plasma nitrided layer at low pressure, beneath a hard coating, is important in determining the use of hard coating.

The experimental results indicated that the mechanical hardness is elevated by penetration of nitrogen, whereas the Young's modulus is significantly elevated. Nitrogen ion implantation leads to the formation of a highly wear resistant and hard surface layer.

Coatings developed under this project should demonstrate performance that exceeds that of PVD coatings.

Nitrogen implantation into hard TiN coatings increases the surface hardness and significantly reduces the tendency of the coatings to form microcracks when subjected to loads or stresses.

The present coating method can produce dance structures, high hardness and the high critical load values can be achieved. Tribological tests confirm that these composite coatings are wear resistant and provide very low friction coefficient

The above findings show that deposition process and the resulting coating properties depend strongly on the additional ion bombardment.

6. **Acknowledgments**

The authors would like to thank to The Scientific Council of Serbia supported this work by grant

References

[1] J.C.A. Batista, C. Godoy and A. Matthews, A. Leyland,Developments Towards Producing Well Adherent Duplex PAPVD Coatings, Surface Engineering, Vol. 9, 2003, 37-43.

[2] Y. Sun and T. Bell, Plasma surface engineering of low alloy steel, Mater. Sci. Eng., A Vol. 140, 1991, 419-434.

[3] H. Haufmann, Industrial applications of plasma and ion surface engineering Surface and Coatings Technology, Vol. 74/75, 1988, 23-28.

[4] Pharr, G.M., Oliver, W.C., Brotzen, F.R., On the generality of the relationship among contact stiffness, contact area, and elastic modulus during indentation, J. Mater. Res., Vol. 7, 1992, 613.

[5] B. Škorić and D. Kakaš, Influence of plasma nitriding on mechanical and tribological properties of steel with subsequent PVD surface treatments Thin Solid Films, Vol. 317, 1998, 486-489.

JJMIE

Volume 5 , Number 1, February .2011
ISSN 1995-6665
Pages 39 - 46

Jordan Journal of Mechanical and Industrial Engineering

Dynamic Analysis and Control of Automotive Occupant Restraint Systems

Abdulwahab A. Alnaqi[a]* and Ahmet S. Yigit [b]

[a] College of technological Studies, Department of Automotive and Marine Engineering, PAAET, Kuwait

[b] Department of Mechanical Engineering, Kuwait University, Kuwait

Abstract

Although much progress has been made in developing seat belts and mandating their use, the injuries related to seat belts during frontal crashes are still widespread. This paper proposes an approach to control the seat belt restraint system force during a frontal crash to reduce thoracic injuries. A fuzzy logic controller based on moving the attachment point of the seat belt is proposed, and the simulation results with this controller are presented. Also, robustness to parameter variations is investigated. The results show that the proposed controller is very effective in reducing all critical values that lead to possible thoracic injuries during a frontal crash. The controller is also demonstrated to be robust with respect to varying impact conditions and parameters.

Keywords: Seat belt, smart restraint systems, fuzzy logic.

1. Introduction

In today's competitive market, the automotive industry is constantly improving the vehicle design with high speed and varied function. One of the most important pieces of safety equipment in a vehicle is the seat belt. However, as the modern automotive technology has developed and produced luxury vehicles with high performance, the one undesirable result is the high rate of accidents and the increasing severity of injuries when collisions do happen. According to a recent study, the Higher Council of traffic in Kuwait reports that for every 100,000 people 37 people died from car accidents, figure in US is 21 deaths for every 100,000 people. Therefore, the occupant's safety during a collision is very important. Seat belt designed for preventing or reducing the severity of injuries is one of the oldest and most commonly used elements in a vehicle. When used properly, seat belts are about 45 % effective at preventing fatal injuries, and 67 % effective at preventing serious injuries. Despite this safety record, and being mandated by most countries, one should be cautioned though, that the seat belts are also blamed for some serious injuries, themselves. Researchers [1] have studied the seat belt injuries and found that the seat belt injuries include abdominal, chest, or neck bruises and abrasions at the site of the belt contact. It is estimated that 30% of people who came with seat belt injuries suffer from some internal injuries. Seat belt injuries were studies in numerous works in [1- 4].

In order to reduce seat belt injuries different studies dealt with the design of the seat and seat belt [5-7]. Also other studies [8] showed that several vehicle contact points including the steering wheel, door panel, armrest panel, armrest and seat are associated with an increased risk of severe thoracic injury when impacting the occupant.

Realizing the need for improving the performance of these systems, there have been numerous investigations on various aspects of occupant restraint systems used in automotive vehicles in the last decade [9-12]. These studies include the development of four-point harnesses [13, 14], pretensioners and load limiters [15]. Some researchers suggested using active control leading to the development of the so-called "intelligent" restraints. They presented an optimal control of restraint forces in an automobile to reduce the thoracic injury caused by seat belt. Also, authors of [9] studied and investigated ways to reduce occupant injuries that are caused by safety systems like the seat belt and the airbag restraints during a crash. The success of the "intelligent" restraint systems requires a very good understanding of the dynamics phenomena involved during a collision, thus, requiring an adequate model. In this study the effect of seat belt injury is investigated and different approaches to reduce the seat belt injuries through controlling the seat belt force are proposed.

2. Mathematical Model for Thoracic Injury

The dynamics of the human thorax under impact can be described using the mechanical model shown in Figure 1, [16]. In the model, the effective mass of the sternum and a portion of the rib structure and thoracic contents are represented by mass m_1. The remaining portion of the thorax and the part of the total body mass that is coupled to the thorax by the vertebral column are represented by mass m_2. The elasticity and viscous damping of the rib cage and thoracic viscera are

*Corresponding author. eng_abdulwahab1982@yahoo.com

represented by the elements coupling masses m_1 and m_2. The spring and the dashpot model the elastic compliance and the dissipative properties of the thorax, for which the corresponding spring and damping forces, $f(x_2 - x_1)$ and $h(\dot{x}_2 - \dot{x}_1)$ are assumed to be piecewise linear. The action of a seat belt on the thorax is represented by a force $u(t)$ which acts between m_1 and the vehicle. The variables x_v, x_1, x_2 and x_3 represent the displacements with respect to an inertial reference frame (absolute displacements) of the vehicle, mass m_1, mass m_2, and mass m_3, respectively. The parameters for thoracic injury model with a prescribed crash deceleration profile are shown in Table 1.

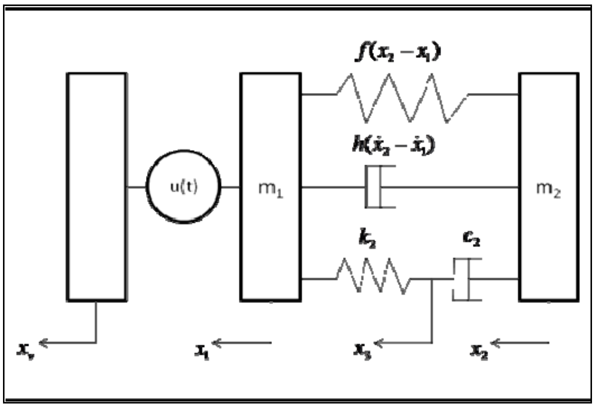

Figure 1. Frontal crash model for thoracic injury

Table 1. The parameters for thoracic injury model

Parameters	Values
m_1	0.3 kg
m_2	18 kg
k_{11}	10522 N/m
k_{12}	7190 N/m
δ_0	0.03 m
c_{11}	403.3 $N.s/m$
c_{12}	2192.1 $N.s/m$
k_2	13153 N/m
c_2	175.4 $N.s/m$
k	10^5 N/m
v_0	48 km/hr

The equations of motion were derived using Newton's second law as follows:

For m_1:

$$m_1\ddot{x}_1 = -u + f(x_2 - x_1) + h(\dot{x}_2 - \dot{x}_1) + k_2(x_3 - x_1) \quad (1)$$

For m_2:

$$m_2\ddot{x}_2 = -f(x_2 - x_1) - h(\dot{x}_2 - \dot{x}_1) - c_2(\dot{x}_2 - \dot{x}_3) \quad (2)$$

It is also required to modify the piece-wise linear functions of the compression deformation and the rate of the chest compression. Using Equations (9) with Equations (7):

For m_3:

$$m_3\ddot{x}_3 = c_2(\dot{x}_2 - \dot{x}_3) - k_2(x_3 - x_1) \quad (3)$$

Then, from Equation (1), (2) and (3) the motion of the vehicle and the occupant is obtained as:

$$\begin{aligned} m_1\ddot{x}_1 &= -u + f(x_2 - x_1) + h(\dot{x}_2 - \dot{x}_1) + k_2(x_3 - x_1) \\ m_2\ddot{x}_2 &= -f(x_2 - x_1) - h(\dot{x}_2 - \dot{x}_1) - c_2(\dot{x}_2 - \dot{x}_3) \\ m_3\ddot{x}_3 &= c_2(\dot{x}_2 - \dot{x}_3) - k_2(x_3 - x_1) \\ \ddot{x}_v &= a(t) \end{aligned} \quad (4)$$

This model assumes that the vehicle motion is determined by a prescribed deceleration function. The initial conditions are:

$$\begin{aligned} &x_1(0) = 0, \quad x_2(0) = 0, \quad x_3(0) = 0, \quad x_v(0) = 0 \\ &\dot{x}_1(0) = v_0, \quad \dot{x}_2(0) = v_0, \quad \dot{x}_3(0) = v_0, \quad \dot{x}_v(0) = v_0 \end{aligned} \quad (5)$$

where v_0 is the impact velocity and $a(t)$ is the prescribed crash deceleration profile of the vehicle, which is given as follows:

$$a(t) = \begin{Bmatrix} -A\sin(\dfrac{\pi t}{T_p}) & 0 \le t \le T_p \\ 0 & t > 0 \end{Bmatrix} \quad (6)$$

where the amplitude of the deceleration profile is given as

$$A = \frac{\pi v_0}{2T_p}$$

The spring force developed in the chest can be defined by the following piecewise linear function of the compression of the chest,

$$f(x_2 - x_1) = \begin{cases} k_{11}(x_2 - x_1) & if \;\; 0 \le (x_2 - x_1) \le \delta_0 \\ k_{12}(x_2 - x_1) - F_0 & if \;\; (x_2 - x_1) > \delta_0 \end{cases} \quad (7)$$

where

$$F_0 = (k_{12} - k_{11})\delta_0$$

In addition, the damping force h is given by a piecewise linear function of the rate of the chest compression given as

$$h(\dot{x}_2 - \dot{x}_1) = \begin{cases} c_{11}(\dot{x}_2 - \dot{x}_1) & if \;\; (\dot{x}_2 - \dot{x}_1) \ge 0 \\ c_{12}(\dot{x}_2 - \dot{x}_1) & if \;\; (\dot{x}_2 - \dot{x}_1) < 0 \end{cases} \quad (8)$$

The state variables are defined as follows:

$$z_1 = x_1, \quad z_2 = \dot{x}, \quad z_3 = x_2, \quad z_4 = \dot{x}_2, \quad z_5 = x_3, \quad z_6 = \dot{x}_3 \quad (9)$$

Using Equations (9) with Equations (4), the equations of motion can be written in terms of state variables as follows:

$$\dot{z}_1 = z_2 \quad (10)$$

$$\dot{z}_2 = \frac{1}{m_1}\left(-u + h[z_4 - z_2] + f[z_3 - z_1] + k_2[z_5 - z_1]\right) \quad (11)$$

$$\dot{z}_3 = z_4 \quad (12)$$

$$\dot{z}_4 = \frac{1}{m_2}\left(-h[z_4 - z_2] - f[z_3 - z_1] - c_2[z_4 - z_6]\right) \quad (13)$$

$$\dot{z}_5 = z_6 \quad (14)$$

From equation (3) $m_3\ddot{x}_3 = c_2(\dot{x}_2 - \dot{x}_3) - k_2(x_3 - x_1) = 0$

$$0 = c_2(z_4 - z_6) - k_2(z_5 - z_1)$$

$$z_6 = \frac{-k_2 z_5 + k_2 z_1 + c_2 z_4}{c_2} \quad (15)$$

$$f(z_3 - z_1) = \begin{cases} k_{11}(z_3 - z_1) & if \;\; 0 \le (z_3 - z_1) \le \delta_0 \\ k_{12}(z_3 - z_1) - F_0 & if \;\; (z_3 - z_1) > \delta_0 \end{cases} \quad (16)$$

Where

$F_0 = (k_{12} - k_{11})\,\delta_0$

Also using Equations (9) with (8)

$$h(z_4 - z_2) = \begin{cases} c_{11}(z_4 - z_2) & if\ (z_4 - z_2) \geq 0 \\ c_{12}(z_4 - z_2) & if\ (z_4 - z_2) < 0 \end{cases} \quad (17)$$

In order to find the velocity and vehicle displacement x_v, it is required to integrate the deceleration (Equation (6)) as follows:

$$\ddot{x}_v(t) = a(t) = \begin{cases} -A\sin(\frac{\pi t}{T_p}) & 0 \leq t \leq T_p \\ 0 & t > 0 \end{cases}$$

Thus,

$$x_v(t) = \begin{cases} \frac{1}{2}\frac{v_0 T_P}{\pi}\sin(\frac{\pi t}{T_p}) + \frac{1}{2}v_0 t & 0 \leq t \leq T_p \\ \frac{1}{2}v_0 T_P & t > 0 \end{cases} \quad (18)$$

The state equations were numerically integrated by using Matlab's ode45 solver. For these simulations a crash velocity of 48 km/h and with impact duration of 0.1 seconds are used to determine the deceleration profile shown in Figure 2, and the simulation was run for 0.12 seconds.

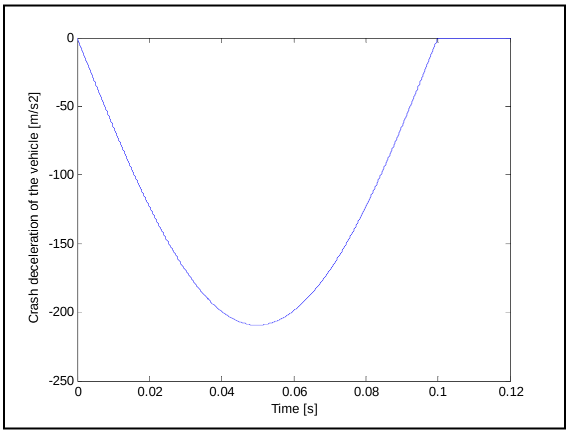

Figure 2. Crash deceleration of the vehicle for the frontal crash with a prescribed deceleration profile ($v_0 = 48\,km/h$)

Extensive studies were conducted in the field of occupant safety to find the injury thresholds that marks the limits for an injury. According to a study of possible prevention of fatal thoracic injuries, the critical value of the chest acceleration is 60g, the critical value of the chest compression is 0.046 m, and the critical value of the chest viscous response can be calculated according which is equal to 0.229 m^2/s. [17]

In order to make sure that the passenger will not have a serious injury, these limits should not be exceeded. Kent et al., (2007) used almost the same value for chest viscous response but the chest acceleration is 80 g and the chest compression is 0.045 m. Figure 3 presents the chest compression $[x_2(t) - x_1(t)]$, the rate of chest compression $[\dot{x}_2(t) - \dot{x}_1(t)]$, the excursion of the occupant $[x_1(t) - x_v(t)]$, seat belt force, the chest viscous response $([\dot{x}_2(t) - \dot{x}_1(t)][x_2(t) - x_1(t)])$, the chest acceleration $\ddot{x}_2(t)$ as a function of time. It was found that the chest compression exceeds the threshold value which is 0.046 m by almost one and a half times (0.11m). Clearly, with this value the occupant will be injured. Also, it is seen from the figure that the maximum value of the chest compression occurred near the end of impact as expected. It was found that the rate of chest compression is within the injury limit (6 m/s). It was found that the occupant will move forward around 5 cm as a result of the large seat belt force. After the impact is finished it is seen that the occupant moves back because there is no seat back force in the model that restricts the motion in this direction. It is seen that the behavior of the response is almost the same as the rate of chest compression with different amplitude. Also it was found that the maximum value of the chest viscous response is within the injury limit (0.229 m^2/s). In addition, it is seen that the maximum value of chest acceleration is within the limit (80 g). Also it can be seen that after the impact the chest acceleration drops to zero.

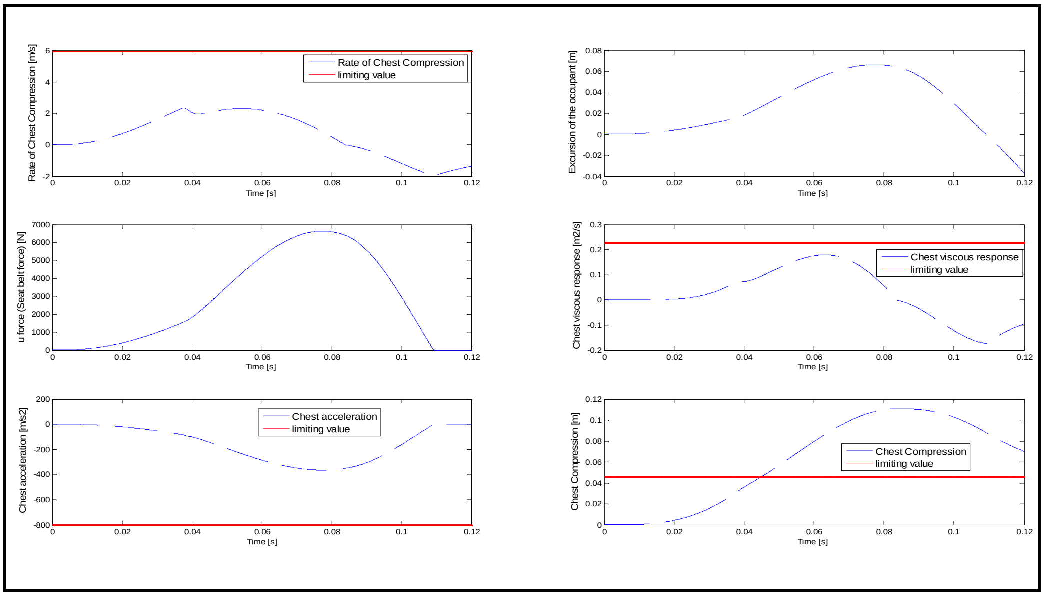

Figure 3. Passive control responses

3. Fuzzy Logic Control

As a benchmark, the performance of an open loop optimal control strategy as well as a feedback controller based on optimal Linear Quadratic Regulator (LQR) approach are investigated. Though very effective in reducing injuries, these controllers were shown to be very sensitive to parameter variations, and modelling uncertainties. As it is well known, to design a control system using a traditional approach such as optimal control, adaptive control or predictive control, it is necessary to have at least a nominal model describing the behavior of the system to be controlled. However, obtaining an adequate and accurate model is very difficult in some cases due to the complex behavior or due to the existence of nonlinearities. This leads to consider other control design approaches which do not rely on any models. One of the successful methods is the fuzzy logic control. In this section the design of a fuzzy controller is explained, and the simulation results when this controller is used in the system are presented. Also, robustness to parameter variations is investigated.

3.1 Design of a fuzzy controller

A fuzzy logic controller can be considered as a control expert system which simulates the occupant thinking. It consists of input and output variables with membership functions, a set of (IF…THEN) rules and an inference system. The controller's inputs are chosen to be the outputs of the process which are x_1 (occupant displacement) and $\dot{x}_1$ (occupant speed) and output is the seat belt force u. It should be noted that these control variables are chosen because they facilitate design of fuzzy rules. In a real implementation, the seat belt force is realized by manipulating the location of the attachment point (i.e., by controlling the length of active portion of the seat belt). Therefore, in effect, the fuzzy controller is trying to control the seat belt force to prevent thoracic injury.

Define five linguistic values denoted as BNE (Big Negative), NE (Negative), ZE (Zero), PO (Positive) and BPO (Big Positive) for each input variables as shown in Figures 4 and 5. The output variable has 9 linguistic values denoted as N_j (j=1 to 9). The index j represents the strength of the linguistic values such that the higher the index, the stronger the linguistic value as shown in Figure 6.

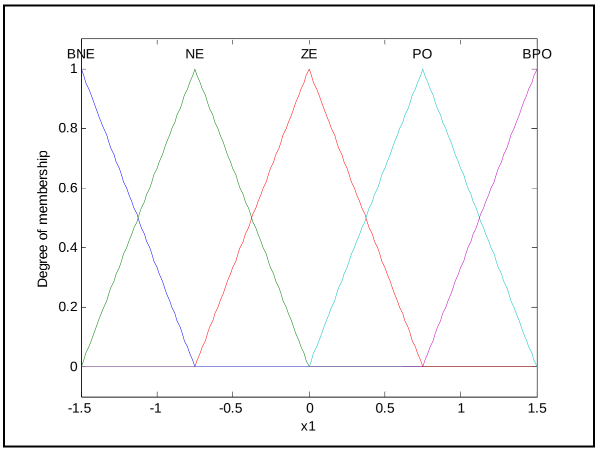

Figure 4. Input x_1 membership function

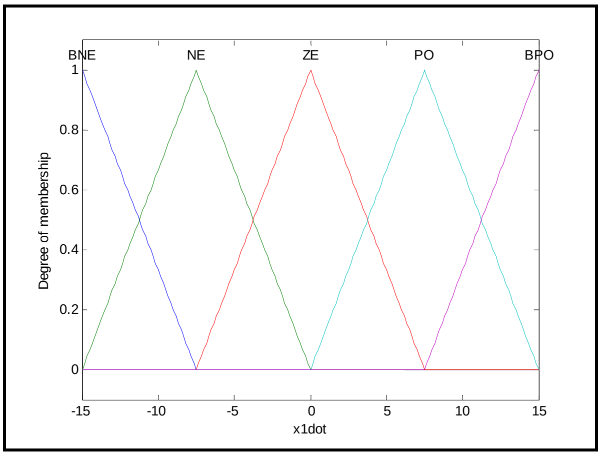

Figure 5. Input $\dot{x}_1$ membership function

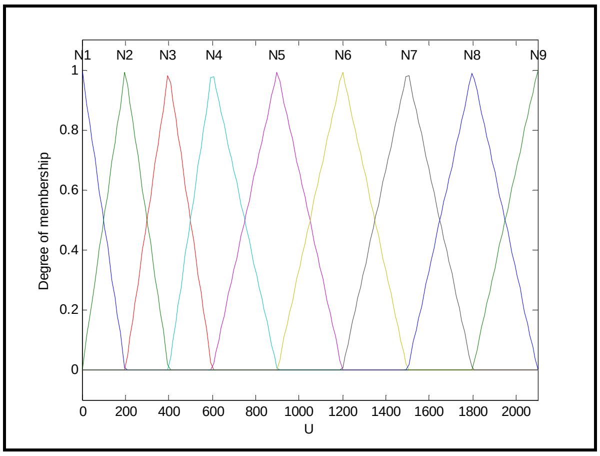

Figure 6. Output u membership function

The Sugeno model (Wang, 1996) is used as the basis of the proposed fuzzy controller. The rule base consists of 25 (IF…THEN) rules derived from occupant knowledge which is presented in Table 3.

Table 3. Rule base system

#	x_1	$\dot{x}_1$	u	#	x_1	$\dot{x}_1$	U
1	BPO	BNE	N7	14	ZE	PO	N7
2	BPO	NE	N7	15	ZE	BPO	N8
3	BPO	ZE	N7	16	NE	BNE	N1
4	BPO	PO	N8	17	NE	NE	N1
5	BPO	BPO	N9	18	NE	ZE	N1
6	PO	BNE	N7	19	NE	PO	N1
7	PO	NE	N8	20	NE	BPO	N1
8	PO	ZE	N6	21	BNE	BNE	N1
9	PO	PO	N7	22	BNE	NE	N1
10	PO	BPO	N8	23	BNE	ZE	N1
11	ZE	BNE	N1	24	BNE	PO	N1
12	ZE	NE	N1	25	BNE	BPO	N1
13	ZE	ZE	N3				

3.2 Simulation results for the nominal case

Matlab is used to implement the fuzzy controller with the dynamic equations in terms of state variables which were defined in the mathematical model section. The simulation time and integration step are chosen as 0.2s and 0.0005s, respectively.

The seat belt force to be applied can be realized by using the concept of releasing and retracting the seat belt or by moving the point of attachment of the seat belt relative to the vehicle (smart seat belt). The motion of the attachment point can be determined by using the control force as follows:

$$X = x_1 - x_v - \frac{u}{k} \qquad (19)$$

From Figure 7 which presents the fuzzy control response, it is noticed that the behavior of the chest compression response is almost within the injury threshold limit. On the other hand, it is concluded that using fuzzy control improves the rate of chest compression with respect to magnitude. As can be seen fuzzy control approach improves the excursion of the occupant as compared to the LQR and optimal open loop control with respect to the magnitude (not presented in this paper due to space limitations). Overall behavior is almost the same. From the figure the behavior of the seat belt force is quite different than that of the optimal control and the LQR. It was seen that both the chest viscous response and the chest acceleration response are under the injury thresholds and comparing with the results obtained from the optimal control and the LQR it is seen that fuzzy control greatly improves the response. It is seen From Figure 8 that the behavior of the displacement of the attachment point response is almost the same as the excursion of the occupant with different amplitude.

It was noticed from the simulation results that using fuzzy logic control improves the response with respect to magnitudes as compared to the LQR and open loop optimal control results. This is remarkable considering that fuzzy logic control does not depend on the system model, and therefore, will not suffer from the inaccuracies of in the model. Indeed, it was found that the responses obtained using fuzzy logic control were less sensitive to parameter variations as compared to the responses obtained from the LQR. Therefore, fuzzy logic control has great potential for implementation since all it requires is the measurement of the output variables. In this work the design of actuator dynamic is not included. In a real implementation, the actuator design and dynamics is very important and should be included in the model. Furthermore, in a real implementation, with current instrumentation it is difficult to measure the occupant motion. In this case, the occupant position and velocity can be obtained from the measurement of vehicle motion and the seat belt force. Clearly, this will make the control somewhat model-based, and care should be taken to investigate the effects of modeling errors. However, due to the robust nature of the fuzzy controller, it is expected that the performance degradation due to state estimation will be acceptable.

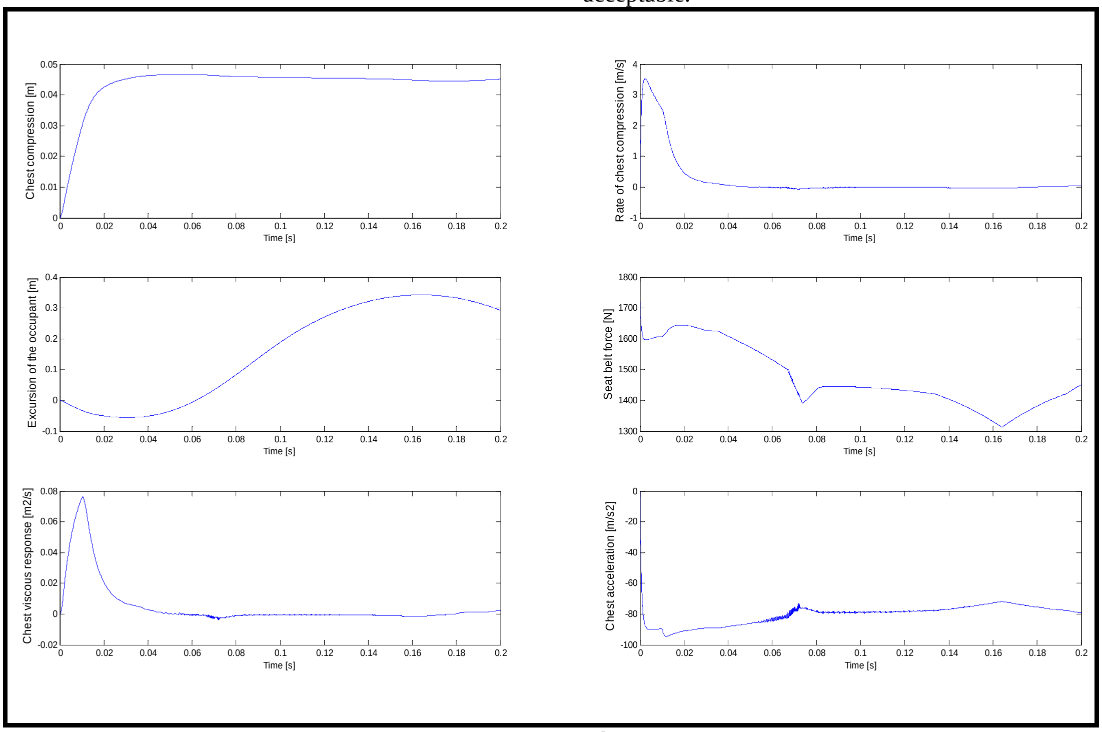

Figure 7. Fuzzy control responses

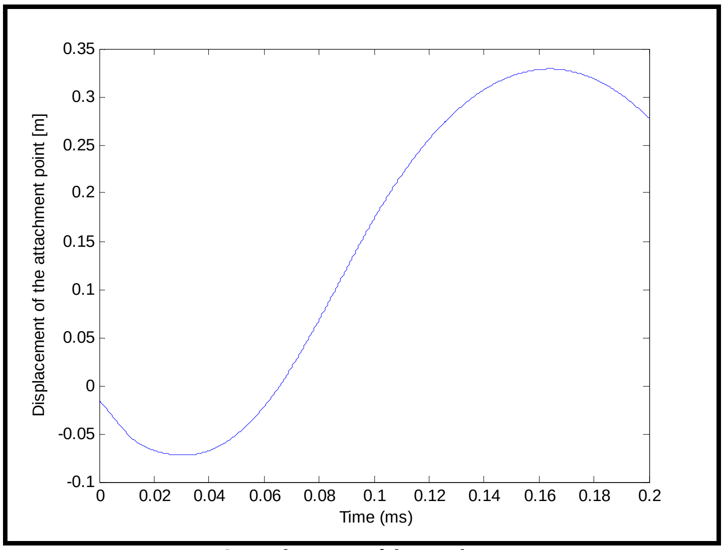

Figure 8. Displacement of the attachment point

4. CONCLUSIONS

A study has been carried out to find ways of reducing thoracic injuries that are caused by seat belt restraint system in a frontal crash. A comprehensive literature review was carried out and a mathematical model with the equation of motion was presented in details. A fuzzy control logic approach was investigated. It was found that using fuzzy logic approach improves the response as compared to the LQR and open loop optimal control. Also it was noticed that the responses obtained using fuzzy logic control is less sensitive to parameter variation. Although this control is non-model based, the implementation may require state estimation by using the model, and this will destroy this attractive property.

Although most of the objectives of the work were achieved for controlling the seat belt system in order to prevent thoracic injury, a number of issues require further work: The frontal crash model was adequate for the purpose of the study. However, for future investigations a more detailed model with the back force of the seat is required to obtain better understanding and more accurate results. Also the number of degrees of freedom could be increased for a more realistic representation.

The design of fuzzy logic controller can also be improved. More sophisticated methods for developing the rule base can be employed [Wang, 1996]. Different combinations with various robust controllers can be applied to improve the robustness (e.g., Neuro-fuzzy logic controllers, fuzzy sliding mode controllers, etc.). In this work, the actuator dynamics is not considered. In a real implementation, the actuator design and dynamics is very important and should be included in the model. One of the available crash simulation software packages can be used to test the performance of the proposed controllers. Experimental work is needed for the frontal crash scenario to validate the results obtained from simulations. The experimental work is needed also for model refinement.

References

[1] Hayes, C. W., Conway, W. F., Walsh, J. W., Coppage, L. & Gervin, A. S., “Seat Belt Injuries: Radiologic Finding and Clinical Correlation”, RadioGraphics, Vol. 11, 1991, 23-36.

[2] Snyder, R. G., Young, J. W., Snow, C. C., Crosby, W. M. & Hanson, P., “Seat Belt Injuries In Impact”, Federal Aviation Administration Washington DC office of Aviation Medicine, 1967.

[3] Carneiro, J., De Melo, F., Pereira, J. & Teixeira, V., “Pseudo-dynamic Method for Structural Analysis of Automobile Seats”, Proceedings of the Institution of Mechanical Engineers Part K-Journal of Multi-Body Dynamics, Vol. 219, No. 4, 2005, 337-344.

[4] Kent, R. W. & Crandall, J. R., “A hybrid Technique for Determining Optimal Restraint System Characteristics”, International Journal of Crashworthiness, Vol. 11, No. 4, 2006, 379-385.

[5] Blaisdell, D. M., Levitt, A. E. & Varat, M. S., “Automotive Seat Design Concepts for Occupant Protection”, Progress in Technology, Vol. 106, 2003, 329-339

[6] Martin, P. G., Crandall, J. R. & Pilkey, W. D., “Injury Trends of Passenger Car Drivers in Frontal Crashes in the USA”, Accident Analysis and Prevention, Vol. 32, 1999, 541-557.

[7] Paulitz, T. J., Blackketter, D. M. & Rink, K. K., “Constant Force Restraint for Frontal Collisions”, Proceedings of the Institution of Mechanical Engineers Part D-Journal of Automobile Engineering, Vol. 220, No. D9, 2006, 1177-1189.

[8] Nirula, R. & Pintar, F. A., “Identification of Vehicle Components Associated with Severe Thoracic Injury in Motor Vehicle Crashes: A CIREN and NASS analysis”, Accident Analysis and Prevention, Vol. 40, 2008, 137-141.

[9] Hesseling, R. J., Steinbuch, M., Veldpaus, F. E. & Klisch, T., “Identification and Control of a Vehicle Restraint System”, Proceedings of the Institution of Mechanical Engineers Part D-Journal of Automobile Engineering , Vol. 220 No. D4, 2006, 401-413.

[10] Kent, R., Crandali, J., Bolton, J. & Duma, S., “Comparison and Evaluation of Contemporary Restraint Systems in the Driver and Front Passenger Enviroments”,

Proceedings of the Institution of Mechanical Engineers Part D-Journal of Automobile Engineering, Vol. 215 No. D11, 2001, 1147-1159.

[11] Kent, R. W., Balandin, D. V., Bolotnik, N. N., Pilkey, W. D. & Purtsezov, S. V., "Optimal Control of Restraint Forces in an Automobile Impact", Journal of Dynamic Systems Measurement and Control – Transactions of the ASME, Vol. 129, No. 4, 2007, 415-424.

[12] Kent, R. W., Purtsezov, S. V. & Pilkey, W. D., "Limiting Performance Analysis of A seat Belt System with Slack", International Journal of Impact Engineering, Vol. 34, No. 8, 2007, 1382-1395.

[13] Bostrom, O. & Haland, Y., "Benefits of a 3+2 Point Belt System and an Inboard torso Side Support in Frontal , Far-Side and Rollover Crashes", 18th Technical Conference on the Enhanced Safety of Vehicles (ESV), 2003, Nagoya, Japan, Paper 451

[14] Rouhana, S., Bedewi, O., Kankanala, S., Prasad, P., Zwolinski, J., Meduvsky, A., Rupp, J., Jeffreys, T. & Schneider, L., "Biomechanics of 4-point Seat Belt Systems in Frontal Impact", Proc. Stapp Car Crash Conf, Vol. 47, 2003, 367-400.

[15] Viano, D., "Lap-shoulder Belts: Some Historical Aspect In Seat Belts: The development of an Essential Safety Fracture", Society of Automotive Engineering, Warrendale, PA, 2003, PT-92.

[16] Lobdell, T. E., Kroell, C. K., Schneider, D. C., Hering, W. E. &Nahum, A. M., "Impact response of the Human Thorax", Human Impact Response Measurment and Simulation, 1973, 201-245.

[17] Balandin, D. V, Bolotnik, N. N. & Pilkey, W. D., "Optimal Protection From Impact, Shock, and Vibration", Netherlands, 2001, The Gorden and Breach Science.

NOMENCLATURE

A	Amplitude of the crash deceleration half-sine pulse
a	Deceleration of the base (crash deceleration)
c_2	damping coefficient of the dashpot
c_{11}, c_{12}	damping coefficients of the thorax when being compressed and when the shape is being restored, respectively
f	elastic characteristic of the rib cage
g	acceleration due to gravity
h	thoracic damping characteristic
k	coefficient of stiffness of the restraint
k_2	stiffness coefficient of the spring in the series connected spring-dashpot component in the thoracic injury model
k_{11}, k_{12}	coefficients of the rib cage stiffness for small and large strains, respectively
m_1	The effective mass of the sternum and a portion of the rib structure and thoracic contents
m_2	The remaining portion of the thorax and the part of the total body mass that is coupled to the thorax by the vertebral column
T_p	duration of the crash deceleration half-sine pulse
u	control force acting on the object to be protected(a car occupant)
x_1	absolute displacement of the sternum in the two-mass thorax injury model
x_2	absolute displacement of the rear portion of the thorax in the two-mass thorax injury model
x_3	absolute displacement of the point at which the spring and the dashpot connected in series are joined in the two-mass thorax injury model
x_v	absolute displacement of the vehicle
δ_0	threshold deformation of the rib cage at which the stiffness coefficient k_{11} changes to k_{12}
v_0	impact velocity

JJMIE

Volume 5, Number1, February 2011
ISSN 1995-6665
Pages 47 - 52

Jordan Journal of Mechanical and Industrial Engineering

Comparative Performance and Emission Properties of Spark-Ignition Outboard Engine Powered by Gasoline and LPG

Zuhdi Salhab*, Mohammad G. Qawasmi, Hussein Amro, Mosa Zalloum, Mohammad S. Qawasmi and Nafez Sharawi

Department of Mechanical Engineering, Palestine Polytechnic University,Hebron, Palestine

Abstract

This paper presents an experimental research into the use of LPG in converting spark-ignition four stroke outboard (experimental) engine. Engine was modified to operate either on gasoline or on alternative fuel. Two different methods were adapted for operation with LPG; the first method is using vacuum produced by engine which supplies a constant mixture to the engine carburetion while the second one is accomplished using fuel injection (LPG). The results obtained indicate that with the use of injected LPG; torque, engine brake power and brake specific fuel consumption were lower compared to gasoline, while for vacuum system are higher except brake power. On the other hand, the carbon monoxide (CO), carbon dioxide (CO_2) and nitrogen oxides (NO_x) emissions were less in LPG mode as compared to gasoline mode while the higher hydrocarbons (HC) emissions were obtained.

Keywords: Gasoline, LPG, Performance, Emissions, Engine.

1. Introduction

Over the past decade, alternative fuel had been studied for the possibility of lower emission, lowerfuel cost, better (more secure) fuel availability and lower dependence on petroleum. The major alternative fuels under consideration are LPG, methanol, ethanol, natural gas and hydrogen.LPG is obtained from hydrocarbons produced during refining of crude oil and from heavier components of natural gas. It is petroleum derived colorless gas LPG consists of propane or butane or mixtures of both. Small quantities of ethane or pentane may also be present. LPG has high octane rating of 112 RON which enables higher compression ratio to be employed & hence gives higher thermal efficiency. Due to low maintenance cost, economic market price and environment friendly characteristics LPG is becoming popular alternative for gasoline. LPG has the following characteristics against gasoline:

- Relative fuel consumption of LPG is about ninety percent of that of gasoline by volume.
- LPG has higher octane number of about 112, which enables higher compression ratio to be employed and gives more thermal efficiency.
- Due to gaseous nature of LPG fuel distribution between cylinders is improved and smoother acceleration and idling performance is achieved. Fuel consumption is also better.
- As LPG is stored under pressure, LPG tank is heavier and requires more space than gasoline tank.
- Engine life is increased for LPG engine as cylinder bore wear is reduced & combustion chamber and spark plug deposits are reduced.
- There is reduction in power output for LPG operation than gasoline operation.
- Starting load on the battery for an LPG engine is higher than gasoline engine due to higher ignition system energy required.
- LPG system requires more safety. In case of leakage LPG has tendency to accumulate near ground as it is heavier than air. This is hazardous as it may catch fire.
- Volume of LPG required is more by 15 to 20% as compared to gasoline.
- LPG operation increases durability of engine and life of exhaust system is increased.
- LPG has lower carbon content than gasoline or diesel and produces less CO_2 which plays a major role in global warming during combustion.
- LPG powered vehicles have lower ozone forming potential and air toxic concentrations [1]-[4].

2. Engine Modification Systems for LPG Operation

Figures 1 and 2 show engine modified systems for LPG op

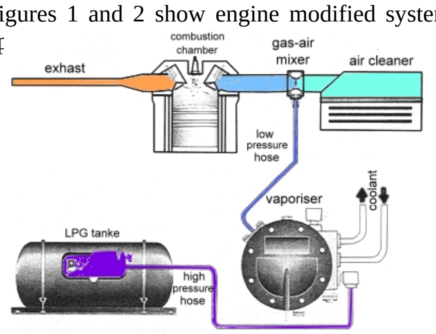

Figure1. Vacuum (mixing) system

*Corresponding author: zuhdisalhab@ppu.edu

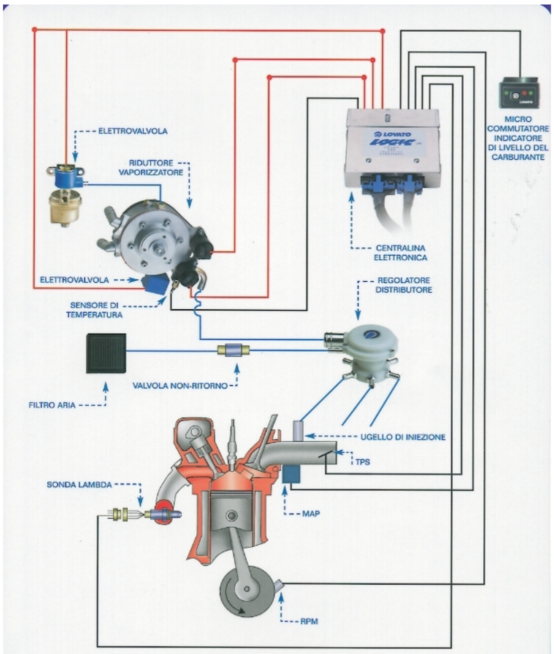

Figure 2. LPG injection system

First method uses vacuum produced by engine. The system supplies a constant air-fuel mixture to the engine (through gas-air mixer) while in the second system the fuel is injected at right time with right quantity according to engine operating conditions.

Usually a mixer (figure 1) is installed to the airflow just before the intake control valve, and it is essentially a tube which the air flows through. It has a carefully designed internal profile though, such that the air initially flows through a medium diameter hole, which then expands to the maximum internal diameter of the tube as the airflow continues. Since air has momentum, this creates a partial vacuum at the expansion point. This vacuum is proportional to the airflow rate and the LPG systems are used to meter the amount of gas joining the airflow. Just at this expansion point, there are some small holes inside the mixer. These pick up the partial vacuum and send this back along a pipe to a vaporizer. The vaporizer has a large diaphragm which responds to the amount of vacuum in the mixer. As this vacuum (i.e. airflow rate) increases, the diaphragm is pulled on (since the other side of it is referenced to normal atmospheric pressure) and this opens a progressive valve, which controls how much LPG is allowed in. So more LPG is expanded to gas. This gas goes back down to the same tube into the mixer, joins the airflow and goes off into the engine to be burnt in the same way as petrol. Open loop LPG system operates in the way described. A restrictor valve is added to the pipe between the mixer and the vaporizer, which the installer will use to tune the system. By adjusting this valve, the installer can tune how much of the vacuum the vaporizer experiences, so can control how much gas can join the airflow and so keep the engine in tune. However, vaporizer diaphragms bed in over time, so gradually the tuning drifts out. Also the response of the diaphragm to the vacuum is fairly course, and it's not always feasible to tune the system such that the correct mixture is presented to the engine under all loads and conditions. These systems do work, but they don't always provide the best performance and economy and need relatively regular re-tuning [5].

In the case of LPG injection system, this system was used on LPG mode by using fuel selector switch. If level in tank drops to certain point, gasoline system is automatically switched on. LPG cylinder supplies liquid LPG to LPG vaporizer which has heating element. Liquid LPG is vaporized and fuel in vapor form is supplied to gas mixer where air is mixed with fuel and supplied to engine manifold. Due to reduction in pressure there may be possibility of freezing within the vaporizer. To overcome this heated coolant is circulated through vaporizer. Fuel metering valve with step motor is used to vary quantity of fuel according to engine speed and load. Fuel shut off valve is used to cutoff fuel supply. Function of step motor and fuel shut off valve are controlled by electronic control unit (ECU). Intake manifold has manifold absolute pressure (MAP) sensor which measures manifold pressure and sends signal to ECU. Oxygen sensor is located in exhaust which measures oxygen in exhaust and sends signals accordingly to ECU. ECU receives these signals and calculates how much fuel is to be supplied and sends signal to fuel metering valve. RPM sensor measures speed and sends signal to ECU. ECU decides amount of fuel to be supplied depending of engine speed and sends signals to fuel metering valve [6].

3. Experimental Equipments

Engine was prepared for operation with gasoline and LPG. The experiments have been performed at the laboratory (automotive workshop) of the Mechanical Engineering Department at Palestine Polytechnic University which interests for a long time in alternative fuels and renewable energy. Experimental engine was connected to the THEPRA EPTS brake hydraulic dynamometer. The rotating torque of the engine is converted to a stationary torque that was measured. The turbulent action of the water absorbs the power of the engine. The load is controlled by the water inlet. The power is converted into heat which is carried away by the continually flowing water. EPTS with vertical Instrument Panel measures engine torque and power continuously from an absorption brake and produces value of torque and power for various RPM bands. Torque and power values are integrated during each shaft revolutions as the engine is slowly accelerated through a range of interest. Fuel consumption was measured while brake specific fuel consumption was determined.

Engine emissions (CO, CO_2, HC and NO_x) were measured on IM-2400- 4/5 gas analyzer at 1500 RPM and different loads. In this presented study, tested engine has characteristics shown in the following table:

Table1. Characteristics of the tested engine

Data	Unit	Gasoline	LPG
Engine type	-	4 stroke outboard	4 stroke outboard
Model	-	Mazda 323i	Mazda 323i
Chemical formula	-	C_8H_{18}	60% C_3H_8- 40% C_4H_{10}
Lower heating value	MJ/kg fuel	43	46.6
Start of ignition	CA^0	350	350
Ignition duration	CA^0	60	60
Number of cylinders	-	4	4
Bore/ stroke	mm	77.5/ 78	77.5/ 78
Connecting rod length	mm	133	133
Stoichiometric air/fuel ratio	-	14.7	15.6
Excess-air ratio	-	1	1
Compression ratio	-	10	10
Maximum power	kW	65	65

4. Experimental Results

Tests were conducted by varying torque and engine speed and measuring engine performance and emissions. The tests were repeated for gasoline and LPG as well. No modification of excess- ratio (air- fuel ratio) was made.

4.1. Engine Performance

Following graphs (figures 3-6) are plotted from tests results for gasoline and LPG (mixing and injection) which indicate the relation between brake specific fuel consumption (bsfc) in (g/kWh) with variation of engine speed at different values of torque measured at dynamometer and the relation between engine brake power (depending on torque) versus engine speed.

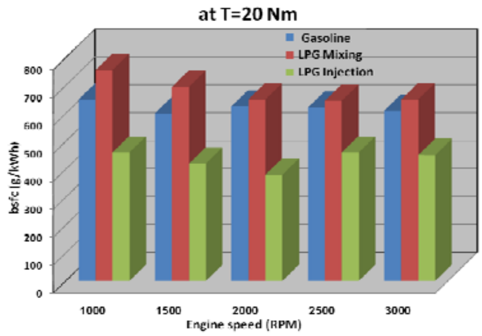

Figure 3. Brake specific fuel consumption (bsfc) versus engine speed at T=20 Nm

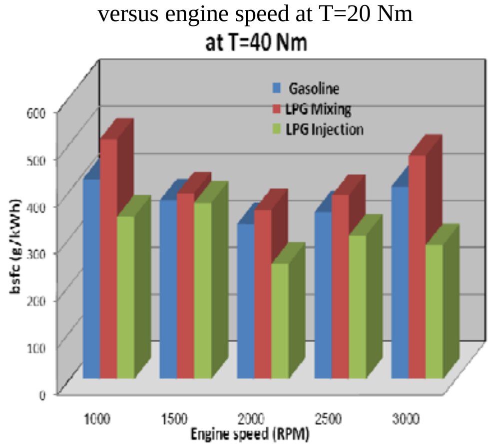

Figure 4. Brake specific fuel consumption (bsfc) versus engine speed at T=40 Nm

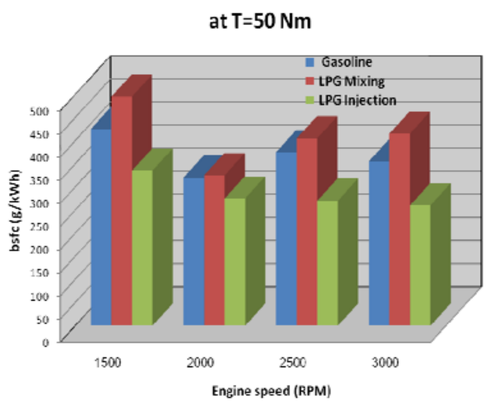

Figure 5. Brake specific fuel consumption (bsfc) versus engine speed at T=50 Nm

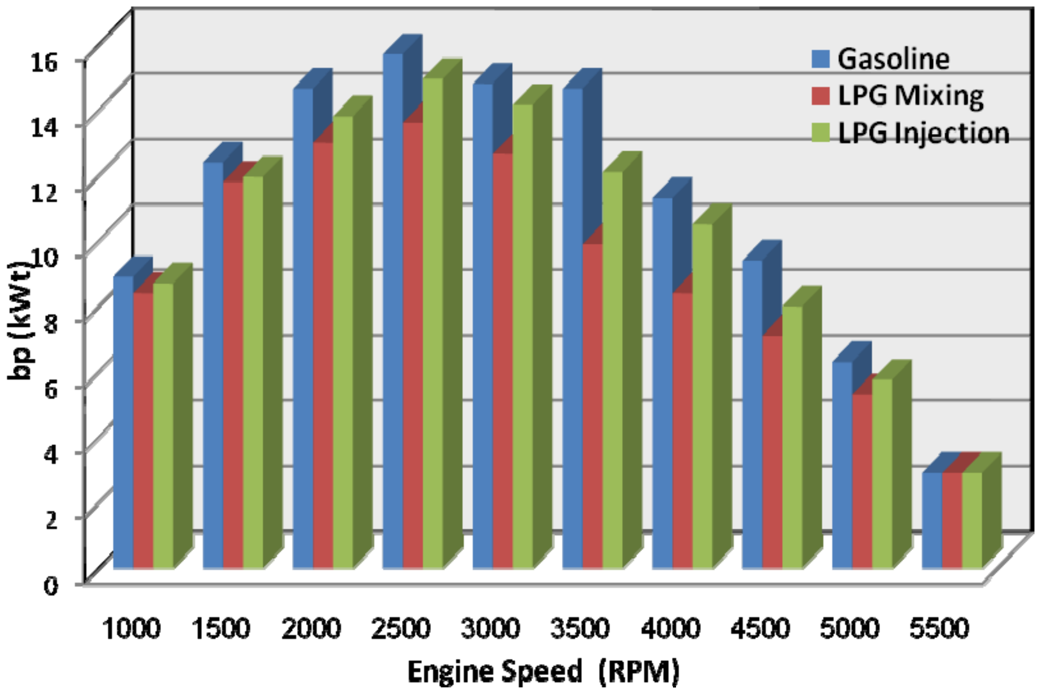

Figure 6. Relation between brake power and engine speed at different torques

Figures 3-5 illustrate the relation between bsfc with engine speed at different torque (20, 40 and 50) Nm. Brake specific fuel consumption with injected LPG is, at every speed and almost for different torque values between 20% and 30% lower. The gaseous form of the dosed LPG allowed the reduction of the enrichment needed for idling stability and therefore reducing idling fuel consumption and operating cost and the better mixing of injected fuel with air also decrease the bsfc.

Figure 6 shows full capacity of operation with LPG and gasoline with a small decrease of power with LPG, probably due to the loss of volumetric efficiency when using a gaseous fuel due to the intake air displacement (lower density for gas). Although the maximum power developed by the injected LPG is almost the same as in gasoline , its performance over the whole speed range is about 7% lower (compared with other results in [7], test results show 6 % less power with LPG than with gasoline).

4.2. Engine Emissions

Figures 7-10 show the level of measured emissions (CO, CO_2, HC, and NO_x) against brake power with fixed engine speed (1500 RPM) and air-fuel ratio.

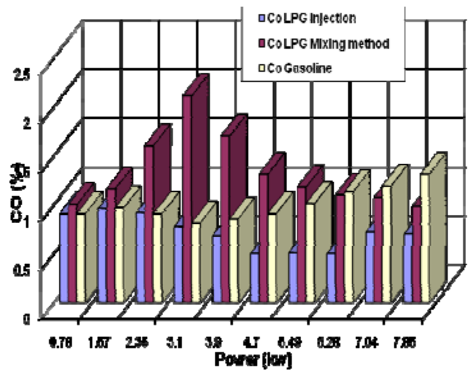

Figure 7. Level of CO

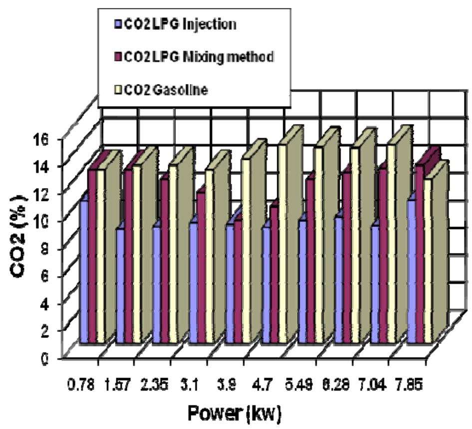

Figure 8. Level of CO_2

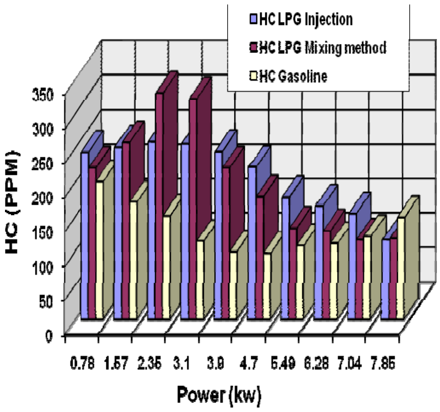

Figure 9. Level of HC

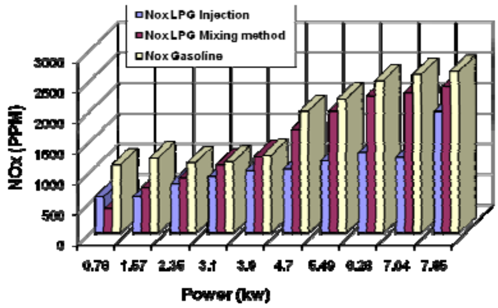

Figure 10. Level of NO_x

CO emissions are controlled by air-fuel ratio, they seem to be also influenced by the kind of fuel. LPG emissions at the same air-fuel ratio were lower. This may be due to the better mixing obtained by gaseous fuel dosification and due to the higher cylinder-to-cylinder uniformity achieved and which also affect the formation of CO_2.

The difference between LPG and gasoline emissions is quite low, may be due to the fact that the controlling characteristic is engine design, with the distribution arrangement and combustion chamber design being of crucial importance. In fact, the longer valve overlap period at low speed may explain the higher HC emissions obtained and may also explain the fact that LPG emissions at low speed are higher than gasoline emissions. The reason could be the higher inertia of gasoline liquid droplets and thus their lower tendency to follow intake air in its bypass path. At higher engine speed, when ram tuning effects control gas motion during the overlap period, LPG HC emissions are comparable or even lower than gasoline emissions for the same engine. The fact of LPG CO emissions being much lower on the overall speed range may support this idea because not much HC may be thus be expected to come from an incomplete combustion.

For the formation of NO_x compounds, the presence of oxygen and high temperature will lead to high NO_x formation rates. At low engine speed, there is no sufficient oxygen for more NO_x emissions formation (lower excess air levels starve the reaction for oxygen, and higher excess air levels drive down the flame temperature, slowing the rate of reaction) and as it is known that the CO reduction is normally coupled with an increase in NO_x production.

5. Conclusion

It can be concluded that the use of LPG instead of conventional gasoline will mean a reduction in low engine brake power, brake specific fuel consumption and pollutant emissions, with loss of power (7%). Also, a reduction in brake specific fuel consumption of about 20%-30% was found, moreover no highly rich mixtures were needed for stable idling operation.

References

[1] Poulton M.L, “Alternate Fuels for road vehicles” Computational Mechanics publications, Ashurst, Southampton, UK, 1990, 84-85, 94-95.

[2] M.Ihsan Karamangil,”Development of the Auto Gas and LPG powered vehicle sector in Turkey: A stastistical case study of the sector for Bursa, ”Vol. 35, No. 1. 2007, 640-649.

[3] .MckenzieC.h.Lim, GodwinA. Ayoko, LidiaMorawska, ZoranD.Ristovski, E.Rohan Jayaratne, Serge Kokot”, A comparative study of the Elemental Composition of the Exhaust Emissions of Cars Powered by Liquified Petroleum Gas and Unleaded Petrol”Vol 40, No. 17, 2006, 3111-3122.

[4] R.R.Saraf,Dr.S.S.Thipse,Dr.P.K.Saxena, ”Experimental Performance Analysis of LPG/Gasoline Bifuel Passenger Car Engines”, 2007, SAE -01-2132.

[5] http://www.chilterngascars.co.uk/cars/lpghowb.htm

[6] R.R.Saraf,Dr.S.S.Thipse,Dr.P.K.Saxena,

”Case study on Endurance test of LPG Automotive Engine”, 2008, SAE -01-2756.

[7] J.E Sinor Consultants Inc, The Clean Fuels Report, Volume 4, No. 5, 1992.

JJMIE
Jordan Journal of Mechanical and Industrial Engineering

Volume 5, Number1, February 2011
ISSN 1995-6665
Pages 53 - 60

Development of an Inertial Measurement Unit for Unmanned Aerial Vehicles

Khaled S. Hatamleh*, Angel Flores-Abad, Pu Xie, Gerardo Martinez, Brandi Herrera and Ou Ma

[a] Department of Mechanical & Aerospace Engineering, New Mexico State University, Las Cruces, New Mexico, USA

Abstract

Unmanned Aerial Vehicles (UAVs) are being deployed in a vast variety of military, civilian, industrial and agricultural applications. Dynamics modeling is an essential step towards designing autonomous controllers for UAV systems. The dynamics modeling on the other hand requires accurate records of the UAVs motion states during real flight tests, this is usually achieved using Inertial Measurement Units (IMUs) and other necessary sensors. This work introduces the purpose, the development and the calibration details of a special six degrees of freedom IMU. The unit is being used in verifying an online UAV dynamics model parameter estimation methodology.

Keywords: IMU, UAV dynamics models, parameter estimation, calibration.

1. Introduction

The extensive use of UAVs demands some kind of manual (highly skilled pilot crew) or autonomous control to be present along. This causes UAVs to be really expensive, and creates a challenge for scientists to design a reliable controller and to develop appropriate means to safely validate the designed controllers without crashing the involved UAVs.

Most of the controllers are dynamics model based. Figure 1 illustrates that the accuracy of a UAV dynamics model depends on the mathematical formulation and on the values of the model's parameters. If the UAV dynamics model changes for any reason during flight (fuel mass loss, or aerodynamic disturbances from wind gusts), the model based controller will not perform as intended. To overcome this problem an on-line dynamics model parameter estimation [1]. The method updates the hanging values of the UAV dynamics model parameters during flight, leading into a more accurate dynamics model and a better flight control quality. More over the estimation method will provide a more realistic offline UAV dynamics model, that can serve as a safe & reliable tool to ensure that the designed controller works properly, minimizing the possibility of crashing the real modeled UAV.

The previous shows the value an accurate UAV dynamics model can add to the UAV control design and test processes. Experimentally dynamics modeling requires motion state records of the dynamic system under investigation; this includes records of position, velocity, angular rate, acceleration, angular accelerations, altitude, pressure, etc. The motion states are obtained using the appropriate sensors and sensory units like Inertial Navigation Systems (INS) and IMUs.

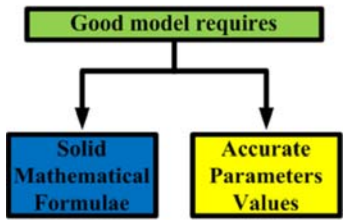

Figure 1. Characteristics of a good dynamics model.

IMUs are electronic devices that are capable of providing three dimensional velocity and acceleration information of the vehicle they are installed on at high sampling rates. They consist of three accelerometers and three gyroscopes mounted in a set of three orthogonal axes [2]. IMUs were expensive in general until the recent development of cheap ceramic and silicon sensors, which has lowered their price and the quality of their measurements. Nowadays IMUs are available at a lower cost, they can be even developed using off-the-shelf components. The major problems encountered with such developed cheap IMUs, are the need to perform the calibration process for the used sensors, and the need to filter the existing noise at the output signals due vibrations and measurements noise. This work will describe the development of a special 6-DOF IMU board to conduct an experimental research study over a special 2-DOF helicopter system. The paper also introduces the calibration procedures and results of the IMU sensors.

*Corresponding author. kshh@nmsu.edu

2. Why custom designed IMU?

Prior to the development of this work, an early study [1] introduced a method to model, and estimates the unknown model parameters of a general 6-DOF flying rigid body. The method is being verified experimentally by means of a 2-DOF helicopter system manufactured by Quanser® and shown in Figure 2. The method requires records of the helicopter position, angular velocity and angular acceleration information in a continuous online manner. The original helicopter system is equipped with a pair of encoders to feedback the angular position information around the pitch and the yaw degrees of freedom which are termed (θ) and (ψ) respectively. The system was modified extensively to be able to provide the angular rate ($\dot{\theta}, \dot{\psi}$) and angular acceleration ($\ddot{\theta}, \ddot{\psi}$) information, details of the system and the modifications done are described by an earlier work of the authors[3].

To be able to provide the necessary motion state information, the first derivative of the encoder's signals can be considered to obtain the angular speeds, while the second derivative produces the angular accelerations. This has been proved inefficient and inaccurate due to error propagation through the first and second derivatives. This made it necessary to use sensors that are able to provide the needed motion states. The angular rate information can be obtained directly using two dual-axis rate gyro sensors. However the case is not as simple for the angular accelerations. There are few sensors that are able to provide measurements of the angular acceleration directly, and those are generally expensive, if attainable. Moreover they represent newly developed technologies that have not been proven efficient yet. The previous made it inevitable to follow an indirect method to measure the angular accelerations. A method that relies on the general relative linear acceleration equation has been proposed. It requires the knowledge of the local acceleration components of at least three different points, of known relative positions, fixed at a rigid body of known angular speed. Therefore three tri-axis linear accelerometers and the two dual-axis rate gyros shall be used to achieve the mission. A detailed derivation and analysis of the indirect angular acceleration measurement is described by Appendix A or reference 3. Most of the commercially available IMUs are equipped with one tri-axis accelerometer, which doesn't satisfy the requirements of the indirect angular acceleration method proposed. This has lead into performing a costume designed 6-DOF IMU system; this is the lowest price solution, and the most suited for the adopted indirect angular acceleration method. The rest of the paper will describe the IMU's components, structure, and calibration process.

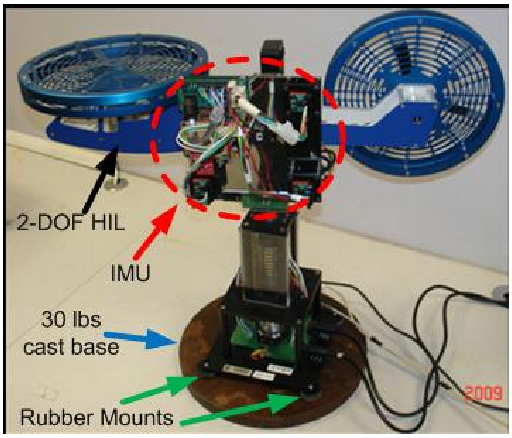

Figure 2. Quanser's modified 2-DOF helicopter

3. Components & Structure

The IMU system shown by Figure 3 consists of a Plexiglas base that holds three (LIS3LV02DQ) tri-axis accelerometers[4], one ±300(◦\sec) dual axis (LPY530AL) rate gyro[6], one ±300(◦\sec) dual axis (LPR530AL) rate gyro[5], a single (PIC24FJ64GA002) microprocessor board, a Li-Po (7.4 Volts, 1300 mhA) battery, X-Bee wireless serial connection and additional interfacing circuits. The developed IMU system functional flow block diagram is illustrated by Figure 4; the 7.4 Volts Lithium Polymer (LiPo) Battery is connected to an interfacing circuit that modulates the voltage into a level that is suitable to power all board components. The three tri-axis accelerometers communicate with the microcontroller through SPI bus channel.

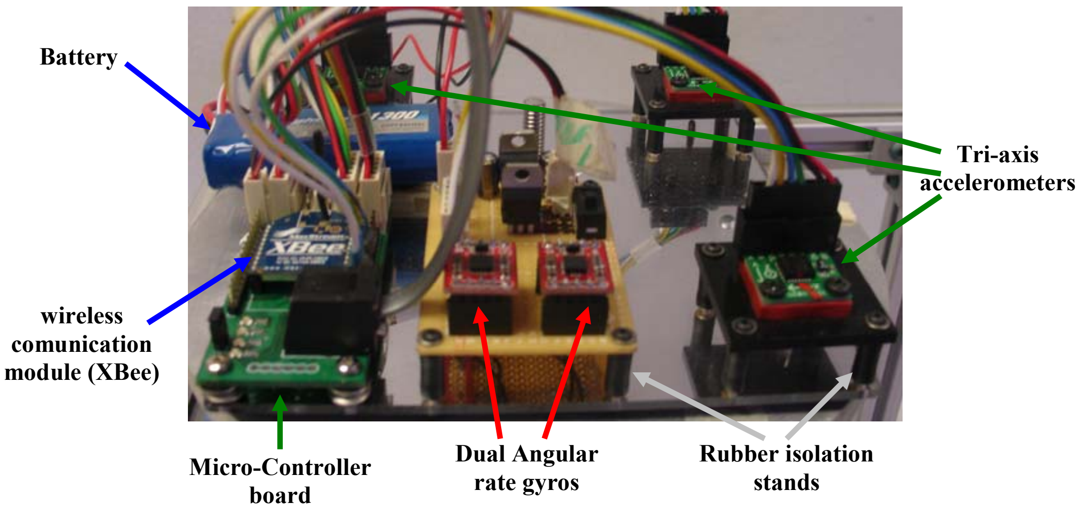

Figure 3. IMU system components

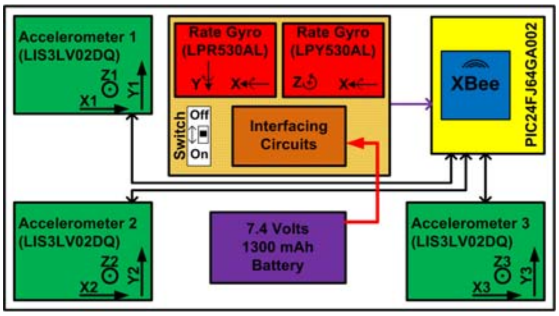

Figure 4. IMU schematic diagram.

The two dual axis rate gyros output is connected to the ADC input channels of the PIC microcontroller. The XBee installed over the microcontroller board sends all the gathered information via a wireless (57600) baud rate serial connection into a stationary PC or laptop where the information are saved as text files.

The Information gathered by the IMU are saved as series of 32 bytes long hexadecimal data frames; each frame contains the acceleration components along the sensitivity axes ($\ddot{x}_k, \ddot{y}_k, \ddot{z}_k$) of each of the three tri-axis accelerometers, (k = 1, 2, 3), every accelerometer reserves 6 bytes of the total frame size. In addition the frame contains the angular velocity readings of the two dual-axis rate gyros followed by the frame sample time; 4 bytes are required for each dual-axis rate gyro while 2 bytes are needed for the sample time. The data frame starts with the Hex number (0x4141) (2 bytes) and ends by the Hex number (0x5A5A) (another 2 bytes). A successful data frame will look similar to the one shown at Figure 5. The IMU is capable of providing the motion states of the UAV at a sampling frequency of about 56 HZ, the gathered text files are processed by a MATLAB® code to convert the hexadecimal information and extract the motion states.

4. IMU Calibration

Because the sensors used to build the IMU are off the shelf components, the performance and accuracy is not guaranteed unless a precise calibration process is performed. The calibration was done for all accelerometers sensors and the two dual axis rate gyros. The procedures followed are similar to those found in [7-8]; where a linear model (shown in Figure 6) of the accelerometer and the rate gyros was assumed. An illustration of the modeling equations, procedures and equipments used during the

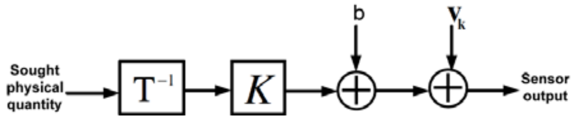

Figure 6. Sensor linear model.

accelerometer and rate gyro calibration is described shortly.

4.1 Accelerometer Calibration

According to the assumed linear model one can write the measured acceleration at an accelerometer local frame (sensitivity axes coordinates) as:

$$\tilde{\mathbf{s}}^{ak} = \mathbf{K}_{ak}\mathbf{s}^{ak} + \mathbf{b}_{ak} + \mathbf{v}_{ak} \qquad (1)$$

where $\tilde{\mathbf{s}}^{ak}$ is the (3x1) output vector of accelerometer k, (k = 1, 2 and 3) that represents the local acceleration components along the sensor's sensitivity axes coordinates $\begin{bmatrix} a_{kx} & a_{ky} & a_{kz} \end{bmatrix}^T$, $\mathbf{v}_{ak}$ is the measurement noise term, $\mathbf{K}_{ak}$ is the (3x3) diagonal scale factor matrix that includes the scaling factors along each of the three sensitivity axes of accelerometer k. $\mathbf{K}_{ak} = diag(k_{akx}, k_{aky}, k_{akz})$, $\mathbf{b}_{ak}$ is the (3x1) bias vector along accelerometer k sensitivity axes $\mathbf{b}_{ak} = \begin{bmatrix} b_{akx} & b_{aky} & b_{akz} \end{bmatrix}^T$ and $\mathbf{s}^{ak}$ is the (3x1) vector of the real acceleration components present at accelerometer k local frame. Prior calibration the values of $\mathbf{K}_{ak}$, $\mathbf{b}_{ak}$ and $\mathbf{v}_{ak}$ are all unknown, on the other hand the values of $\tilde{\mathbf{s}}^{ak}$ are obtained directly from the accelerometer reading. The $\mathbf{s}^{ak}$ term or the so called reference acceleration values are assumed to be known as they are controlled by the experimental setup of the calibration process. The purpose of the calibration process is to estimate the values of $\mathbf{K}_{ak}$, $\mathbf{b}_{ak}$ and $\mathbf{v}_{ak}$, this usually needs a set of different accelerometer readings that accompanies different applied well defined reference acceleration values. The Earth field of gravity was used as the well known reference acceleration value.

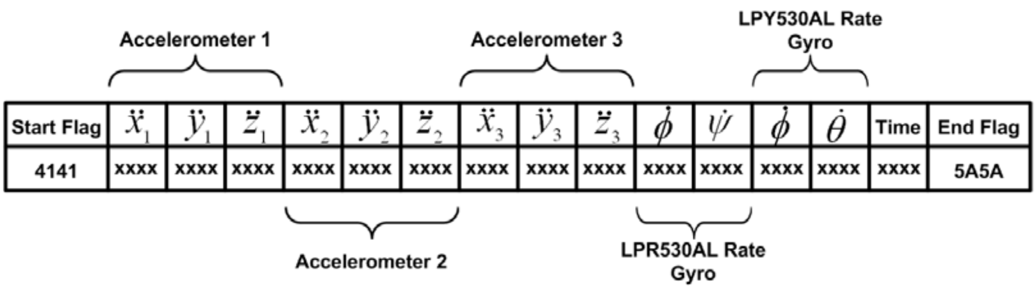

Figure 5. Schematic of the IMU data frame.

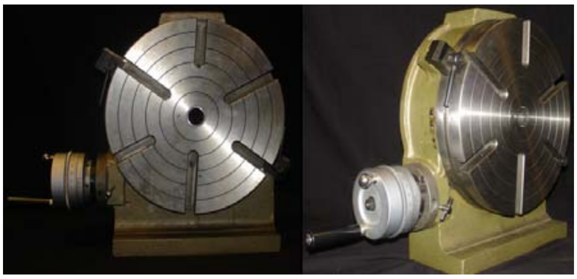

Figure 7. Accelerometer calibration

A tri-axis accelerometer was fixed into precise rotating table (accelerometer calibration platform) that can be turned into any angular position with minutes accuracy by means of a manual handle (See Figure 7). The concept is simple, if an accelerometer is attached to the previously mentioned rotating table as shown by Figure 8, the accelerometer x-axis (pointing up in position-1) should theoretically read $(-g)$ because the gravity field acceleration lies totally along the negative x-axis of the accelerometer. If the table with the attached sensor is rotated into a new angular position such that the gravity field acceleration is at angle θ_r with the x-axis (position-2 of Figure 8), then the value of the gravity field acceleration acting along the x axis reading is defined as ($\mathbf{g}_x = \mathbf{g}\cos\theta_r$).

The calibration platform with the attached IMU board was rotated into 37 different static locations starting from the position 0° into the position 180° by an increment of 5° each time (see Figure 9). The values of the x-axis sensor readings at each static position of the 37 were recorded. The same procedures were repeated for the y and the z axes after flipping the IMU board in a proper orientation such that the axis of concern is pointing up at the initial angular position of the data gathering process. This whole process was done for all three tri-axis accelerometers using the same rotating table and under the same operating temperature. Ignoring the noise term in equation (1):

$$\tilde{\mathbf{s}}^{ak} = \mathbf{K}_{ak}\mathbf{s}^{ak} + \mathbf{b}_{ak}$$

$$\begin{bmatrix} \tilde{\mathbf{s}}_x^{ak} \\ \tilde{\mathbf{s}}_y^{ak} \\ \tilde{\mathbf{s}}_z^{ak} \end{bmatrix} = \begin{bmatrix} k_{akx} & 0 & 0 \\ 0 & k_{aky} & 0 \\ 0 & 0 & k_{akz} \end{bmatrix} \begin{bmatrix} \mathbf{s}_x^{ak} \\ \mathbf{s}_y^{ak} \\ \mathbf{s}_z^{ak} \end{bmatrix} + \begin{bmatrix} b_{akx} \\ b_{aky} \\ b_{akz} \end{bmatrix} \qquad (2)$$

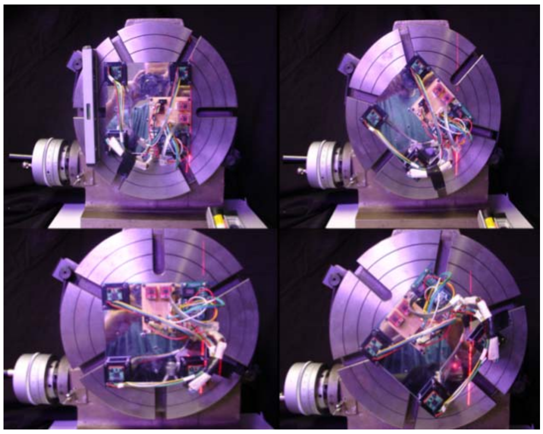

Figure 9. **IMU** board on accelerometer calibration platform at different angular positions.

which can be rewritten into:

$$\begin{bmatrix} \mathbf{s}_x^{ak} & 0 & 0 & 1 & 0 & 0 \\ 0 & \mathbf{s}_y^{ak} & 0 & 0 & 1 & 0 \\ 0 & 0 & \mathbf{s}_z^{ak} & 0 & 0 & 1 \end{bmatrix} \begin{bmatrix} k_{akx} \\ k_{aky} \\ k_{akz} \\ b_{akx} \\ b_{aky} \\ b_{akz} \end{bmatrix} = \begin{bmatrix} \tilde{\mathbf{s}}_x^{ak} \\ \tilde{\mathbf{s}}_y^{ak} \\ \tilde{\mathbf{s}}_z^{ak} \end{bmatrix} \qquad (3)$$

For each accelerometer the recorded data during the calibration process at each angular position is stacked into a similar format of Equation (3) (this requires data from x, y and z sensitivity axes of accelerometer k for the same angular position from all three different sensor board orientations), then the results of all 37 angular positions are stacked into a linear regression format of $(\boldsymbol{\beta}_k \mathbf{r}_k = \mathbf{s}_k)$; where $\mathbf{r}_k$ is the vector that contains all the unknown scale factors and bias values of accelerometer k, $\mathbf{s}_k$ is the acceleration values recorded above by accelerometer k sensitivity axes at all angular positions and $\boldsymbol{\beta}_k$ contains the values of the known reference signal applied along the sensitivity axes of sensor k during calibration process at all according angular positions and calculated by Equation (1). The linear regression form can be solved for $\mathbf{r}_k$ using least squares technique; i.e; ($\mathbf{r}_k = \boldsymbol{\beta}_k^{+1}\mathbf{s}_k$). Results of the calibration process can be used to calculate the real applied acceleration value along any sensor sensitivity axes using a manipulated version of Equation (2):

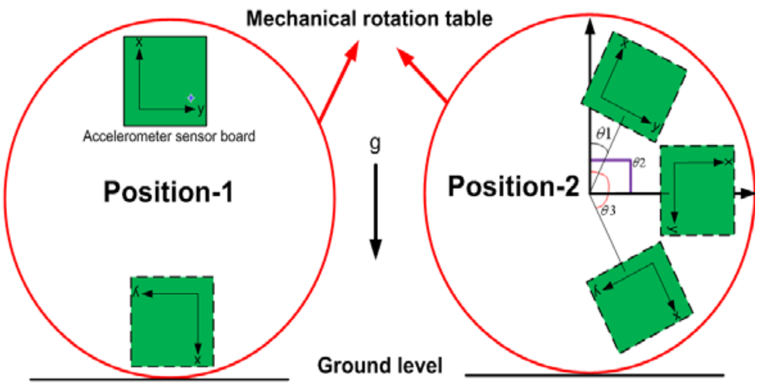

Figure 8. Schematic of a tri-axis accelerometer on the rotating table

$$\mathbf{s}^{ak} = \mathbf{K}_{ak}^{-1}\left(\tilde{\mathbf{s}}^{ak} - \mathbf{b}_{ak}\right) \tag{4}$$

4.2 Rate Gyro Calibration

Applying the same linear sensor model over the rate gyro sensors produces:

$$\tilde{\boldsymbol{\omega}}_g^g = \mathbf{K}_g \boldsymbol{\omega}_g^g + \mathbf{b}_g + \mathbf{v}_g \tag{5}$$

where $\tilde{\boldsymbol{\omega}}_g^g$ is the (3x1) angular rate output vector of all single-axis angular rate sensors, $\boldsymbol{\omega}_g^g$ is the (3x1) vector of the real angular rate applied along the non-orthogonal sensitivity coordinate axes of all single-axis angular rate sensors, $\mathbf{K}_g$ is the (3x3) diagonal scale factor matrix that includes the three scaling factors along each sensor sensitivity axis, $\mathbf{K}_g = diag(k_{gx}, k_{gy}, k_{gz})$, $\mathbf{b}_g$ is the (3x1) bias vector of all angular rate sensors, $\mathbf{b}_g = \begin{bmatrix} b_{gx} & b_{gy} & b_{gz} \end{bmatrix}^T$ and $\mathbf{v}_g$ is the angular rate measurement noise term.

The rate gyros calibration process needs a set of different rate gyros readings for different applied reference angular rate values. The reference signal was attained by means of custom designed PI-controlled angular rotational platform designed by the research group members, the table can rotate at reference angular velocities range of $\pm 4\pi/3$ (rad/sec), Figure 10. shows the prototyped table with the IMU mounted on top of the rotary flat disk. Records of angular speed read by the IMU were obtained as the speed of the calibration table was varied from $-4\pi/3$ (rad/sec) to $4\pi/3$ (rad/sec) by increments of $\pi/9$ (rad/sec) for each recorded set; this yeilds about 23 reference angular rate values/rate gyro readings pairs. This process was repaeted three times for the the three different IMU orientations to calibrate all rate gyro sensitivity axes. When a tri-axis angular rate sensor system built up from three single-axis angular rate sensors a non-orthogonal coordinate frame (or angular rate sensor system sensitivity axes) (x^g, y^g, z^g) is created. Figure 11, shows this coordinate system mounted on the orthogonal coordinate axes (x^p, y^p, z^p) of a platform. Due to sensors mounting imprecision, the two coordinate systems will differ by a set of six small angles. Those angles are needed to estimate the value of the angular rate measured around the non-orthogonal sensitivity axes of the angular rate sensors $\boldsymbol{\omega}_g^g$ at the orthogonal platform coordinates axes where the angular rate vector is denoted $\boldsymbol{\omega}_p^p$, the following equation maps the rate gyro reading into the platform coordinates axes[9]:

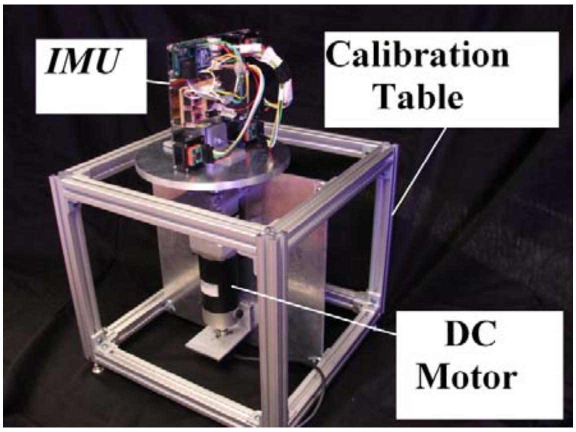

Figure 10. Rate gyro calibration platform with **IMU** on top.

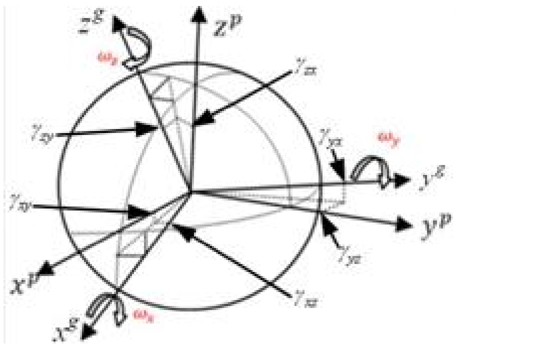

Figure 11. Platform and rate gyro system axes frame.

$$\boldsymbol{\omega}_p^p = \mathbf{T}_g^p \boldsymbol{\omega}_g^g, \qquad \mathbf{T}_g^p = \begin{pmatrix} 1 & -\gamma_{yz} & \gamma_{zy} \\ \gamma_{xz} & 1 & -\gamma_{zx} \\ -\gamma_{xy} & \gamma_{yx} & 1 \end{pmatrix} \tag{6}$$

Where γ_{ij} is the rotation of the *i*-th angular rate sensor sensitivity axis around the *j*-th platform axis and $\mathbf{T}_g^p$ is the rotation matrix that maps the angular rate vector from the non-orthogonal sensitivity axes of the angular rate sensors into the platform orthogonal coordinate system[7]. Defining the platform coordinate system such that its (x^p, y^p) plane coincides with the (x^g, y^g) plane of the (LPR530AL) sensor board sensitivity axes will reduce the total number of the unknown angles down to two; $\{\gamma_{xy}, \gamma_{xz}, \gamma_{yz}, \gamma_{yx}\}$ will be zero. Equation (6) reduces to:

$$\boldsymbol{\omega}_p^p = \mathbf{T}_g^p \boldsymbol{\omega}_g^g, \qquad \mathbf{T}_g^p = \begin{pmatrix} 1 & 0 & \gamma_{zy} \\ 0 & 1 & -\gamma_{zx} \\ 0 & 0 & 1 \end{pmatrix} \tag{7}$$

Substituting equation (7) back into equation (5) after ignoring the noise term yields:

$$\begin{bmatrix} \tilde{\omega}_x^g \\ \tilde{\omega}_y^g \\ \tilde{\omega}_z^g \end{bmatrix} = \begin{bmatrix} k_{gx} & 0 & 0 \\ 0 & k_{gy} & 0 \\ 0 & 0 & k_{gz} \end{bmatrix} \begin{bmatrix} 1 & 0 & \gamma_{zy} \\ 0 & 1 & -\gamma_{zx} \\ 0 & 0 & 1 \end{bmatrix}^{-1} \begin{bmatrix} \omega_x^g \\ \omega_y^g \\ \omega_z^g \end{bmatrix} + \begin{bmatrix} b_{gx} \\ b_{gy} \\ b_{gz} \end{bmatrix} \tag{8}$$

This can be rewritten into:

$$\begin{bmatrix} \omega_x^g & -\omega_z^g & 0 & 0 & 0 & 1 & 0 & 0 \\ 0 & 0 & \omega_y^g & \omega_z^g & 0 & 0 & 1 & 0 \\ 0 & 0 & 0 & 0 & \omega_z^g & 0 & 0 & 1 \end{bmatrix} \begin{bmatrix} k_{gx} \\ k_{gx}\gamma_{zy} \\ k_{gy} \\ k_{gy}\gamma_{zx} \\ k_{gz} \\ b_{gx} \\ b_{gy} \\ b_{gz} \end{bmatrix} = \begin{bmatrix} \tilde{\omega}_x^g \\ \tilde{\omega}_y^g \\ \tilde{\omega}_z^g \end{bmatrix} \quad (9)$$

The data recorded during the rate gyros calibration process will be stacked into a form similar to that shown by equation (9) at each reference speed, all 23 records from all **IMU** different rotational readings during the calibration process will be stacked into one linear regression format $(\boldsymbol{\chi}\mathbf{z} = \tilde{\boldsymbol{\omega}})$, where $\boldsymbol{\chi}$ contains 23 stacks of the matrix $\begin{bmatrix} \omega_x^g & -\omega_z^g & 0 & 0 & 0 & 1 & 0 & 0 \\ 0 & 0 & \omega_y^g & \omega_z^g & 0 & 0 & 1 & 0 \\ 0 & 0 & 0 & 0 & \omega_z^g & 0 & 0 & 1 \end{bmatrix}$, $\mathbf{z} = \begin{bmatrix} k_{gx} & k_{gx}\gamma_{zy} & k_{gy} & k_{gy}\gamma_{zx} & k_{gz} & b_{gx} & b_{gy} & b_{gz} \end{bmatrix}^T$ is the vector that contains all the unknown values to be estimated and $\tilde{\boldsymbol{\omega}}$ is the (69x1) vector that contains the stacks of the tri-axis rate gyro system readings recorded during the calibration process. The system can be easily solved for the values of $\mathbf{z}$ using the equation:

$$\mathbf{z} = \boldsymbol{\chi}^{+1}\tilde{\boldsymbol{\omega}} \quad (10)$$

Once the calibration process is done the readings of the angular rate sensors can be used to calculate the platform's angular rate vector using:

$$\boldsymbol{\omega}_p^p = \mathbf{T}_g^p \mathbf{K}_g^{-1}\left(\tilde{\boldsymbol{\omega}}_g^g - \mathbf{b}_g\right) \quad (11)$$

5. Results

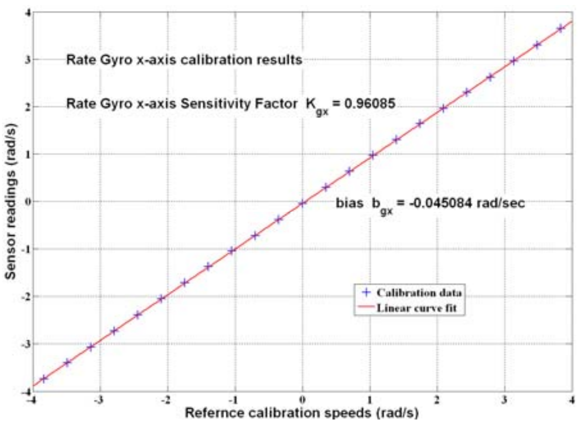

(a)

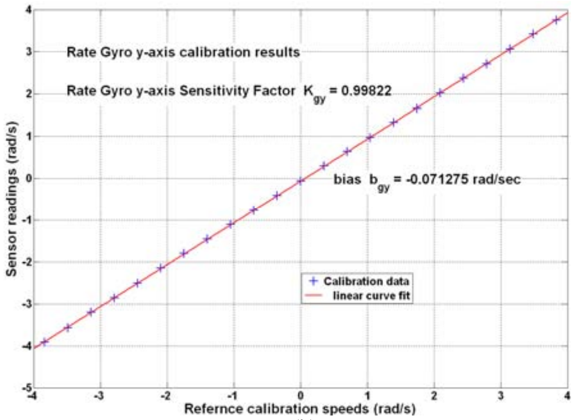

(b)

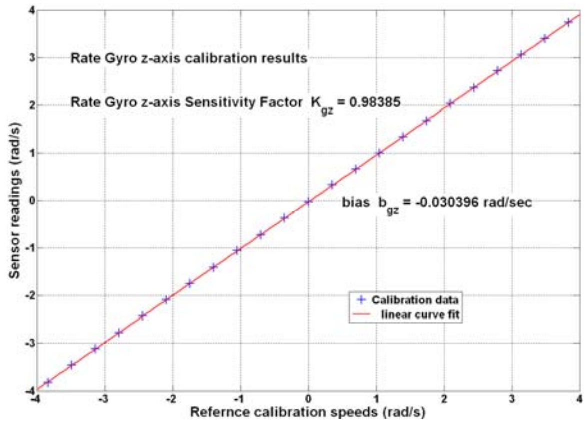

(c)

Figure 12. Rate Gyro calibration results; (a) x-axis, (b) y-axis and (c) z-axis.

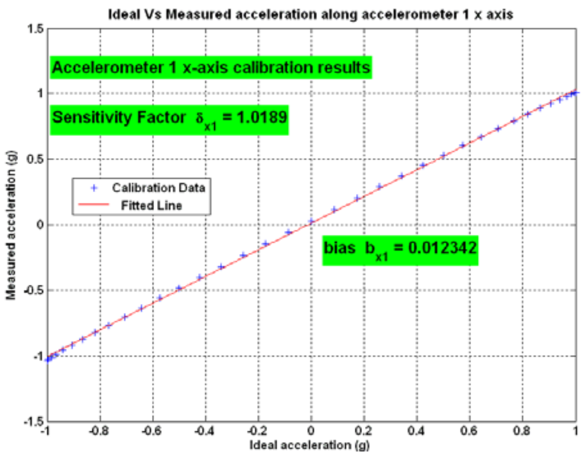

(a)

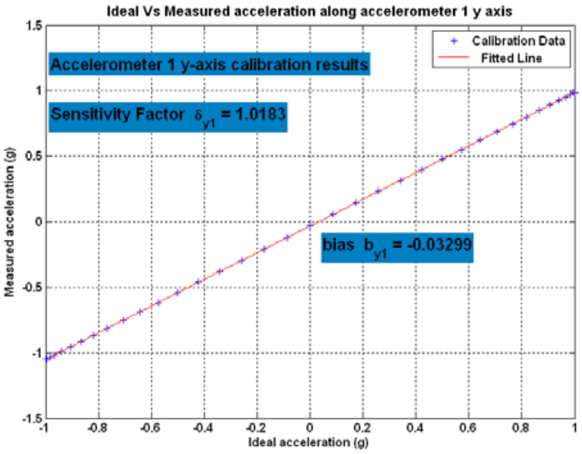

(b)

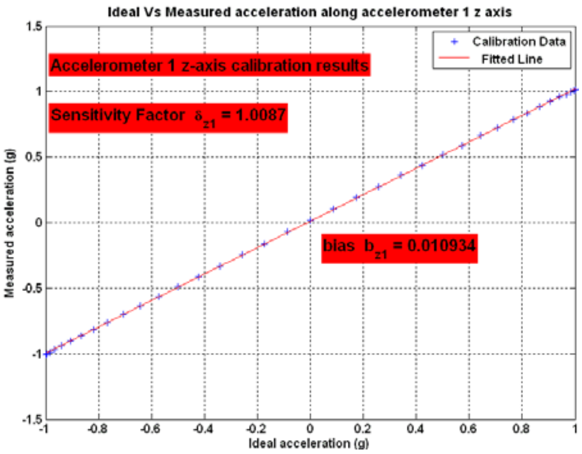

(c)

Figure 13. Accelerometer 1 calibration results along (a) x-axis, (b) y –axis, (c) z-axis.

Figure 12 shows the calibration results of the tri-axis rate gyro system, while figure 13 shows the calibration results along all sensitivity axes of accelerometer 1. The results of all three tri axes accelerometers are summarized in Table. 1; the table shows the scaling factors and bias values for each accelerometer along the three sensitivity axes when operating at 25° C. Values of the scaling factors are close to one indicating the generated accelerometer reading is very close to the applied reference acceleration. The bias values on the other hand are enclosed in the range of (-0.033 to 0.0123) g. It is worthy to mention that the calibration values cannot be used if the operating temperature is different than that of the calibration process (25° C). For different temperatures the calibration process has to be carried out again to extract the new scale factors and bias values.

Table 1. Accelerometers calibration process results

Accelerometer	k_{akx}	k_{aky}	k_{akz}	b_{akx} (g)	b_{aky} (g)	b_{akz} (g)
k=1	1.01	1.01	1.00	0.01	-0.03	0.01
k=2	1.02	1.01	1.01	-0.00	-0.01	0.00
k=3	1.02	1.01	1.00	-0.00	-0.019	-0.025

The rate gyros calibration process results are presented on Table. 2; the table shows values of the scaling factors, the biases and the misalignment angles of the rate gyro z-axis from the rate gyro (x-y) plane. The results are valid under (25° C) operating temperature. The scale factors here are also close to one. The misalignment angles values are very small indicating a tiny physical tilt of the LPY530AL dual axis rate gyro that holds the z axis from the plane of the LPR530AL rate gyro that holds the (x-y) sensitivity axes.

Table 2. Rate gyro sensor system calibration results.

k_{gx}	k_{gy}	k_{gz}	b_{gx} (rad/s)	b_{gy} (rad/s)	b_{gz} (rad/s)	γ_{zx} (rad)	γ_{zy} (rad)
0.96	0.99	0.98	-0.04	-0.07	-0.03	-0.00	-0.01

6. Conclusions

In this work the motivation behind the need for a special IMU system is introduced. An IMU system has been built, programmed, and calibrated to be used in UAVs dynamics modeling applications. The components, structure and communication system of the developed board are described. A linear model of the used accelerometers and rate gyro sensors is assumed. The calibration process of the previously mentioned sensors has been detailed with a description of the calibration platforms and the followed experimental procedures. The calibration results are ready to be used to estimate values of real applied angular accelerations and angular rates directly as described by equations (4) and (11) respectively. The experimental verification of the indirect angular accelerometer method is in progress. The authors of the paper will further verify the IMU readings using several experimental tests prior using the IMU to experimentally verify the online UAV dynamics model parameter estimation method proposed in a previous work.

Acknowledgments

This research project was sponsored by the US Air Force through the contract #FA9200-06-D-0020 to the Physical Science Laboratory (PSL) of the New Mexico State University. Special thanks to Mr. Jesse McAvoy & Mr. Laith Sahawneh for all the support and valuable scientific contributions.

References

[1] Hatamleh, K., Ma, O. and Paz, R., "A UAV Model Parameter Identification Method: A Simulation Study", International Journal of Information Acquisition Vol. 6, No., 2009, 225–238.

[2] Dissanayake, G., Sukarieh, S., Nebto, E. and Durrant-Whyte, H. , "The Aiding Of A Low-Cost Strap Down Inertial Measurement Unit Using Vehicle Model Constraints For Land Vehicle Applications", IEEE transactions on robotics and automation, Vol. 17, No. 5, 2001,731–747.

[3] Hatamleh, K., Xie, P., Martinez, G., McAvoy, J., Ma, O., "An UAV Parameter Identification Method", AIAA Modeling & Simulation Technologies Conf. Chicago, IL, USA, 2009.

[4] STMicroelectronics Digital devices (lis3lv02dq) tri-axis accelerometer, (http://www.sparkfun.com/datasheets/IC/LIS3LV02DQ.pdf.hj).

[5] STMicroelectronics Digital devices (lpr530al) dual axis rate gyro sensor, (http://www.sparkfun.com/datasheets/Sensors/IMU/lpr530al.pdf.)

[6] STMicroelectronics Digital devices (lpy530al) dual axis rate gyro sensor. (http://www.sparkfun.com/datasheets/Sensors/IMU/lpy530al.pdf).

[7] Skog, I., and Handel, P., "Calibration of a mems inertial measurement unit", the 17th IMEKO World Congress, Rio deJaneiro, Brazil, 2006.

[8] Sahawneh, L., and Jarrah, M., A., "Development and calibration of low cost mems IMU for UAV applications", the 5th International Symposium on Mechatronics and Its Applications, ISMA, Amman, Jordan, 2008.

[9] Britting, K. R., Inertial Navigation Systems Analysis, Wiley, New York; 1971.

JJMIE

Volume 5, Number1, February 2011
ISSN 1995-6665
Pages 61- 70

Jordan Journal of Mechanical and Industrial Engineering

Dynamic Modeling and Control of Elastic Beam Fixed on A Moving Cart and Carrying Lumped Tip

Fadi A. Ghaith[a]* and Mohammad N. Hamdan[b]

[a] Department of Engineering and physical Sciences, Heriot-Watt University, Dubai campus, Dubai, UAE.

[b] Mechanical Engineering Department, University of Jordan, Amman, Jordan.

Abstract

In this paper, a Bernoulli – Euler beam fixed on a moving cart and carrying a lumped tip mass is considered. The equations of motion which describe the global motion as well as the vibrational motion were derived using the extended Hamilton's principle. The obtained equations of motion are analyzed by means of the unconstrained modal analysis. In order to eliminate the need of sensor placement at the tip of the cantilever beam, as most of the practical control implementations require that sensors and actuators to be placed in accessible locations, the Linear Quadratic Estimator (LQE) approach was utilized to estimate the vibrations of any point on the span of the elastic cantilever beam in the presence of process and measurement noises. For the purpose of suppressing the vibrations at the tip of the beam, an active optimal controller was designed based on the Linear Quadratic Gaussian (LQG) method. Numerical simulation results demonstrated the capability of the developed optimal controller in eliminating the vibrations at the tip of the beam as well as to improve the positioning accuracy.

Keywords: Unconstrained modal analysis, Linear quadratic estimator, Linear quadratic Gaussian.

1. Introduction

The beam is considered as one of the fundamental elements of an engineering structure. It finds use in varied structural applications. Moreover, structures like forklift vehicles or ladder cars that carry heavy loads, military airplane wings with storage loads on their span and antenna operated in the space can be modeled as a flexible beam carrying a concentrated mass and being fixed on a moving cart. Due to the presence of vibration in such systems, it leads to undesirable effects such as structural and mechanical failures, though vibration suppression has been main requirement for their design and safe operation. Active control falls among the most feasible techniques for vibration suppression in axially moving structures, where passive techniques may become ineffective or impractical. On the other side, unconstrained modal analysis is considered as a powerful tool to generate accurate mode shapes of the system, such analysis may provide useful information which may enhance the design of the optimal controller. Many studies were reported in the literature concerned of the mathematical modeling of similar systems based on the linear formulation. Exact frequency equation of a uniform cantilever beam carrying a slender tip mass whose center of gravity didn't coincide with the attachment point has been developed by Bhat and Wanger [1]. To [2] calculated the natural frequencies and mode shapes of a mast antenna structure, but he modeled it as a cantilever beam with base excitation and tip mass because the total mass of the beam-mass system is negligible compared with that to the base. Park et al. [3] obtained the linear equations of motion, frequency equations and exact solutions of the motion of flexible beam fixed on a moving cart and carrying a lumped tip mass using unconstrained modal analysis. Park et al. [4] considered a Bernoulli-Euler beam fixed on a moving cart and carrying a concentrated mass attached at an arbitrary position along the beam, and the linear equations of motion which describe the global motion as well as vibrations motion were derived. Vibration suppression has been a requirement for the design and operations in many engineering structures. Due to the development in the area of control systems, active controllers have been implemented in several vibration suppression applications. Khulief [5] has proposed the control of a rotating beam mounted on a rigid hub using linear quadratic regulator. Zimmerman and Cudeney [6], Yousfi-Koma and Vukovich [7], Mallory and Miller [8], Lee and Eillott [9], all have also suggested placing sensors at various locations along the span of the beam for monitoring and control purposes. Sinawi and Hamdan [10] developed a new approach for estimating the vibration of any point on the span of a rotating flexible beam mounted on a compliant hub (plant) in the presence of process and measurements

***** Corresponding author. F.ghaith@hw.ac.uk

noise based on the Linear Quadratic Estimator (LQE) technique. At this point one can conclude that an active control law that uses a consistent dynamic model and utilizes the linear quadratic regulator in absence of process and measurement noise is not fully addressed, in particular when unconstrained modal analysis is utilized as the modeling tool. In this paper, the equations of motion of a Bernoulli-Euler cantilever beam clamped on a moving cart and carrying lumped mass are analyzed by means of the unconstrained modal analysis, and a unified characteristic equation for calculating the natural frequencies of the system. The natural frequencies obtained from the unconstrained modal analysis are used to develop an active modal controller based on Kalman filter estimator and linear quadratic regulator in order to reduce the end vibration as well as to improve the positioning accuracy.

2. Model Formulation

The equations of motion of a Bernoulli-Euler cantilever beam clamped on a moving cart and carrying lumped mass on its tip are derived using the extended Hamilton's principle. It should be recognized that the addressed dynamic model is considered to be linear by neglecting the effect of axial shortening.

2.1 System Description and Assumptions

Consider the planar motion of the beam-mass-cart system, shown in Fig.1. The elastic beam is assumed to follow the Bernoulli-Euler beam model and to be clamped tightly on the moving cart. In deriving the equations of motion, it is assumed that the beam material is linearly elastic and undergoes small deformation.

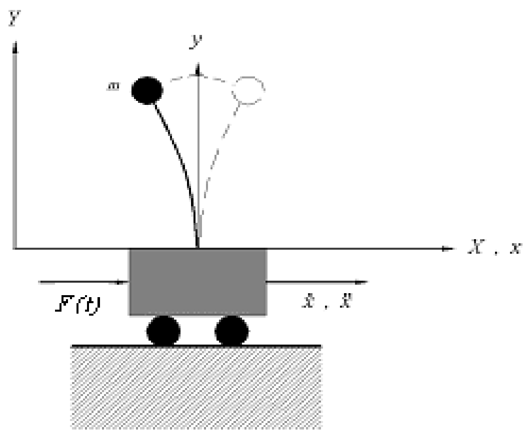

Fig. 1: Schematic of the beam-mass-cart system.

2.2 Equations of Motion

The equations of motion and the boundary conditions of the beam-mass-cart system are derived using the extended Hamilton's principle. Defining the variation of the functional *I*, which represents the integrand of the Lagrangian function *L* over the initial and final time instants, t_o and t_f respectively, and considering the fact that the variation and integral operators commute, we can write for the actual path that:

$$\int_{t_o}^{t_f} \left(\delta L + \delta W_{nc}\right) dt = 0 \qquad (1)$$

where δW_{nc} denotes the work done by non-conservative forces such as external forces and moments. Referring to the Cartesian coordinates shown in Fig. 1, the beam potential and kinetic energy are given by equations (2) and (3) respectively,

$$V = \frac{EI}{2}\int_0^l (u'')^2\, dy \qquad (2)$$

$$T = \frac{1}{2}\,\mathrm{M}\dot{x}^2 + \frac{1}{2}\int_0^l \rho_o\left(\dot{x}+\dot{u}\right)^2 dy + \frac{1}{2} m\,\delta(y-l)\left(\dot{x}+\dot{u}\right)^2$$
(3)

where

M: mass of the cart.
m: lumped mass at the tip of the beam.
ρ_o: mass per unit length of the beam .
l: length of the beam .
u(y,t) : lateral deformation of the beam at a distance y measured from the fixed end of the beam along the neutral axis in the undeformed configuration and at time *t* .
EI: The flexural stiffness of the beam.
δ(y-l): The dirac δ-function.

Substituting equations (2) and (3) into equation (1), noting that $L = T - V$, and after some mathematical manipulations including integration by parts, yields

$$M\,\ddot{x} + \int_0^l \left[\rho_o + m\,\delta(y-l)\right]\left(\ddot{x}+\ddot{u}\right) dy = F(t) \qquad (4)$$

$$EI\,u'''' + \left[\rho_o + m\,\delta(y-l)\right]\left(\ddot{x}+\ddot{u}\right) = 0 \qquad (5)$$

(5) $$u(0,t)=0,\; u'(0,t)=0,\; EI\,u''(l,t)=0,\; EI\,u'''(l,t)=0 \qquad (6)$$

3. Modal Analysis

In this study, the obtained equations of motion are analyzed utilizing the unconstrained modal analysis which admits the presence of the external forcing terms. Assuming that the position of the cart *x(t)* has a solution of the form:

$$x(t) = \alpha(t) + \beta q(t) \tag{7}$$

where *α(t)* describes the motion of the center of mass . Therefore, the motion of the center of the mass without perturbation can be expressed as

$$M_t \ddot{\alpha}(t) = F(t) \tag{8}$$

where M_t is the total mass of the beam-mass-cart system such $M_t = M + m + m_b$ and m_b represents the mass of the flexible beam such $m_b = \rho_o l$.

Also, the deflection of the beam *u(y,t)* is assumed to have the solution of the form

$$u(y,t) = \Phi(y)q(t) \tag{9}$$

Defining $\psi(y) = \beta + \Phi(y)$, and substituting equations (7) and (9) into equation (5), one obtains

$$EI\psi''''(y)\,q(t) + [\rho_o + m\delta(y-l)][\psi(y)\,\ddot{q}(t) + \ddot{\alpha}(t)] = 0 \tag{10}$$

To get the normal mode solutions, where the effect of the external forces vanishes, one can decompose equation (10) into the following two ordinary differential equations using the principle of separation of variables

$$\ddot{q}(t) + \omega^2 q(t) = 0 \tag{11}$$

$$EI\psi''''(y) - \omega^2[\rho_o + m\delta(y-l)]\psi(y) = 0 \tag{12}$$

where *ω* is the natural frequency of the beam-mass-cart system. Hence, the boundary conditions defined by equation (6) can be rewritten as

$$\psi(0) = \beta, \psi'(0) = 0,\ \psi''(l) = 0, \psi'''(l) = 0 \tag{13}$$

Solving equation (12) using Laplace transforms, and after several mathematical manipulations, one can obtain the solution of $\psi(y)$ as

$$\begin{aligned}\psi(y) = &\frac{\beta}{2}(\cos ky + \cosh ky) - \frac{\psi''(0)}{2k^2}(\cos ky - \cosh ky)\\ &- \frac{\psi'''(0)}{2k^3}(\sin ky - \sinh ky)\\ &- \frac{m\omega^2\psi(l)}{2EIk^3}U(y-l)[\sin k(y-l) - \sinh k(y-l)]\end{aligned} \tag{14}$$

where $U(y-l)$ is a unit step function at *y=l*, and *k* represents the modal frequency and can be expressed as $k^4 = \frac{\rho_o\omega^2}{EI}$ .The constants $\psi''(0)$ and $\psi'''(0)$ can be obtained from the last two boundary conditions given by equation (13) as follow

$$\begin{aligned}\psi''(0) = &\frac{m\omega^2\psi(l)}{2EIk}\frac{1}{1+\cos kl\cosh kl}\{2(\sin kl + \sinh kl)\}\\ &+ \beta k^2\frac{\sin kl\sinh kl}{1+\cos kl\cosh kl}\end{aligned} \tag{15}$$

and

$$\begin{aligned}\psi'''(0) = &-\frac{m\omega^2\psi(l)}{2EI}\frac{1}{1+\cos kl\cosh kl}\{2(\cos kl + \cosh kl)\}\\ &- \beta k^3\frac{\cos kl\sinh kl + \sin kl\cosh kl}{1+\cos kl\cosh kl}\end{aligned} \tag{16}$$

Thus, from equations (15) and (16) , *ψ(y)* can be expressed as

$$\psi(y) = A(y)\psi(l) + B(y)\beta \tag{17}$$

where

$$A(y) = \frac{m\omega^2}{4EIk^3}\left\{\begin{aligned}&\frac{\cos ky - \cosh ky}{1+\cos kl\cosh kl}[-2(\sin kl + \sinh kl)]\\ &+\frac{\sin ky - \sinh ky}{1+\cos kl\cosh kl}[2(\cos kl + \cosh kl]\\ &-2U(y-l)[\sin k(y-l) - \sinh k(y-l)]\end{aligned}\right\} \tag{18}$$

and

$$B(y) = \frac{1}{2}\left[\begin{aligned}&\cos ky + \cosh ky - \frac{\sin kl\sinh kl}{1+\cos kl\cosh kl}(\cos ky - \cosh ky)\\ &+\frac{\cos kL\sinh kL + \sin kl\cosh kl}{1+\cos kl\cosh kl}(\sin ky - \sinh ky)\end{aligned}\right] \tag{19}$$

Integration of equation (5) with respect to *y* and substituting equation (4) into the resulting equation gives

$$M\ddot{x} + EI\,u'''(0,t) = F(t) \tag{20}$$

When *F(t)* is assigned to be zero, and among substituting equations (7) , (8) and (11) into equation (20) yields

$$\beta = \frac{EI}{M\omega^2}\Phi'''(0) = \frac{EI}{M\omega^2}\psi'''(0) \tag{21}$$

Utilizing equations (16) and (21), *β* can be found as

$$\beta = \frac{C\psi(l)}{1-D} \tag{22}$$

where $C = \frac{-m}{2M}\frac{1}{1+\cos kl\cosh kl}\{2(\cos kl + \cosh kl)\}$

and

$D = -\frac{\rho_o}{Mk}\frac{\sin kl\cosh kl + \cos kl\sin kl}{1+\cos kl\cosh kl}$.

Finally, equations (17) and (22) lead to

$$\psi(y) = \left[A(y) + \frac{C}{1-D} B(y) \right] \psi(l) = F(y)\psi(l) \quad (23)$$

3.1 The Frequency Equation

Equation (23), at $y=l$, gives the following equation:

$$[1 - D - A(l) + A(l)D - B(l)C]\psi(l) = 0 \quad (24)$$

As $\psi(l) = 0$ yields a trivial solution, the inner part of the bracket in equation (24) must vanish. From this condition, and after some mathematical manipulations, the frequency equation can be obtained as follow

$$\begin{aligned} &1 + \cos\xi \cosh\xi + 2r_1 \cos\xi \cosh\xi \\ &+ \frac{r_2}{\xi}(\cos\xi \sinh\xi + \sin\xi \cosh\xi) \\ &+ r_3\xi(\cos\xi \sinh\xi - \sin\xi \cosh\xi) = 0 \end{aligned} \quad (25)$$

where $r_1 = \dfrac{m}{M}$, $r_2 = \dfrac{m_b}{M}$, $r_3 = \dfrac{m}{m_b}$ $and\ \xi = kl.$

3.2 Beam Deflections

If a function $\rho(y)$ is defined as

$$\rho(y) = \rho_o + m\,\delta(y - l) \quad (26)$$

Substituting equations (12) and (26) into equation (10), multiplying both sides of the resulting equation by $\Phi_j(y)$ and integrating over the problem domain, leads to

$$\begin{aligned} &\sum_{i=1}^{\infty} \left[\ddot{q}_i(t) + \omega_i^2 q_i(t)\right] \int_0^l \rho(y)\psi_i(y)\Phi_j(y)dy \\ &= -\ddot{\alpha}(t) \int_0^l \rho(y)\Phi_j(y)dy \end{aligned} \quad (27)$$

Now, substituting equations (7) and (9) into equation (4) and doing appropriate mathematical manipulation, one obtain that β

$$\beta_j = -\frac{1}{M_t} \int_0^l \rho(y)\Phi_j(y)dy \quad (28)$$

Substituting equations (8) and (28) into equation (27), for $i = j$

$$\ddot{q}_i(t) + \omega_i^2 q_i(t) = F(t)\beta_i\,, \quad i = 1,2,...,\infty. \quad (29)$$

Note that q_i *(t)* can be obtained by integrating equation (27) for given values of ω_i and applied force *F (t)*. For given $\psi_i(l)$, β_i and $q_i(t)$, the beam deflection can be expressed as

$$u(y,t) = \sum_{i=1}^{\infty} \Phi_i(y)q_i(t) = \sum_{i=1}^{\infty} [\psi_i(y) - \beta_i]\, q_i(t) \quad (30)$$

Accordingly, the position of the cart can be expressed as

$$x(t) = \alpha(t) + \sum_{i=1}^{\infty} \beta_i q_i(t) \quad (31)$$

Now, the nonhomogeneous equations (8) and (29) can be transformed into a set of *n+1* second-order ordinary differential equations of the form

$$\begin{pmatrix} M_t & 0 \\ 0 & I \end{pmatrix}\begin{pmatrix} \ddot{\alpha} \\ \ddot{q}_i \end{pmatrix} + \begin{pmatrix} 0 & 0 \\ 0 & K \end{pmatrix}\begin{pmatrix} \alpha \\ q_i \end{pmatrix} = \begin{pmatrix} 1 \\ \beta_i \end{pmatrix} F(t),\ i = 1,2,...,n. \quad (32)$$

Where K represents an $n \times n$ stiffness matrix such that $K = diag\{\omega_i^2\}$. Equation (32) can be solved using the fourth order Runge-Kutta method for an arbitrary given forcing function *F(t)*.

4. Design of Active Modal Controller

In this section, the design of an active optimal controller for the vibration suppressing of elastic cantilever beam mounted on a moving cart and carrying tip lumped mass is tackled. The elastic beam was already modeled in section 3 via the unconstrained modal analysis from which the transient response of the tip beam deflection can be obtained as per equation (29). To eliminate the need for sensor placement on the tip of the cantilever beam since most of the practical control implementations required that sensors and actuators be placed at certain accessible structural locations, Linear Quadratic Estimator (LQE) technique is used for estimating the vibration of any point on the span of the flexible cantilever beam mounted on a moving cart and carrying tip lumped mass and subjected to process and measurement noises. Linear-quadratic-Gaussian (LQG) control is a modern state-space technique for designing optimal dynamic regulators. It enables to trade off regulation performance and control effort. Also it takes into account process disturbances and measurement noises. Fig. 2 illustrates the schematic of the LQG approach. The main goal of this control scheme is to regulate the output y around zero. The plant is subjected to disturbances w and is driven by controls u. The regulator relies on the noisy measurements $\bar{y} = y + v$ to generate these controls. The plant states and measurement equations are expressed as

$$\dot{z} = Az + Bu + Bw\,,\ y = Cz + Du + v \quad (33)$$

where A is the plant state matrix , B is the plant input matrix , C is the plant output matrix , D is the plant feed forward, and both w and v are modeled as white noise. The LQG regulator consists of an optimal state-feedback gain and a Kalman state estimator. The design of these two components is discussed hereafter with more details.

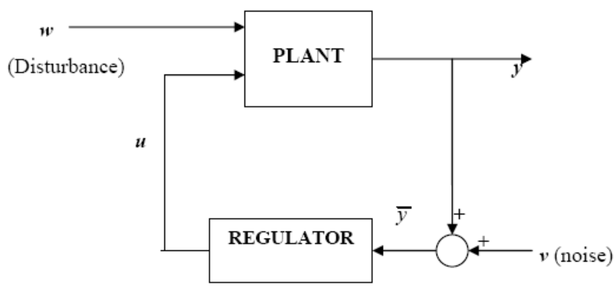

Fig. 2: Schematic of the proposed LQG approach.

Optimal state feedback gain: In LQG controller, the regulation performance J is measured by a quadratic performance criterion of the form

$$J(u) = \int_{0}^{\infty} \left[z^T(t) Q\, z(t) + u^T R\, u(t) \right] \qquad (34)$$

The weighting matrices Q and R define the trade-off between regulation performance (how fast goes to zero) and control effort. The first design step seeks a state-feedback law $u = -\overline{K}\, x$ that minimizes the cost function *J(u)* . The minimizing gain matrix $\overline{K}$ is obtained by solving the associated algebraic Riccati equation.

Kalman Filter Estimator: Kalman filter is an optimal recursive data processing algorithm. One aspect of this optimality is that the Kalman filter incorporates all information that can be provided to it such as knowledge of the system , measurement device dynamics ,statistical description of the system noises , measurement errors, and uncertainty in the dynamic model .Unlike certain data processing concepts , the Kalman filter doesn't require all previous data to be kept in storage and reprocessed every time , but a new measurement is taken each time .Fig. 3 depicts a typical situation in which a Kalman filter can be used advantageously . The input disturbances are included in the state space model by adding the noise input vector w to the exogenous input vector u. Moreover, to include measurement noise, the vector v is added to the output of the system. Such noise signals are usually part of the actual mode of the system. Up to this end, the LQG regulator can be established by combining the Kalman filter and LQ-optimal gain K as shown in Fig. 4.

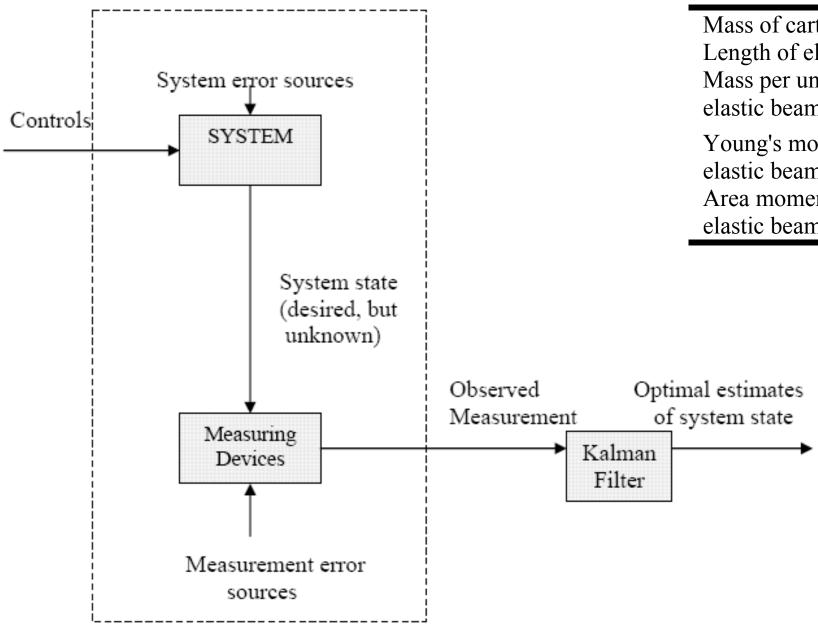

Fig. 3: Typical Kalman filter application.

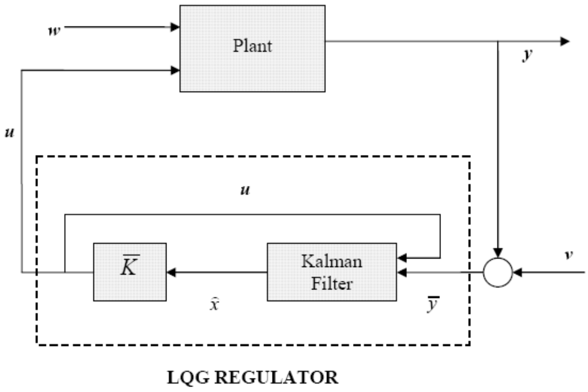

Fig. 4: Schematic flow chart for Linear Quadratic Guassian Regulator.

5. Numerical Simulation

The main objective of the current numerical study is to examine both open and closed loop responses after implementing the developed LQG controller. The beam tip deflection was estimated using Kalman filter estimator, in the presence of process and measurement noises using Kalman filter estimator. Numerical values of the system parameters are selected as shown in table 1.

Table 1: System Parameters

Parameters	Value
Mass of cart, M	10.0 kg
Length of elastic beam, L	1.0 m
Mass per unit length of elastic beam, ρ_o	0.788 kg/m
Young's modulus of elastic beam, E	2.07×10^{11} N/m^2
Area moment of inertia of elastic beam, I	5.208×10^{11} m^4

5.1 Open-loop Response of the beam-mass-cart system

Numerical simulations were carried out to examine the open-loop response of the system, subjected to a periodic forcing function, such that $f(t) = 10\cos(10t)$. Equation (32) has been solved numerically, using ODE 45 solver within MATLAB® software, and numerical solutions were obtained by integrating the discretized form of the equations forward in time. The natural frequencies of the system have been obtained by solving the frequency equation presented in equation (25) utilizing Newton-Raphson method, for each mode of vibration. Table 2 show the obtained modal and natural frequencies for the first three modes of vibration, in addition to the corresponding values of the constants *C*, *D*, ψ_i *(l)* and β_i which have been evaluated based on their definitions presented in the aforementioned modal analysis. Figures 5 show the time responses of both displacement and velocity at the tip of the beam for the first three modes of vibration when the system is subjected to the sinusoidal force. Referring to fig. 5, it was found that the most critical mode is the first one, as the applied sinusoidal force leads to large deflection of the elastic beam compared with the other modes of vibration. This finding is considered reasonable enough to design a controller to suppress the vibration for the first dominant mode. It is obvious that the vibration signal appears just like noise at high modes of vibration.

The phase plane plot shows that there is one equilibrium point for the beam-mass-cart system where there is no excitation force and the expected shape of phase plane plot in that case is a center profile. On the other hand, the importance of the phase plane plot appears clearly in determining the qualitative behavior of the dynamic systems such as stability.

5.2 Estimated beam tip deflection in the presence of process and measurement noises using Kalman filter estimator.

In this part, Kalman filter is used to estimate the beam tip deflection in the presence of process disturbance *w* and noise measurements *v*. In order to illustrate the efficiency of the filtration process, the excitation force applied to the system is chosen to be similar to the selected force in the open loop analysis. The process disturbance signal *w* is selected to be a random force of magnitude of ± 2 N. Matlab Simulink model has been developed to represent the Kalman filter estimator in order to predict the beam tip deflection in the presence of process and noise measurements. Kalman filter matrix was obtained using a simple Matlab algorithm, while the beam-mass-cart system has been defined in its state space representation. In order to demonstrate the capability of the proposed filtration scheme, the estimated beam tip deflection is compared with the corresponding value obtained via the unconstrained modal analysis. Fig. 6 shows the capability of the proposed estimator in producing fairly accurate tip deflection. Kalman filter was found as powerful tool to eliminate hysteresis obtained by process and measurement noises and to purify the output signal.

Table 2: The values of the modal and natural frequencies and associated modal constants for the first three modes of vibration.

First Mode (i=1) (k =1.2267, ω_n=5.566 rad/s)				Second Mode (i=2) (k =4.03, ω_n=60.073 rad/s)				Third Mode (i=3) (k =7.132, ω_n=188.143 rad/s)			
C	*D*	$\psi_i(L)$	β_i	*C*	*D*	$\psi i\ (L)$	β_i	*C*	*D*	$\psi_i\ (L)$	β_i
-0.135	-0.082	0.871	-0.109	0.164	-0.006	0.244	-0.04	-0.1511	-0.003	0.166	-0.025

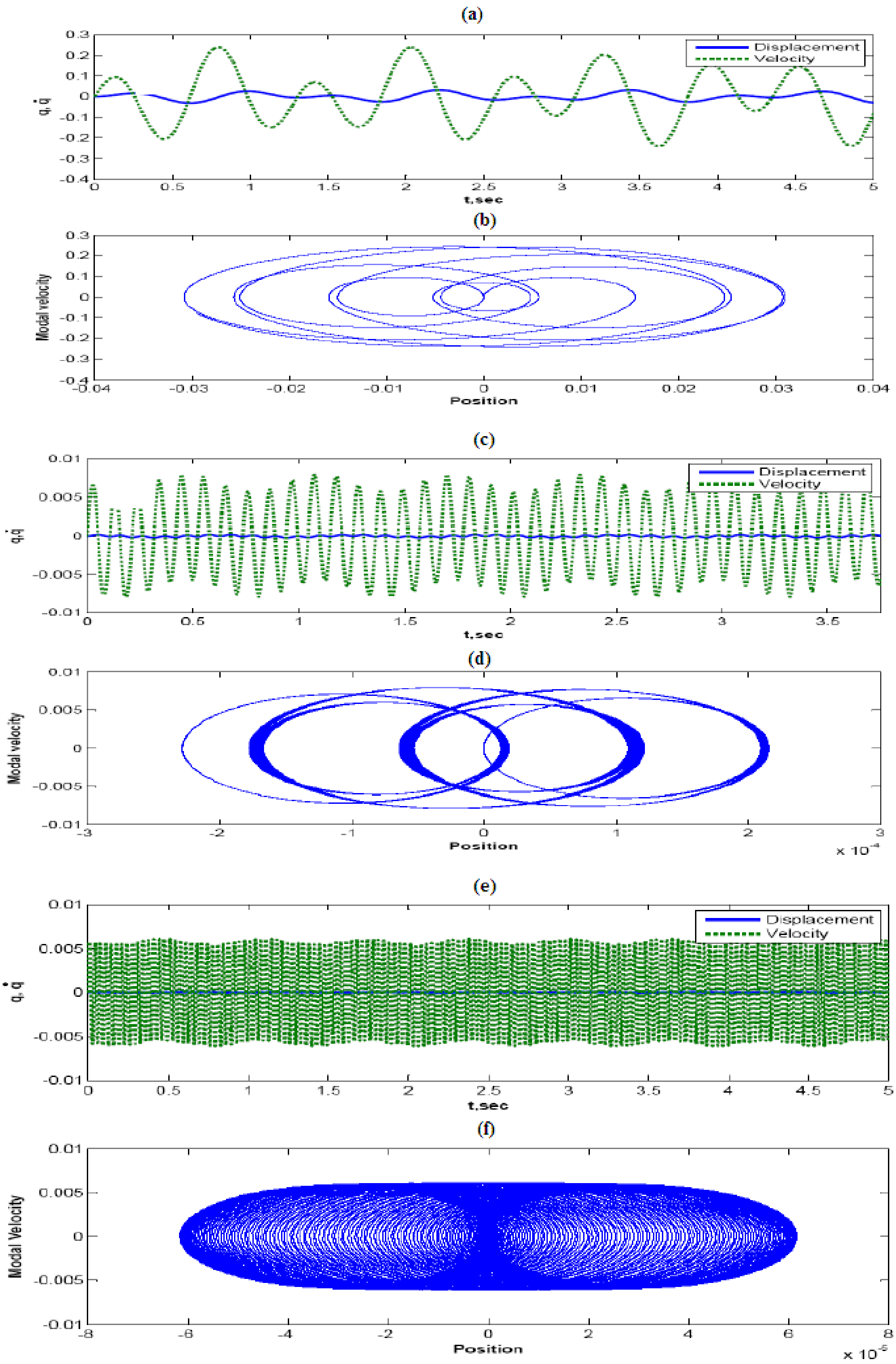

Fig. 5: (a) Open-loop response of the local beam deflection at the first mode of vibration when $f(t) = 10\cos(10t)$. (b) Corresponding phase plane plot. (c) Open-loop response of the local beam deflection at the 2nd mode of vibration (d) Corresponding phase plane plot. (e) Open-loop response of the local beam deflection at the 3rd mode of vibration. (f) Corresponding phase plane plot.

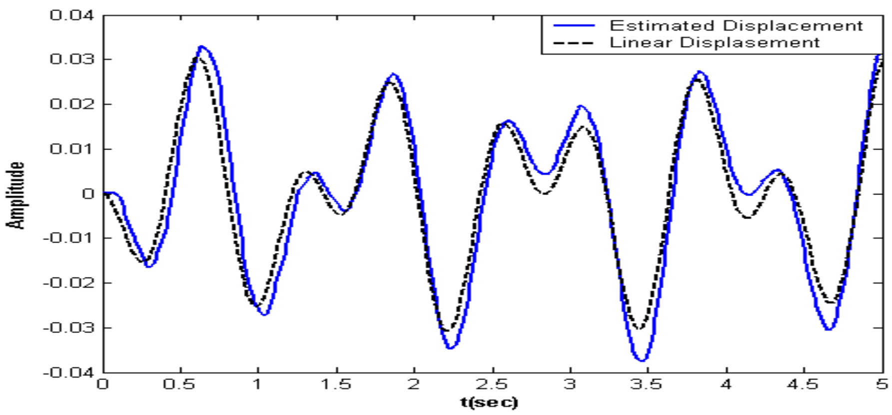

Fig. 6: Estimated beam tip deflection in presence of process and measurement noises using Kalman filter estimator versus deflection obtained using unconstrained modal analysis for the first mode of vibration.

5.3 Closed-loop response using LQG optimal controller

In order to illustrate the regulator performance, both open and closed responses of the deflection at the tip of the beam subjected to the periodic functions were compared as shown in figures 7 and 8 for different weighting matrices. Referring to these figures, it was found that the linear quadratic regulator is considered as efficient tool to eliminate the vibrations and stabilize the system for various inputs. It is important to recognize that the dynamic matrix of the system shows that the system is conditionally stable since the roots are pure imaginary while the new eigenvalues for the system after using regulator are with negative real parts which assure stability for the system. By examining figures 7 and 8, we can conclude that the time required to achieve the steady state response can be controlled by by increasing the weight of (Q) matrix and/or decreasing the weight matrix (R) which has been used in LQ regulator .Fig. 8 shows a fast closed loop response which was obtained by decreasing the value of the weighting matrix (R). Generally if application requires fast decay of vibration, weighting matrix (Q) must be increased while (Q) matrix shall be decreased, and the opposite can be performed if reduction of the control effort is required.

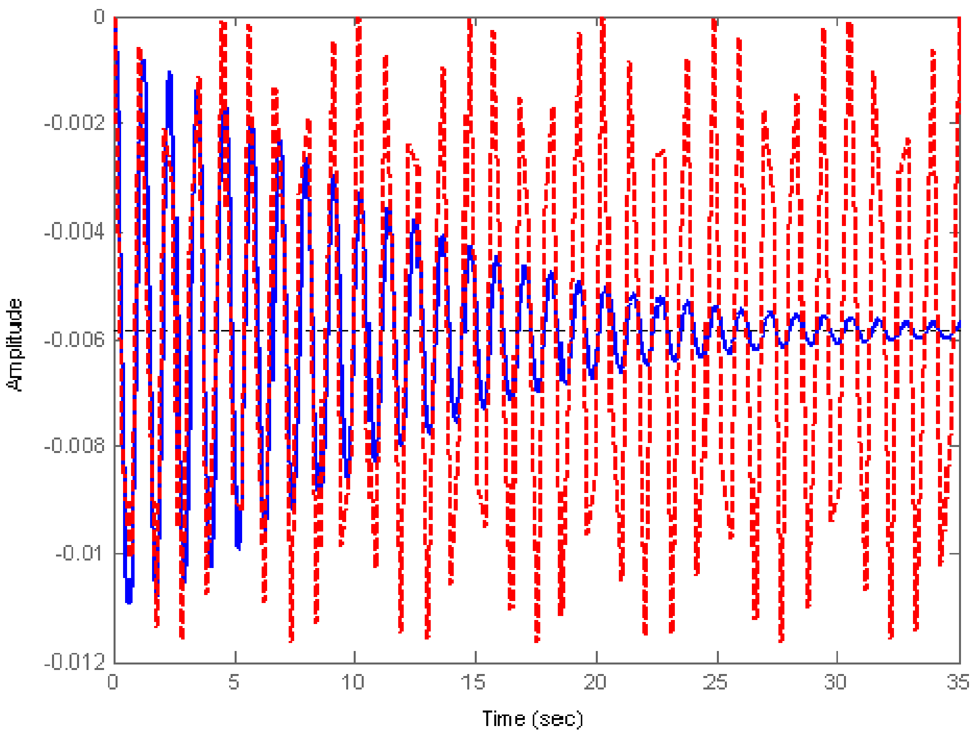

Fig. 7: Open loop versus closed loop (Regulated) responses for periodic input with weighting mat (R=0.01).

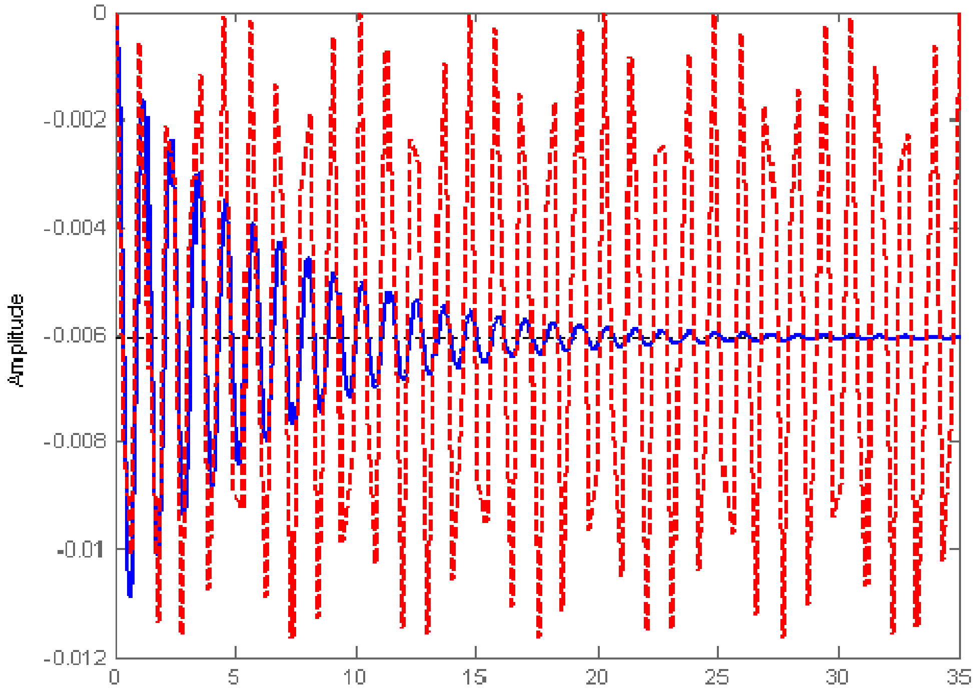

Fig. 8: Open loop versus closed loop (Regulated) responses for periodic input after with weighting matrix (R=0.001)

6. Conclusions

In the present work, a Bernoulli – Euler beam fixed on a moving cart and carrying lumped tip mass was considered and the equations of motion which describe the global motion as well as the vibration motion were derived by means of the extended Hamilton's principle .A unified frequency equation was obtained and the roots of the frequency equation were found for the first three modes of vibrations. Exact and assumed-mode solutions were obtained by the unconstrained modal analysis for the beam-mass-cart system which emphases the importance of unconstrained modal analysis in studying the effect of the axial movement of the cart and achieving accurate mode shapes. In order to eliminate the need for sensor placement on the tip of the cantilever beam ,since most of the practical control implementations required that sensors and actuators be placed at certain accessible structural locations ,a new approach based on the Linear Quadratic Estimator (LQE) technique for estimating the vibration of any point on the span of the flexible cantilever beam mounted on a moving cart and carrying tip lumped mass and subject to process and measurement noise has been developed. Numerical simulation results demonstrated the capability of the proposed estimator in producing fairly accurate tip deflection. The analytical design of an active optimal scheme for vibration suppression was employed via the Linear Quadratic Regulator (LQR) to obtain the output feedback control gain. Closed-loop responses obtained by the proposed technique were compared to the open-loop responses generated by the unconstrained analysis and the results showed good vibration suppression.

References

[1] Bhat, R. and Wanger H., "Natural frequencies of a uniform cantilever with a tip mass slender in the axial direction", Journal of Sound and Vibration, Vol.45, 1976, 304-307.

[2] To, W. S., "Vibration of a cantilever beam with a base excitation and tip mass', Journal of Sound and Vibration, Vol. 83, 1982,445-460.

[3] Park, S. D., Chung, W. K., Youm, Y. and Lee, J. W., "Analysis of the motion of a cart with an inverted flexible beam and a concentrated tip mass", Proceedings of Korean Automatic Control Conference (KACC), 367-372, 1998.

[4] Park, S. D., Chung, W. K., Youm, Y. and Lee J. W., ''Natural frequencies and open-loop responses of an elastic beam fixed on a moving cart and carrying an intermediate lumped mass", Journal of Sound and Vibration, Vol. 230, 2000, 591-615.

[5] Khulief, Y. A.,"Vibration suppression in rotating beams using active modal control", Journal of Sound and Vibration, Vol. 242, 2000, 681-699.

[6] Zimmerman, C. and Cudeney H. H., "Practical implementation issues for active control of large flexible

structures", Journal of Vibration, Acoustics, Stress, and Reliability in Design, Vol. 111, 1989, 283-289.

[7] Yousifi-Koma and Voukovich G., "Vibration suppression of flexible beams with ponded piezo transducers using wave-absorbing controllers", Journal of Guidance, Control, and Dynamics, Vol. 23, 2000, 347-354.

[8] Mallory W. and Miller D., "Decentralized state estimation for flexible space structures", Journal of Guidance, Control, and Dynamics, Vol. 23, 2000, 665-672.

[9] Lee Y. and Elliott S., "Active position control of flexible smart beam using internal model control", Journal of Sound and Vibration, Vol. 242, 2001, 767-791.

[10] El-Sinawi A. and Hamdan M., "Optimal vibration estimation of a non-linear flexible beam mounted on a rotating compliant hub", Journal of Sound and Vibration, Vol. 259, 2003, 857-872.

JJMIE

Volume 5, Number1, February 2011
ISSN 1995-6665
Pages 71- 76

Jordan Journal of Mechanical and Industrial Engineering

Experimental Investigation of the Effect of Hydrogen Blending on the Concentration of Pollutants Emitted From a Four Stroke Diesel Engine

Haroun A. K. Shahad*, Nabil Abul Hadi

Department of mechanical engineering, College of Engineering
University of Babylon, Babylon, Iraq

Abstract

The problem of pollutants emitted from internal combustion engines becomes increasingly important since it affects directly and indirectly human life on earth through air pollution, global warming, acid rains.. etc. The concentration of these pollutants must be reduced. One approach to reduce these concentrations is by blending hydrogen gas with hydrocarbon fuels used in internal combustion engines. In this paper an experimental research is carried out to study the effect of hydrogen blending. A four stroke air cooled diesel engine is used in this program. The engine is run at different loads, speeds and hydrogen blending percentages. It is found that increasing the blending percentage reduces the emitted concentration of carbon oxides and smoke. However it is found that nitrogen oxides concentration is increased with increasing hydrogen blending percentage due to higher cylinder temperatures. The results showed that 10% hydrogen blending reduces smoke opacity by about 65%, increases the nitrogen oxides concentration by about 21.8% and reduces CO_2 and CO concentrations by about 27% and 32% respectively. This trend is found at all tested speeds and loads.

. Keywords**:** Diesel engine, Hydrogen Blending, Hydrogen Fuel, Pollution

1. Introduction

It is well recognized worldwide that the internal combustion engines are a major contributor of environmental pollutants such as carbon oxides, nitrogen oxides, un burnt hydrocarbons and soot in case of diesel engines. Huge quantities of these pollutants are added to the atmosphere causing air and other types of environmental pollution. This problem becomes a major concern of scientists, researcher, politicians and ordinary people all over the world. Solutions must be sought for this problem since it causes global warming in addition to air pollution.

A lot of research work has been carried out over the years to find possible solutions for this problem, i.e. reducing the amount of these pollutants emitted from the internal combustion engines. Different possible techniques are used. One of theses techniques is by using alternatives fuels other than hydrocarbon fuels which contain less or no carbon atoms such as alcohols, bio-fuels, hydrogen, ..etc. These alternative fuels can be used either pure or blended in certain percentages with conventional fuels.

Al-Baghdadi [1] developed a mathematical model to simulate the operation of a four stroke spark ignition engine fueled with gasoline, ethanol and hydrogen either pure or blended. It was found that ethanol can be used as a supplementary fuel up to 30% of gasoline in modern spark ignition engines without major changes, and it improves the output power and reduces the NOx emissions of a hydrogen supplemented fuel engine. The hydrogen added improves the combustion process, especially in the later combustion period, reduces the ignition delay, speeds up the flame front propagation, reduces the combustion duration, and retards the spark timing. Blending of ethanol and hydrogen with gasoline reduces CO concentration but increases NO_x concentration in the exhaust gases. Also blending with hydrogen and ethanol improves combustion process and increases heat release rate.

Takemi C et al [2] investigated the use of methanol as an auxiliary fuel in diesel engine. The effect of auxiliary fuel proportion and timing of injection of auxiliary fuel and main fuel on engine performance and pollutants emission was studied. It was found that with 5% energy substitution of total energy input combustion process took place without misfiring and knocking. The combustion process was smokeless, smoother, with low NO_x emission and less noise than combustion with diesel fuel.

Shahad and Al-Baghdadi [3] developed a computer program to study the effect of equivalence ratio, compression ratio and inlet pressure on performance and NO_x emission of a four stroke supercharged hydrogen engine. The results showed that acceptable NO_x emission, high engine efficiency and lower sfc compared with gasoline operation mode.

The effect of hydrogen air enrichment medium with diesel fuel as an ignition source on performance of a stationary diesel engine was studied experimentally by Saravanan and Nagarajan [4]. They found that hydrogen air enrichment increased engine efficiency and reduced specific energy consumption. Also it resulted in lower smoke level and particulate and NOx emission.

Mihaylov and Barzev [5] carried out an experimental study to evaluate the influence of the addition of hydrogen oxygen mixture (obtained from electrochemically decomposed water) to the inlet air of a single cylinder direct injection diesel engine. The result showed improvement in combustion process efficiency due to better combustion characteristics of hydrogen.

Shahad and Abdul Haleem [6] performed an experimental investigation on a single cylinder spark ignition engine to study the effect of hydrogen blending on pollutants emission and engine performance. They found that hydrogen blending improves engine efficiency until a blending ratio of 20% by mass. They also found that hydrogen blending reduces CO_2, CO and particulate emissions but increases NO_x emission.

2. Experimental Rig

The experimental work is carried out on a test rig consists of the following parts; the engine unit, the hydrogen fueling system and the pollutants concentration measuring system as shown in figure 1.

The engine unit consists of a single cylinder compression ignition engine type Lumberdini with the following specifications (CR=18, stroke= 68 mm, bore=78 mm and a clearance volume of 19.2 cm^3). A data acquisition system type SAD/END is used to acquire , record and process the results.

The hydrogen fueling system consists of a hydrogen bottle, two pressure reduction valves to reduce the hydrogen pressure to 2 bars, a hydrogen flow meter and an injector. The injector is mounted on the inlet pipe at 10 cm from the engine with an angle of 45^o with the direction of injection. The hydrogen injection timing is controlled by an electronic control unit designed for this purpose.

The pollutants concentration measuring system consists of the following parts;

1- Exhaust gas analyzer type IMR 1400 to measure NO and NO_x concentration.
2- Smoke meter type MOD.SMOKY to measure the smoke concentration.

ORSAT apparatus to measure CO_2, CO, and O_2 concentrations.

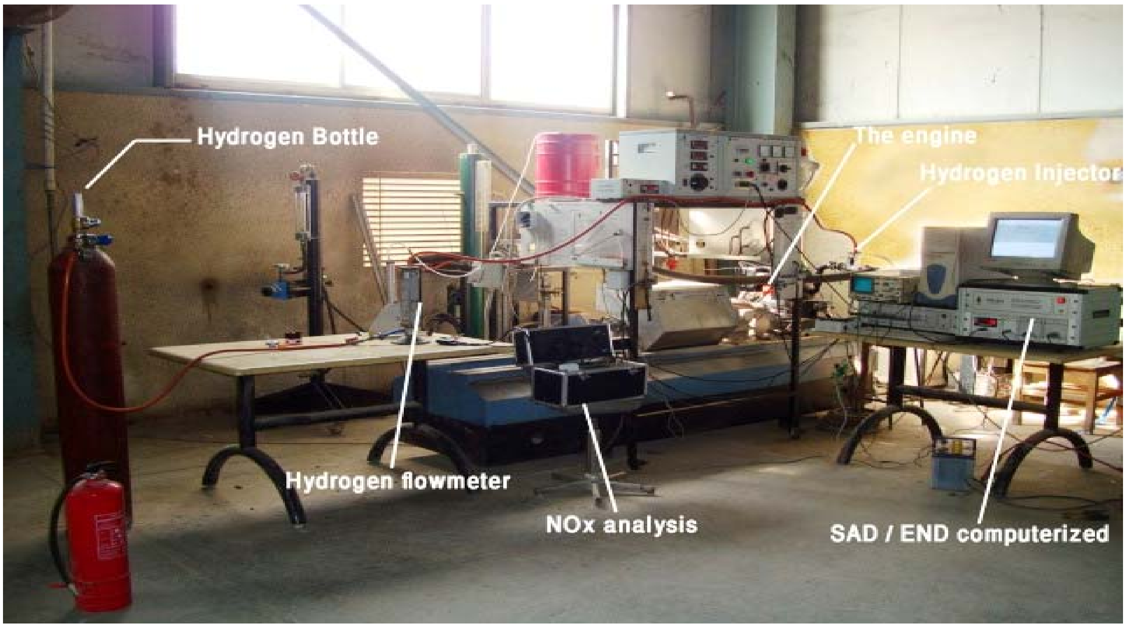

Figure 1. The test rig

3.Results and Discussion

A test program was designed to cover different speeds, loads and hydrogen blending ratios. Three different speeds was chosen namely 1000, 1250 and 1500 rpm. The load range was varied from no load to 80% of full load and the hydrogen blending ratio was varied from zero (pure diesel) to 10% (by mass) of the injected diesel fuel.

Figure 2 shows the variation of carbon dioxide concentration in the exhaust gases at different blending ratios and loads for an engine speed of 1000 rpm. It shows that hydrogen addition reduces CO_2 concentration at all loads. It must mentioned that two factors affect the concentration of CO_2 in the exhaust; the reduction of the carbon atoms in the cylinder charge which reduces the CO_2 concentration and the improvement of combustion process which increases the CO_2 concentration. The net effect is a reduction in concentration.

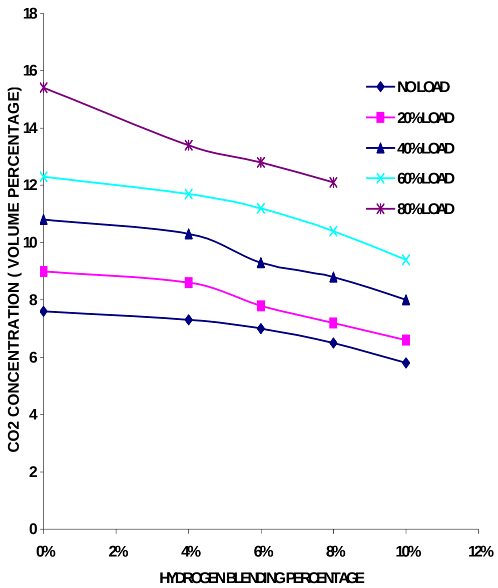

FIG (2) VARIATION OF CO2 CONCENTRATION WITH HYDROGEN BLENDING PERCENTAGE FOR DIFFERENT LOADS AT 1000 RPM

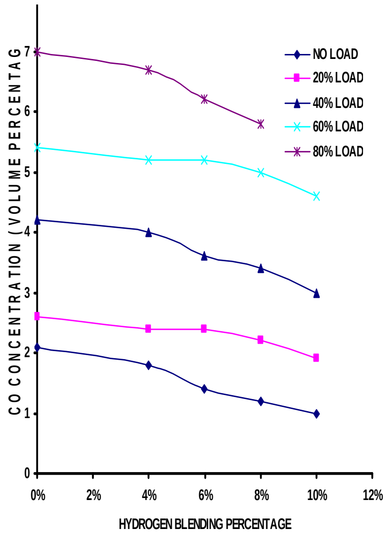

FIG (3) VARIATION OF CO CONCENTRATION WITH HYDROGEN BLENDINGPERCENTGE FOR DIFFERENT LOADS AT 1000 RPM

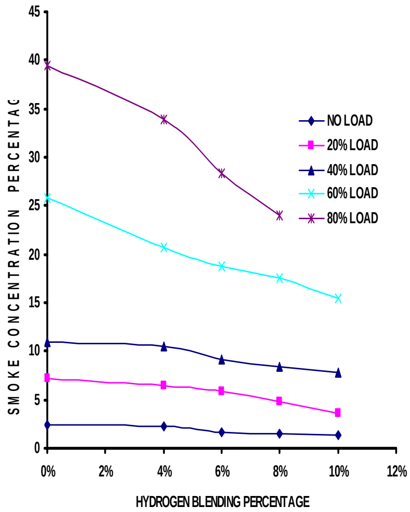

FIG (4) VARIATION OF SMOKE CONCENTRATION WITH HYDROGEN BLENDING PERCENTAGE FOR DIFFERENT LOADS AT 1000 RPM

Figure 3 shows that the concentration of carbon monoxide decreases with increasing hydrogen blending ratio for all loads and at the constant speed of 1000 rpm. This is due to better combustion process.

Figure 4 shows the effect of hydrogen blending on smoke concentration at different loads for an engine speed of 1000 rpm. It is well known that smoke is a major draw back of diesel engines. The fig shows that the hydrogen blending reduces smoke concentration. The effect is more noticeable at high loads where diesel smoke is very high. This due to better combustion process which is the effect of the presence of hydrogen in the mixture.

Figure 5 shows that the concentration of oxygen in the exhaust gases decreases as the load is increased and increases with hydrogen blending ratio since the added hydrogen consumes less air than the replaced diesel fuel. The results are at an engine speed of 1000 rpm.

Figure 6 shows the variation of NO_x concentration with hydrogen blending ratio at different loads for an engine speed of 1000 rpm. The fig shows that the concentration of NO_x generally increases with hydrogen blending ratio for all loads. This is due to the improvement of combustion process caused by the presence of hydrogen in the fuel mixture which leads to higher cylinder temperature. It is very well known that the NO_x formation reactions are highly temperature dependent. The decrease in the concentration of NO_x in the exhaust for 80% load at 6% hydrogen blending and more is probably due to the deterioration of combustion process at high loads.

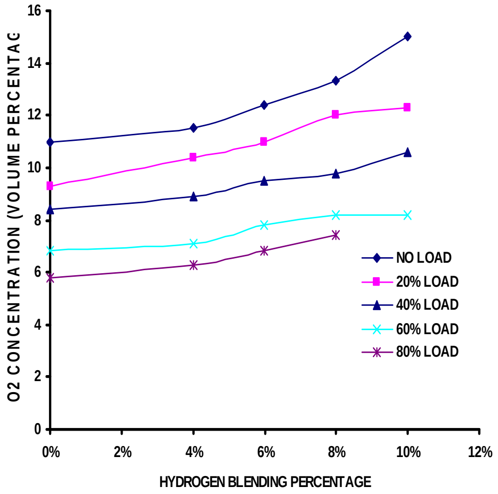

FIG (5) VARIATION OF O2 CONCENTRATION WITH HYDROGEN BLENDING PERCENTAGE FOR DIFFERENT LOADS AT 1000 RPM

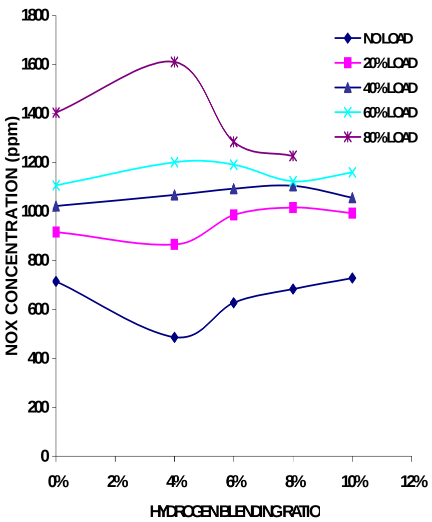

FIG (6) VARIATION OF NOX CONCENTRATION WITH HYDROGEN BLENDING RATIO FOR DIFFERENT LOADS AT 1000 RPM

The concentrations of all above mentioned pollutants are measured at other engine speeds namely; 1250 and 1500 rpm. Figure 7 shows that the concentration of CO_2 decreases with the increase of speed at fixed load and hydrogen blending ratio while the concentration of both CO and O_2 increase. This shows that the combustion process is deteriorating with speed which is a characteristic of compression ignition engines.

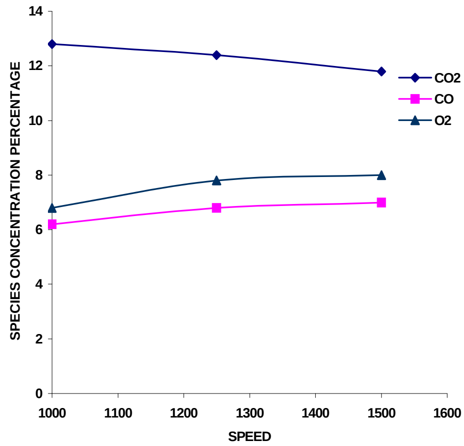

Fig (7) EFFECT OF SPEED ON SPECIES CONCENTRATION AT 80% LOAD AND 6% HYDROGEN BLENDING RATIO

Figure 8 shows that the smoke concentration increases with speed due to incomplete combustion of fuel which leads to the formation of smoke and low cylinder temperature.

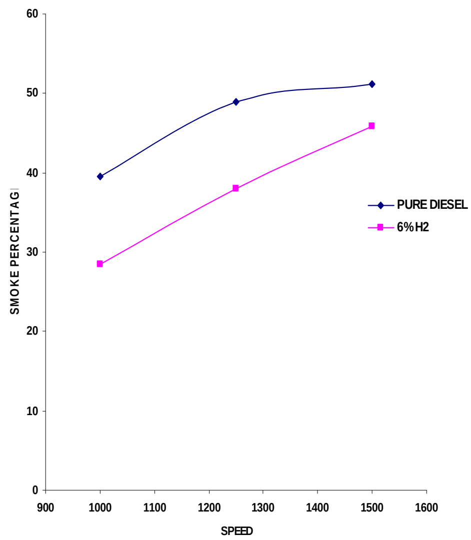

FIG (8) VARIATION OF SMOKE CONCENTRATION WITH SPEED FOR PURE DIESEL AND 6% HYDROGEN BLENDING RATIO

This result is reflected in figure 9 which shows that the NO_x concentration decreases with speed since the NO_x formation is highly dependent of temperature.

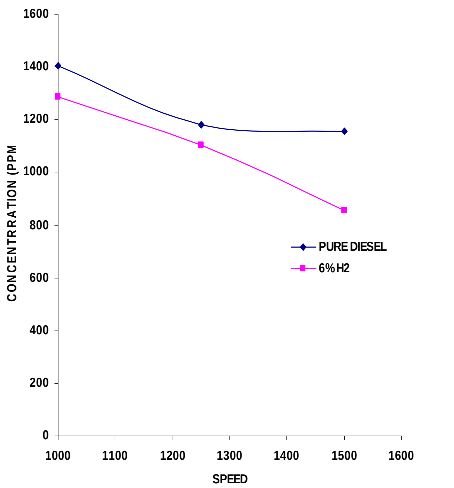

fIG (9) VARIATION OF NOx CONCENTRATION WITH SPEED FOR PURE DIESEL AND 6% HYDROGEN BLENDING RATIO

Figure 10 shows the variation of CO_2, CO and O_2 concentrations with speed at 80% load for pure diesel fuel. The fig shows that O_2 concentration increases with speed due to deterioration of combustion process while the concentration of CO_2 decreases for the same reason.
The results of the present study are compared with the results of ref. [7]. The comparison shows good agreement in trends.

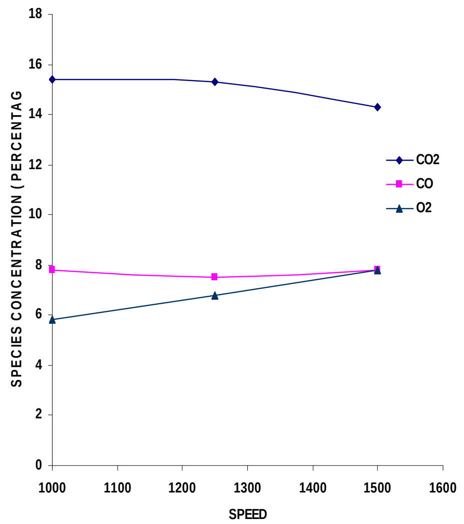

FIG (10) VARIATION OF CO2, CO AND O2 CONCENTRATIONS WITH SPEED FOR PURE DIESEL AND 80% LOAD

4. Conclusions

It can be concluded that:
1-The addition of hydrogen to the diesel fuel improves the combustion process.
2-The improvement of combustion process led to reducing pollutants concentrations.
3-The addition of hydrogen to diesel fuel shows a noticeable decrease in smoke levels specially at high loads. However the effect of speed on smoke levels is still significant even with the addition of hydrogen.

References

1-Maher A.R. Sadiq Al-Baghdadi, "A simulation model for a single cylinder four stroke spark ignition engine fueled with alternative fuels". Turkish J. Eng. Env. Sci, Vol. 30, No. 6, 2006.
2-Takemi, C. Noboru, M and Tadashi, M, "Smokeless, low NO_x and low noise diesel combustion with methanol as a main fuel".1981, SAE paper No. 811375.
3-Shahad H. A. K. and Al-Baghdadi, M. A. R., "A prediction study of a spark ignition supercharged hydrogen engine". Energy Conversion and Management, Vol. 44, No. 20, 2003.
4-Saravanan, N. and Nagarajan, G., "An experimental investigation of hydrogen enriched air induction in a diesel engine system". Int. J. of Hydrogen Energy, Vol. 33, No. 6, 2008.
5-Mihaylov, M. and Barzev, K., "Investigation of the effect of hydrogen addition on performance and exhaust emission of a diesel engine". FISITA World Automotive Congress, 23-27 May, Barcelona, Spain, 2004.
6-Haroun A. K. Shahad and Samir M. Abdul Haleem, (2009), "Experimental investigation of using hydrogen blending to improve performance and to reduce pollutants emission of a spark ignitions engine". Nuclear and renewable Energy Resources Conference With International Participation. 28-29 Sept., Ankara, Turkey.
7- Saravasnan N. and Nagarajan G., "An experimental investigation on DI diesel engine with hydrogen fuel". Renewable Energy Journal, Vol. 33, No. 2, 2008, 415-421.

JJMIE

Volume 5, Number1, February 2011
ISSN 1995-6665
Pages 77 - 82

Jordan Journal of Mechanical and Industrial Engineering

Control of Soot Emission from Diesel Engines

Raed Al-HASANAT[a]*, Moh'd QAWASMI[b],

[a] Ministry of Education and Higher Education, Hebron, Palestine
[b] Department of Mechanical Engineering, Palestinian Polytechnic University, Hebron, Palestine

Abstract

Soot emission is a problem in major cities in the world. The number of diesel cars raised a lot in last years in Palestine, were 57,3% of the new cars in 2010 were equipped with diesel engines. This evolution was motivated by diesel engine excellent fuel economy and durability. This paper discusses soot combustion fundamental processes in term of the in-cylinder combustion and emission. The new research requested both simulation and experimental researches to study fundamental process involved in diesel engines in order to decrease the soot emissions of diesel engines and to contribute to the global emission reduction.

This project of soot modeling is developed to integrate to the conception cycle the ability of predicting the soot particle concentration from combustion in diesel engines. The goal is to develop a model that can be applied during the concept phase of the engines; this model has for vocation to predict the soot concentration during the combustion cycle.

Keywords**:** harm emission reduction, soot combustion proces, diesel engines.

1. Introduction

Diesel is also responsible of emission, in particulate diesel particulate matter which includes soot particulates. These very fine particulates are considered as responsible for damaging health effects as cardiac, pulmonary and cancer effects. The effect of the particulates was also underlined; soot warms arctic in two primary ways.' When it is in the atmosphere, soot absorbs incoming solar radiation and warms the atmosphere while possibly decreasing cloudiness. On the ground, it blackens snow and ice, making it less reflective so that absorbs more warning radiation'[2]. In order to regulate the soot emissions different norms were created including soot, the Euro norms shown in table (1).

Soot particles are commonly believed to be formed by coagulation of PAH species, the resulting small particles essentially grow by heterogeneous surface reactions with acetylene being the most important growth species. These reactions are commonly modeled by the reaction mechanism. The combustion of soot particles occurs mainly by heterogeneous reactions with OH radicals and molecular oxygen [3-5].

In the present study numerical simulation of soot particles formation in diesel cylinder are presented, the kinetic model used to describe physical chemistry interactions, the formation and combustion of soot particles is described by detailed kinetically based soot model, In order to develop this model, all the formation and oxidation steps shown in fig(1) have to be described in the model from the gas phase to the solid interactions:

-The gas phase

-The formation of the first particles from the gas phase by collision of two pyrenes (molecules with four aromatic rings), this step is called nucleation or inception

-The condensation of the PAHs on the surface of the first particles

-The coagulation which accounts for the collisions of the particles between them to form bigger ones

-The surface growth and oxidation based on the Hydrogen Abstraction Carbon Addition mechanism [1,7].

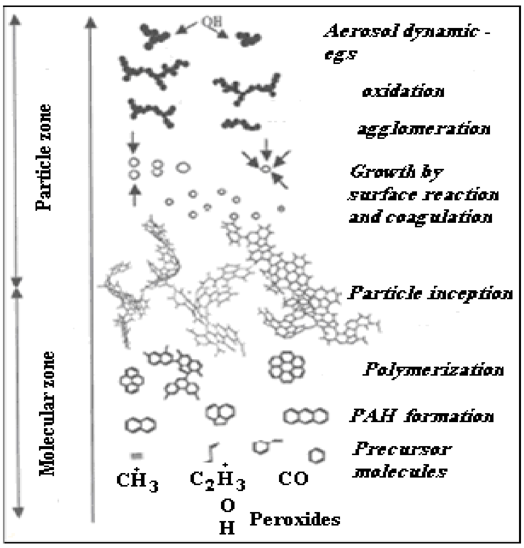

Fig(1) soot formation steps

*Corresponding author.*rhasanat@hotmail.com*

Norms	Years	Exhaust emission standard, g/kW.h			
		NO_X	Smoke	Solid particles	CO
EURO-3	**2000**	**5,0**	**0,8**	**0,100**	**2,1**
EURO-4	**2005**	**3,5**	**0,5**	**0,02**	**1,5**
EURO-5	**2008**	**2,0**	**0,5**	**0,02**	**1,5**
EURO-6	**2013**	**0,13**	**-**	**0,01**	**1,5**

Table(1) exhaust emission norms for diesel heavy-duty, automobiles and buses

In the present study of soot particles formation in diesel cylinder are presented the chemical kinetics used to describe physical chemistry interactions, the formation and combustion of soot particles described kinetically, different assumptions for soot particles concentration are applied and the results are discussed in a comparison with experimental data provided.

2-Mathimatical Model Of Soot Formation

A predictive model of soot formation in flames is being developed by using elementary reaction to describe the basic flame chemistry, soot particles growth and combustion in the case of application fuel additives. Sectional equations for soot formation, growth and oxidation are expressed in a form suitable for concurrent soot modeling [4,7].

By using additives, which contain Ba, K, Ca and other metals, and by conserved general model construction, provided only summary about metal's character. The primary carbonyl fraction with appearance particular soot $\dot{C}$, growing and burning their surface, considered in the following form:

$C_XH_Y \rightarrow C_3H_6+C_2H_6+C_2H_4+CH_4+H_2$ (1)

$C_3H_6 \rightarrow C_2H_4+CH_4+H_2$ (2)

$C_2H_6 \rightarrow C_2H_4+H_2$ (3)

$CH_4 \rightarrow C_2H_4+H_2$ (4)

$C_2H_4 \rightarrow C_2H_2+H_2$ (5)

$C_5H_5Me(CO)_3+C_5H_5 \rightarrow (C_5H_5)_2Me+CO_3$ (5a)

$(C_5H_5)_2Me+C \rightarrow Me+C_5H_5$ (5b)

$C_2H_2 \rightarrow C_2\dot{H}+\dot{H}$ (6)

$C_2+C_2H_2 \rightarrow C_{m+2} \rightarrow (nC)_{sur.}+H_2$ (7)

$(nC)_{sur.}+C_4H_2 \rightarrow (C_{n+4})_{sur.}+H_2$ (8)

$(nC)_{sur.}+C_2H_2 \rightarrow (C_{n+2})_{sur.}+H_2$ (9)

$C+O_2 \xrightarrow{\underline{Me}} CO_2$ (10)

$C+O_2 \xrightarrow{\underline{Me}} CO$ (11)

$C+CO_2 \xrightarrow{\underline{Me}} CO$ (12)

$C+H_2O \xrightarrow{\underline{Me}} CO+H_2$ (13)

$H_2+O_2 \rightarrow H_2O$ (14)

$Me+ CO \rightarrow MeO+ C$ (14a)

In presented system, equation(1) describes the primary fraction of fuel to individual hydrocarbons, equations(2-5) describe high-temperature of fraction individual hydrocarbons to acetylene C_2H_2, equation(5a) illustrates isolate carbonyl groups then joining radicals, equation (5b)shows isolation metal by carbon, equation(6) describes the decomposition of acetylene with generation embryonic charged soot particles, equation(7) process carbonation and appearance physical embryonic acetylene, equations(8-9) self-accelerated growth the surface of soot particles, equation (10-14)show burning of soot particles, equation(14a) restores metal oxide by oxides of carbon[3,6,7].

Provided system kinetic equations in the form of differential equations to describe in-cylinder processes, Computer simulation gives possibility to solve the equations with high accuracy to define the instantaneous rational amount of soot $\bar{N}$ relative to crank angle position (φ^o), presented simulation describes in-cylinder processes soot generation and the combustion in diesel engine.

A part study described by the model was performed for C_2H_2-soot which correctly predicted experimental soot mass concentration, the study included cases in which only C_2H_2 added to the soot.

Mathematical model (Index 2) considers the change of soot particles concentration with crank angle position in degrees (φ^o) and so when exhaust valve opens estimated the quantity of soot particles with exhaust gases[3,7].

3. Results

The high-quality of computing results indicated in comparison with experimental data. In fig(3) presented experimental and computing rational amount of soot formation in diesel cylinder as a function of crank angle position in degrees (φ^o). Graphics show good agreement for soot particles concentration in diesel cylinder, so it confirm our assumption of chemical kinetics[3,6].

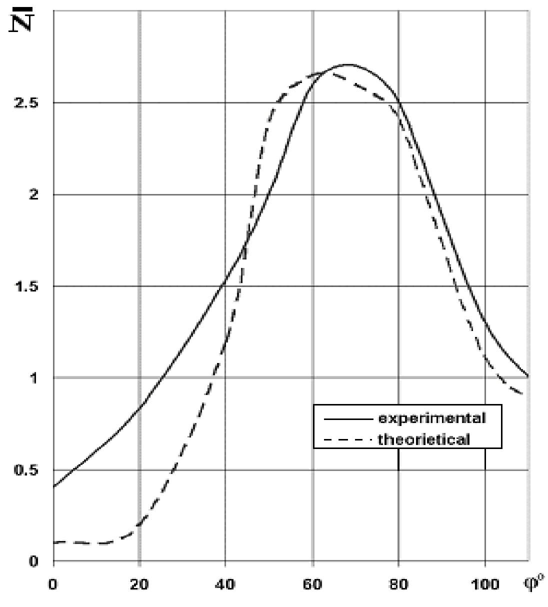

Fig(3) Soot emission with exhaust gases (rational amount of soot). Pe=3bar

In fig (2) presented experimental results of soot concentration (rational amount of soot) in diesel cylinder as a function of φ^o. An 8-cylinder diesel engine study of water-in-diesel emulsion was conducted to investigate the effect of water emulsification on soot emission with exhaust gases. Emulsified diesel fuel 17% water/diesel ratio by volume, were used direct injection diesel engine, operating at 1700 rpm and molti-loads (Pe=1,21…4,85). Graphics indicate that the addition of water in the form of emulsion decreases soot emission with exhaust gases to 20% [7,8,10].

In the result of dripping emulsified fuel increases mixture quality. Decreasing temperature on account of water Dissociation and sharply decelerate chemical reactions of soot formation. The system saturates with hydrogen's radicals which assist to suppress formation of chains at the stage of sootier radical formation so the burning speed of soot particles increases on account of increasing of carbon gasification[8,10].

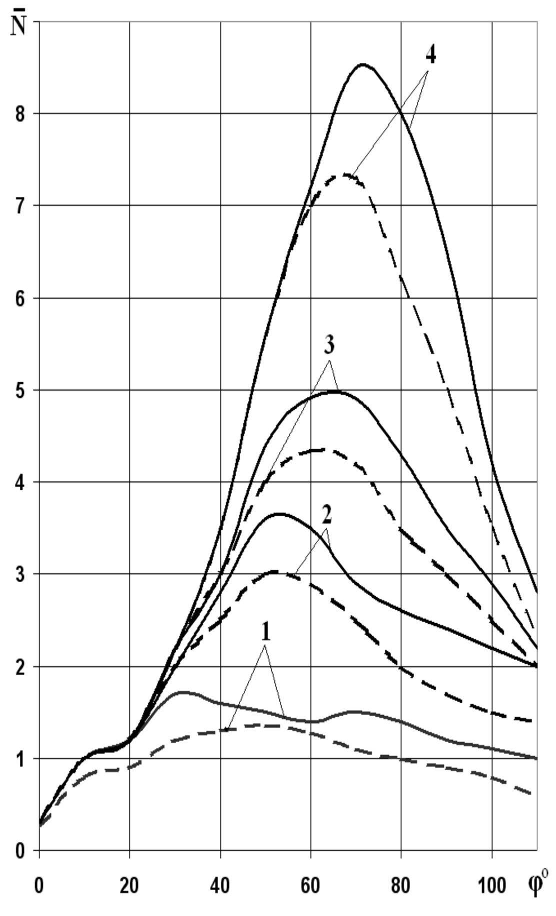

Fig(2) the effect of water emulsification on soot emission with exhaust gases(rational amount of soot). 1-Pe=1,21bar 2-Pe=2,42 bar 3-Pe=3,64 bar 4-Pe=4,85 bar, ___diesel fuel, ---- Emulsified diesel fuel, 1700rpm

The results of numerical simulation show soot particles concentration (rational amount of soot) in diesel cylinder as a function of crank angle positioning in degrees (φ^o). In fig(4) presented computing results of soot formation in diesel cylinder. A single cylinder diesel engine study of metallo-organic compound fuel additives for diesel was conducted to investigate the effect of antismoking additives on soot emission with exhaust gases. Modified diesel fuel 0,5% additive/diesel ratio by mass, were used direct injection diesel engine, operating at multi-loads (Pe=2bar, Pe=5bar, and Pe=7bar) and 1300 rpm Graphics indicate that the addition of antismoking additives (SLD) decreases soot emission with exhaust gases to 40% [7].

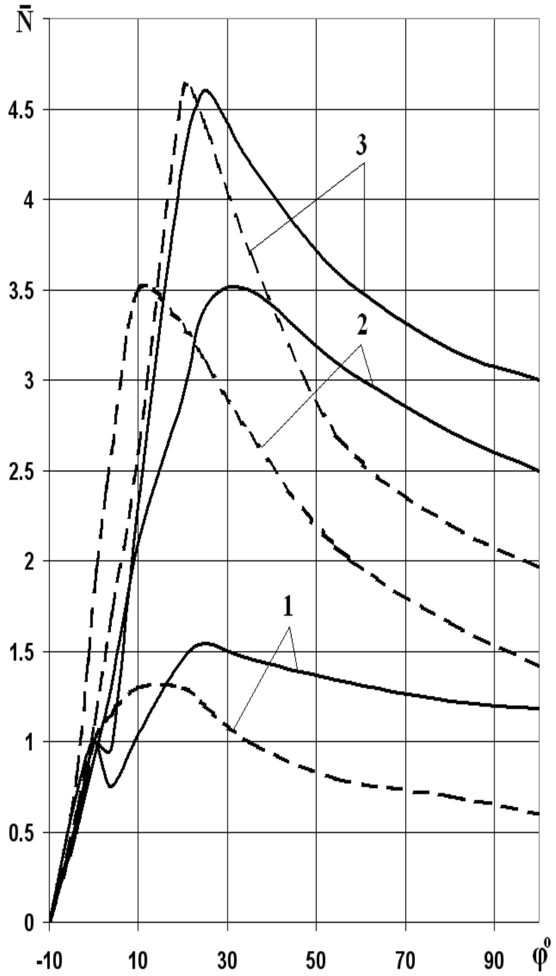

Fig (4) the effect of antismoking additives on soot emission with exhaust gases(rational amount of soot). 1-Pe=2bar 2-Pe=5 bar 3-Pe=7 bar, ____diesel fuel, ---- modified diesel fuel, 1300rpm

The soot particles reducing effects of many additives are well-known, but little is understood about the details of soot particles suppression mechanism, a laminar diffusion flame burning was seeded with a metallo-organic additive, by evaporating the additive from a crucible placed in the heated fuel gas flow, found that additives suppress the formation of PAH and accelerate the burning process[7,8,10].

4. Conclusions

The test for computer matrix simulations was developed, and parametric test results were obtained by using standard fuel and fuel with metallo-organic compound fuel additives. Simulation results indicate the following:

- Antismoking additives is effective in reducing soot.
- In period of time, metallo-organic compound fuel additives suppress the formation of PAH, but in period diffusion flame accelerate burning process, this reduce PM in exhaust gases at least 40%.
- Achieved a fundamental understanding of the formation and description in diesel particulate matters.

The presented work confirmed effective of modifications on processes of soot formation in diesel cylinder, and permit to make conclusion about mechanism their effect on the actual processes of soot formation in diesel engine, and by using dripping emulsified fuel, decreased harm emission with exhaust gases in atmosphere. A mechanism for the catalysis is proposed. We hope that this paper stimulates interest in pursuing further solutions of environmental problems.

REFERENCES:

1. H. Bockorn, "Soot Formation in Combustion", Springer Series in Chemical Physics, Vol.59, Springer, Berlin, 1994.
2. Koch D., J. Hansen, "Distant origins of Arctic black carbon", A Goddard Institute for Space Studies Model Experiment. J. Geophys. Res., 110, D04204, doi:10.1029/2004JD005296, 2005.
3. Novosolov A.L., “Application of Antismoking Additives in Diesel Fuel”, Engine's Structure11, 10-11, Russia, 1980.
4. Pisch H., Riesmier E., Peter N., Unsteady Flamlete Modeling of Soot particles Formation in Turbulent Diffusion flames, works of Heidelberg University, Germany, 2002.
5. Agafonov G.L. Nulmeier M., Detailed Kinetic Modeling of PAH Growth and Soot particles Formation in Shock Tube Pyrolysis of Benzene and Ethylene, works of Heidelberg University, Germany, 2004.
6. Mateevsky D.D. Antonov P.A., “Effects of antismoking additives actual performance and the smoking of diesel engine”, Works of Altai State Technical University, Barnaul, 1972.
7. Raed A.F. Hasanat, Experimental Computing Research in the Effect of Metal-containing Antismoking Additives on the Actual Performance and Soot particles Emission with Exhaust Gases of Diesel Engine, Ph.D. thesis, Russia, 2001.
8. http://solid.phy.ethz.ch/ K. Siegman. B. Xue, Laboratory for Combustion Aerosol and Suspended Particles, China, 1996.
9. Ministry Of Transport// delivered post No.908/2010.
10. Baturin S.A. Makarov B.B., “Physic-chemical Mechanism and Methods of Calculating Amount of Soot particles in Diesel engine”, Works of SNUTA19, 82-93, Russia, 1976.

Index (1): List of Symbols:

Sur.	surface
F	Specific surface of soot particles, M^2/kg
n	Engine angular speed, min^{-1}
$N_{comb.}$	Soot particles combustion
$N_{form.}$	Soot particles formation
φ^{o}	Crank angle position
α	Theoretical air fuel ratio
α_{comb}	Actual air fuel ratio
σ	Equivalence ratio
X	Specific heat generation (Combustion efficiency)
N_n	Initial value of soot particles concentration in diesel cylinder at firing instant
R_5	Reaction speed of soot particles growth
P	Pressure of gases in diesel cylinder
r_5	Acetylene volumetric concentration
G_{air}	Cyclic entered air for 1kg fuel, m^3
G_D	Soot particles concentration with exhaust gases kg/m^3
Me	Metal
M	Metal molecule
PM	Particulate Matter
$\dot{C}$	Particular Soot
$\bar{N}$	Rational amount of soot particles
1H13/14	One Cylinder KAMAZ Engine, Cylinder Diameter 13cm, Length of Stroke 14 cm.
SLD	Antismoking Additive, which contains Barium.
rpm	Revolution per minute
Pe	Effective Pressure
TDC	Top Dead Center

Index (2): mathematical model of soot formation

1- $\frac{d\Gamma}{d\varphi}C_{14}H_{30} = \left(-K_{+1}\Gamma_{C14H30} + K_{-1}C_{\Sigma}^{5.5}\cdot\Gamma_{C_3H_6}^{2}\cdot\Gamma_{CH_4}\cdot\Gamma_{C_2H_4}^{3.5}\right)/6n,$

2- $\frac{d\Gamma}{d\varphi}C_3H_6 = \left(\left(-K_{+2}\Gamma_{C_3H_6} + K_{-2}C_{\Sigma}\cdot\Gamma_{C_2H_4}\cdot\Gamma^{0,5}_{C_2H_4}\cdot\Gamma^{0,5}_{H_2}\right) - 2\frac{d\Gamma}{d\varphi}C_{14}H_{30}\right)/6n,$

3- $\frac{d\Gamma}{d\varphi}CH_4 = \left(\left(-K_{+3}\Gamma_{CH_4} + K_{-3}C_{\Sigma}^{0,5}\cdot\Gamma_{C_2H_4}\cdot\Gamma_{H_2}\right) - \frac{d\Gamma}{d\varphi}C_{14}H_{30}\right)/6n,$

4- $\frac{d\Gamma}{d\varphi}C_2H_4 = \left(\left(-K_{+4}\Gamma_{C_2H_4} + K_{-4}C_{\Sigma}\cdot\Gamma_{C_2H_2}\cdot\Gamma_{H_2}\right) - 6\frac{d\Gamma}{d\varphi}C_{14}H_{30} - \frac{d\Gamma}{d\varphi}C_3H_6 - 0,5\frac{d\Gamma}{d\varphi}CH_4\right)/6n,$

5- $\frac{d\Gamma}{d\varphi}H = \left(\begin{array}{l}\left(K_{+5}C_{\Sigma}\Gamma_{H_2}\Gamma_M - K_{-5}C_{\Sigma}^2\Gamma_H^2\Gamma_M^2\right) + 7\frac{d\Gamma}{d\varphi}C_{14}H_{30} + \\ +1,5\frac{d\Gamma}{d\varphi}C_3H_6 + 0,5\frac{d\Gamma}{d\varphi}CH_4 + \frac{d\Gamma}{d\varphi}C_2H_4 + \frac{o\Gamma}{d\varphi}C_2H_2\end{array}\right)/6n,$

6- $\frac{d\Gamma}{d\varphi}C_2H_2 = \left(\begin{array}{l}\left(-K_{+6}C_{\Sigma}\Gamma_{H_2}\Gamma_{C_2H_2} + K_{-6}C_{\Sigma}\Gamma_{H_2}\Gamma_{\dot{C}_2H}\right) - 7\frac{d\Gamma}{d\varphi}C_{14}H_{30} - \\ -1,5\frac{d\Gamma}{d\varphi}C_3H_6 + 0,5\frac{d\Gamma}{d\varphi}CH_4 + \frac{d\Gamma}{d\varphi}C_2H_4\end{array}\right)/6n,$

7- $\frac{d\Gamma}{d\varphi}H_2 = D'\left(K_{+7}\Gamma_{C_2H_2} + 0,5K_{+8}\Gamma_{\dot{C}_2H}\right)/6n,$

8- $D' = \frac{\left(10^{-3}P_{\Sigma}\Sigma_{\mu_i}\Gamma_i\cdot N\cdot \mathrm{F}\cdot 10^4\right)}{\left(12\cdot 1,003\cdot G\cdot(\sigma - x)(\alpha_{\text{com.}}+1)\right)},$

$\Gamma_{\dot{C}_2H} = \left(1 - \sum_{i=1}^{8}\Gamma_i\right),$

9- $\frac{dN}{d\varphi} = \frac{10^4 P_{\Sigma}\cdot N''\cdot \mathrm{F}}{1,033\cdot 6n}\cdot\left(K_{+7}\Gamma_{C_2H_2} + 0,5K_{+8}\Gamma_{\dot{C}_2H}\right),$

10- $\frac{dN}{d\varphi} = \frac{10^4 P_{\Sigma}\alpha_{Д}\cdot N''\cdot S_{уд.}}{6nRT(1+N_3)(1+N_1+N_2)}\left(\begin{array}{l}\Gamma_{O_2}\left(N_1''(1+2N_3)+2N_2(1+N_3)\right)+ \\ +\Gamma_{CO_2}N_3(1+N''+N_2)+\Gamma_{H_2O}N_4\cdot \\ \cdot(1+0,5N_1+N_3)\end{array}\right),$

11- $\frac{dN}{d\varphi} = \frac{d\Gamma_i}{d\varphi}\cdot\frac{i}{x} + \Gamma_i\frac{1}{\sigma+x}\cdot\frac{d\sigma}{d\varphi} - \Gamma_i\frac{1}{\sigma-x}\cdot\frac{dx}{d\varphi},$

JJMIE

Volume 5, Number 1, February 2011
ISSN 1995-6665
Pages 83 - 88

Jordan Journal of Mechanical and Industrial Engineering

Aero/hydrodynamic Study of Speedo LZR, TYR Sayonara and Blueseventy Pointzero3 Swimsuits

Hazim Moria*, Harun Chowdhury, Firoz Alam and Aleksandar Subic

Department School of Aerospace, Mechanical and Manufacturing Engineering, RMIT University, Melbourne, Australia

Abstract

Aero/hydrodynamics plays a critical role in swimming. Studies estimate that over 90% of the swimmer's power output is spent overcoming aero/hydrodynamic resistance. Recently, swimsuits have been aggressively marketed, principally as a means for reducing the skin friction component of the total drag, thereby conferring a competitive advantage over other swimmers. Some manufacturers have claimed significant reduction of drag, but it is difficult to find independent research in the open literature that supports these claims and counter claims. In fact, it is not at all clear that swimsuits in reality reduce skin friction or other forms of drag. At present, there is no standard methodology for the evaluation of swimsuits performance. The primary purpose of this work is to conduct a comparative study of three competitive commercially manufactured swimsuits.

Keywords: Aero/Hydrodynamics, Swimsuit, Speedo, TYR, Blueseventy, Drag, Wind Tunnel, Experimental Measurement.

1. Introduction

Swimming is one of the major athletic sports and became one of the top 10 new sports technologies that changed the 2008 Olympics in Beijing. The competitive swimming game event consists of different distances from 50m to 1500m. These distance events required excessive energy and speed to achieve best recorded within short wining time margins. Studies estimate that over 90% of the swimmer's power output is spent overcoming hydrodynamic resistances [1-10]. These resistive forces were essentially behind the generation of drag during swimming. Reduced hydrodynamic resistance can significantly improve overall swimming performance [11]. The total hydrodynamic resistance can be divided approximately into three, almost independent components: wave drag, form drag, and skin friction drag. The wave drag is associated with the work required to generate waves, form drag is the resistance to motion due to the shape of the body, and skin friction is the resistance to motion due to the area of the body with the water (the wetted area) [1]. The form drag is believed to be constituted almost 90% of the total drag [2]. All three components are velocity-dependent as the swimmer completes the stroke, and all three components depend on the speed of the swimmer, as well as his/her shape, length, and style.

Modern swimsuits have travelled a long path and gone through a series of changes of styles and designs over the decades [1]. More recently, several commercial swimsuit manufacturers have claimed and counterclaimed about their swimsuits performance by reducing hydrodynamic resistance forces and enhancing buoyancy. Since the Beijing Olympic Games 2008, almost all major manufacturers introduced full-body swimsuits made of semi- and- full polyurethane combined with Lycra fabrics. Most publicized swimsuits of these categories are Speedo®, TYR®, Blueseventy®, Arena®, Diana®, and Jaked®. In Beijing Olympic, out of 32 events, 21 had world records broken and 66 Olympic records were broken. The manufacturers claimed these suits have features such as ultra-light weight, water repellence, muscles oscillation and skin vibration reduction by compressing the body. Strangwood et al., [12], Chowdhury et al. [13] and Moria et al. [1] revealed that technological innovation in both design and materials has played a crucial role in sport achieving its current standing in both absolute performance and its aesthetics. Currently, swimsuits have been aggressively marketed principally as a means for reducing the skin friction component of the total drag, thereby conferring a competitive advantage over other swimmers however, it is difficult to find independent research in the open literature that supports these claims and counter claims [14]. In order to understand the comprehensive hydrodynamics of swimmer, swimsuits and find answers of many contemporary questions on swimsuits, a large research project on swimsuit aero/hydrodynamics has been undertaken in the School of Aerospace, Mechanical and Manufacturing Engineering, RMIT University. As a part of this large research project, we have undertaken a comparative study of a series of commercially acclaimed swimsuits. The study was conducted experimentally using RMIT Industrial Wind Tunnel and specially developed testing methodology.

*Corresponding author. hazim.moria@student.rmit.edu.au

2. Testing Methodology

2.1 Description of Standard Cylinder and Experimental Arrangement

With a view to obtain aerodynamic properties experimentally for a range of commercially available swimsuits made of various materials composition; a 110 mm diameter cylinder was manufactured. The cylinder was made of PVC material and used some filler to make it structurally rigid. The cylinder was vertically supported on a six-components transducer (type JR-3) had a sensitivity of 0.05% over a range of 0 to 200 N as shown in Figure 1. The aerodynamic forces and their moments were measured for a range of Re numbers based on cylinder diameter and varied wind tunnel air speeds (from 10 km/h to 130 km/h with an increment of 10 km/h). Each test was conducted as a function of swimsuit's seam orientation and seam positions (see Figure 2).

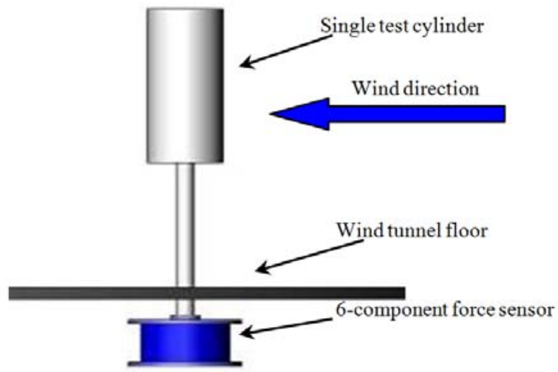

Figure 1. Schematic CAD model of bare cylinder in RMIT Industrial Wind Tunnel [1]

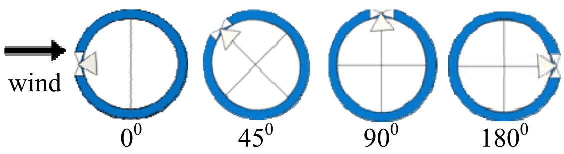

Figure 2. Seam orientation (Bird's eye view)

2.2 Experimental Facilities

As mentioned earlier, the RMIT Industrial Wind Tunnel was used to measure the aerodynamic properties of swimsuit fabrics. The tunnel is a closed return circuit wind tunnel with a turntable to simulate the cross wind effects. The maximum speed of the tunnel is approximately 150 kilometers per hour (km/h). The rectangular test section dimensions are 3 meters wide, 2 meters high and 9 meters long, and the tunnel's cross sectional area is 6 square meters. A plan view of the tunnel is shown in Figure 3. The tunnel was calibrated before and after conducting the experiments and air speeds inside the wind tunnel were measured with a modified National Physical Laboratory (NPL) ellipsoidal head Pitot-Static tube (located at the entry of the test section) which was connected through flexible tubing with the Baratron® pressure sensor made by MKS Instruments, USA. The cylinder was connected through a mounting sting with the JR3 multi-axis load cell, also commonly known as a 6 degree-of-freedom force-torque sensor made by JR3, Inc., Woodland, USA. The sensor was used to measure all three forces (drag, lift and side forces) and three moments (yaw, pitch and roll moments) at a time. Each data point was recorded for 20 seconds time average with a frequency of 20 Hz ensuring electrical interference is minimized. Multiple snaps were collected at each speed tested and the results were averaged for minimizing the further possible errors in the experimental raw data. Further details about the wind tunnel can be found in Alam et al. [15].

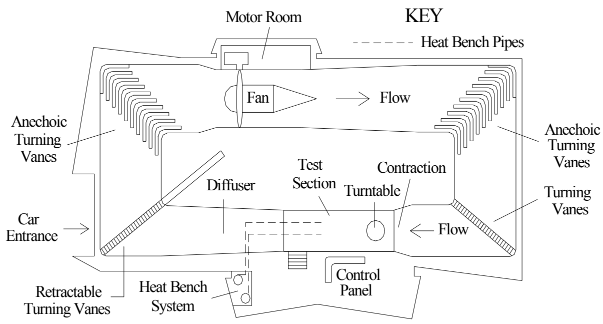

Figure 3. A plan view of RMIT Industrial Wind Tunnel [15]

The bare cylinder was tested initially in order to benchmark the aerodynamic performance as shown in Figure 4. Then the cylinder was wrapped with different swimsuit fabrics to measure their aerodynamic forces and moments. The end effects of the bare cylinder were also considered [13].

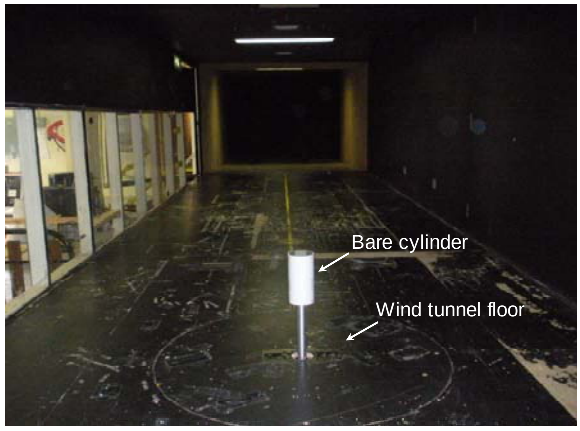

Figure 4. Experimental bare cylinder set up in RMIT Industrial Wind Tunnel

2.3 Description of Swimsuit Fabrics

Three brand new of full-body swimsuit materials have been selected for this study as they were officially used in various competitive events in the World and Olympic Games. These swimsuits are: a) Speedo® LZR, b) TYR® Sayonara and Blueseventy® Pointzero3 (see Figure 5). The Speedo® LZR swimsuit is composed of 70% Nylon (Polyamide) and 30% Elastane (Lycra) and the polyurethane panel was superimposed over some parts on the Speedo® swimsuit while the seam is made by flash joining the two edges using an under layer material (e.g. applying so called ultrasonic weld). The width of the seam is approximately 18 mm. On the other hand, the TYR®

Sayonara swimsuit is made of 55.5% PU-Chloroprene, 40.5% Nylon and 4% Titanium Alloy; and the Blueseventy® Pointzero3 is made of 75% Nylon and 25% PU-CR. The seams of TYR® Sayonara and Blueseventy® Pointzero3 swimsuits are made using four-way flat lock method. The seam has 18 stitches per inch (25.4 mm) length. The width of the seam is approximately 6 mm.

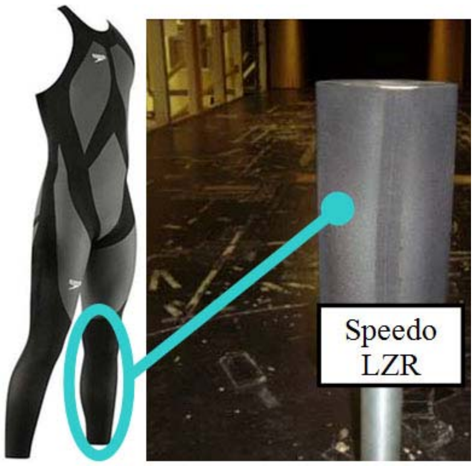

a) Speedo® Swimsuit's Seam

b) TYR® Swimsuit's Seam

c) Blueseventy® Swimsuit's seam

Figure 5. Speedo® LZR, TYR® Sayonara and Blueseventy® Pointzero3 swimsuits used in this study

3. Results and Discussion

In this paper, only drag force data and its dimensionless quantity drag coefficient (C_D) are presented. The C_D was calculated by using the following formula:

$$C_D = \frac{D}{\frac{1}{2}\rho V^2 A} \quad (1)$$

Where, D, V, ρ and A are the drag, wind speed, air density and cylinder's projected frontal area respectively.

Also another dimensionless quantity the Reynolds number (Re) is defined as:

$$\mathrm{Re} = \rho V d / \mu \quad (2)$$

Where, d and μ are the diameter of the cylinder and absolute air viscosity respectively.

The drag (D) versus wind speeds and the C_D as a function of Re for a range of seam positions for the tested swimsuits are presented in Figures 6 to 12. In order to compare the results of swimsuits materials, the drag force and dimensionless parameter C_D of the bare cylinder were also shown in all figures. The drag forces and the C_D values for the Speedo® LZR swimsuit with four seam orientations (0°, 45°, 90° and 180°) are shown in Figures 6 and 7. Figure 6 shows that the drag for the bare cylinder is continuously increasing without any abrupt changes as expected. However, a sudden drop in drag forces in between 90 and 110 km/h speeds is evident for the Speedo® LZR suit at all seam angles.

The C_D variation with Re (shown in Figure 7) clearly indicates that the Speedo® LZR material has undergone a rapid drag crisis (transition effect from viscous or frictional drag to pressure or form drag at speed range of 90 and 110 km/h) for all seam positions except the seam position at 45°. The transitional effect starts much earlier at 70 km/h compared to 90 km/h for other seam positions. The seam position at 45° enhances the favorable pressure gradient more and delays the separation by increasing the turbulent boundary layer compared to other seam positions. In general, the rougher surface of swimsuits extends the turbulent boundary layer by reducing the length of laminar boundary layer and ultimately delays the flow separation in comparison with the smooth surface of bare cylinder. As expected, there is no noted difference in drag or C_D for the seam positions of 0° and 180° at all speeds tested (Re). Nevertheless, minor variations in drag and C_D were noted for the seam angle at 90° compared to other seam positions. The 90° seam position is not favorable for the drag reduction as it triggers the earlier flow separation compared to no seam at 0° situations.

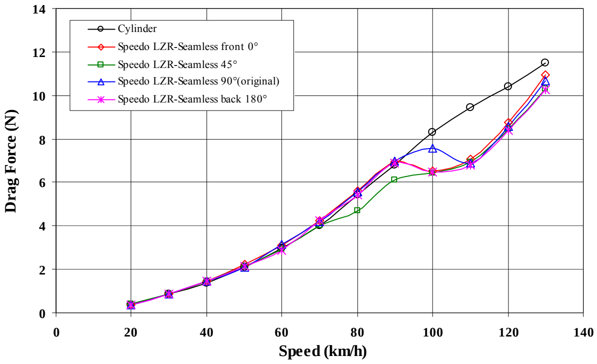

Figure 6. Drag variation with speeds of Speedo® LZR suit

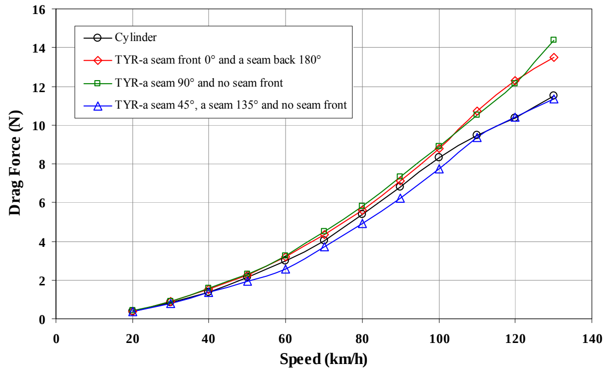

Figure 8. Drag variation with speeds of TYR® Sayonara suit

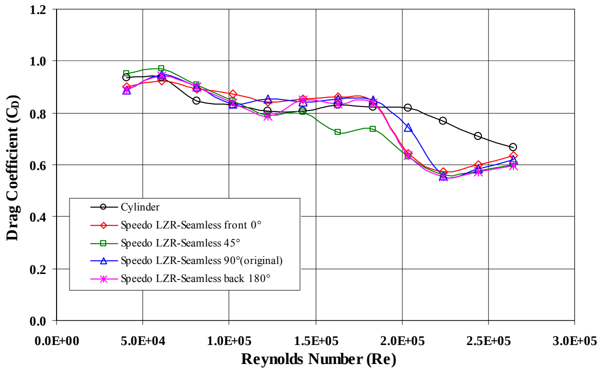

Figure 7. C_D variation with Re of Speedo® LZR suit

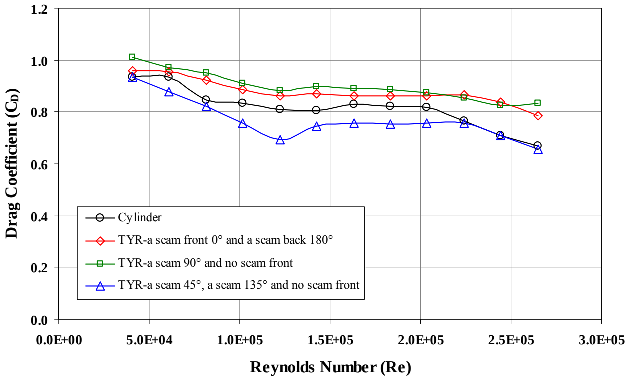

Figure 9. C_D variation with Re of TYR® Sayonara suit

The drag and the C_D values for the TYR® Sayonara swimsuit are shown in Figures 8 and 9. There is no clearly noted transitional effect on the drag and drag coefficient (C_D) except the seam position of 45°. The seam position TYR® Sayonara swimsuit at all other angles tested has the higher drag and C_D values compared to the bare cylinder (see Figures 8 and 9). A close inspection has revealed that the surface of the material is very smooth compared to Speedo® LZR swimsuit. The relatively smooth surface does not assist the flow to have transitional effect.

A very similar effect was also noted for the Blueseventy® Pointzero3 swimsuit (see Figures 9 and 10) in comparison with the TYR® Sayonara swimsuit. However, due to the complexity of seam position on the suit, the seams were positioned on the test cylinder simultaneously at 45° and 90°; and at ±45°. The average drag and C_D values at these seam positions are around 13% less compared other seam positions (±90°, 0° and 180°). A close inspection has also revealed that both TYR® Sayonara and Blueseventy® Pointzero3 swimsuits are made of several layers, thicknesses of which are 0.3 mm and 0.5 mm respectively. The Speedo® LZR is made of single layer and the thickness is less than TYR® Sayonara and Blueseventy® Pointzero3 as mentioned above.

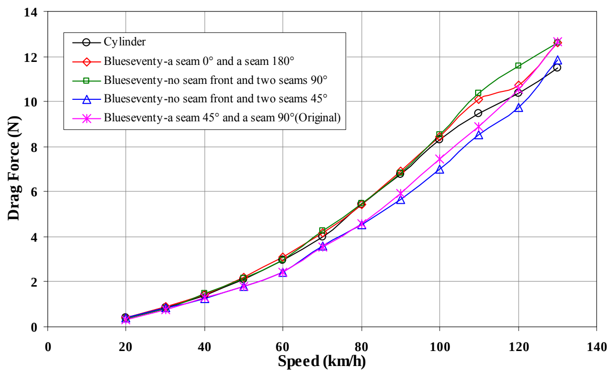

Figure 10. Drag variation with speeds of Blueseventy® Pointzero3 suit

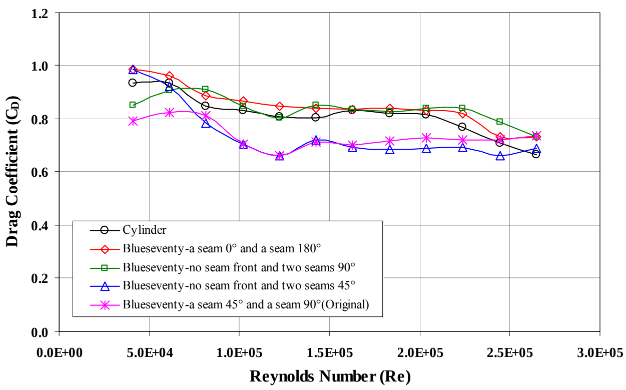

Figure 11. C_D variation with Re of Blueseventy® Pointzero3 suit

A comparison of C_D values for the Speedo® LZR, TYR® Sayonara and Blueseventy® Pointzero3 swimsuits for the seam position of 45° is shown in Figure 12. It is clearly evident that the seam of the Speedo® LZR swimsuit has the lowest value of the drag coefficient after transition to two other swimsuits' seam positions (TYR® Sayonara and Blueseventy® Pointzero3). Although the two other suits have earlier transition, they have relatively higher C_D values at high speeds. These suits have relative advantages at lower speeds compared to Speedo® LZR. The Blueseventy® Pointzero3 swimsuit possesses lower C_D values compared to the TYR® Sayonara swimsuit as these suits do not have much effect on flow transition.

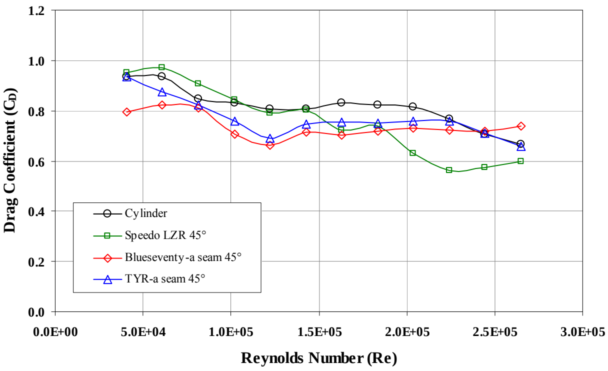

Figure 12. Comparison of C_D variation with Re of Speedo® LZR, TYR® Sayonara and Blueseventy® Pointzero3 swimsuits

4. Conclusions

The following concluding remarks have been made based on the experimental study presented here:

The surface structure (surface roughness, seam and its orientation) of the swimsuit has significant effect on the aero/hydrodynamic drag.

The seam orientation at 45° has the potential to reduce the drag up to 15% depending seam geometry.

The TYR® Sayonara and Blueseventy® Pointzero3 swimsuits have relative advantages due to lower C_D values at speeds below 80 km/h wind speed or equivalent speeds in water.

The Speedo® LZR has relative advantage at speeds over 80 km/h wind speed or equivalent speeds in water compared to other two suits as it has significantly lower C_D values at high speeds.

Acknowledgments

We express our sincere gratitude to Government of Kingdom of Saudi Arabia for providing the PhD Scholarships to the first author. The authors would express their sincere thanks to Mr. Patrick Wilkins and Mr. Gilbert Atkins, the school of Aerospace, Mechanical and Manufacturing Engineering, RMIT University for their assistance in experimental set up.

References

[1] Moria, H., Chowdhury, H., Alam, F., Subic, A., Smits, A. J., Jassim, R., and Bajaba, N. S., "Contribution of Swimsuits to Swimmer's Performance", Procedia Engineering, Vol 2, No. 2, 2010 , 2505-2510.

[2] Vorontsov, A. R. and Rumyantsev, V. A., Resistive Forces in Swimming & Propulsive Forces in Swimming in Biomechanics in Sport edited by Zatsiorsky, V., 2000, 184-231, ISBN 0-632-05392-5, Blackwell, UK.

[3] Toussaint, H., The FastSkin body suit: Hip, hype, but does it reduce drag during front crawl swimming?, XXth International Symposium on Biomechanics in Sports Swimming, Caceres, Spain, University of Extramedura, 15-24, 2002.

[4] Toussaint, H. M., de Groot, G., Savelberg, H. H. C. M., Active Drag related to velocity in male and female swimmers, Journal of Biomechanics, Vol. 21, 1988, 435-438.

[5] Naemi R., Eassonb, W. J. and Sanders, R. H., Hydrodynamic glide efficiency in swimming. Journal of Science and Medicine in Sport, available online from 18 June, 2009

[6] Shahbazi, M. M., Sabbaghian, S., Drag force to body dimensions in Butterfly swimming, Proceedings of XXIII International Symposium of Biomechanics in Sports University of Ottawa, 2005, 225-228.

[7] Pendergast, D. R., Mollendorf, J. C., Cuviello, R. and Termin, A. C., Application of theoretical principles to swimsuit drag reduction, Sport Engineering, Vol 9, 2006, 65-76.

[8] Blümich, B., NMR Imaging of Materials, Clarendon Press, Oxford, 2006.

[9] Chan, E.C., & Lien, F-S., Permeability Effects of Turbulent Flow through a Porous Insert in a Backward-Facing-Step Channel, Transp Porous Med, Vol. 59, 2005, 47-71.

[10] Fish, F., Smits, A. J. and Bart-Smith, H., Biomimetic swimmer inspired by the manta ray, Chapter 19 in Biomimetics: Nature-Based Innovation, Ed. Y. Bar-Cohen, CRC Press/Taylor & Francis Group, 2010.

[11] Rushall, B.S., Sprigings, E.J., Holt, L. E., & Cappaert, J. M., "A Re-Evaluation of Forces in Swimming". Journal of Swimming Research, Vol. 10, 1994, 6-30.

[12] Strangwood, M., Subic, A., Modelling of materials for sports equipment. Materials in Sports Equipment, Volume 2, Woodhead Publishing Ltd., Cambridge, UK, 2007.

[13] Chowdhury, H., Alam, F., Mainwaring, D., Subic, A., Tate, M., Forster, D., Beneyto-Ferre, J., Design and Methodology for Evaluating Aerodynamic Characteristics of Sports Textiles. Sports Technology, Wiley/ Blackwell. (DOI: 10.1002/jst.92), 2009.

[14] Nakashima, M. and Sato, Y., "Optimization of arm stroke in freestyle swimming by Simulation", Engineering of Sports III, Vol 1, 2009, 207-211

[15] Alam, F., Zimmer, G., Watkins, S., "Mean and time-varying flow measurements on the surface of a family of idealized road vehicles", Experimental Thermal and Fluid Sciences, Vol 27 , No. 5, 2003, 639–654.

JJMIE
Volume 5, Number1, February 2011
ISSN 1995-6665
Pages 89 - 96
Jordan Journal of Mechanical and Industrial Engineering

Road Test Emissions Using On-board Measuring Method for Light Duty Diesel Vehicles

Jerzy Merkisz*, Jacek Pielecha and Ireneusz Pielecha

Institute of Internal Combustion Engines and Transport, Poznan University of Technology

Piotrowo 3, 60-965 Poznan, Poland

Abstract

The paper presents the results of exhaust emission tests of diesel vehicles fitted with diesel particulate filters under real road conditions. The tests were carried out in portions of about a dozen kilometers in length under city traffic conditions. The SEMTECH portable analyzer from SENSORS Inc. was used to measure the exhaust emissions. The measurements of particulates matter emission used particle counter and mass spectrometer. The above results were used for defining the vehicle emissions rate which can be used for the classification of car fleets, that differ among one another in the date of manufacture hence the exhaust emissions requirements.

Keywords: Exhaust emission, Road tests, Diesel engines, Diesel particulate filters.

1. Introduction

These days one can observe a strong trend to deal with environmental perils from the automotive industry in global terms. The regulations that allow the operation of vehicles (homologation tests and production conformity tests), periodical technical check-ups and other laws directly and indirectly related to the production, operation and management of products of civilization treat the problem of environmental protection on a full scale [1]. Over the years in each country there were different systems of tests and vehicle exhaust emission control, however, for some time there has been a well-developed unification. A growing number of cars in the world and the pollution of the environment result in higher requirements as far as the emission of exhaust components is concerned. The present level of technical and technological advancement in all the branches of industry, including all types of transport, causes increased requirements for the production of tools for emission measurement. In order for these requirements to be fulfilled to the necessary extent according to the regulations which change from time to time, it was necessary for the industry to concentrate on this issue. The studies on the emission of exhaust components are a complex process. Contemporary emission analyzers require special laboratory conditions and the homologation procedures include engine and chassis dynamometer tests which do not reflect the real on-road emissions. The latest results of studies conducted under the real conditions show that in the case of some emission components certain emissions are higher by several hundred per cent. Thus, there is a trend to legislate the measurement of the emission under real operating conditions [2].

*Corresponding author. jerzy.merkisz@put.poznan.pl

2. Testing Methods

The purpose of the research was to verify the emission characteristics of a vehicle with a diesel engine (meeting Euro 4 standard) under real traffic conditions. The research was at the same time an attempt at creating an on-board system for measuring of the exhaust emissions level. The determination of the emission characteristics in on-road conditions and comparing it with the results obtained on a test-bed in a type-approval test enabled determining of the emission factor. The emission factor obtained was used to answer the question whether the emission in on-road conditions is comparable with the emission obtained during a type-approval test. It is at the same time a verification of driving conditions in a type-approval test (developed several decades ago) and the real traffic conditions.

The measurement of the emission level was carried out in the road conditions in the city of Poznan (Fig. 1). The tests were conducted on the main roads of the city in the afternoon with a moderate traffic.

The conditions were selected in such a way as to enable a comparison of the tests results with the NEDC homologation test (Fig. 2) – with reference to which the emission level indexes were introduced. The specified route was characterized by parameters similar to the NEDC test in terms of the road length, driving time and average speed value (Table 1). The tests measured the concentration of CO, HC, NOx and then with the use of GPS and diagnostic system data the road emissions were specified.

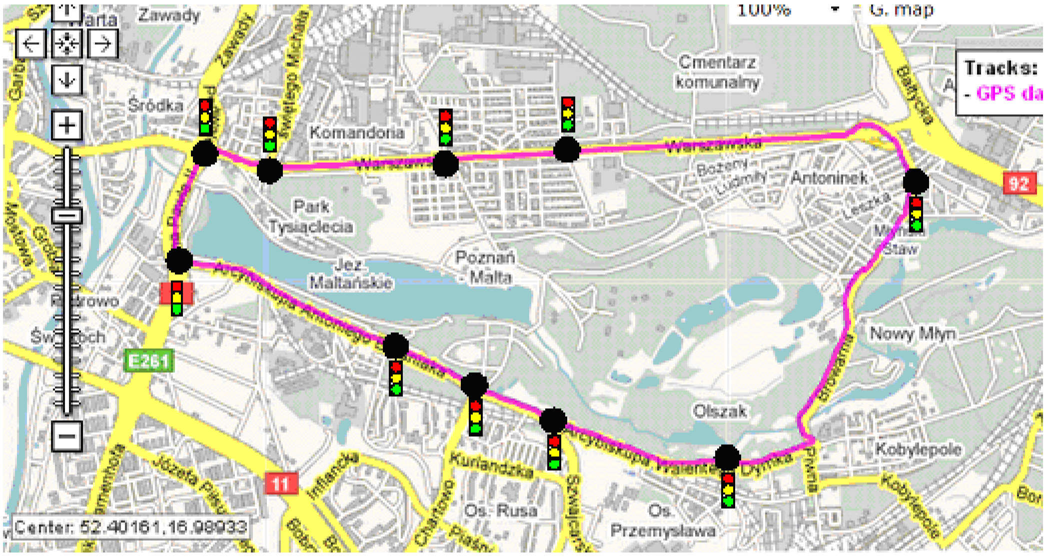

Figure 1. The route used to test the emission level of a vehicle (city of Poznan, Poland)

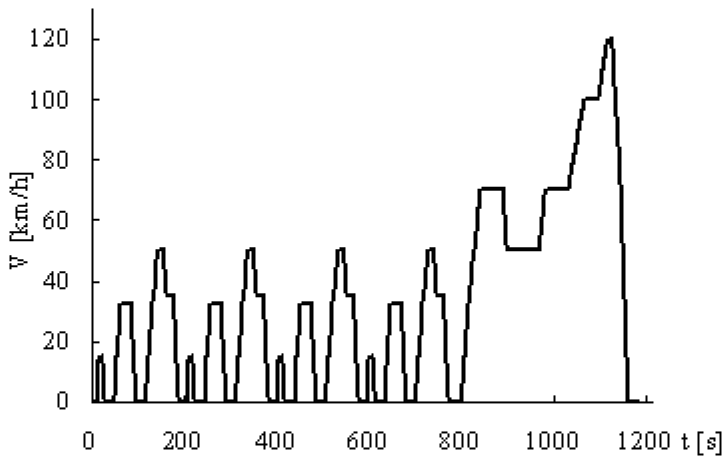

Figure 2. NEDC European homologation test for passenger vehicles [3]

Table 1. Characteristics of the test and comparison with the NEDC test

Test parameter	Diesel	NEDC
Total duration [s]	1110	1180
Max speed [km/h]	105	120
Average speed [km/h]	34.2	33.6
Length [m]	11,780	11,007

3. Experimental Set Up

Vehicle

The object of the tests was Chevrolet Captiva fitted with a 2.0 dm^3 diesel engine (European standard, Sulfur < 10 ppm); manual transmission, 4 cylinder, 110 kW@4000 rpm, torque: 320 Nm@2000 rpm, catalytic converter, diesel particulate filter, OBD II protocol CAN 2.0b, mileage: 10,000 km, vehicle weight: 1700 kg. The tested vehicle was homologated according to Euro 4 standard.

Measurement instruments

a) Portable gas analyzer – Semtech DS

In order to measure the concentration of the individual emissions a portable analyzer for emission testing – SEMTECH DS by SENSORS Inc. [4, 5] was used. The analyzer allowed the measurement of the concentration of the individual emissions with a simultaneous measurement of mass flow rate of the exhaust gases. The exhaust gas introduced to the analyzer through a probe maintaining the temperature of 191 ^{o}C was then filtered out of particle matter and directed to the flame-ionizing detector (FID) where hydrocarbons concentration was measured. Then the exhaust gas was cooled down to the temperature of 4 °C and the measurement of the concentration of NO_x (NDUV analyzer), CO, CO_2 (NDIR analyzer) and O_2 followed in the listed order. It is possible to add data acquired directly from the vehicle diagnostic system to the central unit of the analyzer and make use of the GPS signal (Table 2).

In the tests the measurements of exhaust emission were performed and, for comparison, signals such as engine speed, load, vehicle speed, engine temperature from an on-board diagnostic system were registered [6, 7]. Some of these signals served to specify the time density maps presenting the share of the operating time of a vehicle under the real operation. GPS signal was used for further visualization of the obtained data (Fig. 3 and 4).

Table 2. Characteristics of a portable exhaust analyzer SEMTECH DS

Parameter	Measurement method	Accuracy
1. Emission		
CO	NDIR, range 0–1000 ppm	±3%
HC	FID, range 0–10,000 ppm	±2%
NO_x	NDUV, range 0–2500 ppm	±3%
CO_2	NDIR, range 0–20%	±3%
O_2	Electrochemical, range 0–25%	±1%
2. Data storage capacity	Over 10 hours at 1 Hz data acquisition rate	
3. Vehicle interface capacity	SAEJ1850 (PWM), SAEJ1979 (VPW), ISO 14230 (KWP-2000), ISO 15765 (CAN), ISO 11898 (CAN) SAEJ1587, SAEJ1939 (CAN)	

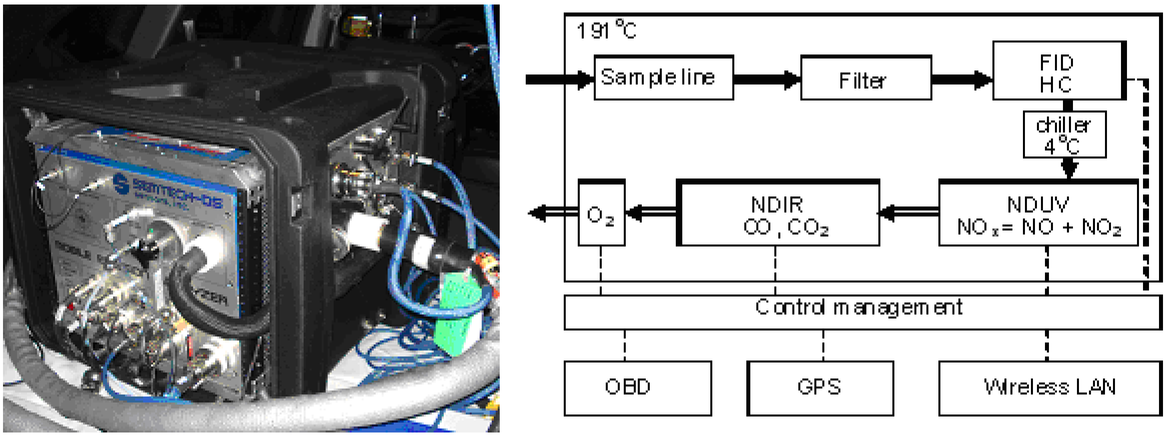

Figure 3. View and diagram of a portable analyzer; exhaust gas flow channels (==) and electrical connections circled (– –)

Figure 4. View of SEMTECH DS analyzer fitted in a vehicle

b) AVL Particle Counter 489

Condensation particle counters (CPCs) accurately measure PN concentration of the exhaust emissions. It is a fact, the GRPE Particle Measurement Program (PMP) has recently completed the light-duty, inter-laboratory correlation exercise (LD ILCE) and concluded that PN measurements using a CPC plus thermodilution are 20 times more sensitive and much less variable than the traditional method (i.e., gravimetric filter analysis). As a result, the measurement of solid PN emissions has been proposed for Euro 5 Regulation 83. Proposed ECE Regulations 83 and 49 mandate that only the number concentrations of solid particles are measured. Therefore, nucleation mode particles (i.e. nanoparticles) formed by the condensation of volatile compounds found in the engine exhaust gases must be suppressed or eliminated. As a result, the proposed regulations specify a particle sampling and measurement system shown in Fig. 5.

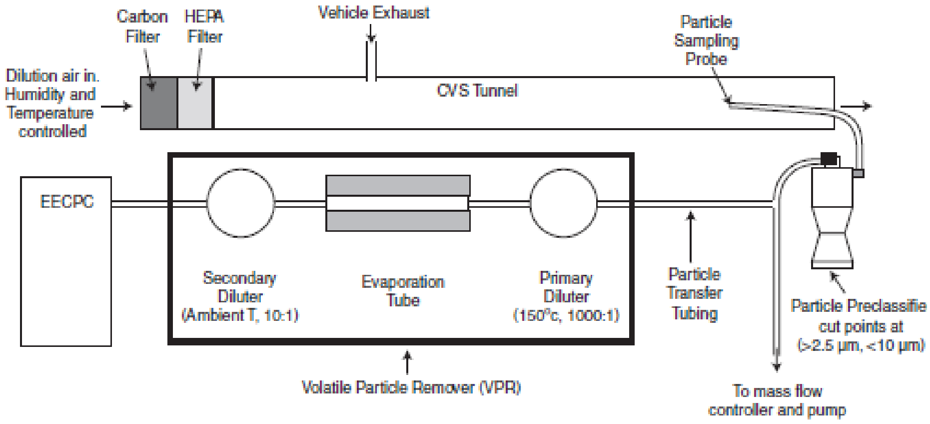

Figure 5. Proposed Regulation 83 Particle Sampling and Measurement System [8]

Exhaust gas is sampled from a CVS tunnel and diluted with HEPA filtered compressed air using the AVL Chopper Diluter. Inside the evaporation tube the diluted exhaust gas is heated to a degree that causes the volatile emission components to vaporize, leaving behind nothing other than solid particles. After that, the exhaust gas is diluted once again using a porous tube diluter and fed into the condensation particle counter (CPC). In the CPC, butanol is condensed on to the particles inside the exhaust gas to enlarge them so that they become visually detectable. The enlarged particles are then counted based on the scattered light pulses generated when the particles pass through the laser beam. This makes it possible to determine the number of particles per volume unit. The evaporation tube is a tube heated to a maximum temperature of 350 °C using heating cartridges, in which the volatile particles from the primarily diluted exhaust gas are vaporized. The secondary diluter is a porous tube diluter with a dilution ratio that is determined by the flow rates through MFC1 and MFC2. The secondary diluter is immediately followed by a stabilization chamber from which the diluted exhaust gas is sampled for the CPC. The aerosol to be measured enters the CPC by the sample inlet. Inside the heated saturator, lined with a piece of wick soaked in butanol, the butanol vaporizes and in its vapor state mixes with the aerosol. In the cooled condenser, the butanol vapor is cooled down until it becomes supersaturated and ready to condense on the aerosol particles (heterogeneous condensation). This temperature is just slightly below the temperature at which homogeneous condensation (condensation without condensation nuclei) occurs. Butanol that condenses on the condenser walls is drained off either by a water remover or it flows back to the butanol-soaked pieces of wick when the water remover is turned off. The so enlarged particles enter the counting device via a nozzle. This nozzle consists of a laser diode, a focusing lens, a collecting lens and a photodetector. The laser beam is exactly focused on the point above the nozzle. Whenever a particle enters through the nozzle, the laser light is scattered and the scattered light is caught by the collecting lens and focused on the photodetector. The entire optics is kept at a higher temperature than the saturator in order to prevent the butanol from condensing on the lenses. In order to control the volume flow through the CPC, a critical orifice is used with the difference in pressure upstream and downstream of the orifice, the absolute pressure and the pressure downstream of the nozzle being measured and monitored in order to ensure correct flow through the CPC (Fig. 6) [9].

c) Engine Exhaust Particle Sizer TM Spectrometer (TSI 3090)

A schematic of the EEPS spectrometer is shown in Figure 7. Particles enter the instrument as part of the aerosol inlet flow through a cyclone with a 1 µm cut. Next, the particles pass through an electrical diffusion charger in which ions are generated. These mix with the particles and electrically charge them to provide a predictable charge level based on particle size. The charger is mounted inline with the analyzer column and located at the top of the instrument. Particles then enter the sizing region through an annular gap, where they meet a stream of particle free sheath air. The sizing region is formed by the space between two concentric cylinders. The outer cylinder is built from a stack of sensing electrode rings that are electrically insulated from each other. The electrodes are connected to a very sensitive charge amplifier, also called an electrometer, with an input near ground potential. The inner cylinder is connected to a positive high voltage supply, which forms the high voltage electrode. This creates an electric field between the two cylinders. While the positive charged particles stream with the sheath air from the top to the bottom of the sizing region, they are also repelled from the high voltage electrode and travel towards the sensing electrodes. Particles that land on the sensing electrodes transfer their charge. The generated current is amplified by the electrometers, digitized, and read by a microcontroller. The data are processed in real time to obtain 10 particle size distributions per second.

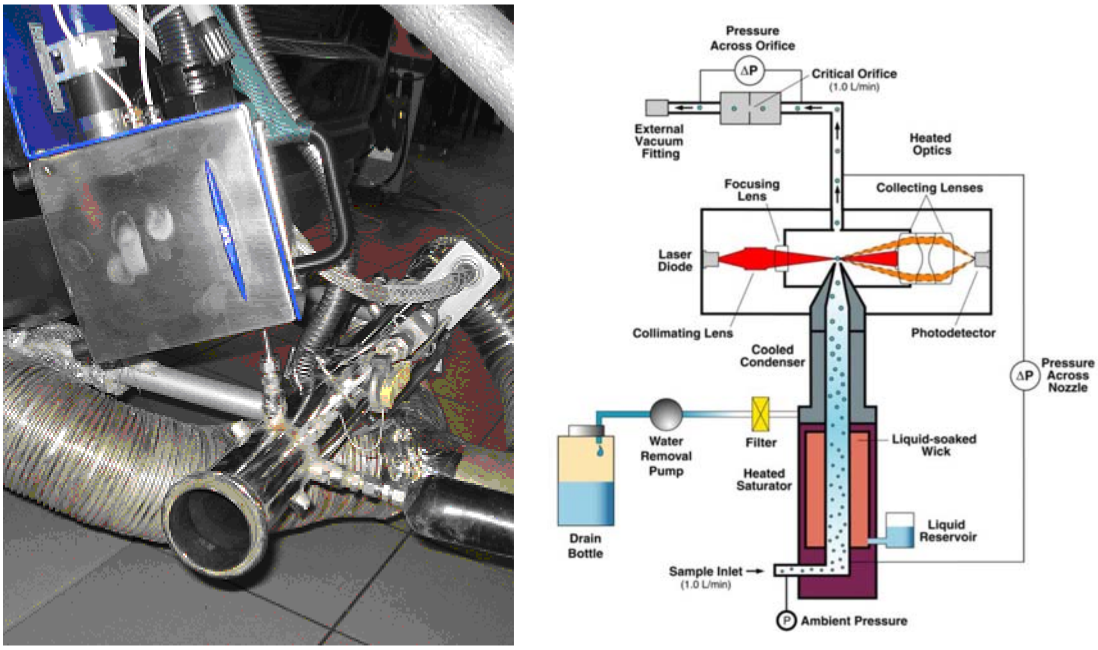

Figure 6. View and diagram of the condensation particle counter [9]

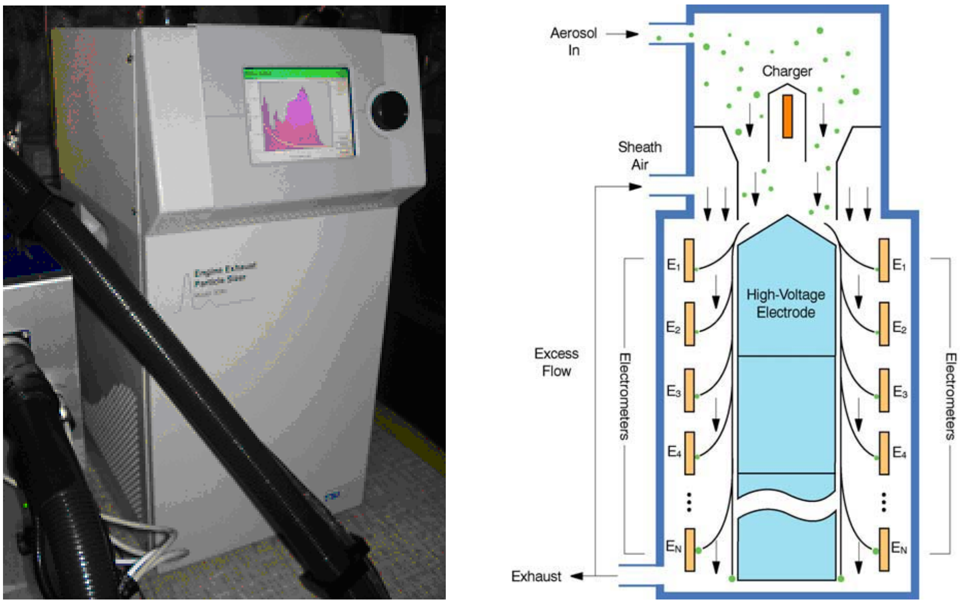

Figure 7. View and schematic diagram of the 3090 EEPS Spectrometer [10]

4. Experimental Results and Analysis

The obtained data were used to specify dependence characteristics for the influence of dynamic engine properties on exhaust emissions. The dynamic engine properties were indirectly taken into account, using all the speed range and the range of acceleration calculated for city traffic to prepare a matrix of emission intensity. The data used were averaged within each speed and acceleration range, which generated characteristics of vehicle operation in each range (Fig. 8) and characteristics of emission matrices of exhaust. The greatest share of the engine operation in the studied traffic conditions was obtained for minimum and medium speed and zero vehicle acceleration.

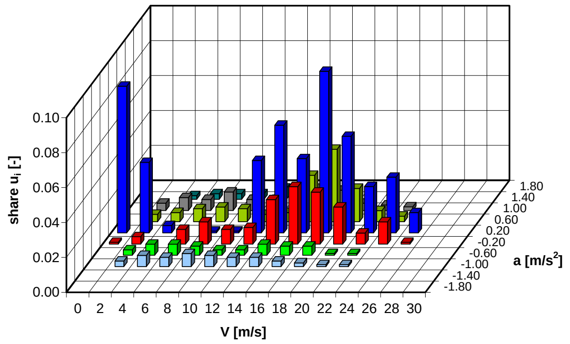

Figure 8. Characteristics of the use of the vehicle operation time in each speed and acceleration range under city traffic conditions

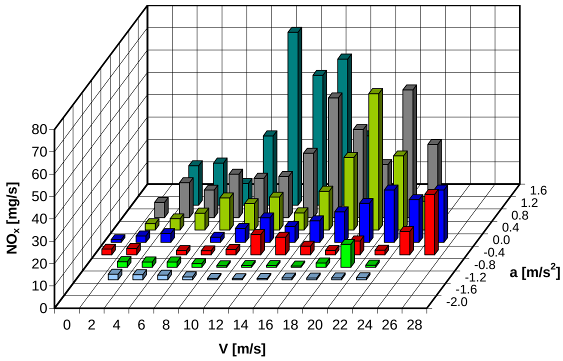

Figure 11. NOx emission in each speed and acceleration range under city traffic conditions

Maximum intensity of emission of carbon monoxide (Fig. 9) and hydrocarbons (Fig. 10) expressed in grams per second falls within the area of maximum vehicle speeds and accelerations within the range of 0.0 to 1.2 m/s^2 which are convergent for both exhaust components. The area of an increased emission of nitric oxides (Fig. 11) falls within the range of increased speeds of a vehicle and increased acceleration of a vehicle i.e. a considerable engine load.

The mass emission of particles (Fig. 12) is ambiguous – for minimum vehicle speed the emission amounts to 15 mg/m^3 and decreases along with the increase of vehicle speed (5–10 µg/m^3), and then for high speed values (above 20 m/s) it increases to 15-20 µg/m^3 again. The measurements of particle quantity showed a different distribution than particle mass.

The highest quantity of particles (Fig. 12 and 13) was generated in the vehicle operating conditions of rather low driving speed (2–6 m/s) and average acceleration (0–1 m/s^2) and with the increasing speed the quantity of particles was decreasing. Such distribution of particle mass and quantity is characteristic of vehicles fitted with diesel particulate filter that can be subject to periodic regeneration. In the tests conducted over the specific road section partial regeneration was not activated. It resulted mainly from the short distance covered by the vehicle as well as from the high performance of the diesel particulate filter. Too low the temperature of exhaust gases (in the exhaust gas measurement point it did not exceed 250 ^{o}C) was the reason of the lack of diesel particulate filter regeneration.

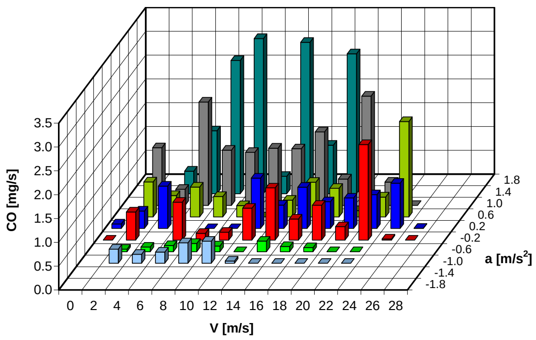

Figure 9. CO emission in each speed and acceleration range under city traffic conditions

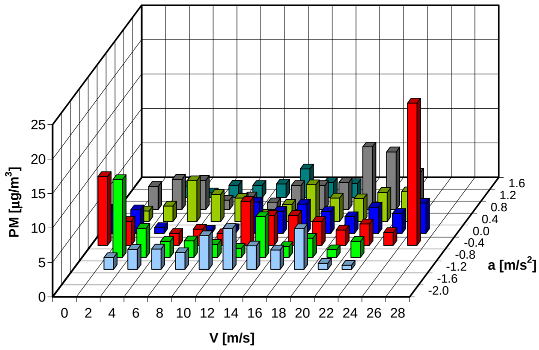

Figure 12. Particle mass emission in each speed and acceleration range under city traffic conditions

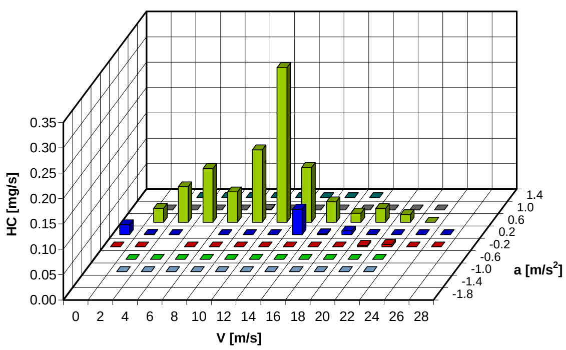

Figure 10. HC emission in each speed and acceleration range under city traffic conditions

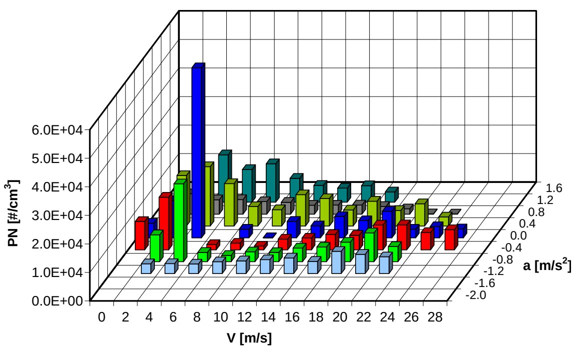

Figure 13. Particle number emission in each speed and acceleration range under city traffic conditions

The obtained results of a vehicle driving time in the conditions determined by its speed, acceleration and intensity of exhaust emissions in the European homologation test (NEDC). This comparison was used subsequently to specify the value of the emission increase from a vehicle under real conditions in relation with the conditions of a vehicle operation in the homologation test (Fig. 14).

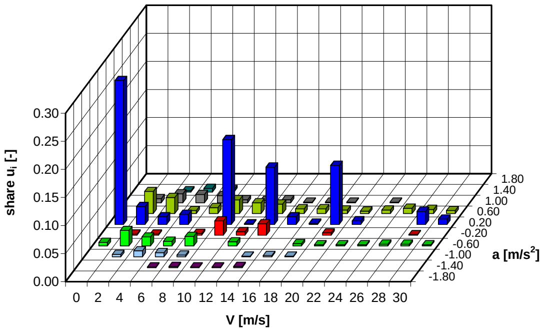

Figure 14. Characteristics of the use of vehicle operating time in each range of speed and acceleration for the conditions of the NEDC test

Having compared the participation of driving time of a vehicle within the areas of vehicle speed and acceleration in the road and homologation test a similarity of both of the obtained characteristics can be observed. Compatibility of the compared characteristics for a breakdown of the occurrence of the vehicle driving time share has been maintained. In the NEDC test the share of a vehicle drive at minimum speed and zero acceleration is bigger. However, for real conditions the area of the used speeds and acceleration of a vehicle is bigger. However, the relative comparison of the values reveals the discrepancies reaching the values above 100% for the same ranges of vehicle speed and acceleration.

5. Quantity Indexes of Emission Level

With the use of values of the collective emission of the exhaust components and the values recorded from the GPS system the road length during the test was determined and then the average road emission was specified for each exhaust emission (Fig. 15). The remaining road emission values exceed these values. That means a higher road emission of a vehicle during operation than during a homologation test.

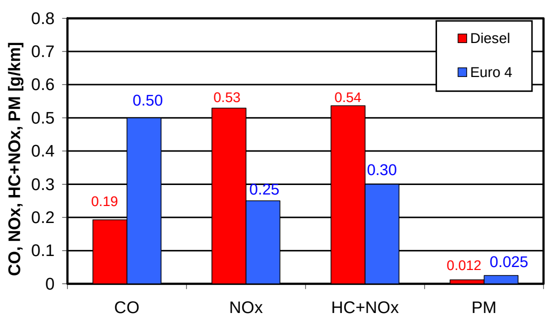

Figure 15. A comparison of road emission values and Euro 4 standard (PM approx.)

Based on the presented information, e.g. the characteristics of share of a vehicle operating time in each section of speed and acceleration and the characteristics of emission intensity, a multiplication factor of the emission increase (or decrease) under the real traffic conditions can be calculated in relation to the homologation test. The index of a vehicle emission level (for a given exhaust component) was defined as follows:

$$k_j = \frac{E_{\text{road, j}}}{E_{NEDC,j}}, \tag{1}$$

where:

j – exhaust compound for which emission level index was set forth,

$E_{road,j}$ – emission intensity obtained under the real conditions ([g/s] or [g/km]),

$E_{NEDC,j}$ – emission intensity obtained in the NEDC test ([g/s] or [g/km]) (emission limits: [8, 11]).

The emission intensity under the real conditions can be calculated through the characteristics of a vehicle driving time breakdown ($u_{a,V}$) and the characteristics of emission intensity for j-th exhaust compound $e_{j(a,V)}$ expressed in grams per second:

$$E_{road,j} = \sum_a \sum_V \left(u_{a,V} \cdot e_{j(a,V)}\right). \tag{2}$$

If the information concerning the exhaust emission in the NEDC test is missing, acceptable values according to the Euro emission standard can be assumed binding for a specific vehicle. The acceptable emission values for a specific compound expressed in g/km can be recalculated for the emission intensity values (in g/s) if the duration and the distance covered in the homologation test are known. Such relations served to establish the emission level indexes for the exhaust components of a tested vehicle (Fig. 16).

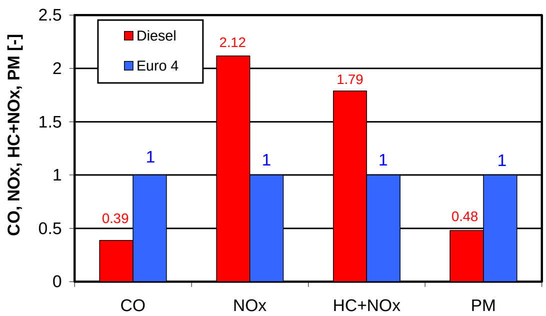

Fig. 16. Comparison of vehicle emission factor

6. Conclusion

The analysis of the data proves that the emission values obtained in the NEDC homologation test for a tested vehicle (in accordance with Euro 4 standard) and the values under real operation differ from each other. These differences in the case of some components are significant and amount to:

a) CO emission is 60% lower,

b) emission of nitric oxides is 120% higher,

c) emission of hydrocarbons and nitric oxides is 80% higher,

d) emission of particulate matter is 50% lower.

The obtained data enabled to define the vehicle emission factor that can be used to classify fleets of vehicles in relation to exhaust emissions that differ e.g. in production date (emission limits, vehicle mileage or operating conditions).

The results of the tests carried out under the real conditions show that in the case of some exhaust emissions this emission is several hundred per cent higher. Therefore, one can observe a trend to legislate the exhaust emission measurement under real operating conditions of vehicles in Europe.

References

[1] Zhao F.F., Technologies for Near-Zero-Emission Gasoline-Powered Vehicles, SAE International, Warrendale 2007.

[2] Merkisz J., Pielecha J., Gis W., Gasoline and LPG Vehicle Emission Factors in a Road Test, SAE Technical Paper Series 2009-01-0937.

[3] AVL, Current and Future Exhaust Emission Legislation, AVL List GmbH, Graz 2008.

[4] Doh-Won L., PEMS Testing on Non-Road Equipment – New Challenges, Sensors 5th Annual SUN (SEMTECH User Network) Conference, Ann Arbor 2008.

[5] Shahinian V.D., SENSORS tech-ct Update Application Software for SEMTECH Portable Emission Analyzers, Sensors 4th Annual SUN (SEMTECH User Network) Conference, Ann Arbor 2007.

[6] Gao Y., Checkel M.D., Emission Factors Analysis for Multiple Vehicles Using an On-Board, In-Use Emissions Measurement System, SAE Technical Paper Series 2007-01-1327.

[7] Greening P., European Light-Duty & Heavy Duty OBD – Legislative Update, On-Board Diagnostic Symposium: Light and Heavy Duty, Villeurbanne 2007.

[8] Worldwide Emissions Standards, Passenger Cars & Light Duty Trucks, Heavy Duty & Off-Road Vehicles, Delphi, 2010.

[9] AVL, Particle Counter 489. Product Guide, Rev. 02.2008.

[10] TSI, TSI Model 3090 Engine Exhaust Particle SizerTM Spectrometer, Operation and Service Manual. Rev. E, 2008.

[11] Merkisz J., Radzimirski S., Trends in the European Legislation on LDV Pollutant Emissions, Combustion Engines No. 3 (134), Polish Scientific Society of Combustion Engines, Bielsko-Biala 2008.

JJMIE

Volume 5 , Number 1, Febreuary 2011
ISSN 1995-6665
Pages 97 -106

Jordan Journal of Mechanical and Industrial Engineering

Fuzzy Logic Control of an Electrical Traction Elevator

Musa O. Abdalla [a,*] and Tagreed M. Al-Jarrah [a]

Department of Mechanical Engineering, University of Jordan, Amman, Jordan

Abstract

A novel elevator speed regulation scheme that is based on Fuzzy Logic (FL) technology is presented. The Fuzzy Logic controller has the ability to track a user defined elevator's speed profile without compromising the accuracy in reaching a designated position. The response of the FL controller will be compared with the ubiquitous PID controller by means of computer simulations. Standard cybernetics performance criteria will be used in judging the performance of both controllers. Finally, such a FL based controller maybe easily complimented with additional intelligent features.

Keywords: Feedback Control System, PID controller, Fuzzy Logic, Elevator Control

1. Introduction

Elevators are the primary mean of transportation that is used nowadays in tower buildings. In this century, the trend is higher is better. Dubai has just finished opening its one kilometer tower while Saudi Arabia has announced that they are working on building a one mile tower building! Such high buildings demand high performance elevators, with extra ordinary speed control.

In general, elevators may be classified according to their driving method into three categories; electric, hydraulic and pneumatic elevators. Hydraulic elevators use hydraulic oil driven actuators to raise and lower car and its load, this type of elevators is typically used for low to medium rise buildings. Electric elevators consist of two main types: winding drum and traction elevators.

The applications of winding drum machines are very limited by both code restrictions and practical considerations1.

On the other hand electric traction elevators are elevators in which the energy is applied by means of an electric driven machine. Medium to high speeds and virtually limitless rise allow this elevator type to serve high-rise, medium-rise and low-rise buildings.

Electric traction elevator can be further divided into geared and gearless categories: geared traction elevators are designed to operate within the general range of 100 to 450 ft/min, restricting their use to medium rise buildings, while gearless traction elevators speeds are available in the range of 500 to 1500 ft/min. Such designs offer the advantages of longer life and smoother rides[2].

Many studies were carried out in controlling the elevator systems. For example, Kang, et al.[3] proposed a new strategy to reduce the vertical vibration of the lift car while keeping high speed control and as a result it improved the efficiency of riding elevators. An extended full-order observer is designed to estimate the acceleration feedback of the car and the identification of some mechanical parameters. Both experimental evaluations and computer simulations proved the feasibility of this strategy.

Mannan, et al.[4] proposed an electro-hydraulic system for the control of an elevator with twin cylinders that are located on each side of the elevator car. A PD fuzzy controller is applied to regulate velocity, where as a constrained step PD controller is used to guarantee a minimum non-synchronous error between the motions of the two cylinders.

* Corresponding author. e-mail: admin@mechatronix.us

Sha, et al.[5] has introduced an approximate linear model for a hydraulic elevator that includes an improved dynamic frictional based model and has investigated a sliding mode control (non-linear) for velocity tracking in the discrete domain. Simulation experiments showed that this approach offers an effective and improved solution for the hydraulic elevator control.

Huayong, et al.[6] studied the computational simulation and experimental research on the variable voltage variable frequency VVVF hydraulic elevator speed control. The research results provided a theoretical basis for the design and application of the VVVF hydraulic elevator. Kim, et al.[7] proposed a two-stage non-linear robust-controller, using Lyapunov method to control the velocity of the hydraulic elevator. On the first stage, a robust controller of the mechanics is synthesized to control the velocity of the car. On the second stage, a robust controller for the hydraulic is designed to track the pressure that is generated by the first controller.

Zhou, et al.[8] introduced a hybrid backup power system, including batteries, ultra capacitors and hydrogen fuel cells in order to get a reliable and effective continuous function elevator in spite of miscellaneous power failures.

In this work Fuzzy Logic (FL) controller is presented to track a reference speed profile for a 2:1 gearless traction elevator and the results will be compared with the standard tuned PID controller performance.

2.1 Elevator model

The long-life, smoothness and high horsepower of gearless traction elevators provide a durable elevator service that can outline the building itself. The first high-rise application of gearless traction elevator was in the Beaver building New York City in 1903, which was followed by such notable installations such as the singer building which was demolished in 1972 and the Woolworth buildings, to name few. Typically elevator machines are either roped with a single or double wrap arrangement. Single wrap arrangement provides traction by the use of grooves that will pinch the ropes with varying degrees of pressure depending on the groove's shape and it's undercutting. The most effective single-wrap arrangement gives 180 degrees of the rope contact with the sheave without deflecting the sheave. On the other hand, double-wrap arrangement is used for high-speed gearless traction machines of 4mps or more to obtain traction and to minimize rope wear.

Conventional elevators are either roped as 1:1 or 2:1 for both car and counter-weight. The savings on using a faster motor that can be built smaller and lighter than lower speed DC motors makes 2:1 roping more attractive for a full range of speed requirements from (0.5-3.5 mps) or more. Also, an advantage in lifting capacity as the 2:1 argument allows the use of higher-speeds and therefore a smaller but faster elevator motor. Finally, the mechanical advantage of 2:1 roping requires that only half the weight to be lifted[9].

The most popular electrical elevator models based on roping techniques are shown in Figure 1. For a complete and thorough discussion of the pros and cons of such schemes the reader is directed to consult some elevator design based handbooks.

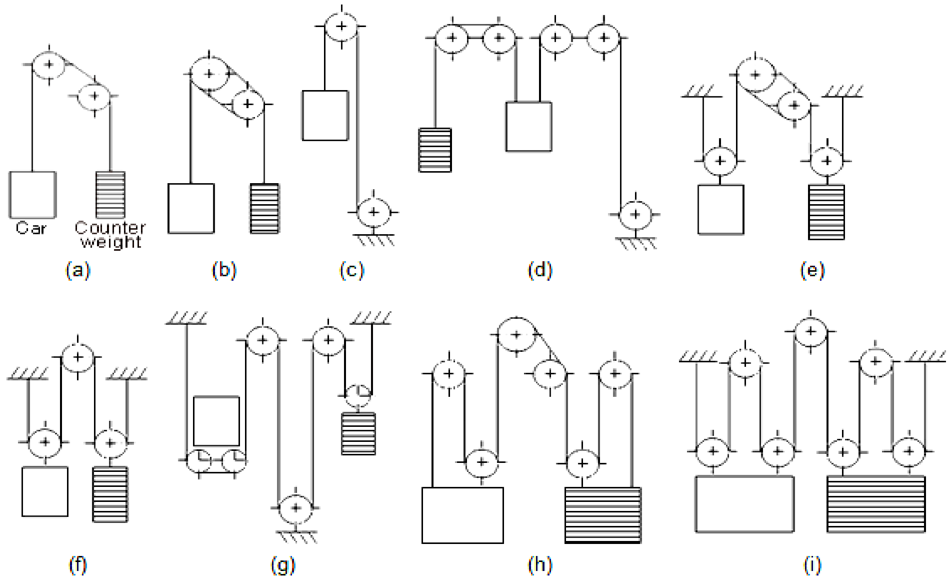

Figure 1. a) 1:1 Half wrap b) 1:1 Full wrap c) 1:1 Drum winding d) 1:1 Drum winding e) 2:1 Full wrap f) 2:1 Half wrap g) 2:1 Half wrap h) 3:1 Half wrap i) 4:1 Half wrap

In this work the controller design will be verified using computer simulations and through a direct comparison with the ubiquitous PID controller. All simulation results in this work are based on a 2:1 gearless electric (DC) traction elevator physical model that is depicted in Figure 2. A summary of the ODE of the elevator mathematical model[10] is provided her as a reference:

$$\dot{i}_a = \frac{V_{in}}{L_a} - \frac{R_a}{L_a} - \frac{K_b}{L_a}\dot{x}_2 \quad ...(1)$$

$$\ddot{x}_2 = \frac{R_2}{J_2}(T_3 - T_2) + K_m i_a \quad ...(2)$$

$$\ddot{x}_1 = \frac{R_1^2 K_{EL}}{2J_1}(x_{EL} - x_1) + \frac{R_1^2 B_{EL}}{2J_1}(\dot{x}_1 - \dot{x}_{EL}) + (X_0 K_0 + T_{\cdots}$$

$$\ddot{x}_{EL} = \frac{K_{EL}}{M_{EL}}(x_1 - x_{EL}) + \frac{B_{EL}}{M_{EL}}(\dot{x}_1 - \dot{x}_{EL}) \quad ...(4)$$

$$\ddot{x}_{CW} = \frac{K_{CW}}{M_{CW}}(x_3 - x_{CW}) + \frac{B_{CW}}{M_{CW}}(\dot{x}_3 - \dot{x}_{CW}) \quad ...(5)$$

$$\ddot{x}_3 = \frac{K_{CW}R_3^2}{2J_3}(x_{CW} - x_3) + \frac{B_{CW}R_3^2}{2J_3}(\dot{x}_{CW} - \dot{x}_3) + (T_3 + T_4)\frac{R_3^2}{2J_3}$$

... (6)

Where list of symbols can be found in Table 1.

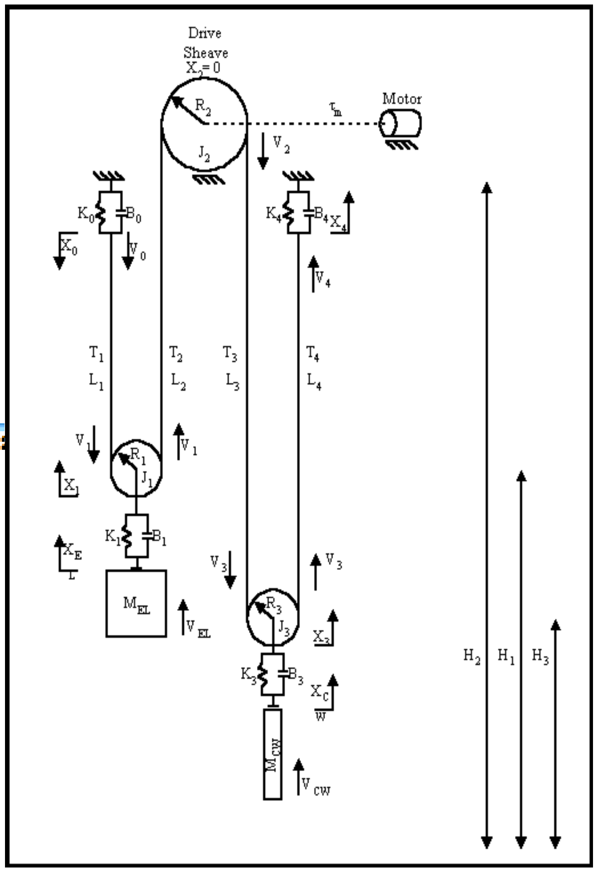

Figure 2. A 2:1 Gearless Elevator Physical Model

Table 1. List of symbols

Symbol	***Description***
i_a	*Armature current*
V_{in}	*Input voltage*
R_a	*Armature resistance*
L_a	*Armature Inductance*
K_m	*Motor armature constant*
K_b	*The emf motor constant*
T_f	*Coulomb friction value (Offset)*
K_f	*Coefficient of viscous friction(Gain)*
R	*Radius*
T	*Tension*
J	*Moment of inertia*
M_{EL}	*Mass of the elevator*
M_{CW}	*Mass of the weight*
K_{EL}	*Stiffness of the elevator*
K_{CW}	*Stiffness of the counter weight*
B_{EL}	*Stiffness of the elevator*
B_{CW}	*Stiffness of the counter weight*
τ_m	*Motor torque*

2.2. Motion Status for the elevator car

A typical speed profile of an elevator car is depicted in Figure 3. The speed profile describes the motion status of the car. When a car starts to move, it enters an acceleration mode until it reaches the constant speed. This speed is maintained until the car has to come to a stop. Before the car commences the stop position, it has to slow down for a safe stop at the destination floor. Besides the motion status of the car, other useful information is given by the speed profile, which include: the time the car takes to reach the contract speed, the time the car spends to travel one floor at constant speed, the time taken to decelerate before the car reaches a complete stop, the distance traveled to reach the constant speed and the distance traveled to slow down from the constant speed before the car stops[11].

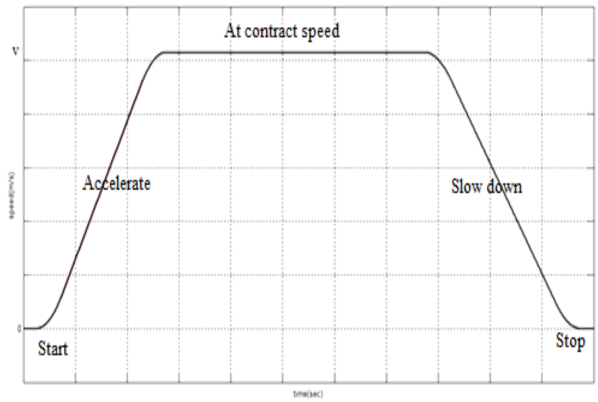

Figure 3. The speed profile for an elevator system

* Corresponding author. e-mail: admin@mechatronix.us

2.3 Discrete system model

The previous elevator system's model is simulated using Simulink / Matlab for testing the designed controllers. A switching technology through Pulse Width Modulation (PWM) and a universal bridge is used for enabling speed regulation of the PMDC motor system. Figure 4 depicts the closed loop system (feedback) of the major blocks, while Figures 5 and 6 illustrate the details of the subsystems.The speed profile is given as an input for the controller in addition to the desired height (floor level).

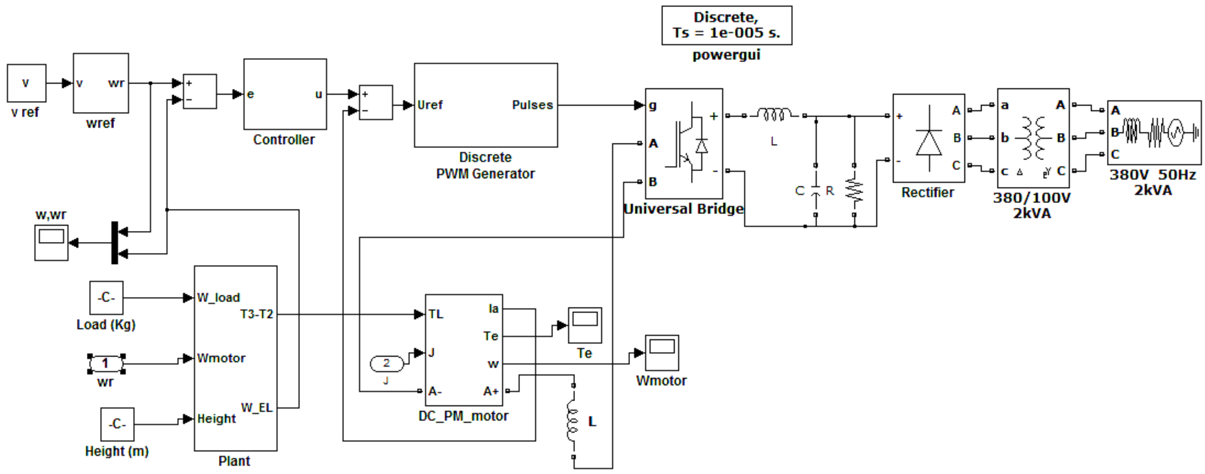

Figure 4. Elevator speed control closed loop system

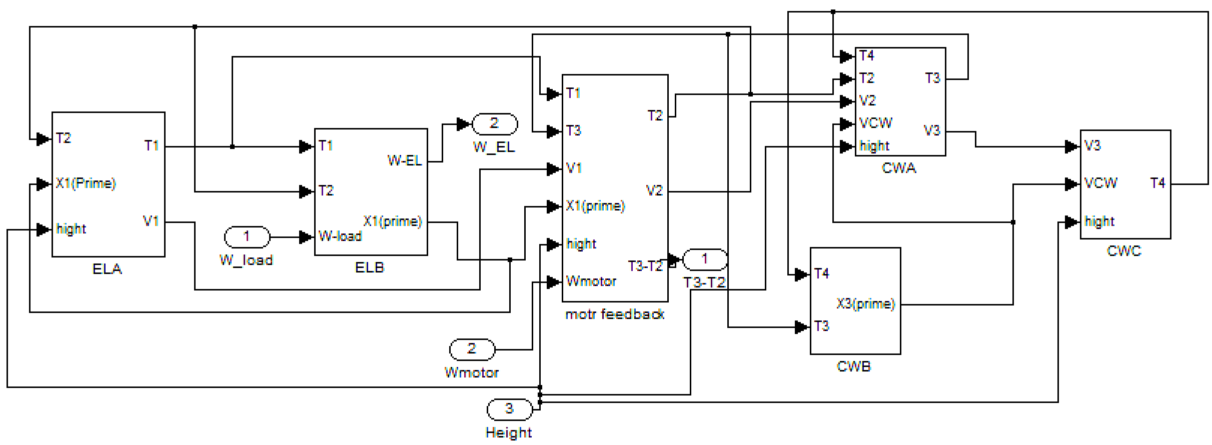

Figure 5. Elevator internal subsystems

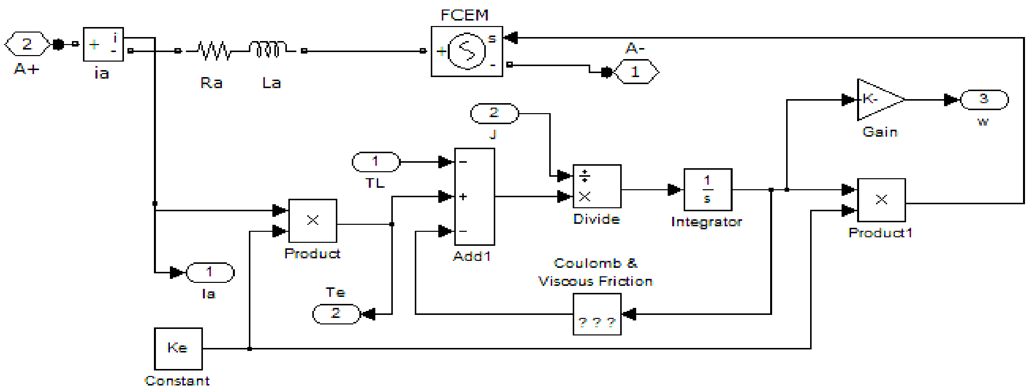

Figure 6. PMDC motor subsystem

3. Fuzzy Logic Controller (FLC) design

A typical Fuzzy Logic Controller (FLC) structure is depicted in Figure 7 The major steps in the FLC design constitutes creating a knowledge base of the rules, establishing membership functions for the inputs (fuzzification) and implementing member functions for the outputs (defuzzification). In this work the sensed input signals that are fed to the FLC are the error and the error rate of change (e , e').

$$e(t) = V_d(t) - V(t) \qquad ...(7)$$

Where $V_d(t)$ is the reference speed (speed profile), and $V(t)$ is the elevator actual speed.

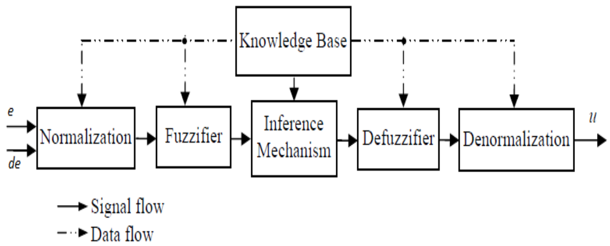

Figure 7. Fuzzy Logic Controller internal structure

Fuzzy Logic Matlab Toolbox is used to simulate the FLC, which can be further integrated into the previous simulations with Simulink.

The membership functions for the two inputs and the output are shown in Figure 8. Seven linguistic variables were selected to span the whole input/output range, which are defined as:

Negative Big (NB), Negative Medium (NM), Negative Small (NS), Zero (ZE), Positive Small (PS), Positive Medium (PM), and Positive Big (PB).

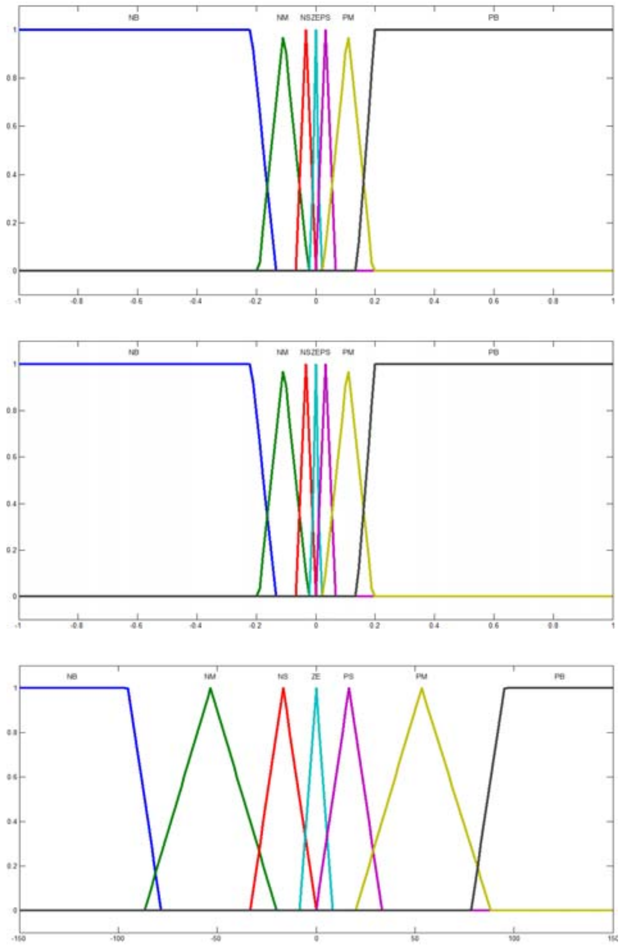

Figure 8. Membership functions, (a) Membership function of error, (b) Membership function of rate of change of error, (c) Membership function of the reference voltage

The proposed rules for the Fuzzy logic controller are summarized in Table 2. The fuzzy inference operation is implemented by using all the 49 rules. The min-max compositional rule of inference and the center-of-gravity method have been used in the defuzzifier process.

Table 2. Fuzzy logic controller rules

$\dot{e}$ \ e	*NB*	*NM*	*NS*	*ZE*	*PS*	*PM*	*PB*
NB	NB	NB	NB	NB	NM	NS	ZE
NM	NB	NB	NB	NM	NS	ZE	PS
NS	NB	NB	NM	NS	ZE	PS	PM
ZE	NB	NM	NS	ZE	PS	PM	PB
PS	NM	NS	ZE	PS	PM	PB	PB
PM	NS	ZE	PS	PM	PB	PB	PB
PB	PS	PS	PM	PB	PB	PB	PB

Table 3. Elevator system physical parameters

Armature resistance R_a	*0.49* Ω
Armature inductance (L_a)	*4.3 mH*
motorarmature constant (K_m)	*0.49*
Coulomb friction value (Offset)(t_f)	*0.18*
Coefficient of viscous friction(Gain(K_f)	*4.6e-4*
Radius 1 (R1)	*0.2 m*
Radius2 (R2)	*0.3 m*
Radius3 (R3)	*0.2 m*
Moment of inertia (J1)	*0.08 $Kg.m^2$*
Moment of inertia (J2)	*0.15 $Kg.m^2$*
Moment of inertia (J3)	*0.08 $Kg.m^2$*
Mass of the elevator (M_{EL})	*$100<M_{EL}<500$ Kg*
Mass of the weight (M_{CW})	*100 Kg*

5. Numerical example

To test the effectiveness of the Fuzzy Logic Controller (FLC) in contrast to the traditional Proportional, Integral, and Derivative (PID) controller, we have used Matlab computer simulations. The parameters that were used for the 2:1 gearless elevator are fully depicted in Table 3.

The results for both controllers are obtained for the first floor test (Four meter height) and for the 10th floor test (Forty meters height) in order to demonstrate the controller's effectiveness.

Figure 9 and 10 depicts the results for the PID controller. Each figure illustrates position, car velocity profile, car acceleration and jerk. Typically the acceleration range[9] should be between (-1.5 - 1.5) mps^2, which is obviously met by the tuned PID controller. Also, the controller tracking of the speed profile is done nicely with minimal amount of jerk.

On the other hand, Figures 11 and 12 demonstrate the response of the Fuzzy Logic Controller even without membership functions tuning. In addition the FLC may be embedded with some form of an artificial intelligence making it superior over the PID controller.

Further analysis was done using standard performance measures and the results are summarized in Tables 3 and 4, respectively. FLC results demonstrated a superior performance.

However, the FLC rule base and the membership functions were not optimized yet they still provided a very competitive speed tracking and regulation.

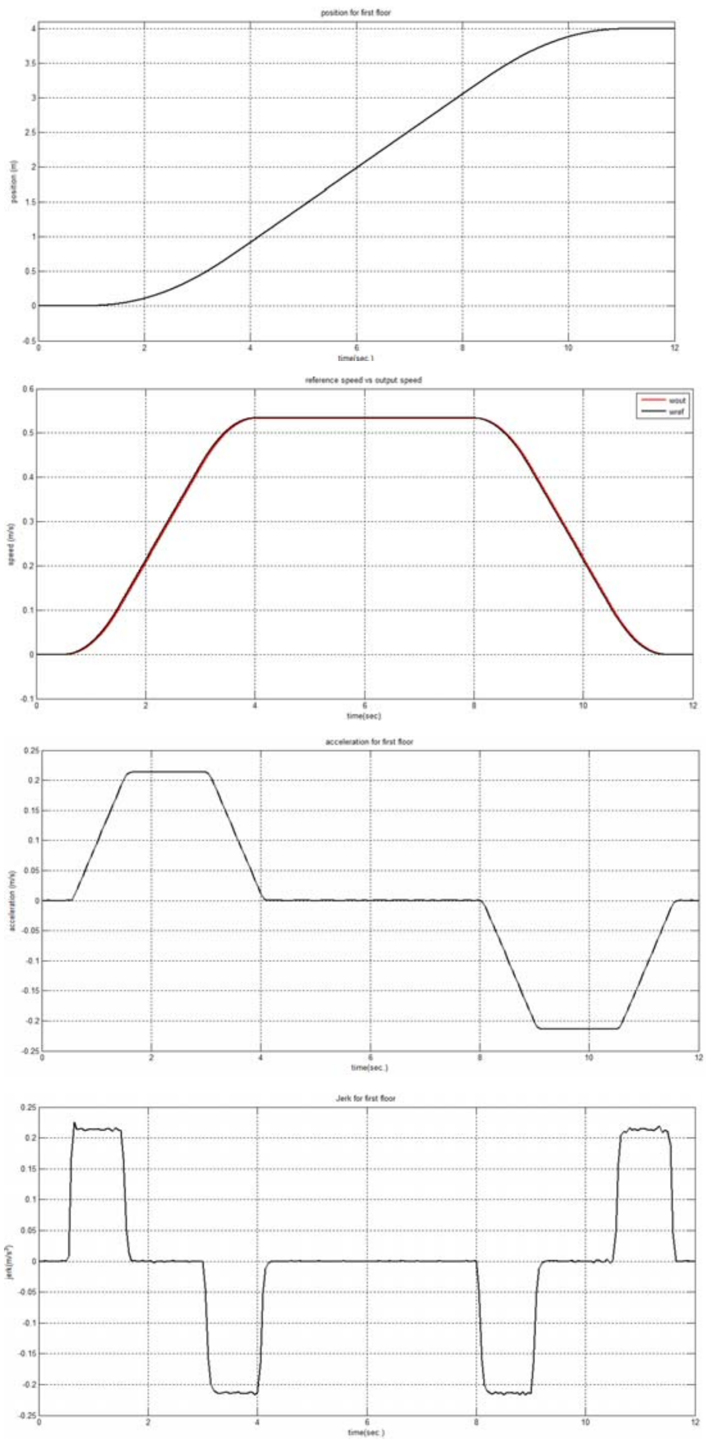

Figure 9. PID controller responses a) Position at 4m height b) Reference speed vs. actual speed for 4m height c) Acceleration for 4m height d) Jerk at 4m height

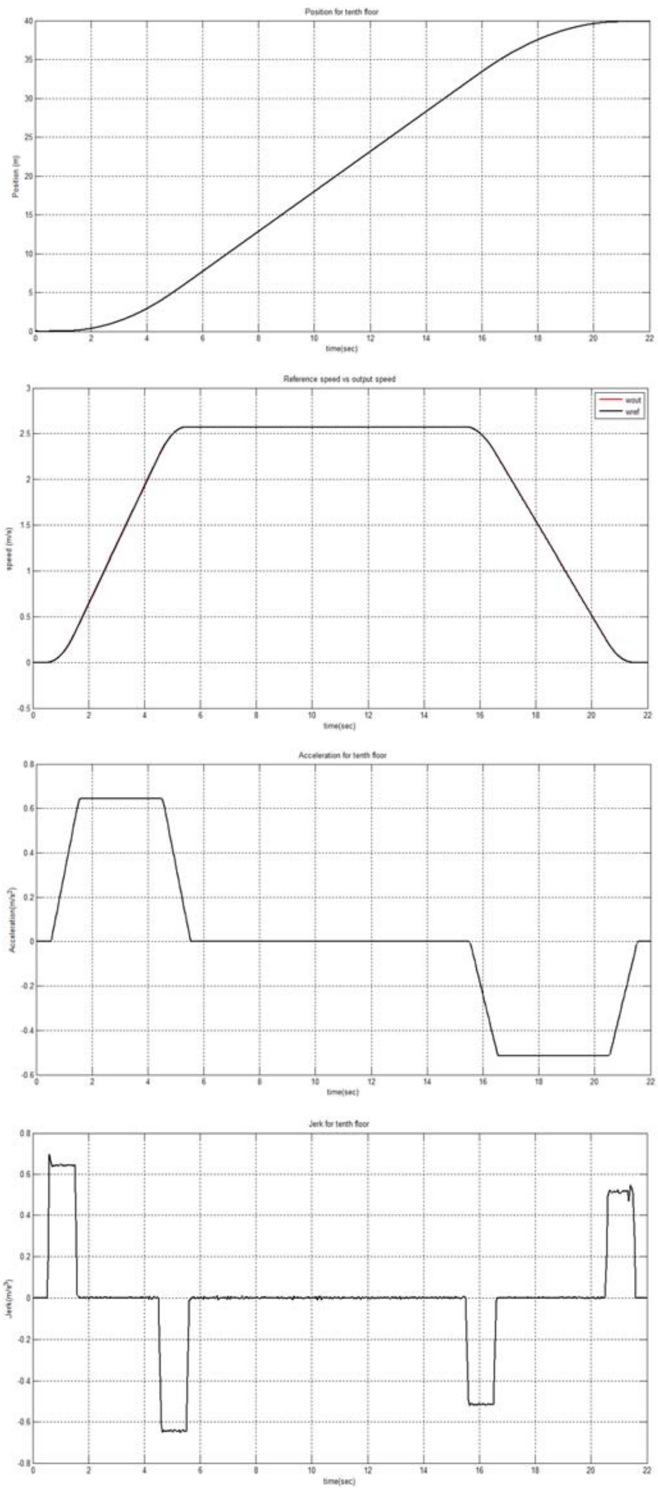

Figure 10. PID controller responses a) Position at 40m height b) Reference speed vs. actual speed for 40 m height c) Acceleration for 40 m height d) Jerk at 40 m height

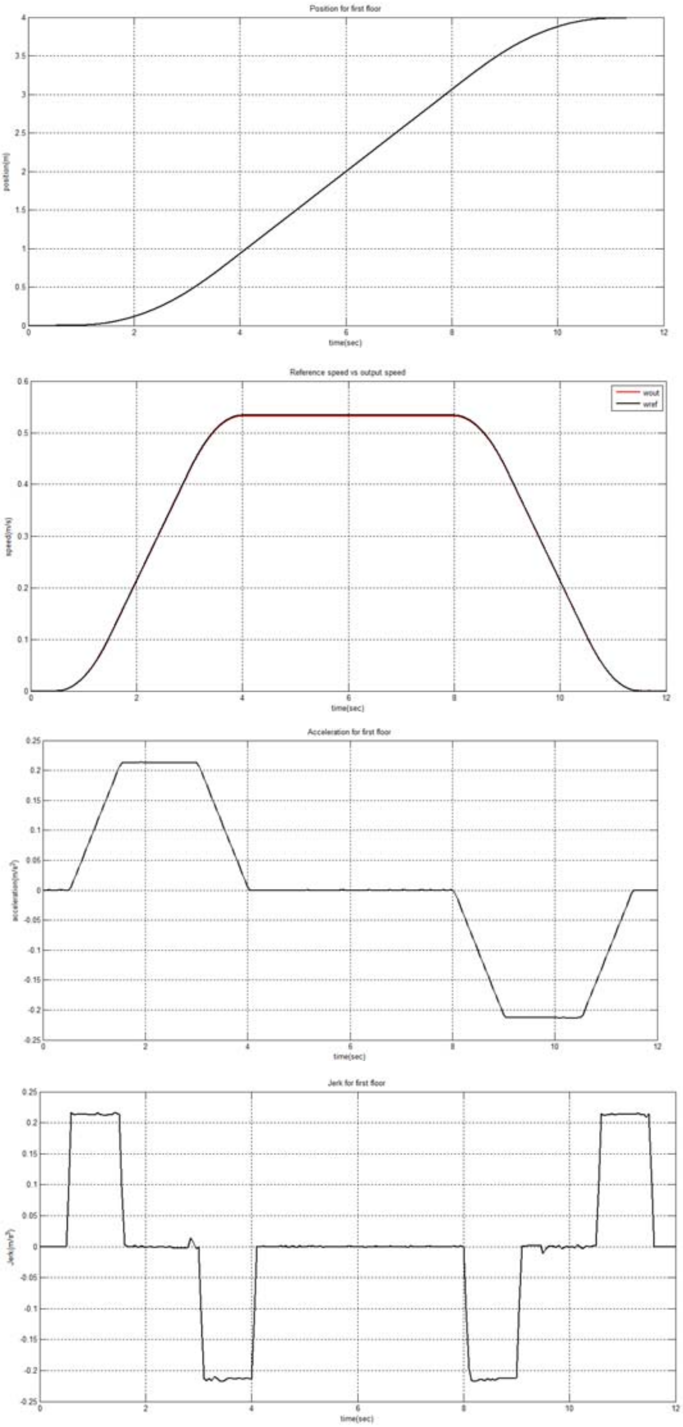

Figure11. FLC responses a) Position at 4m height b) Reference speed vs. actual speed for 4m height c) Acceleration for 4m height d) Jerk at 4m height

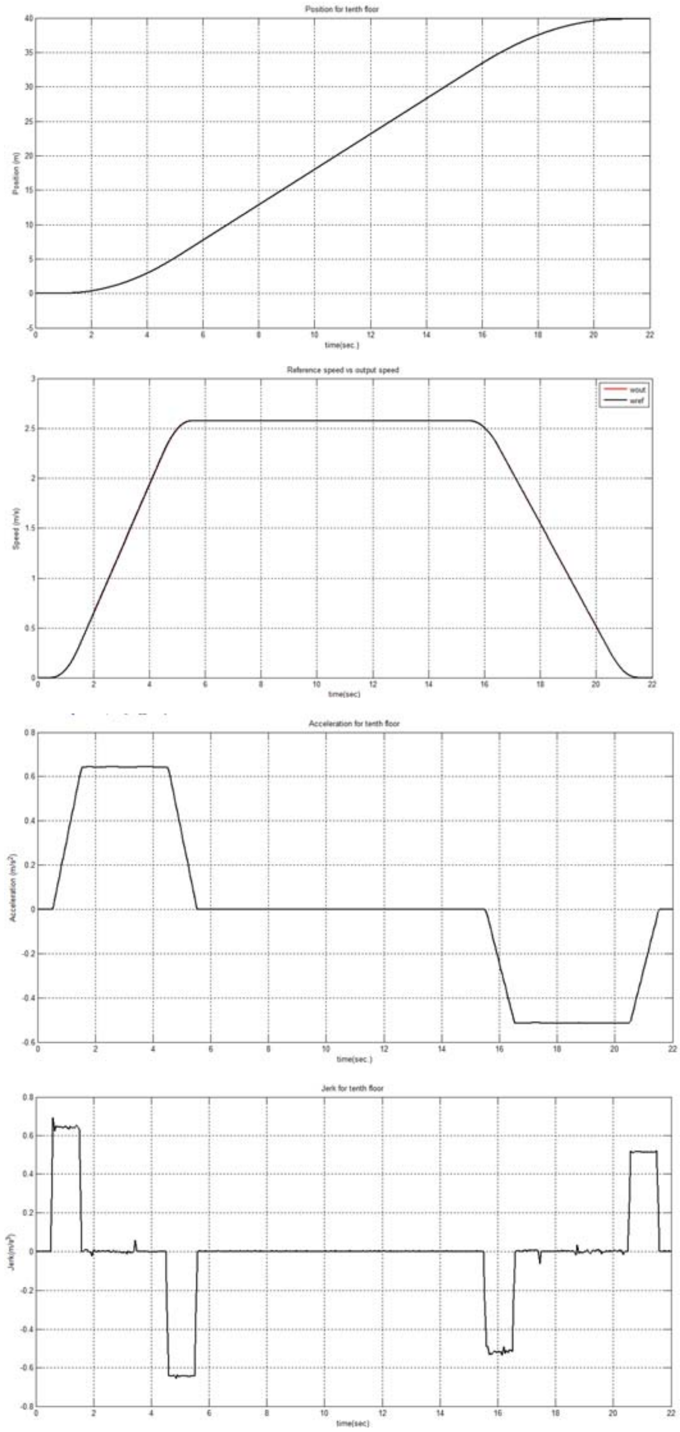

Figure12. FLC responses a) Position at 40 m height b) Reference speed vs. actual speed for 40 m height c) Acceleration for 40 m height d) Jerk at 40 m height

Table 3. Cost function for PID and FLC at 4m height

Controller	*ISE*	*IAE*	*ITAE*
PID	8.012e-005	0.02204	0.1069
FLC	1.701e-005	0.01037	0.05161

Table4. Cost function for PID and FLC at 40m height

Controller	*ISE*	*IAE*	*ITAE*
PID	0.0001099	0.03416	0.3159
FLC	7.282e-005	0.03333	0.3149

6. Conclusions and Future Work

A fuzzy logic based controller was introduced to regulate the speed and position of a 2:1 electric traction elevator system. The FLC successfully tracked a given user speed profile with minimal amount of jerk.

A complete comparison with the standard tuned PID controller was carried out. The standard performance criteria results showed superiority of the FLC over the PID controller speed regulation.

The fuzzy logic performance may be enhanced further by tuning the parameters of the membership functions and compliment it with some form of intelligence.

Referenced

[1] Filippone, J., Feldman, J.D., Schloss, R., D., Cooper, D., A. Elevator and Escalator Accident Reconstruction. 2nd edition. USA, 2006.

[2] Ramsey, Sleeper. Architectural Graphic Standards. eleventh edition. American Institute of Architects, 2007.

[3] J. K. Kang, and S. K. Sul , “Vertical-Vibration Control of Elevator Using Estimated Car Acceleration Feedback Compensation”. IEEE Transactions on Industrial Electronics, volume 47, 2000, 873-897.

[4] K. Li, M.A. Mannan, M. Xu, Z. Xiao, “Electro-hydraulic proportional control of twin-cylinder hydraulic elevators”. Control Engineering Practice, volume 9, 2001, 367–373.

[5] D. Sha, V. B. Bajic, H. Yang , “New model and sliding mode control of hydraulic elevator velocity tracking system”. Simul Pract Theory, 2002, 65-85.

[6] Y. Huayong, Y. Jian, X. Bing, “Computational simulation and experimental research on speed control of VVVF hydraulic elevator”. Control Engineering Practice, volume 9, 2004, 563-568.

[7] C. S. Kim, K. S. Hong, M. K. Kim, “Nonlinear robust control of a hydraulic elevator: experiment-based modeling and two-stage Lyapunov redesign”. Control Engineering Practice volume 13, 2005, 789-803.

[8] L. Zhou, Z. Dong, S. Wang, and Z. Qi, “Design and Analysis of a Hybrid Backup Power System for a High-Rise and High-Speed Elevator”. Proceedings of the 2008 IEEE/ASME International Conference on Mechatronic and Embedded Systems and Applications, 2008. 12-15.

[9] George R. Strakosch, The vertical transportation handbook, 3rd edition.

[10] Strakosch, G. R. The Vertical Transportation Handbook, 3rd edition, John Wiley and Sons, New York, 1998.

[11] J.Jamaludin, N.A.Rahim, W.P. Hew, “Development of a self-tuning fuzzy logic controller for intelligent control of elevator systems”. Engineering Applications of Artificial Intelligence, 2009, 1-12.

JJMIE

Volume 5 , Number 1, February 2011
ISSN 1995-6665
Pages 107 - 112

Jordan Journal of Mechanical and Industrial Engineering

Evaluating Thermal Performance of Solar Cookers under Jordanian Climate

M. Abu-Khader[a], M. Abu Hilal[b], S. Abdallah[c]*, and O. Badran[a]

[a] Department of Chemical Engineering, FET, Al-Balqa Applied University, Amman, Jordan

[b] Department of Mechanical Engineering, An-Najah National University, Nablus, Palestine

[c] Applied Science University, Mechanical and Industrial Engineering Department, Amman, Jordan

Abstract

This study presented a short review on the solar cooker designs and applications. Two designs of cookers were tested. The first type has a painted black base and second has internal reflecting mirrors. These designs were examined under two modes of operations: at fixed position and on tracking system. The cooker at a fixed position had recorded thermal efficiencies ranging from 17 % to a sharp peak of 41.2% at the maximum solar intensity of the day around 11-12 am with an average overall efficiency around 27.6%. Whereas, cooker with internal reflecting mirrors installed on a sun tracking system gave higher water and pot temperatures, and thermal efficiency ranged from 25.3% to 53.1% with an average overall efficiency around 40.6 %. Cookers installed on sun tracking system had the advantage of maintaining a higher and closer range of thermal efficiencies through the daylight than the ones at fixed positions.

Keywords: Solar cooker, Tracking system, Efficiency, Jordan .

1. **Introduction**

Due to the high increase in the prices of fuel and energy, the search for alternative cheaper source of energy is of necessity. Therefore, solar energy is becoming a viable option. Solar cookers are rather important applications in thermal solar energy conversion. The use of solar cooker for cooking purposes is spreading widely in most developing countries and in particular in villages and remote areas. The solar cooker must be high quality, affordable, user friendly, light weight, stackable and a family size. Current designs of solar cookers normally used are box cookers, concentrators, and flat plate collector cookers.

The basic purpose of a solar box cooker is to heat things up - cook food, purify water, and sterilize instruments. A solar box cooks because the interior of the box is heated by the energy of the sun. Sunlight enters the solar box through the glass. It turns to heat energy when absorbed by the dark absorber plate and cooking pots. This heat input causes the temperature inside of the solar box cooker to rise until the heat loss of the cooker is equal to the solar heat gain. Temperatures sufficient for cooking food and pasteurizing water are easily achieved.

As the density and weight of the materials within the insulated shell of a solar box cooker increase, the capacity of the box to hold heat increases. The interior of a box including heavy materials such as rocks, bricks, heavy pans, water, or heavy foods will take longer to heat up because of this additional heat storage capacity. The incoming energy is stored as heat in these heavy materials and the air in the box.

*Corresponding author: salahabdalah@asu.edu.jo

The important parts of a hot box solar cooker include a) outer box: made of galvanized iron or aluminum sheet, b) inner cooking box: made from aluminum sheet and coated with black paint so as to easily absorb solar radiation and transfer the heat to the cooking pots, c) thermal insulator: The space between the outer and inner box is packed with insulating material such as glass wool pads to reduce heat losses from the cooker, d) mirror: used in a solar cooker to increase the radiation input on the absorbing space and fixed on the inner side of the main cover of the box. This radiation is in addition to the radiation entering the box directly and helps to quicken the cooking process by raising the inside temperature of the cooker, e) cooking containers: generally made of aluminum or stainless steel. These pots are also painted black on the outer surface so that they also absorb solar radiation directly.

The main objective of this present work is to investigate two designs of solar coolers. Figure 1 presents two designs of solar cookers under investigation. Also, evaluate the various parameters affecting cookers performance under different modes of operation such as at fixed position and moving on a tracking system. Experimental work and validation of mathematical modeling are carried out and compared. An overview and up to date literature will be presented.

Figure 1 Tested solar cookers: a) Black painted box type cooker, and b) Mirrors box type cooker

2. Solar Cookers: Review

Solar cookers are simple, cheap, trouble-free, with good efficiency. Solar cookers were used as early as 1776 by DeSaussure, who used a hot box-type oven. Telkes [1] and Burkhardt [2] presented one of the earliest reviews on solar cookers. From early design considerations on the development of an urban solar cooker goes back for more than 30 years [3-10]. There are several different designs for the hot box-type ovens which can be summarized as follows:

1. Simple plane hot box ovens where the food pot is enclosed inside the oven box. The oven is heated by direct solar radiation transmitted through its glass cover [11-15].
2. Booster plane reflectors can be used in conjunction with the hot box to increase the oven temperature to enhance its efficiency [14, 16]. Mannan et al. [17] described a solar oven with compound conical reflectors.
3. Indirect hot box ovens in which the cooker is heated indirectly by means of steam flowing through heat pipes which are enclosed in a plate collector, Whillier [18].
4. The Telkes oven is one of the most familiar configurations of hot box oven types [19- 20].

Several research works were conducted on the thermal testing and performance evaluation for concentrating solar cooker and combined concentrating/oven type solar cooker, and parameters that characterize the performance of the solar cooker [21- 24]. Evaluation of solar cooker thermal performance using different insulating material [25]. The hot box solar cooker was tested in an indoor solar simulator with covers consisting of 40 and 100 mm thick Transparent Insulation Material (TIM), [26]. The addition of a plane reflector to a box-type solar cooker increases the obtained cooker temperature and thermal performances [27]. A series of out-door experiments were performed on the double-glazed solar cooker [28].

A simple solar cooker of hot box type with a plane booster mirror reflector was designed and evaluated under Egyptian climate. The performance of the cooker was measured experimentally [29, 30]. In Brunei Darussalam, a program to develop, test and evaluate a solar cooker was carried out [31]. Whereas, In Turkey, a box-type solar cooker was designed and its thermal performance is analyzed experimentally. The cooker tracks the sun in two axes, altitude and sun azimuth, by hand control for hourly periods [32]. A cylindrical shaped box type solar cooker was constructed and its thermal performance was tested under the prevailing weather conditions in Karabuk, Turkey. Experiments were conducted on a single glazed cooker with a plane reflector and one cooking pot [33].

One of the earliest mathematical models to test the thermal performance of a Solar Cooker was presented by Garg et. al. [34], and Vaishya et al., [35]. Also, Jubran and Alsaad [36] presented theoretical model for a single and double, glazed box-type solar cookers with or without reflectors. Whereas, Das et. al [37, 38] and Binark and Turkmen [39] developed thermal models for the solar box-cookers loaded with one, two, or four vessels. On the other hand, Funk and Larson [40] presented a model for prediction of the cooking power of a solar cooker based on three controlled parameters (solar intercept area, overall heat loss coefficient, and absorber plate thermal conductivity) and three uncontrolled variables (insulation, temperature difference, and load distribution). A simple mathematical model is presented for a box-type solar cooker with outer-inner reflectors [41]. Ozkaymak [42] developed a mathematical model for a box- type solar cooker with three reflectors hinged at the top of the cooker. Energy-balance equations were applied to components of the cooker such as absorber plate, cooking vessel, cooking fluid, enclosure air inside the cooker, and glass cover.

For transient mathematical models, Yadav and Tiwari [43] presented transient analytical study of box type solar cookers. Elsebaii, et. al [44] designed and constructed a box-type solar cooker with multi-step inner reflectors. The inner reflectors were arranged in a three-step fashion to create different angles with respect to the horizontal. A transient mathematical model is presented for the cooker. Also, Elsebaii and Aboulenein [45] developed such a model for a box-type solar cooker with a one step outer reflector hinged at the top of the cooker.

A novel solar cooker that does not require any tracking, has been designed, fabricated and tested and its performance has been compared with the hot-box solar cooker. The performance of the novel solar cooker is almost similar with the hot-box solar cooker though it is kept fixed while the hot box is tracked towards the sun every hour. The overall efficiency of the novel solar cooker has been found to be 29.5%. [46]. A double reflector hot box solar cooker with a Transparent Insulation Material has been designed, fabricated, tested and the performance compared with a single reflector hot box solar cooker without TIM [47].

3. Experimental System Set-up

The experimental tests on the solar cookers were carried out during the successive days from the 29^{th} and 31^{st} /10/2007 and 2^{nd} /11/ 2007. Each experiment starts from 7:30 am in the morning to 16:00 pm in the afternoon. The electrical and electronic parts were tested and calibrated before being used on the various designs on both solar cookers. The experimental work was fully carried out in the Renewable Energy laboratory at the Applied Science University, Amman-Jordan.

The first part of this research work concentrated on testing of two box type cookers: traditional black painted cooker and internal installed mirrors cooker as shown in Figure 1. Both cookers are fixed at a position towards the south. The second part is testing the traditional black painted cooker with a tracking system to the sun movement. Figure 2 shows schematic diagram of three dimension of the solar cooker installed on a horizontal sun tracking system. It shows the base, motor and bearing and sun cooker.

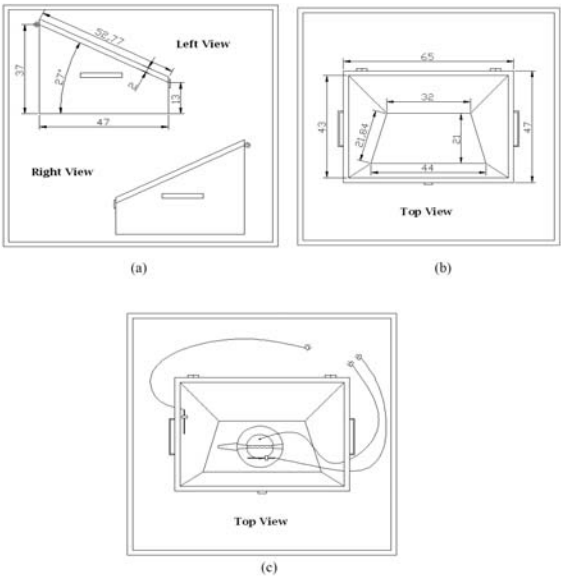

Figure 2 Three dimensional views of the designed solar cooker, (a) and (b) are cooker dimensions in cm, and (c) thermocouple connections in the cooker

Three thermocouples at different locations were installed on the solar cooker. These locations are: a) Outer glass temperature, b) Metallic pot side temperature, and c) water temperature inside the pot. Also, ambient shaded and un-shaded temperature measurements were taken.

Solar intensity radiation was measured by Kipp and Zonen Pyranometer type (CM5) and fixed at a horizontal position. A Digital multi-meter was used to record the output voltage in mV. The device records the data on an accumulative basis and shows the radiation on an instantaneous basis. The temperature measurements were carried out using *K* type thermocouple coupled to digital thermometer with range from -50 to150 ^oC. The accuracy of this thermometer is in the range of 0.3 ^oC for the temperature measurements between 1 to 99 ^oC.

4. Results and Discussion

The total input solar energy $Q_{total} = (\tau\alpha) I_s A_g$ which is equal to the summation of the stored internal energy inside the cooker Q_i and the energy loss from the top side Q_{top}, and the energy loss from both bottom and lateral Q_{bottom}. Well established model which neglects the heat capacity of the pot is presented by Jansen 1985 and Kreith and Kreider 1978. It applies the following expression:

$$Q_{water} = Q_{total} - Q_{losses} = Q_{total} - (Q_{top} + Q_{bottom})$$

$$mc(T' - T_w)/\Delta t = [(\tau\alpha) I_s A_g - U_t A_g (T_g - T_a) - U_b A_{wall} - (T_{wall} - T_a)]$$

In the case of fixed cooker, the $\tau\alpha$ (transmittance – absorptance product) changes at different altitude angle as the sun changes its position hourly. Whereas, in the case of tracking system $\tau\alpha$ is at maximum of 0.9.

The thermal performance of both proposed cookers with internally black coated surface and reflecting mirrors is investigated in this section. The results obtained are plotted as recorded water and metal temperatures against the operating time for fixed position and on tracking system.

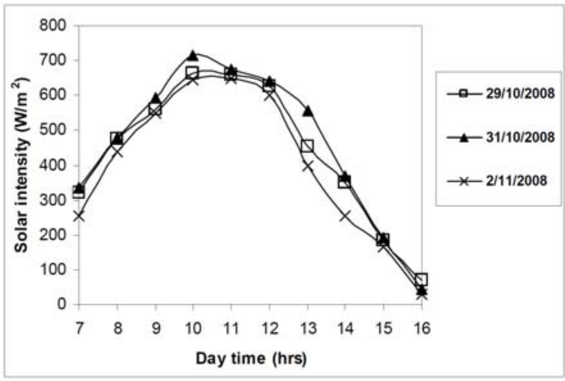

Figure 3 Solar intensities for the three working days

Figure 3 shows the change in the hourly solar intensity for the three working days. It is clear the maximum solar intensity was around mid noon (10:00-12:00 pm).

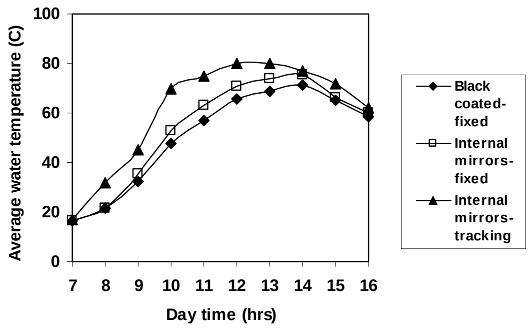

Figure 4 Average water temperature for the three proposed systems at the three working days.

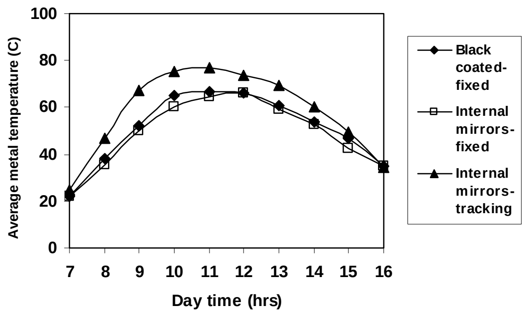

Figure 5 Average metal temperature for the three proposed systems at the three working days

Figures 4 and 5 show the recorded water and metal temperatures through typical summer days (29/10, 31/10, 2/11/2008) from 7:00 am to 16:00 pm. Experiments were carried out for three working days to validate the results obtained. The Figures show an increase in water and metal temperature during early hours of the day until it reaches the maximum temperature around mid noon corresponding to the highest solar radiation then decreases as the sunsets. It is clear that cookers at fixed position with either black coated surface or internal reflecting mirrors gave close water and metal temperature readings. Whereas, cookers installed on a tracking system gave higher temperature readings and this is expected due to maintaining maximum solar energy entering the cooker system. It was noticed that the maximum water temperatures were recorded around 13:00 – 14:00 pm. Whereas, the maximum metal temperature were recorded around 11:00 – 12:00 am. This is logic where the metal of pot will heat up first then the inside water.

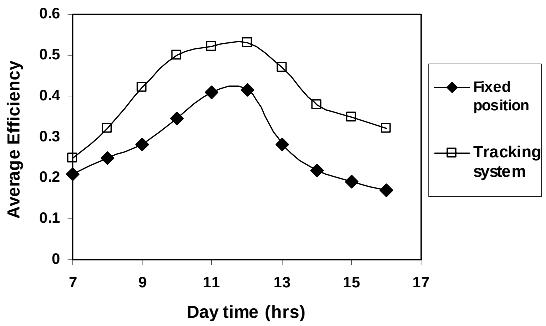

Figure 6 Average efficiency for cookers at fixed and on tracking systems for the three working days

Figure 6 illustrates that cookers at a fixed position had recorded thermal efficiencies ranging from 17 % to a sharp peak of 41.2% at the maximum solar intensity of the day around 11-12 am with an average overall efficiency around 27.6%. Whereas, cooker with internal reflecting mirrors installed on a sun tracking system gave higher water and pot temperatures, and thermal efficiency ranged from 25.3% to 53.1% with an average overall efficiency around 40.6 %. Cookers installed on sun tracking system had the advantage of maintaining a higher and closer range of thermal efficiencies through the daylight than the ones at fixed positions.

5 Conclusion

After conducting statistical analysis on the data obtained from the cookers, It is clear that both types of cookers (black coated and internal reflecting mirrors) at fixed position gave similar thermal performance where the averaged water and pot temperatures were close within $\pm$ 7% margin of error. The cookers thermal efficiencies at a fixed position ranges from 12 % to an increasing sharp peak of 41.2% at the maximum solar intensity of the day around 11-12 am with an average overall efficiency around 27.6%. Whereas, cooker with internal reflecting mirrors installed on a sun tracking system gave higher water and pot temperatures, and thermal efficiency ranged from 25.3% to 53.1% with an average overall efficiency around 40.6 %. Cookers installed on sun tracking system had the advantage of maintaining a higher and closer range of thermal efficiencies through the daylight than the ones at fixed positions.

References:

[1] M. Telkes, "Solar cooking ovens". Solar Energy Vol. 3,1958, 1-11.

[2] H. Burkhardt, "Solar cooking: the dormant giant in appropriate technology". Report 39, Ryerson Energy Centre, Toronto, 1982.

[3] A.W.G. Cope and N. Tully, 1981, "Considerations on the development of an urban solar cooker"., South African Mechanical Engineer, Vol. 31. No. 9, 1981, 226-234.

[4] K. S. Malhotra, N.M. Nahar, B.V.R. Rao, "An improved solar cooker". International Journal Of Energy Research, Vol. 6, No. 3, 1982, 227-231.

[5] J.D. Walton, "Development of a solar cooker using the spiral Fresnel concentrator". Appropriate Technology, Vol. 10, No. 2, 1983, 27-29.

[6] V. John et.al., "A solar cooker for the common Man". Research And Industry, Vol. 30, No. 1,1985, 1-5.

[7] G.N. Tiwari ,Y.P. Yadav, "A New Solar Cooker Design". Energy Conversion and Management Vol. 26, No. 1, 1986, 41-42.

[8] A.M.A. Khalifa, M.M.A. Taha, M. Akyurt, "Design, simulation, and testing of a new concentrating type solar cooker". Solar Energy Vol. 38, No. 2, 1987, 79-88.

[9] P.C. Pande and K.P. Thanvi, "Design and development of a solar cooker for maximum energy capture in stationary mode". Energy Conversion and Management, Vol. 27, No. 1, 1987, 117-120.

[10] M. Grupp, P. Montagne, M. Wackernagel, "A novel advanced box-type solar cooker". Solar Energy, Vol. 47, No. 2, 1991, 107-113.

[11] Garg H.P and Thanvi, K.P., 1976, Design and performance studies on simple hot box type solar cooker. Res. Ind. 21, 186-187.

[12] Garg, H.P., Mann H.S. and Thanvi, K.P., 1978, Performance evaluation of five solar cookers. Sun : Mankind's Future Source of Energy, Vol. 3, pp. 1491 1496. Pergamon Press, Oxford.

[13] M.M. Hoda, Solar cookers, ISES-U.K. Conference, London, 1977.

[14] M.G. Osman, "Solar energy for cooking in Egypt". Solar Energy: International Progress Vol. 4, 1980, 1768-1795.

[15] V.M. Shrestha, "Modification of the solar cooker". Solar Wind Technol. Vol. 4, 1987, 305-311.

[16] N.M. Nahar, "Performance and testing of a low cost solar water heater cum solar cooker". Solar Wind Technol. Vol. 5, 1988, 611-615.

[17] K.D Mannan et al., "Thermal performance and cooking evaluation of compound cone solar ovens". Proc. Solar Energy Soc. Indian National Solar Energy Convention, Bangalore.1982

[18] A. Whillier, "A stove for boiling foods using solar energy". Sun at Work Vol. 10, 1965, 9-12.

[19] T.E. Bowman, 1979, "Solar cookers: test results and new designs". Simp. Int. de Ing., San Salvador, 1979.

[20] A. Khalifa, M. Taha, and M. Akyurt, "An energy thrifty solar cooker,the Mina oven". Solar Wind Technol. 1, 8141, 1984.

[21] N.M. Nahar, "Performance and testing of an improved hot box solar cooker". Energy Cconversion and Management Vol. 30, No.1, 1990, 9-16.

[22] S.C. Mullick, T.C. Kandpal, S. Kumar, 1991, "Thermal test procedure for a paraboloid concentrator solar cooker". Solar Energy, Vol. 46, No. 3, 1991, 139-144.

[23] S. John, et.al., " Studies on a new combined concentrating oven type solar cooker". Energy Conversion and Management, Vol. 32, No. 6, 1991, 537-541.

[24] N.M Nahar, J.P. Gupta, P. Sharma, "Performance and testing of an improved community size solar cooker". Energy Conversion and Management, Vol. 34, No. 4, 1993, 327-333.
[25] R.S. Mishra and S.P.S.J. Prakash, "Evaluation of solar cooker thermal performance using different insulating materials". International Journal of Energy Research, Vol. 8, No. 4, 1984, 393-396.
[26] N.M. Nahar, R.H. Marshall, B.J. Brinkworth, "Studies on a hot box solar cooker with transparent insulation materials". Energy Conversion and Management, Vol. 35, No. 9, 1994, 787-791.
[27] A.H. Algifri,H.A. Al-Towaie, "Efficient orientation impacts of box-type solar cooker on the cooker performance". Solar Energy, Vol. 70, No. 2, 2001, 165-170.
[28] S. Kumar, "Estimation of design parameters for thermal performance evaluation of box-type solar cooker". Renewable Energy, Vol. 30, No. 7, 2005, 1117-1126.
[29] S.M.A. Ibrahim, M.K. Elreidy, "The performance of a solar cooker in Egypt". Energy Sources, Vol. 15, No. 3, 1993, 415-431.
[30] S.M.A. Ibrahim, M.K. Elreidy, "The performance of a solar cooker in Egypt, Renwable Energy, Vol. 6, No. 8, 1995, 1041-1050.
[31] A.Q. Malik, H. Binhussen, " Development of a solar cooker in Brunei Darussalam". Renewable Energy, Vol. 7, No. 4, 1996, 419-425.
[32] G. Oturanc, N. Ozbalta, A. Gungor, "Performance analysis of a solar cooker in Turkey". International Journal of Energy Research, Vol. 26, No. 2, 2002, 105-111.

[33] H. Kurt, "Experimental investigation of thermal performance of hot box type solar cooker". Journal of the Energy Institute, Vol. 79, No. 2, 2006, 120-124.
[34] H.P. Garg, B. Bandyopadhyay,G. Datta, "Mathematical-modeling of the performance of a solar cooker". Applied Energy, Vol, 14, No.3, 1983, 233-239.
[35] J.S. Vaishya et.al., "A hot box solar cooker - performance analysis and testing". Energy Conversion and Management, Vol. 25, No. 3, 1985, 373-379.
[36] B.A. Jubran, M.A. Alsaad, "Parametric study of a box-type solar cooker". Energy Conversion and Management, Vol. 32, No. 3, 1991, 223-234.
[37] T.C.T. Das ,S. Karamakar,D.P. Rao, "Solar box-cooker, 1. Modeling". Solar energy, Vol. 52, No. 3, 1994, 265-272.
[38] T.C.T. Das ,S. Karamakar,D.P. Rao, "Solar box-cooker, 2. Analysis and simulation". Solar Energy, Vol. 52, No. 3, 1994, 273-282.
[39] A.K. Binark, N. Turkmen, "Modelling of a hot box solar cooker". Energy Conversion and Management, Vol. 37, No. 3, 1996, 303-310.
[40] P.A. Funk, D.L. Larson, "Parametric model of solar cooker performance". Solar Energy, Vol. 62, No. 1, 1998, 63-68.
[41] A.A. Elsebaii, "Thermal performance of a box-type solar cooker with outer-inner reflectors", Energy, Vol. 22, No. 10, 1997, 969-978.
[42] M. Ozkaymak, "Theoretical and experimental investigation of a hot box-type solar cooker performance". Journal of Power and Energy, Vol. 221, 2007, 91-97.
[43] Y.P. Yadav, G.N. Tiwari, "Transient analytical study of box-type solar cooker". Energy Conversion and Management, Vol. 27, No. 2, 1987, 121-125.
[44] A.A. Elsebaii, R. Domanski, M. Jaworski, "Experemental and theoretical investigation of a box-type solar cooker with multistep inner reflectors". Energy, Vol. 19, No. 10, 1994, 1011-1021.
[45] A.A. Elsebaii, S. Aboulenein, "A box-type solar cooker with one-step outer reflector". Energy, Vol. 22, No. 5, 1997 ,515-524.
[46] N.M. Nahar, "Design, development and testing of a novel non-tracking solar cooker". International Journal of Energy Research, Vol. 22, No. 13, 1998, 1191-1198.
[47] N.M. Nahar, "Design, development and testing of a double reflector hot box solar cooker with a transparent insulation material". Renewable Energy, Vol. 23, No. 2, 2001, 167-179.
[48] Jansen TJ. Solar engineering technology. Englewood Cliffs, NJ: Prentics Hall; 1985.
[49] Kreith F and Kreider JF. Principles of solar engineering. New York: McGrawHill; 1978.

Nomenclature

T' : The temperature after a certain time (one hour in the conducted experiments)
T_w : Water temperature
T_{wall}: Water temperature
T_g : Glass temperature
mc : Water heat capacity (kJ K^{-1})
$\tau\alpha$:The transmittance – absorptance product
A_g : The glass area (m^2)
U_t : The top loss coefficient (w m^{-2} K^{-1})
T_a : The ambient temperature (K)
U_b : The bottom and lateral loss coefficient (w m^{-2} K^{-1})
A_w : The insulated wall area (m^2)
I_s : Values were measured

المملكة الأردنية الهاشمية

الجامعة الهاشمية

المجلة الأردنية للهندسة الميكانيكية والصناعية

JJMIE

مجلة علمية عالمية محكمة

http://jjmie.hu.edu.jo/

ISSN 1995-6665

المجلة الأردنية للهندسة الميكانيكية والصناعية
مجلة علمية عالمية محكمة

المجلة الأردنية للهندسة الميكانيكية والصناعية: مجلة علمية عالمية محكمة تصدر عن عمادة البحث العلمي والدراسات العليا في الجامعة الهاشمية بالتعاون مع صندوق دعم البحث العلمي في الأردن.

ترسل البحوث إلى العنوان التالي :

ترسل البحوث إلى العنوان التالي:
رئيس تحرير المجلة الأردنية للهندسة الميكانيكية والصناعية
عمادة البحث العلمي والدراسات العليا
الجامعة الهاشمية
الزرقاء - الأردن

هاتف : 3903333 5 00962 فرعي 4147
Email: jjmie@hu.edu.jo
Website: www.jjmie.hu.edu.jo